$GaAs_{0.75}P_{0.25}$/Si Tandem Solar Cells: Design Strategies and Materials Innovations Enabling Rapid Efficiency Improvements

Dissertation

Presented in Partial Fulfillment of the Requirements for the Degree
Doctor of Philosophy in the Graduate School of The Ohio State University

By
Daniel Leon Lepkowski, B.S., M.S.
Graduate Program of Electrical and Computer Engineering

The Ohio State University
2021

Dissertation Committee:
Professor Steven A. Ringel, Advisor
Professor Tyler J. Grassman Co-Advisor
Professor Sanjay Krishna

ABSTRACT

The solar energy industry has been growing rapidly due to decreasing costs of manufacturing and increasing panel efficiencies. As the industry dominant crystalline Si solar cell technology approaches its fundamental efficiency limits, new strategies for achieving higher efficiency while maintaining low cost is a necessity to continue the industries growth. The only demonstrated way to surpass the fundamental single junction efficiency barrier is through the use of multijunction photovoltaic cells. The multijunction cell architecture splits the solar spectrum to be absorbed by two or more different semiconductor materials with the highest energy photons being absorbed by the wider bandgap top cells, and lower energy light being absorbed by the narrower band gap bottom cells. This technology has been very successfully demonstrated in the III-V materials system and scaled by the space solar industry; however, terrestrial power generation has much stricter requirements on production cost than the space solar industry.

Thus, arises the potential for an interesting marriage of technologies. Imagine combining the highly scaled Si manufacturing infrastructure, the low-cost Si wafer materials, and high efficiency III-V multijunction cells. This is the precise combination present in III-V/Si tandem solar cells. To date, two fabrication methods, mechanical stacking and surface activated wafer bonding, have demonstrated impressive 3-junction solar cells with efficiencies of 35.9%[1] and 34.1%[2] respectively. The issue is that these techniques are not largely considered scalable for terrestrial scale power generation;

however, these prototype devices demonstrate great promise for this III-V/Si device architecture. The most scalable method of III-V/Si integration is through the use of epitaxy to monolithically integrate the III-V and Si solar cells; however, this approach can lead to defect formation due to differences in the lattice parameter, crystal structure, and thermal expansion coefficient between III-V compounds and Si [3]–[6]. The most prevalent defects as a result of this heterogeneous integration are threading dislocations which propagate from the III-V/Si interface and extend all the way to the surface of the III-V material. These threading dislocations are detrimental to top cell performance [7]–[10] and thus overall device efficiency.

This research in this dissertation explores various aspects of ideal bandgap pairing (1.1 eV/1.7 eV) $GaAs_{0.75}P_{0.25}$/Si tandem solar cells with the intent of gaining scientific understanding about the impact of crystalline defects on $GaAs_{0.75}P_{0.25}$ top cell performance, extracting maximum performance for a given TDD through defect resilient designs, and of course improving overall tandem efficiency.

To understand the impact of crystalline defects on $GaAs_{0.75}P_{0.25}$ cell performance, the $GaAs_{0.75}P_{0.25}$ top cell was first coarsely optimized through model informed design changes resulting in high performance $GaAs_{0.75}P_{0.25}$ cells on a low TDD GaAs-based virtual substrate. These low TDD virtual substrates were used as an analog to the technologically relevant Si-based virtual substrate [11]. Porting this identical, semi-optimized design to the higher TDD Si-based virtual substrate allowed for the extraction of performance as a function of TDD [12]. Analytical modeling was used to properly quantify the impact of TDD on transport properties for better informed model-based design throughout the remainder of the work.

To create defect resilient designs, both transport- and optics-based strategies were employed to improve performance at a given TDD. Critical aspects of recombination associated with threading dislocations were exploited by using a rear-emitter design to improve voltage [13], [14]. During this study, the critical role of the window layer properties on passivation was discovered [15]. Optically speaking, a model-based exploration, informed by experimental data, of a $Ga_{0.64}In_{0.36}P/Al_{0.66}In_{0.34}P$ DBR was performed in order to enable a reduction of the base thickness and provide resilience against TDD-induced diffusion length shortening. This strategy shows real promise for further experimental exploration in the near future.

Lastly the improvement of tandem solar cells was driven by a combination of the device design and material quality improvements discussed throughout the dissertation. These advancements raised the AM1.5G efficiency of the $GaAs_{0.75}P_{0.25}/Si$ tandem solar cell from 13.3% to 23.4%, the current verified world record for this technology. Notably this work resulted in the first certified demonstration of efficiency >20% for a monolithic III-V/Si cell, even outperforming the best 3-junction III-V/Si device at the time. Based on the recent reduction in TDD down to 3×10^{6} cm^{-2} and defect resilient device designs on these new virtual substrates discussed herein, the near-term expectation is for efficiency of the $GaAs_{0.75}P_{0.25}/Si$ tandem cell to exceed 27% in the next round of tandem devices. These devices are currently being fabricated. Finally, the realistic pathway to >30% efficient tandem cells was explored, as a function of TDD, through data informed analytical modeling. These results indicate that if TDD can be reduced to ~1×10^{6} cm^{-2}, then efficiencies of greater than 30% should be achievable. This is a critical mark for technology viability in an ever changing technoeconomic landscape.

DEDICATION

To my family, friends, and all those who have inspired me to pursue scientific knowledge.

ACKNOWLEDGEMENTS

I have to start off by saying that I am incredibly lucky to have so many people that have helped, inspired, and befriended me along the way. All of these people formed and molded me into the person and scientist that I am today. This obviously starts with my parents who always tried to instill in me a strong work ethic and a passion for science and the way the world works. It was truly incredible growing up in a family where both of my parents were engineers. I can with great certainty say that the conversations around the dinner table were certainly unique to a family like ours. I wouldn't trade those experiences for the world. I learned my passion for science, my work ethic, and my integrity from you both and it has been something that has served me well throughout my academic journey. Not only am I lucky enough to have my biological family, but also my second family in Ms. Patty and Mr. John. Mr. John your passion for electronics, genuine love of engineering, and willingness to have in-depth discussions about the world are a huge reason that I pursued electrical engineering. Ms. Patty, the joy with which you live life is inspiring and has cheered me up on numerous occasions. So, thank you both for being my family.

Beyond my family, there have been numerous professors, mentors, and friends who have been incredibly influential in my life and without them, none of my successes in graduate school would have been possible. Dr. Stadler, thank you for giving me an opportunity to begin research so early and teaching me proper research fundamentals. Mr. Scalzo, thank you for being the teacher to push me to be my best and not letting me get away with putting in only 90% effort. John West, thank you for going above and beyond to be willing to teach and mentor me when I was at TI, and even more importantly becoming one of my good friends. And lastly, all of my coworkers throughout my time at NSU, NIST, and TI before coming to OSU, thank you for teaching me and being my mentors and friends.

When I met my advisor, Steve, something about our styles, or personalities, or whatever just clicked, and I knew I wanted him to guide me through this journey. We spoke during our first meeting about how technology is driven by decades of incremental advances. This is something that is easy to lose sight of in a scientific ecosystem that is more excited by revolution than evolution. The seemingly small advancements developed over years of research, when stacked atop one another, have revolutionized society in a way no one could have imagined. This is something I have kept in my mind since that day and has always guided my research philosophy. Thank you for inspiring me, pushing me, supporting me, and reassuring me throughout the last 4.5 years. The opportunities you have given me throughout this process, from traveling to conferences around the world, to the next steps in my career, were invaluable. I truly could not have done this without you. I look forward to continuing to work with you down the road on new and innovative technologies and meeting for drinks on the other side of the world.

Tyler, from day one you have always gone above and beyond to guide me and mentor me even when I wasn’t technically your student. You have always taken the time to meet with me, have a beer, or just chat about the world and for that I am forever grateful. The technical knowledge you have imparted on me has truly driven my research to levels where it would never have reached without. Your early work on $GaAs_yP_{1-y}/Si$ integration was foundational in this field and provided a platform for my research to stand out. Without your guidance and mentorship none of this would have been possible. Although not formally until recently, I have always valued you as my advisor, so thank you for investing in me and being my close friend and mentor.

To all of the staff and faculty in SEAL and at Nanotech West, including Mark, John, Aaron, Aimee, Dave, Derek, Paul and others, thank you for assisting me with processing and growth, keeping the tools running thanklessly, and being a friendly face in the lab. Your contributions to this work cannot be overstated.

To my mentors and colleagues in the EMDL, thank you for being the best possible coworkers and friends. Dan C. I would not be the researcher I am today without your guidance, knowledge, and mentorship. When I became a senior student, I always strived to be more like you and mentor younger students as effectively as you mentored me. Jacob, we made a hell of a team for the last 4.5 years and made outstanding progress in this field. Your friendship is something I will always cherish. Zak, Tal, Ari, and Marzieh thank you for being eager to learn and reminding me what it is like to be excited about research. Your exuberance and desire to learn were a breath of fresh air and inspired me to work harder every single day, even when I was burnt out after years of grad school. Lastly, of course, all of the other members of the EMDL past and present: Julia, Christine, Pran, Wenyuan, Hemant, Joe, Mike, Rachel, etc. thank you for all of the laughs, lunches, happy hours, and fun over the last 4.5 years. I will miss all of you dearly.

I would be remised not to mention the financial support I received from the Dept. of Energy PVRD project, NSF Graduate Research Fellowship, and from The Ohio State University. Lastly, to a man I have never met but who has inspired me and many others like me, Dr. Jack Kilby, the Nobel Laureate who invented the integrated circuit. When I look up at the Si wafer signed by you on my wall, I am reminded of the transformational impact you have had on this world. I strive daily to try to solve problems with unique and creative solutions the way you did.

VITA

July 28, 1994	Born –Plano, TX
2016	B.S. Electrical and Computer Engineering, Louisiana State University
2020	M.S. Electrical & Computer Engineering, The Ohio State University
2019 to present	Ph.D. Candidate, The Ohio State University

PEER REVIEWED PUBLICATIONS

D. L. Lepkowski, et al., “Investigation of Rear-Emitter GaAs$_{0.75}$P$_{0.25}$ Top Cells for Application to III–V/Si Tandem Photovoltaics,” *IEEE Journal of Photovoltaics* 9 (6), 1644-1651 (2019).

D. L. Lepkowski, et al. "The Critical Role of AlInP Window Design in III–V Rear-Emitter Solar Cells," *IEEE Journal of Photovoltaics 10 (3), 758-764 (2020).*

D. L. Lepkowski, et al. “Designing an Epitaxially-Integrated DBR for Dislocation Mitigation in Monolithic GaAsP/Si Tandem Solar Cells,” *IEEE Journal of Photovoltaics 11 (2), 400-407 (2020)*

D.L. Lepkowski & D. J Chmielewski, et al. “Metamorphic Tunnel Junctions Grown via MOCVD Designed for GaAs0.75P0.25/Si Tandem Solar Cells*” IEEE Journal of Photovoltaics 11 (2), 408-414 (2020)*

D.L. Lepkowski et al. “23.4% Monolithic Epitaxial GaAsP/Si Tandem Solar Cells and Quantification of Losses from Threading Dislocations” *Solar Energy Materials and Solar Cells, (In Review)*

Z.H. Blumer, J.T. Boyer, A.N. Blumer **D.L. Lepkowski** et al. “Si-matched B$_x$Ga$_{1-x}$P grown via hybrid solid- and gas-source molecular beam epitaxy” *Appl. Phys. Lett.* **117**, 122102 (2020)

J.T. Boyer, A.N. Blumer, Z.H. Blumer, **D.L. Lepkowski** “Reduced Dislocation Introduction in III–V/Si Heterostructures with Glide-Enhancing Compressively Strained Superlattices,” *Cryst. Growth Des.* 2020, 20, 10, 6939–6946

J. T. Boyer, **D. L. Lepkowski**, et al., “Modeling and experimental demonstration of short-wavelength carrier collection enhancement in Ga0.51In0.49P solar cells using graded $(Al_zGa_{1-z})_xIn_{1-x}P$ window-emitter structures,” *Solar Energy Materials and Solar Cells*, **202**, 110133 (2019).

D. J. Chmielewski, **D. L. Lepkowski**, et al., “Comparative Study of >2 eV Lattice-Matched and Metamorphic (Al)GaInP Materials and Solar Cells Grown by MOCVD,” *IEEE Journal of Photovoltaics* 8 (6), 1601-1607 (2018).

CONFERENCE PRESENTATIONS/PROCEEDINGS:

D. L. Lepkowski, et al. “Loss analysis and design strategies enabling >23% efficiency GaAsP/Si Tandem Solar Cells” 2020 IEEE 47th Photovoltaic Specialist Conference (PVSC), Virtual, 2020

D. L. Lepkowski, et al. "Investigation of Rear-Emitter GaAsP Top Cells for use in III-V/Si Tandem Photovoltaics," 2018 IEEE 7th World Conference on Photovoltaic Energy Conversion (WCPEC) Waikoloa Village, HI, 2018, pp. 2642-2647.

D. L. Lepkowski, et al. “The Critical Role of Window Design in Rear-Emitter Solar Cells” 2019 IEEE 46th Photovoltaic Specialist Conference (PVSC), Chicago, IL, 2019, pp. 1021-1024.

D. L. Lepkowski et al., “Progress Towards >30% Efficient III-V/Si Tandem Solar Cells,” 61st Electronic Materials conference, Ann Arbor, MI, (2019)

D. L. Lepkowski et al., “Theoretical Evaluation of DBR Structures for Improving Tolerance to Threading Dislocations in GaAsP/Si Tandem Solar Cells,” 62nd Electronic Materials Conference, Virtual, (2020)

T. Kasher, Z. H. Blumer, J. T. Boyer, **D. L. Lepkowski** et al., "Exploration of RF sputtered Ga_2O_3 as a Transparent conductive Oxide for application to photovoltaics," 62nd Electronic Materials Conference, Virtual (2020)

J. T. Boyer, A. N. Blumer, Z. H. Blumer, **D. L. Lepkowski**, et al., "Development of Low-TDD GaP/Si Virtual Substrates via Correlation of Dislocation Dynamics, Electron Channeling Contrast Imaging and MOCVD Growth," 62nd Electronic Materials Conference, Virtual (2020)

T. J. Grassman, **D. L. Lepkowski**, et al., "Toward >25% Efficient Monolithic Epitaxial GaAsP/Si Tandem Solar Cells," 2019 IEEE 46th Photovoltaic Specialist Conference (PVSC), Chicago, IL 0734-0737 (2019)

J. T. Boyer **D. L. Lepkowski** et al., "Development and Characterization of III-V/Si Multijunction Photovoltaics for Space Application," 2019 IEEE 46th Photovoltaic Specialists Conference (PVSC), Chicago, IL, USA, 2019, pp. 2822-2825.

J. T. Boyer, A. N. Blumer, Z. H. Blumer, F. A. Rodriguez, **D. L Lepkowski** et al., " Development of Low-TDD $GaAs_yP_{1-y}$/GaP/Si Metamorphic Materials for High-Efficiency III-V/Si Photovoltaics," 2020 IEEE 47th Photovoltaic Specialists Conference (PVSC), Virtual, 2020.

D. J. Chmielewski, **D. L. Lepkowski**, et al., "High Performance Metamorphic Tunnel Junctions for GaAsP/Si Tandem Solar Cells Grown via MOCVD," 2018 IEEE 7th World Conference on Photovoltaic Energy Conversion (WCPEC) Waikoloa Village, HI, 2018, pp. 2631-2634.

T. J. Grassman, **D. L. Lepkowski**, et al., “Progress Towards High-Performance Monolithic Epitaxial GaAsP/Si Tandem Solar Cells,” 2018 IEEE 7th World Conference on Photovoltaic Energy Conversion Waikoloa Village, HI, (2018).

C. Yi, F. Ma, H. Mehrvarz, **D. L. Lepkowski,** et al., "Effect of Silicon Front Surface Doping Profile on GaP/Si Heterostructure for III-V/GaP/Si Multi-junction Solar Cells," 2018 IEEE 7th World Conference on Photovoltaic Energy Conversion, Waikoloa Village, HI, 2018, pp. 0275-0278.

D. J. Chmielewski, C. Jackson, J.T. Boyer, **D. L. Lepkowski**. et al., "Comparative Study of >2 eV Lattice-Matched and Metamorphic (AL)GaInP Materials and Solar Cells Grown by MOCVD," 2017 IEEE 44th Photovoltaic Specialist Conference (PVSC), Washington, DC, 2017, pp. 215-218.

Jacob T. Boyer, **D. L. Lepkowski** et al. “Graded (AlzGa1-z)xIn1-xP Window-Emitter Structures for Improved Short-Wavelength Response” 2017 IEEE 44th Photovoltaic Specialist Conference (PVSC), Washington DC, 2017, 2079-2083

A. C. Silvaggio, **D. L. Lepkowski**, “Optimization of a GaAsP Top Cell for implementation in a III-V/Si tandem structure,” 2017 IEEE 44th Photovoltaic Specialist Conference (PVSC), Washington D.C.,2017, pp. 2554-2557

FIELDS OF STUDY

MAJOR FIELD: Electrical & Computer Engineering

TABLE OF CONTENTS

CHAPTER 3: GROWTH AND FABRICATION OF GAAS$_{0.75}$P$_{0.25}$/SI SOLAR CELLS 40

CHAPTER 4: MATERIALS AND DEVICE CHARACTERIZATION TECHNIQUES 69

CHAPTER 5: SOLAR CELL DEVICE MODELING 96

LIST OF TABLES

LIST OF FIGURES

CHAPTER 1:

INTRODUCTION

1.1. ECONOMIC DRIVING FACTORS IN SOLAR TECHNOLOGIES

The solar industry has been rapidly growing with over 100 GW of new solar installed in 2018 alone bringing to total to 503 GW of global installed solar capacity [16]. This growth has been driven by rapidly improving cell performance and economies of scale which lead to decreasing costs. At present the solar industry is dominated by crystalline Si photovoltaics (Si-PV), making up >90% of the installed solar capacity worldwide. Recent improvements to manufacturing techniques and cell designs have enabled a record solar cell efficiency of 26.7% [17]. This value is exceedingly close to the theoretical efficiency limit of Si (29.4%) [18] and practical limit of ~27% [19] due to the highly mature cell technology which has been in development since the first Si solar cell in the 1954 [20]. Therefore, improvements to efficiency are becoming increasingly difficult and expensive.

Other technologies have attempted to usurp Si-PV's dominance in the market by using low-cost thin film semiconductors to replace the much thicker wafers used in

Si-PV. This is done with the intent of reducing costs both in materials use as well as manufacturing. These technologies, like CdTe, tend to sacrifice efficiency in favor of cost in order to be competitive; however, the continued cost reductions of the Si-PV industry, as they have scaled to >100 GW/yr scale production capacities, has largely crippled this strategy.

1.2. MULTIJUNCTION SOLAR CELLS

Instead of reducing costs, making monumental strides in efficiency is another pathway to be cost competitive with the dominant Si-PV industry. The only demonstrated way to surpass the fundamental single junction efficiency barrier is using multijunction photovoltaic cells (MJ-PV). This MJ-PV strategy splits the solar spectrum to be absorbed by two or more different semiconductor materials with the highest energy photons being absorbed by the wider bandgap top cells, and lower energy light being absorbed by the narrower band gap bottom cells (as discussed in Chapter 2). This technology has been very successfully demonstrated in the III-V materials system and scaled by the space solar industry to ~ MW/year scale; however, terrestrial power generation has much stricter requirements on production cost than the space solar industry. The cost of less widely available substrates such as Ge and GaAs make fabrication of large area multijunction cells infeasible from an economic perspective. Concentrator photovoltaics (CPV), where large low-cost optics focus light onto micro MJ-PV cells, had exhibited moderate success in the terrestrial marketplace, but eventually lost the cost battle to Si-PV due to high module and solar tracking costs.

1.3. SI-BASED TANDEMS

The technoeconomic driving forces, discussed in the prior subsections, open the doors for a particularly interesting marriage of technologies. The combination of the highly scaled Si manufacturing infrastructure, the low-cost Si wafer materials, and high efficiency III-V MJ-PV architectures may enable low-cost, high efficiency solar cells if coupled together properly. As such, there are numerous methods for integrating III-V MJ-PV with Si in a monolithic device such as epitaxial integration (the focus of this work), mechanical stacking, and surface activated wafer bonding.

The latter two integration pathways have been very successful, demonstrating 3-junction III-V//Si efficiencies of 35.9% [1] and 34.5% [17], [21] for mechanical stacking and wafer bonding respectively. These two techniques rely on separately produced III-V top cells grown on GaAs or Ge substrates. These III-V cells are then removed from their native substrates and placed on top of a separately produced Si solar cell. The drawback to such an approach is that the separate production of the III-V top cells is costly because of the expensive GaAs or Ge substrates. This effectively removes one of the big benefits of leveraging existing Si-PV infrastructure because there is effectively no cost savings in terms of substrates over traditional III-V flat panel cells. These manufacturing techniques are therefore not considered scalable for terrestrial power generation due to the reasons explained above; however, these prototype devices demonstrate great promise for the concept of monolithically integrated III-V/Si tandem device architectures and can be looked to to provide aspirational efficiency targets.

By far, the most scalable method of III-V on Si integration, and the one focused on in this dissertation, is through the use of epitaxy to monolithically integrate the III-V top cell and the Si bottom cell. This not only allows for the Si cell to generate power, but also provides a secondary role as the substrate for the III-V epitaxy. However, this approach leads to defect formation due to differences in the lattice parameter, crystal structure, and thermal expansion coefficient between III-V compounds and Si [3]–[5], [22]. These challenges have limited achieved efficiencies thus far. While the efficiency of epitaxially-integrated III-V/Si have rapidly improved during my tenure, largely due to the advancements presented in this dissertation, efficiencies still lag behind the mechanically stacked and wafer bonded approaches. To date a record 3-junction efficiency of 25.9% [17], [23] and a record 2-junction efficiency, demonstrated in this dissertation, of 23.4% [24] have served to act as a baseline for continued efficiency improvement towards the aspirational values presented by the mechanically stacked and wafer bonded approaches. Additionally, Fan et al. have recently achieved an unverified efficiency of 25.0% for a small area, 2-junction cell [25]. These 2-junction cells are promising as they require a less complex structure than the 3-junction 25.9% efficient cell and have greater reliability against variation in input solar spectrum. Nonetheless, it’s clear that further effort and scientific understanding of growth processes, defect formations, and design constraints are needed to bring these epitaxially-integrated structures on par with the aspirational values provided by their mechanically stacked and wafer bonded counterparts.

While the III-V/Si multijunction cells attempt to leverage the knowledge and years of development in understanding Si-based PV by using an active Si bottom cell, another competitive III-V on Si-PV technology uses a SiGe metamorphic buffer and subsequent III-V multijunction or single junction cells all on an inactive Si substrate[26], [27]. The addition of a SiGe bottom cell can be used to create more ideal bandgap pairings for dual and triple junction cells [28]. Initially, much work on III-V/Si integration has explored this integration pathway, and is still largely preferred in the integrated electronics industry. However, the non-transparent SiGe buffer means that the use of a Si bottom cell is forbidden and would limit the ability to incorporate the already scaled and developed Si-PV industry. Moreover, III-V/Si PV has incredible added value. The integration of Si with III-V technologies offers a tantalizing pathway for adding high performance III-V functionality to Si electronics well beyond the limits of conventional Si in the "beyond Moore's Law" future we are entering. Materials science and device physics advances that are explored in this dissertation advancing III-V/Si solar technology can be substantially leveraged for the future of III-V/Si integrated electronics.

Other Si-based tandem cells not based on III-V materials are under exploration, but traditionally suffer from reliability and stability concerns. Development in thin film materials systems such as hybrid organic-inorganic lead halide-based perovskites (Perovskites), has given rise to new bandgap tunable material systems which can execute the active Si-based tandem concept. To date Perovskite/Si tandem solar cells have achieved impressive efficiencies of 29.52% [17], [29]. This has been done using top cells with bandgaps which are less than the optimal 1.72eV target due to issues in material quality that arise from wider bandgap perovskite materials [30]. Additionally, as noted previously, these thin film cell materials often suffer from degradation induced by light, heat, and moisture which prevents realistic deployment of these technologies. Perovskites, in particular have issues with stability under light and moisture, the origin of which is still under investigation [31]–[34]. Stability has improved substantially in recent years from cell lifetimes of mere minutes to now thousands of hours if properly encapsulated [35]–[38]. However, even these improvements are still not sufficient to justify module deployment and long term bank financing such as is typical in the PV solar plant industry, as 25 year deployments require roughly 220,000 hours of stability, putting high risk on ensuring payback of the up front investment. While stability of monolithically integrated III-V/Si has not been fully explored, III-V materials have demonstrated impressive stabilities in both space and concentrator PV applications and are more likely to achieve degradation rates which are amenable to long-term, 25+ year, deployments [39], [40]. The combination of these economic factors and the promise demonstrated by the mechanically stacked and wafer bonded cells make III-V/Si tandem cells a promising avenue for the next generation of cell performance.

1.4. THE $GAAS_{0.75}P_{0.25}$/SI TANDEM SOLAR CELL

In order to extract maximum power from a tandem solar cell, the optimal bandgap pairing to ensure current matching for series connected devices is necessary. Based on the detailed-balance calculations assuming AM1.5G solar insolation shown in Figure 1.1 [41], the ideal bandgap for the 1.1eV Si bottom cell turns out to be 1.72 eV. Thus $GaAs_{0.75}P_{0.25}$ was chosen at the top cell absorber material due to its 1.72 eV bandgap, and the fact that it has the closest lattice constant to Si for this bandgap. The substantially higher theoretical efficiency for this structure (~44%) over the single junction efficiency

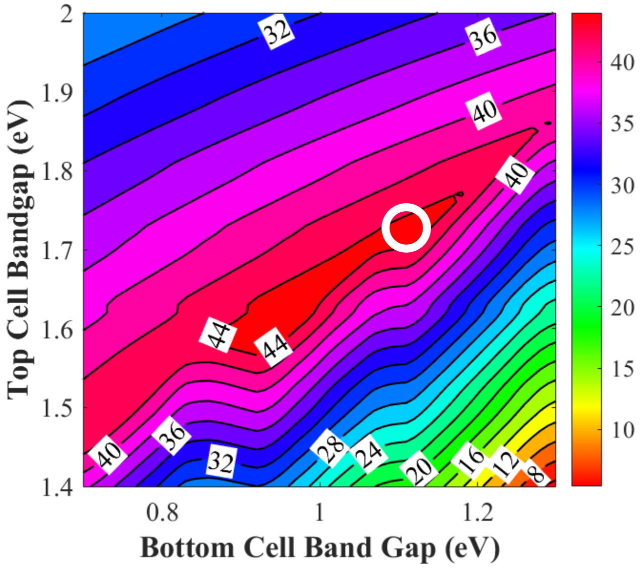

Figure 1.1 MATLAB calculation of the AM1.5G detailed balance theoretical efficiency by any two bandgap pairs. The peak efficiency of >44% is possible for a bandgap pairing of a 1.1 eV bottom cell and a 1.72 eV top cell.

limit of 34% [42] (or 29% for Si [19]), indicates great promise for this technology. Due to the necessity of stacking two p-n junctions on top of one another without the creation of a parasitic diode between them, the two junctions of the $GaAs_{0.75}P_{0.25}$/Si tandem solar cell (with structure shown in Figure 1.2) are connected using a $GaAs_{0.75}P_{0.25}$ tunnel junction interconnect. This creates a series interconnection between the $GaAs_{0.75}P_{0.25}$ top cell and Si bottom cell.

While, in theory, $GaAs_{0.75}P_{0.25}$/Si tandem solar cells sound like a near ideal marriage of existing mature technologies, epitaxial integration of $GaAs_{0.75}P_{0.25}$ and Si provides unique challenges which have yet to be completely solved. The different atomic spacing (lattice constant) between the atoms in the $GaAs_{0.75}P_{0.25}$ alloy and that of the Si substrate results in high quantities of threading dislocations that reduce efficiency. To reduce nucleation of dislocation loops, a GaP nucleation layer and $GaAs_yP_{1-y}$ step-graded

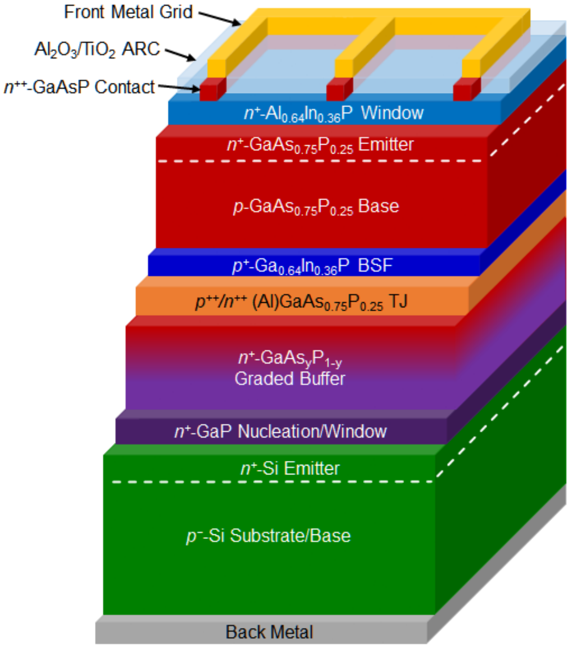

Figure 1.2 The schematic structure of the $GaAs_{0.75}P_{0.25}$/Si tandem solar cell.

buffer are employed to control the rate of strain introduction and provide additional interfaces for dislocation glide. This strategy, shown in the bandgap vs. lattice constant chart in Figure 1.3, provides a semi-transparent lattice constant bridge allowing the light intended for the Si bottom cell to reach the subcell unimpeded. However, even with this reduced rate of strain incorporation, reduction of threading dislocation density (TDD) to less than the commonly agreed upon target of 10^6 cm^{-2} has not yet been achieved [43]–[45]. Additionally, differences in the thermal expansion coefficient between the III-V epitaxial layers and the Si substrate [3] are challenging because of wafer bow and epitaxial cracking during the cool down from growth. The difference in thermal expansion coefficients places a limit on the thickness of III-V material which can be grown on Si to be roughly 8-10um. This limits the thickness of the $GaAs_{0.75}P_{0.25}$ top cell and $GaAs_yP_{1-y}$ step graded buffer.

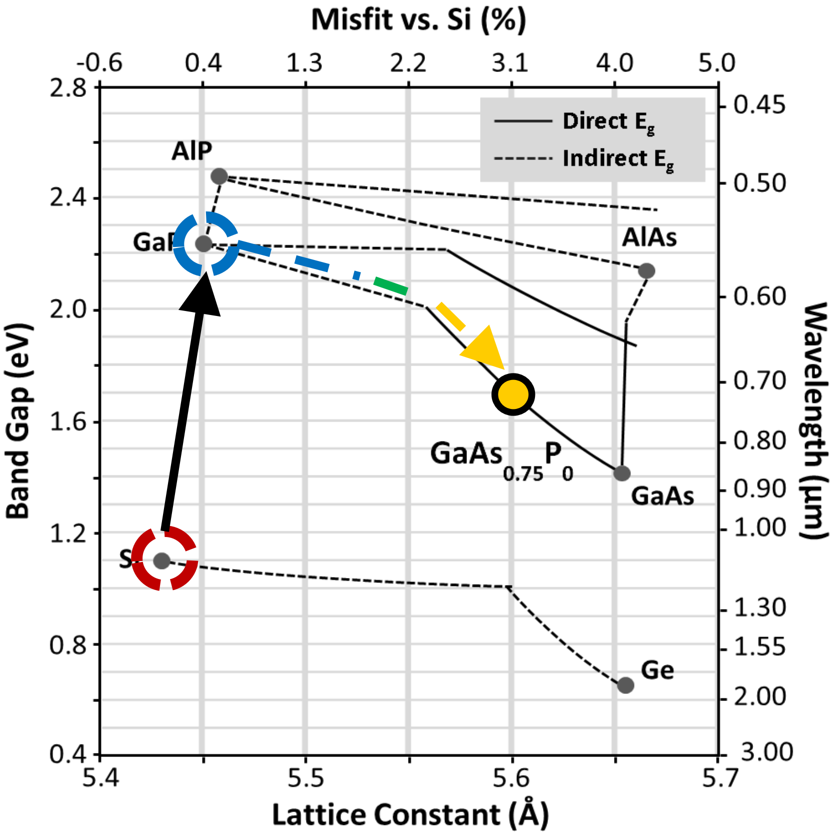

Figure 1.3 Bandgap lattice constant diagram showing the $GaAs_{0.75}P_{0.25}$/Si tandem cell pathway. The difference in lattice constant between $GaAs_{0.75}P_{0.25}$ and Si is problematic as it results in crystalline defects. The $GaAs_yP_{1-y}$ step graded buffer is used to control strain and reduce the quantity of these defects while providing a transparent lattice constant bridge.

1.5. OBJECTIVES

The objective of this dissertation, largely based on overcoming the scientific challenges outlined above and in Chapters 2-5, is generally to improve the efficiency of $GaAs_{0.75}P_{0.25}$/Si tandem solar cells to values that surpass that of Si. In this process, I also focused on creating accurate and robust device development guidelines for a III-V/Si tandem solar cell, and to quantify the pathway to >30% efficient devices. To tackle this problem, I have focused on a number of primary materials science and device engineering goals that generate a holistic effort to meet the objective.

1. The development of experimentally validated device modeling necessary to inform epitaxial device design of the $GaAs_{0.75}P_{0.25}$ top cell.
2. Quantification of the role of dislocations in $GaAs_{0.75}P_{0.25}$ cell performance to better understand the impact of material quality improvements on the potential of the $GaAs_{0.75}P_{0.25}$/Si tandem cell.
3. Design, implementation and demonstration of high performance $GaAs_{0.75}P_{0.25}$ top cells that extract the maximum performance for a given TDD.
4. Reduction of TDD in $GaAs_{0.75}P_{0.25}$/Si materials.

It is through efforts in these 4 main areas that have led to substantial increases in tandem cell efficiency over the past 4.5 years. Ultimately, this resulted in tandem cell efficiencies improving from 13.3% to 23.4% (an ~ 80% relative improvement) with a near term pathway to efficiencies >27%.

1.6. DISSERTATION ORGANIZATION

The dissertation is laid out in the following manner. Chapter 2 looks at the fundamentals of solar cell operation and multijunction solar cells. Chapters 3 and 4 discuss the growth, fabrication, and characterization techniques that were used in the experimental results. Chapter 5 takes a deep dive into the fundamental operation of solar cells and the physical models that describe their operation, including the prior literature that modeled the impact of TDD on device performance. Chapters 6 and 7 focus on development of the $GaAs_{0.75}P_{0.25}$ top cell. Chapter 6 presents top cell development efforts that begin using GaAs-based virtual substrates to achieve lower TDDs while waiting for the development of low TDD Si-based virtual substrates. Then, after the efforts presented in Chapter 8, the $GaAs_{0.75}P_{0.25}$ top cell was redesigned to make use of the improved Si-based virtual substrate. Chapter 7 details two strategies that were explored which attempted to mitigate the impact of elevated TDD on device performance to extract maximum performance from a given TDD. This includes the use of a rear-emitter solar cell and the addition of a distributed Bragg reflector to improve voltage and current performance respectively. Chapter 8 summarizes collaborative efforts between Dr. Jacob Boyer (PhD student colleague in our group) and myself that enabled nearly 10× reduction in TDD. Chapter 9 presents the development of $GaAs_{0.75}P_{0.25}$/Si tandem cells including the pinnacle result of this work, an increase of efficiency from 13.3%, demonstrated just before my arrival at OSU, to now 23.4% and a near term projected efficiency of ~27%. These efforts are detailed on a generation-by-generation basis looking at the key improvements and limitations in each one. Chapter 10 will summarize the key results and detail the remaining efforts that I believe are needed to further improve efficiency to 30% as well as broader applications of this research to new optoelectronic devices and solar cell geometries. Lastly, in the Appendix, numerous MATLAB live scripts are provided that detail many of the analytical models used throughout this work. These live scripts are heavily commented and read more similarly to a textbook rather than code, and therefore can be a good reference in understanding the modeling basics.

CHAPTER 2:

SOLAR CELL DEVICE FUNDAMENTALS

2.1. BACKGROUND

A solar cell is a semiconductor device that absorbs incoming photons and converts them into an electrical current and voltage. The incoming photons create electron-hole pairs by promoting an electron from the valence band to the conduction band. These electrons and holes can freely move about the crystal and are extracted from the semiconductor as current through the ohmic contact at the front and rear of the cell. The buildup of excess electrons and holes generate a voltage in the device causing electrons to flow through an attached load thereby doing work. This chapter will focus on the basic operation of single and multijunction solar cells with the intent being to provide the background necessary to explain the inner workings of the $GaAs_{0.75}P_{0.25}/Si$ tandem solar cell

2.1.1. .SOLAR SPECTRA

The incident light on a solar cell is a critical determining factor in efficiency and power output. The PV community has determined standardized spectra that accurately mimic the average "color" and intensity of light observed both on earth and in space. Both solar spectra are shown in Figure 2.1. The solar spectrum outside of Earth's atmosphere is known as the air mass 0 (AM0) solar spectrum [46]. This spectrum is similar in shape to a 6000 kelvin black body and is often approximated as such. On earth, the average solar spectrum is known as the air mass 1.5 global (AM1.5G) spectrum and has an intensity of 1000 W/m^2 [47]. This spectrum was defined by saying that the average solar ray passes through a thickness of 1.5 atmospheres (measured at normal incidence) before arriving at the earth's surface. This spectrum includes both the direct and scattered

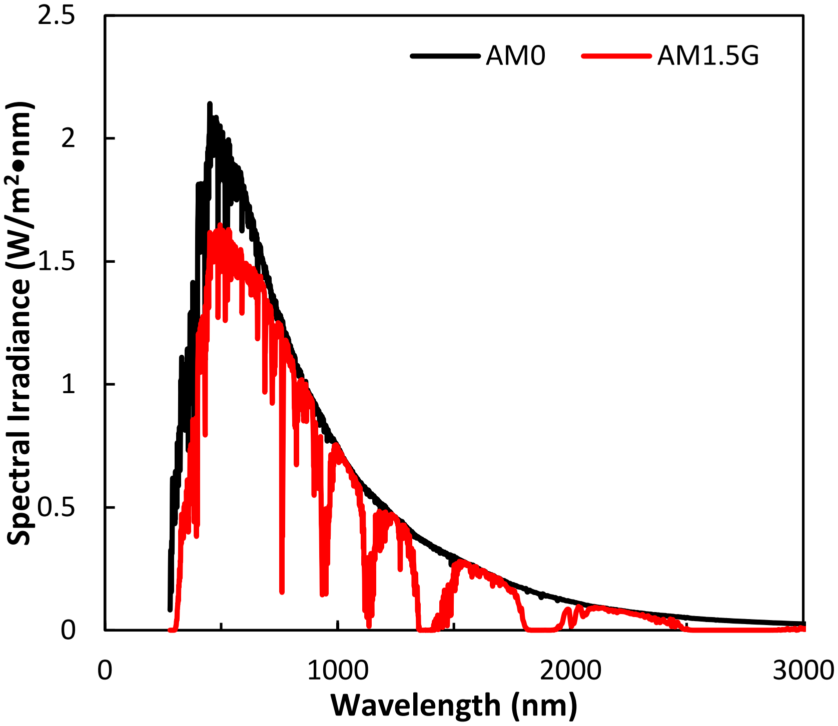

Figure 2.1 Plots of spectral irradiance vs wavelength for the AM0 [46] and AM1.5G [47] solar spectra.

light, which may not arrive at normal incidence. Obviously, due to the tilt of the earth, its spherical shape, the nonuniformity of the earth's atmosphere, and weather patterns different locations see more or less light than the AM1.5G spectrum at any given point in time. However, to standardize the solar spectrum for testing solar cells this averaged AM1.5G spectrum is used as a standard.

The atmosphere does not absorb and scatter uniformly as one might expect. There is a significant loss of short wavelength (blue/UV) light, and sharp absorption bands due to water and oxygen in the atmosphere. These create localized wavelength ranges of less light especially in the near infrared as seen in Figure 2.1.

2.1.2. FUNDAMENTAL LIMITS OF SOLAR CELLS

Optically speaking, there is a fundamental tradeoff that places a limit on the maximum efficiency of a solar cell. The semiconductor absorber used in the creation of a solar cell can only absorb light at energies greater than its bandgap. This means that a portion of the solar spectrum will always be transmitted and unable to produce electron hole pairs, as seen in Figure 2.2a. When the energy of the light is equal to the bandgap energy, some electrons are promoted from the valance band into the conduction band. However, the probability of this transition occurring is low due to a small number of electronic states present at the valence and conduction band edges. Thus, absorption is weak, and a very thick semiconductor absorber is needed to completely absorb all photons (Figure 2.2b). When energies of the photons far exceed the bandgap of the semiconductor absorber, electrons from the valance band are promoted into high energy states in the conduction band. Because there is a continuum of states present in the

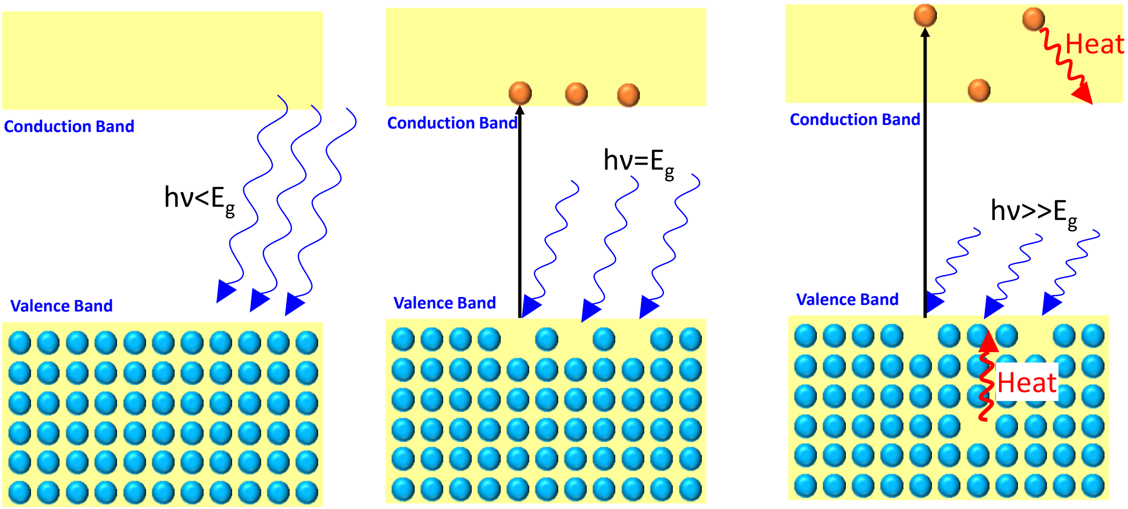

Figure 2.2 Photon interactions with the electrons in the valence band for various photon energies.

conduction band, these newly promoted electrons release energy as heat and reduce their energy to the lowest available energy state (i.e. the conduction band edge), as seen in Figure 2.2c. Thus, the difference in energy between the incoming higher energy photons and the bandgap is lost as heat.

These optical losses provide the basis for the fundamental limit on efficiency as seen in the calculations performed in Figure 2.3. The greyed-out regions of the AM1.5G solar spectrum indicate the optical losses for a semiconductor absorber with a bandgap of 1.1eV. One could imagine that there is now a tradeoff present whereby a lower bandgap increases the thermalization losses and a higher bandgap increases transmission losses. This concept is formalized in the Shockley-Queisser (S-Q) efficiency limit which formally dictates the detailed balance theoretical efficiency limit as a function of bandgap [42]. The calculation of the S-Q limit is shown in Figure 2.4. The peak theoretical efficiency is ~34% at a bandgap of 1.45eV. However, this calculation only accounts for the optical and thermodynamic losses. In reality, the voltage output of a solar cell cannot

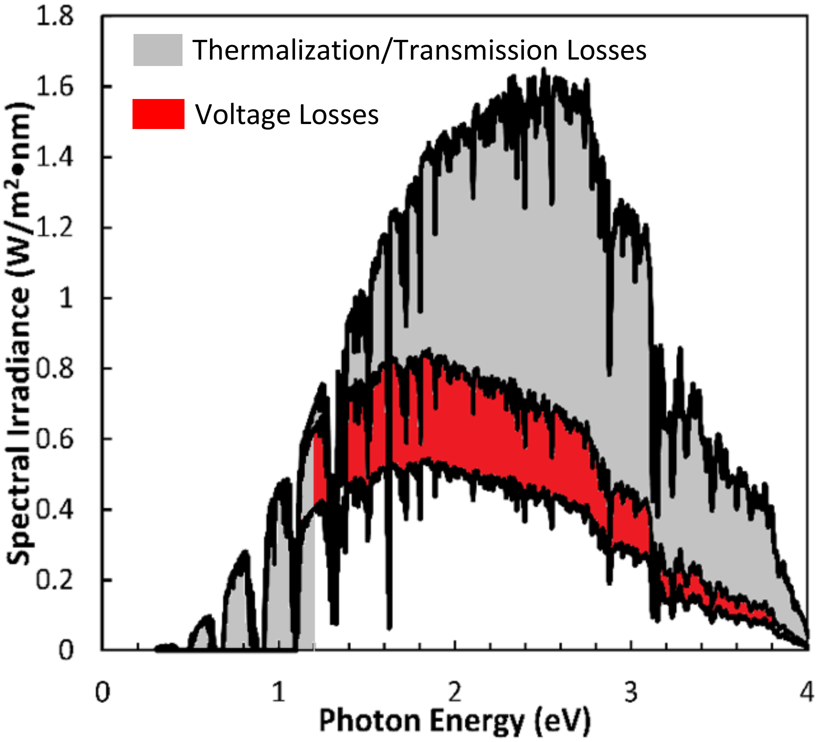

Figure 2.3 AM1.5G solar spectrum detailing the thermalization/transmission losses and losses associated with not achieving a voltage equivalent to the bandgap (voltage losses).

be equal to its bandgap (even if the Fermi levels are coincident with their respective majority carrier band edges on both sides of the junction) due to necessary minority carrier recombination. This results in further losses as seen in the red region in Figure 2.3. Ultimately, this results in a peak experimentally achieved single junction efficiency record of 29% for a GaAs cell and 26.7% for a Si cell [17].

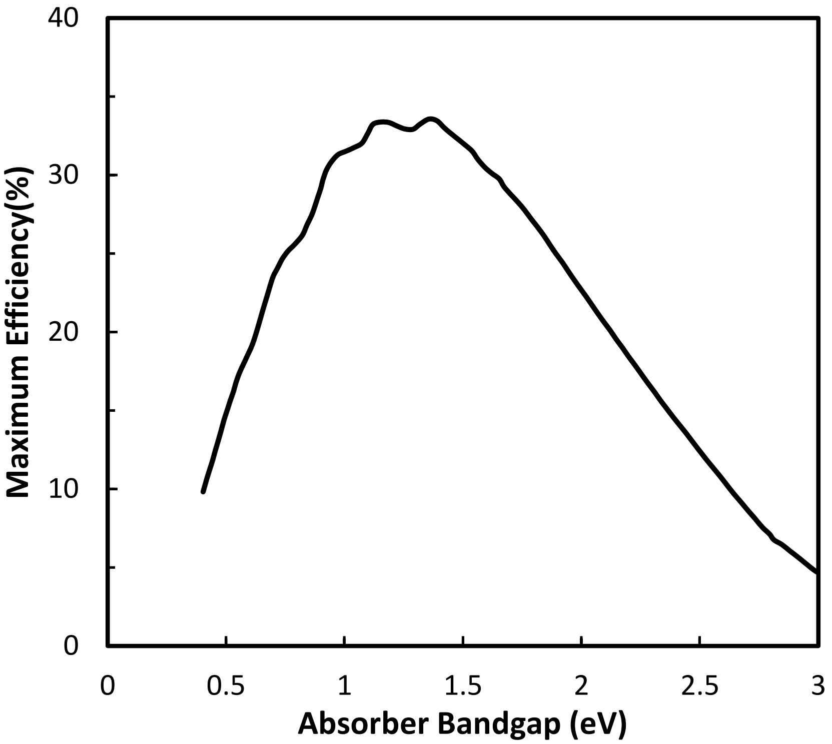

Figure 2.4 Calculation of the detailed balance/Shockley-Queisser efficiency limit for a single junction solar cell [42].

2.2. FUNDAMENTAL SOLAR CELL OPERATION

The majority of the background presented in this section was learned from the textbooks by Hovel [48], Green [49], Smets [50], and Fonash [51]. I found these to be highly valuable references for the basics of solar cell operation. Present day solar cells are based upon *p-n* junctions or diodes. These diodes provide the mechanism to separate electrons and holes, thereby creating a voltage. Solar cells typically employ a highly-doped emitter layer, which is usually thin, and a lightly-doped base layer that is much thicker. In III-V solar cells, the primary focus of this dissertation, to avoid recombination at surfaces and ohmic contacts, a double heterostructure can be employed (Figure 2.5). The concept is to sandwich (i.e. clad) the emitter and base layers between two wider

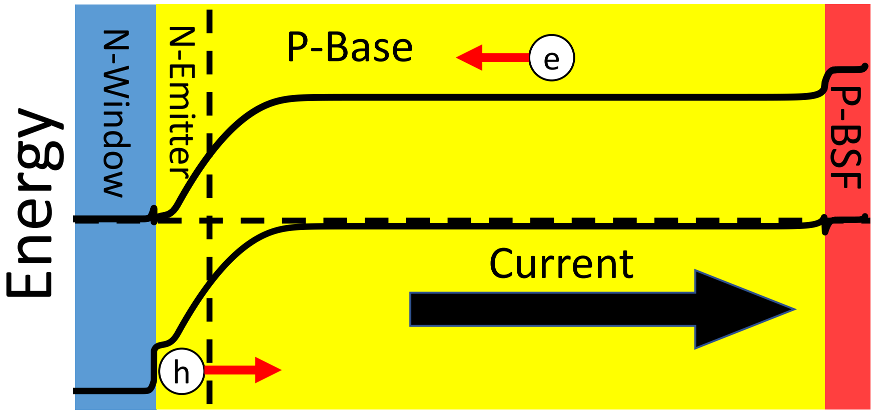

Figure 2.5 Band Diagram/Structure of a typical front-emitter III-V cell architecture.

bandgap materials. This strategy is also used in III-V LEDs and laser diodes as it effectively contains minority carriers and improves carrier lifetimes. The cladding on the front of the solar cell is referred to as the window and the one on the back is referred to as a back surface field (BSF). If the cladding layers are properly designed, very little recombination will occur at the cladding/emitter and base/cladding interfaces. These cladding layers reflect minority carriers that diffuse the wrong way and prevent them from reaching surfaces with high interface recombination velocities. It is also important to note how the window and BSF act as carrier selective contacts for the minority carriers in the emitter and base respectively. An example structure of a solar cell with band diagram is shown in Figure 2.5. The electrons, generated in the *p*-type base, diffuse to the edge of the depletion region where they are acted upon by the built-in electric field, sweeping across to the emitter. This causes a current to flow out of the device in the direction of the *p*-type side of the junction. This is opposite direction of the current in a standard forwards biased diode or *p*-*n* junction. The mechanisms for collection of the minority carriers are discussed later in this chapter and more in depth in Chapter 5.

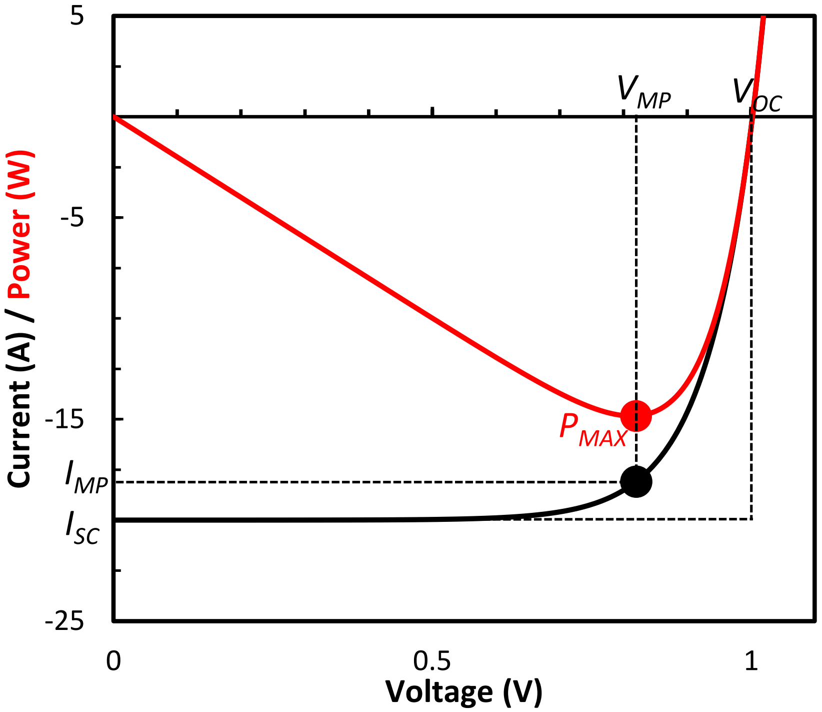

Figure 2.6 Illuminated I-V and P-V curves with critical solar cell metrics defined. These curves are often replaced by J-V curves which normalize the current to the device area.

The illuminated I-V (LIV) curve of a solar cell is shown in Figure 2.6. The curve exists in the 4th quadrant as this is a power generation quadrant. Oftentimes, the PV community flips this *I-V* curve into the 1st quadrant for the sake of convenience; however, it is not technically accurate as the 1st quadrant implies power consumption rather than generation. Additionally, many in the community prefer to normalize the device *I-V* curve to the device area as it more easily allows for the calculation of efficiency and comparison across devices of different sizes. This results in an illuminated *J-V* curve but is still mostly referred to as an LIV curve.

There are several of key metrics that can be extracted from the LIV curve of a solar cell that will be referred to throughout this dissertation. The first is the short circuit current density or J_{SC}. This is directly related to the quantity of light absorbed and the ability of the solar cell to collect minority carriers. The next key metric is the open circuit voltage (V_{OC}). This is the voltage that the diode self-biases to when not attached to a load, which is a direct result of the material quality and minority carrier transport properties. Sometimes the bandgap-voltage offset (W_{OC}) [52],

$$\left(W_{OC} = \frac{E_g}{q} - V_{OC}\right) \qquad \text{Eq. 2.1}$$

is used to compare the material quality of materials with different bandgaps. Next, is the maximum power point. This is the current (J_{MP}) and voltage (V_{MP}) biasing conditions that result in the largest power output ($J \times V$) from the cell. The efficiency (η) is therefore determined as the maximum power output (P_{max}) divided by the input power from the standard spectrum of choice.

$$\eta = \frac{P_{max}}{P_{in}}. \qquad \text{Eq. 2.2}$$

Lastly, the fill factor (FF) is a measure of how square the LIV curve is. It is the ratio between the areas of the squares created by the J_{MP} and V_{MP}, with the square created by the J_{SC} and V_{OC}.

$$FF = \frac{J_{MP}\, V_{MP}}{J_{SC}\, V_{OC}}. \qquad \text{Eq. 2.3}$$

This is a critical metric to explore the impact of non-idealities such as series resistance, shunt resistance, and volage dependent collection efficiency. These nonidealities will be explored more in Chapter 5.

2.3. SOLAR CELL DEVICE PHYSICS

The process of power generation from a solar cell can be described by three critical steps: electron-hole pair generation, minority-carrier collection, and voltage generation.

2.3.1. ELECTRON HOLE PAIR GENERATION

A single photon can classically generate one electron hole pair. Photons interact with electrons in the valance band, transferring their energy, and promoting the electron to the conduction band. The rate at which this process occurs is dictated by the band structure of the semiconductor and the energy of the photon. While this can be a complex

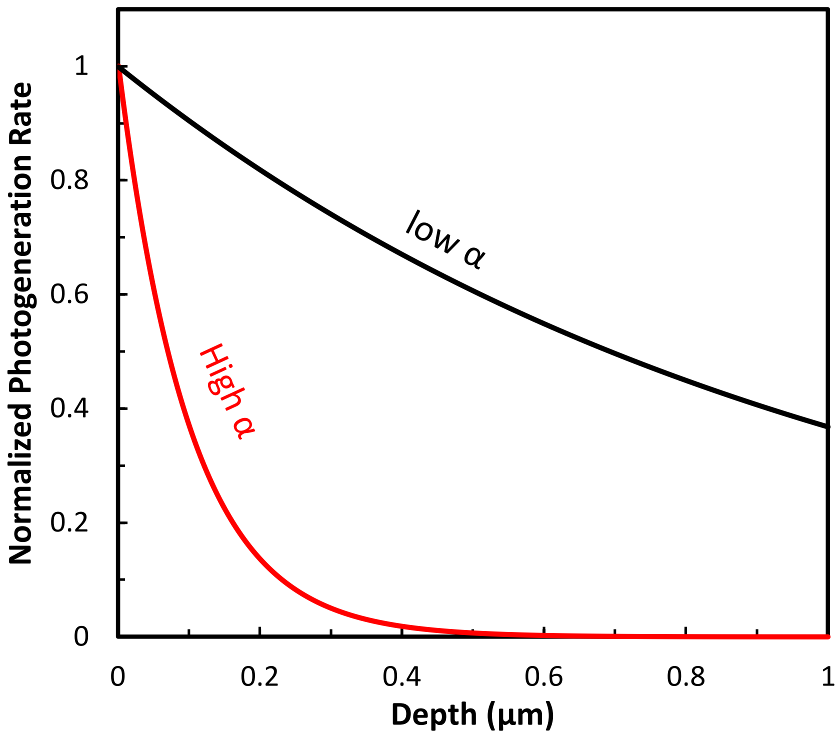

Figure 2.7 Normalized photogeneration as a function of depth for a high absorption coefficient (high energy) and a low absorption coefficient (near band edge photons).

set of processes, it can be distilled down to a single term known as the absorption coefficient. This term is calculated as in Equation 2.4,

$$\alpha = \frac{4\pi k}{\lambda} \qquad \text{Eq. 2.4}$$

where k is the extinction coefficient of the index of refraction and λ is the wavelength of light. Direct bandgap semiconductors such as GaAs have large absorption coefficients while indirect bandgap materials such as Si have much weaker absorption coefficients, due to the necessity for a change in crystal momentum for the indirect bandgap materials.

The electron hole pair/minority carrier generation rate as a function of position and wavelength is dictated by the negative derivative of the Beer-Lambert law given in Equation 2.5.

$$G(x, \lambda) = \Phi_0 \alpha(\lambda) * \exp(-\alpha(\lambda)x). \qquad \text{Eq. 2.5}$$

We observe that for near band edge photons the generation profile shown in Figure 2.7 is much flatter, extending all the way back to the rear of the material, while short wavelength photons are absorbed much more quickly near the front of the material.

2.3.2. MINORITY CARRIER COLLECTION

Once the electron hole pair is generated, they must be separated. We refer to this as collection of the minority carrier. This is done via a combination of diffusion and the built-in electric field of the junction. Ideally all photogenerated minority carriers would be collected; however, recombination of a minority carrier with a majority carrier results in the loss of the photogenerated minority carrier. This is obviously a process that must be minimized so understanding the mechanisms for minority carrier recombination is important. The average time that a minority carrier is able to diffuse around in the crystal

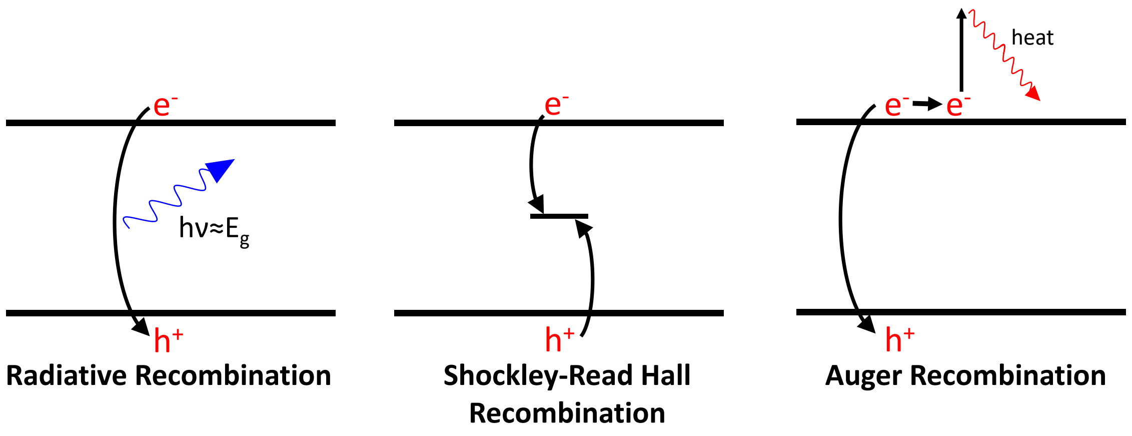

Figure 2.8 Schematic description of the three main types of minority carrier recombination. The doping density and quantity of defect states can determine which mechanism is dominant.

before recombining is known as the minority carrier lifetime (τ). The average distance that the carrier can move before recombining is known as the diffusion length (L_D) and is determined by the minority carrier lifetime and diffusivity (D).

$$(L_D = \sqrt{D\tau}). \qquad \text{Eq. 2.6}$$

The minority carrier lifetime is dictated by the quality of the materials and/or the doping. The mechanisms for recombination are shown in Figure 2.8. Radiative recombination occurs when an electron returns to the valence band while emitting a photon with an energy roughly equivalent to the bandgap energy. This is the preferred process as this photon can potentially be reabsorbed leading to a process known as photon recycling [53], [54]. This process is dominant in direct bandgap material when the doping is high. This is typically dominant in the emitter layers of the III-V cells discussed in this dissertation. Shockley-Read-Hall (SRH) recombination is defect assisted recombination whereby defect states within the bandgap aid in the recombination of electrons and holes [55]. This can happen at point defects like interstitials or extended defects like dislocations. This recombination mechanism is also dominant at surfaces. Surfaces are riddled with defect states as they are the termination of a crystal and therefore break the periodic boundary conditions that help in forming the band structure. The last mechanism for recombination is auger recombination whereby two minority carriers and one majority carrier interact with one another causing thermal energy to be released and one of the minority carriers to recombine. This process is dominant at very high doping or in defect free indirect bandgap semiconductors. All of these processes can be lumped together to determine the minority carrier lifetime via the inverse sum of the lifetimes from each process.

$$\frac{1}{\tau_{tot}} = \frac{1}{\tau_{rad}} + \frac{1}{\tau_{SRH}} + \frac{1}{\tau_{aug}}. \qquad \text{Eq. 2.7}$$

Considering all of these recombination processes, there exists a probability of collecting a minority carrier generated at a particular depth within the cell before it recombines (f_c). This is determined by the transport properties of the minority carriers as well as the distance from the depletion region. In the depletion region, the collection probability is said to be unity because of the high electric field rapidly sweeping carriers across the junction. Further details about the mathematical relationships that determine the collection probability are presented in Chapter 5, but to generalize, plots of collection probability are either exponential or linearly decaying as you move away from the depletion region (Figure 2.9). This depends on whether the recombination is dominated by the bulk or by surfaces/interfaces. If the recombination is bulk dominated the collection probability will exponentially decay based on the diffusion length. If the diffusion length is long, then the collection probability will remain high over the entire

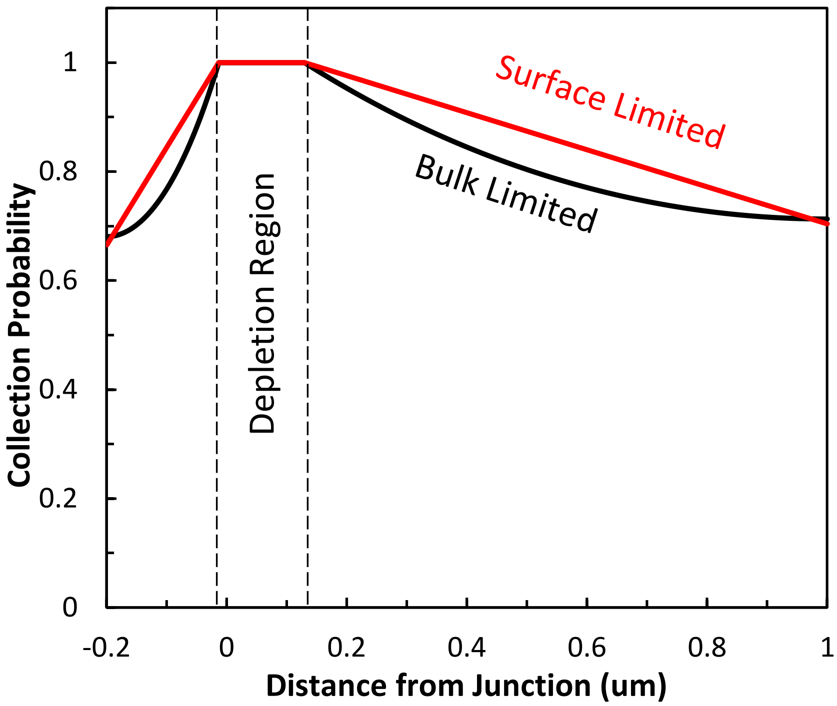

Figure 2.9 Collection probability as a function of distance from the P-N junction. If the recombination is bulk dominated, the collection probability curve is exponential in nature, and if it is surface limited then it appears quasi linear.

length of the cell. Combining the photogeneration processes form the first section and the collection probability discussed in this section allows for the calculation of the photocurrent or J_{SC}. This is formalized in Equation 2.8.

$$J_{photo} = \mathrm{q} * \int_0^{t_{max}} f_c(x) * \int_0^{\frac{E_g}{1240}} G(x,\lambda)\, d\lambda\, dx. \qquad \text{Eq. 2.8}$$

2.3.3. VOLTAGE GENERATION

The voltage from a solar cell is generated by the splitting of the quasi Fermi levels due to a buildup of minority carriers in the base and emitter of the diode. Therefore, we can write the voltage output from the cell as the difference in the quasi Fermi levels in the base and emitter (Equation 2.9) as seen in Figure 2.10 where E_{Fn}^{p} and $E_{\mathrm{Fp}}^{\mathrm{n}}$ are the electron and hole quasi Fermi levels in the p- and n-type layers respectively.

$$qV = E_{\mathrm{Fn}}^{\mathrm{p}} - E_{\mathrm{Fp}}^{\mathrm{n}} \qquad \text{Eq. 2.9}$$

To understand the I-V characteristics of a solar cell, we can think of the LIV curve of a solar cell as the superposition of the illuminated diode and the dark diode crudely illustrated in Figure 2.11. There are instances where this breaks down such as voltage dependent collection efficiency, discussed in more detail in Chapter 5. It does, however, serve as a strong starting place in order to understand the basic solar cell operation. As of now we can write this as the following:

$$J_{tot} = J_{dark} - J_{light} = J_0\left(\exp\left(\frac{qV}{nkt}\right) - 1\right) - J_{photo} \qquad \text{Eq. 2.10}$$

The J_{photo} term is derived from Equation 2.8 and the J_0 term is the dark diode reverse saturation current. This term is explored in more depth in Chapter 5, but is dependent on the doping, layer thickness, interface quality, and minority carrier transport properties. In general, the higher the minority carrier lifetime and doping that the base layer has, the

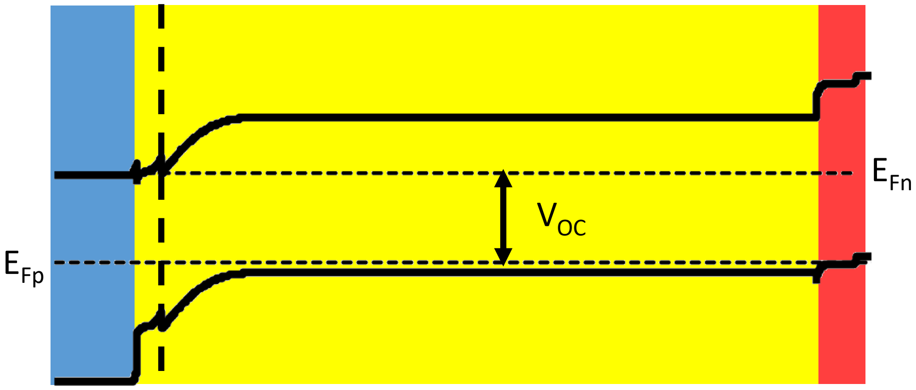

Figure 2.10 Quasi Fermi level splitting indicating a forward bias. The completely flat quasi Fermi level indicates no current flow in the device.

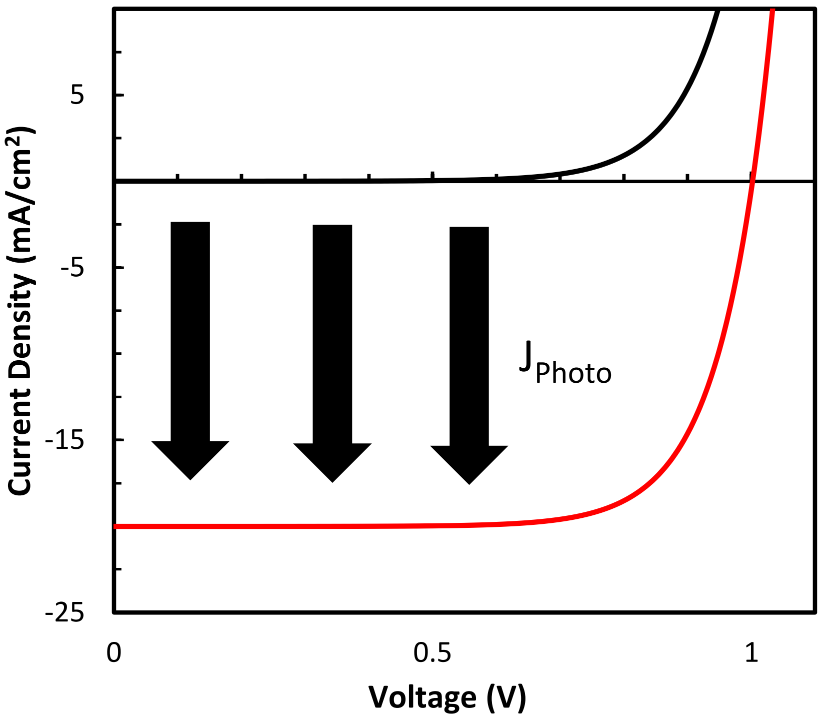

Figure 2.11 Illustration of the super position of light and dark Diodes. The shifting of the I-V curve into the fourth quadrant creates the traditional solar cell IV curve.

lower the J_0 value. Setting the total current equal to zero and solving for the applied voltage allows for the extraction of the V_{OC} and results in the following formulation:

$$V_{OC} = \frac{nkT}{q} * \ln\left(\frac{J_{photo}}{J_0} + 1\right) \qquad \text{Eq. 2.11}$$

This brings out a few important trends. First the V_{OC} trends logarithmically with the photocurrent. This is especially valuable in concentrator solar cells that make use of this effect resulting in higher efficiencies than is possible at standard 1 sun illumination. Secondly, the V_{OC} trends inverse logarithmically with the diode dark current. This means that we want to ensure that our material has the lowest diode dark current and thus the longest possible minority carrier lifetime. Defects such as dislocations, arising from lattice mismatch, reduce the minority carrier lifetime and adversely affect V_{OC} as described in detail in Chapter 5.

2.4. CRITICAL ASPECTS IN THE DESIGN OF SINGLE JUNCTION SOLAR CELLS

Now that the basic operation of a solar cell has been presented, it is important to briefly review some of the key design tradeoffs in single junction solar cells before expanding our understanding to include multijunction device architectures.

2.4.1. ANTIREFLECTION COATING DESIGN

Based on the relatively high index of refraction (n ~ 3-4) of most semiconductor materials in the wavelengths of interest, the Fresnel reflection created between the ambient air environment leads to ~30% broadband reflectance for a given semiconductor such as GaAs or Si. To combat this, an optical matching network known as an anti-reflection coating (ARC) is used.

For the sake of this electrical engineering dissertation, and the fact that light is indeed just electromagnetic waves, I will make direct comparisons to RF matching networks and electrical impedance. Obviously, the ARC can also be explained in a classical optic sense but makes much more sense to me as an RF design problem. Just as in RF component design, a matching network seeks to match the input impedance of the device (semiconductor) to the output impedance of the source (air). Oftentimes, this is done in RF devices using a quarter wave (¼ λ) matching network. This causes the proper phase shift to minimize reflected waves. A similar strategy can be done in the ARC with a ¼ λ thick layer of a transparent moderate index material. However, this strategy only minimizes reflectance for a single wavelength. Although as was discussed earlier, a solar cell must not only collect various different wavelengths (especially in a multijunction solar cell), but must also consider the most valuable wavelengths in terms of energy content and desired subcell for absorption. The ARC therefore must provide minimized reflections over a wide wavelength band. To do this, we attempt to create a matching network that has two minima in reflectance using a low index material in contact with the air on top of a high index material in contact with the semiconductor. The materials with the largest difference in index of refraction should be chosen to minimize broadband reflectance. It is for this reason that TiO_X/Al_2O_3 is a common ARC pairing along with TiO_X/SiO_2 and ZnS/MgF_2 for even higher performance. It is important, however, to keep track of parasitic absorption especially in the high index material, as its generally lower bandgap may result in short wavelength losses even if the measured reflectance is low.

While these ARCs can be designed analytically for a single semiconductor material, the complex semiconductor stack including cladding layers, step graded buffers and potentially semitransparent substrates. This means that an analytical design process would get impossibly complicated very quickly. Instead, an optical modeling software such as Filmstar is used providing much easier optimization of such a device structure.

2.4.2. TRADEOFFS IN EMITTER DESIGN

In a traditional front-emitter *n*-on-*p* design, the emitter is typically a thin and highly-doped *n*-type material. The emitter serves 3 main purposes. First, and most obviously, is that is serves to create the p-n junction responsible for charge carrier separation and voltage creation. For this purpose, we would prefer the doping to be as

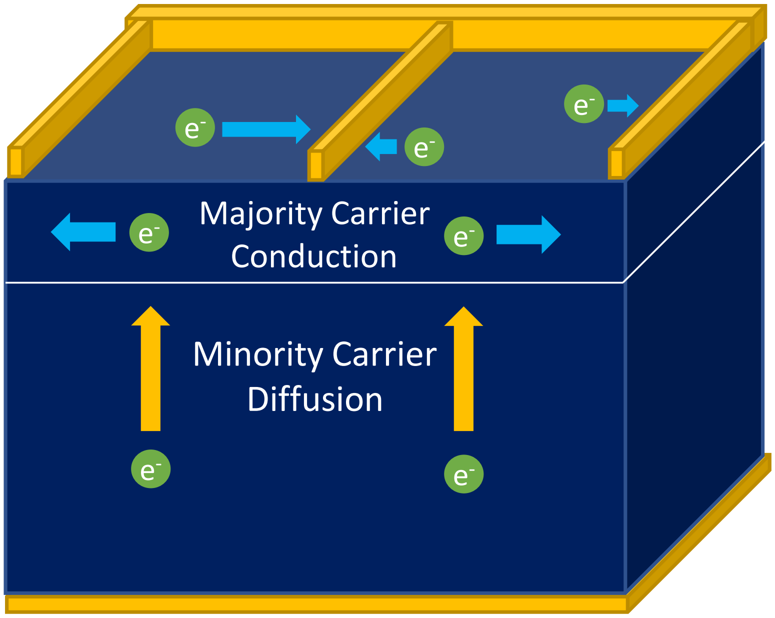

Figure 2.12 3-D structure diagram detailing the grid metal and letteral conduction in the emitter. This results in tradeoffs with doping and thickness in the emitter.

large as possible to reduce the diode dark current (as discussed further in Chapter 5). Its, second purpose is to absorb the short wavelength photons that generate electron hole pairs near the front of the cell and to collect these electron hole pairs efficiently. To maximize performance in this aspect, a shorter, more lightly-doped layer is preferred as high doping reduces the minority carrier lifetime and thus the collection probability in this layer. Work not contained directly in this thesis on design of wide bandgap emitter and window layers explored methods to improve collection using graded bandgap structures which, in turn, allow us to keep the emitter more heavily doped while achieving improved diffusion lengths [56], [57].

These two roles of the emitter already dictate design choices that are counter to one another without even talking about the last and equally important aspect, lateral conductivity. Thus far we have discussed solar cells as 1-D optical devices; however, to both extract photogenerated carriers out of the device, and allow light to enter the semiconductor, a gridded front metal design is used. This leaves large areas of the semiconductor a measurable distance from the nearest ohmic contact as shown in Figure 2.12. Conduction of the photogenerated electrons from this point in the semiconductor to the nearest grid finger results in series resistance losses. The impact of these series resistance losses is discussed in more detail in Chapter 5 via an analytical model; however, in short, the added series resistance negatively impacts the FF of the device and therefore the power output. Increasing the lateral conductivity of the emitter helps to reduce these losses and is achieved by making the layer thicker and more highly-doped. This is, of course, counter to the second function of the emitter which is to collect photogenerated carriers resulting in a very important design tradeoff that can often be overlooked if only looking at the 1-D problem.

2.4.3. TRADEOFFS IN BASE/ABSORBER DESIGN

While we have already talked about the tradeoffs in selecting the bandgap of the absorber, thickness and doping also play a significant role in the efficiency of the device. To maximize the voltage output of the device, the diode dark current must be minimized. If the emitter is sufficiently doped, this means that the more lightly doped base is the primary dictator of this term. As will be discussed in Chapter 5, maximizing the doping and minimizing the thickness of the layer will result in the lowest diode dark current and thus highest V_{OC}. However, this is directly counter to the other primary objective of the base, absorbing and collecting the photons with energies slightly greater than the bandgap. If the base is not sufficiently thick, too many near band edge photons will be transmitted leading to high optical losses. If the base is too highly doped the reduced diffusion length will result in reduced collection probability thereby increasing minority carrier recombination. These optical and recombination losses manifest themselves as a reduction in J_{SC} and can have very strong impacts on performance. Thus, another tradeoff is presented which pits the desire for high V_{OC} against the desire for adequate long wavelength collection and therefore J_{SC}.

2.4.4. TRANSPARENCY IN WINDOW DESIGN

While the window is not typically seen as an important layer in minority carrier collection, the results presented in Chapter 6 and 7, will present specific cases where that is indeed not true. In this introduction however, we will focus on the optical losses that occur in the window layer. Assuming that nearly no carriers can be collected from the window due to their proximity to the defective front surface, the window is often treated as a dead layer. It is for this reason that one would prefer the window to be as thin and wide bandgap as possible. In fact, straining the $Al_xIn_{1-x}P$ window layer to be more Al-rich in a typical GaAs or $Ga_{0.51}In_{0.49}P$ solar cell can result in enhanced collection of short wavelength photons due to its wider bandgap [58].

2.5. MULTIJUNCTION SOLAR CELLS

2.5.1. MULTIJUNCTION CONCEPT

Recalling mechanisms which limit efficiency as described by the S-Q limit, the fundamental tradeoff when using a single bandgap absorber is that either transmission or thermalization losses will result in poor utilization of the solar spectrum. The

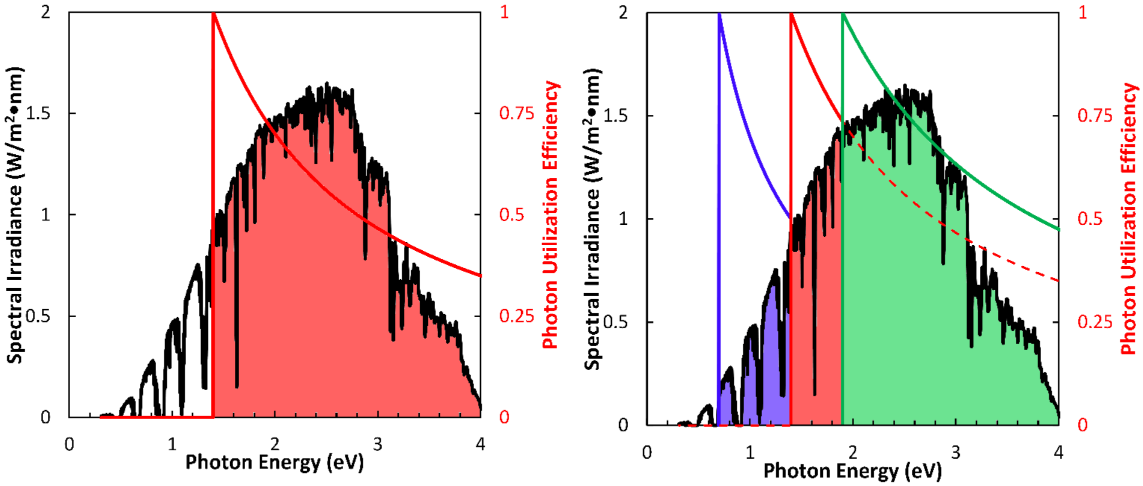

Figure 2.13 Photon utilization efficiency plots for a single junction cell with a 1.4 eV bandgap and a 0.7/1.4/1.9 eV multijunction.

multijunction solar cell device architecture solves this problem by using more than one semiconductor absorber to both absorb more of the solar spectrum and utilize high energy photons more effectively. The structure is composed of two or more subcells stacked on top of each other with the highest energy bandgap on top. The widest bandgap solar cell absorbs the blue/UV light, the next junction picks off another part of the solar spectrum, until finally the long wavelength infrared light is absorbed by the bottom junction. The concept is given in the shaded spectrum plots in Figure 2.13 with the structure for a 3-junction cell given in Figure 2.14. Notice that the photon utilization efficiency is higher not only at low photon energies (where photons were originally transmitted) but also at higher energies due to the wider bandgap of the top cell when compared to a single junction cell.

Adding additional junctions does provide continued efficiency improvements, assuming the ideal bandgap profiles for proper solar partitioning can be achieved. Currently a small area, 6-junction cell created by NREL holds the record for efficiency at

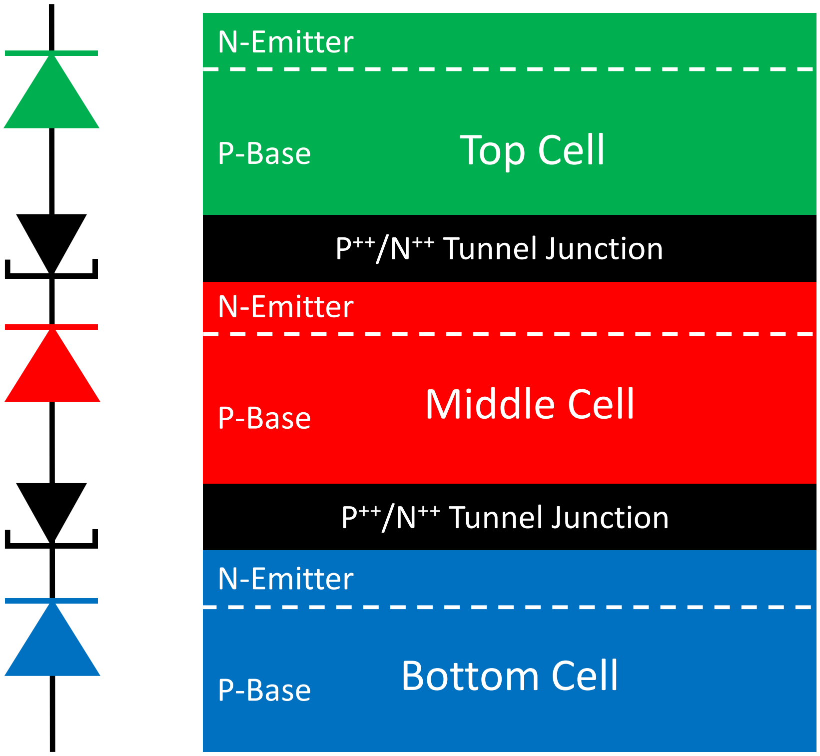

Figure 2.14 Multijunction cell structure and circuit diagram with tunnel junction interconnects.

39.2% AM1.5G efficiency [59]. While this is indeed an excellent proof of concept, efficiencies of 37.9% have been achieved using only 3 junctions [60]. This reinforces the aspect of diminishing returns present when using more than 3 junctions. This is one of the primary reasons why we have chosen to focus on the 2-junction III-V/Si tandem cell as it provides a substantial potential increase over single junction performance, but without the added complexities and epitaxial thickness of additional subcells. It is also critical to note that we preferred the 2-junction design over a 3-junction as it is more resilient to diurnal changes to the incident solar spectrum. Thus, it is a potentially more viable technology for large scale terrestrial deployment.

Because of the diode polarities, a forward biased tunnel junction interconnect is placed in between the subcells as seen in Figure 2.14. This prevents the formation of parasitic diodes between the junctions and enables proper series interconnection. These of course must be transparent to the remaining flux after the subcell above it as well as provide negligible series resistance and/or voltage loss.

The forward biased tunnel junction is based on the Esaki diode concept [61]. For the sake of brevity, the physics which dictate their operation will not be explored in this dissertation; however, for further reading please see the dissertation by Dr. Daniel Chmielewski [62], former student in our group, whose primary research focus was tunnel junction interconnects. In short, high doping causes overlap between the conduction and valence bands in adjacent *n*-type and *p*-type layers. This allows electrons from the conduction band on the *n*-type side to tunnel through the thin potential barrier and recombine with holes in the valence band of the highly doped *p*-type side. This leads to hopefully negligible series resistance as the voltage necessary for tunneling through the ultra-thin potential barrier is very small.

2.5.2. I-V CURVE OF A MULTIJUNCTION SOLAR CELL

Like other devices connected in series, the subcells in a multijunction solar cell must have the same current flowing through them to satisfy Kirchhoff's current law. This means that the subcell that produces the least photocurrent will limit the output current of the entire device. This is seen in Figure 2.15 for a 3-junction example where the current limiting subcell sets the J_{SC} for the entire cell and dictates the shape of the I-V curve. As

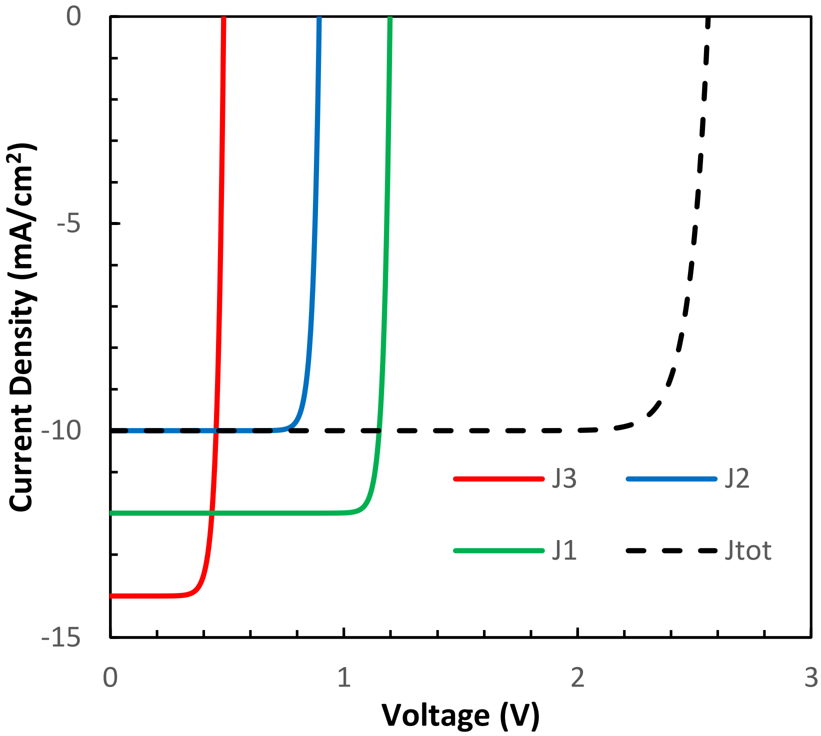

Figure 2.15 Illuminated I-V curves of multijunction solar cell and subcells. Notice how the lowest current producing subcell sets the current for the multijunction device.

with other series connected devices, the voltages are additive resulting in a V_{OC} for the multijunction cell that is the sum of all the subcell V_{OC}.

The FF of the multijunction is also dictated by the current limiting subcell. At zero bias the current limiting cell is set in a large reverse bias, and the overfilled cells are biased at a voltage close to their V_{OC}. As bias is applied to the multijunction cell, the current limiting subcell will receive all of the additional bias until after the max power point where the current of the devices begins to trend quickly towards 0 mA/cm^2. Then voltage is dropped proportionally, based on the ideality factors of the *p-n* diodes making up the subcells. This means that intentional current mismatching between the subcells could be attractive if it leads to a commensurate increase in FF.

2.6. THE GAAS$_{0.75}$P$_{0.25}$/SI TANDEM SOLAR CELL

Just to reinforce the concepts described above, a brief redescription of the GaAs$_{0.75}$P$_{0.25}$/Si tandem solar cell is provided here with descriptions of critical aspects of each subcell. The structure of this cell is given in Figure 2.16 with indicated diode orientations and tunnel junction. The approximate band diagram is shown in Figure 2.17 under short circuit and open circuit conditions. The flow of electrons and holes through the dual junction structure is indicated. The addition of the voltages is clearly indicated via the sum of the quasi Fermi level splitting in the two subcells.

The GaAs$_{0.75}$P$_{0.25}$ top cell consists of a *n*-on-*p* diode with an *n*$^+$ emitter and a *p*$^-$ base. The emitter is cladded with an *n*-type Al$_{0.66}$In$_{0.34}$P window layer. Al$_{0.66}$In$_{0.34}$P has the widest available bandgap for the III-V materials at this lattice constant and therefore makes an effective transparent carrier selective contact. The BSF is made of Ga$_{0.64}$In$_{0.36}$P

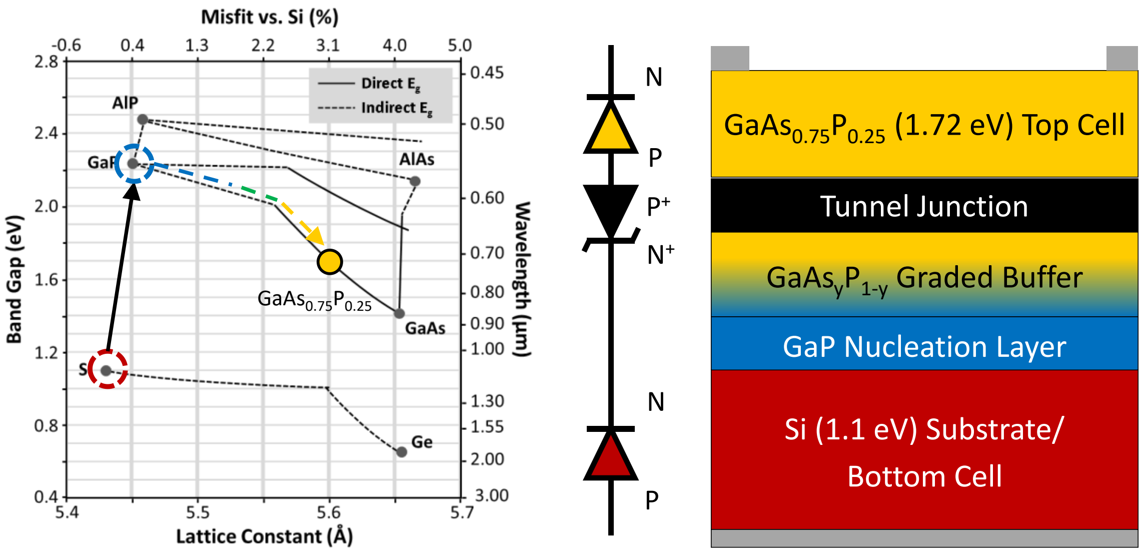

Figure 2.16 Bandgap/lattice constant, circuit diagram and structure of the GaAs$_{0.75}$P$_{0.25}$/Si tandem solar cell.

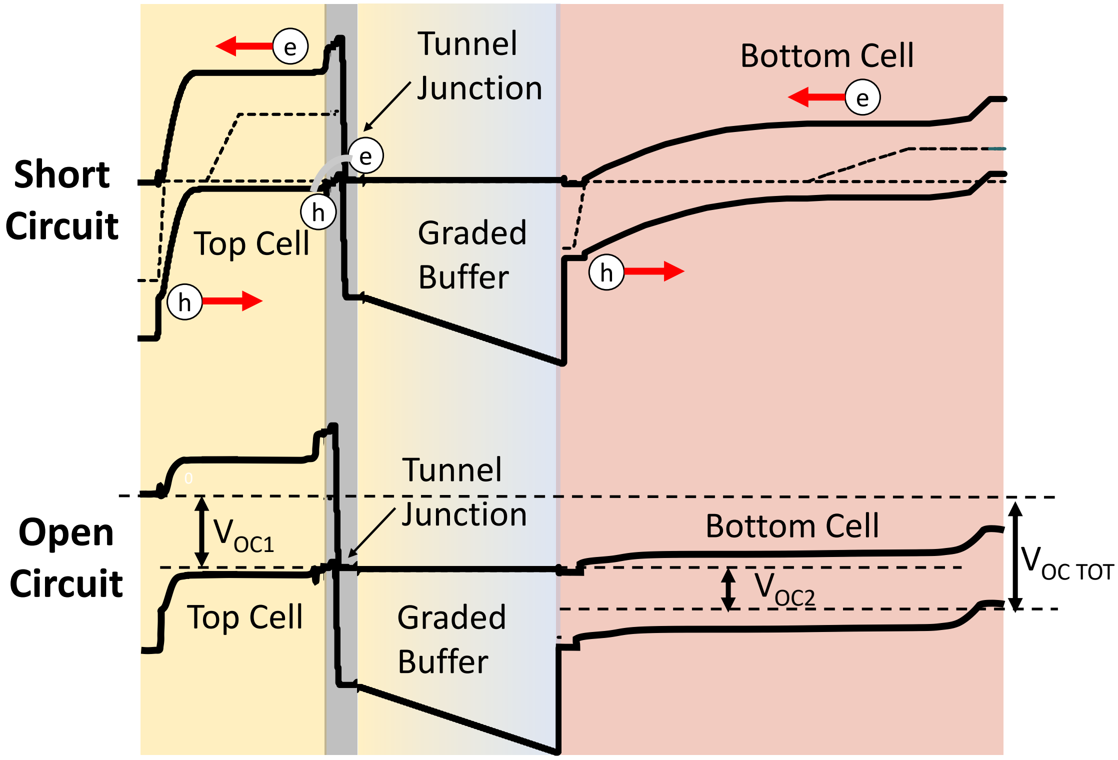

Figure 2.17 Band diagrams in short circuit and open circuit conditions for the $GaAs_{0.75}P_{0.25}$/Si tandem solar cell.

due to its moderate conduction band offset with $GaAs_{0.75}P_{0.25}$. As mentioned briefly in Chapter 1 and discussed further in Chapters 3 and 5, threading dislocations stemming from the lattice mismatch of $GaAs_{0.75}P_{0.25}$ and Si propagate through the $GaAs_{0.75}P_{0.25}$ top cell. These threading dislocations act as spatially localized SRH recombination centers. These cause a reduction in the minority carrier diffusion lengths and an increase in the diode dark current thus resulting in reductions to both J_{SC} and V_{OC}. The precise impact of these dislocations is quantified via analytical modeling discussed in Chapters 5,6 and 7. These dislocations ultimately make the design tradeoffs discussed in the prior sections even more sensitive and difficult to balance.

The Si subcell is also an *n*-on-*p* diode with n^+/p^- doping polarity. The GaP nucleation layer that acts as the initial III-V layer, also acts as the window of the Si solar cell providing a large valance band offset to reflect minority carrier holes in the emitter. Sadly, GaP does not have an exceptionally low interface recombination velocity with Si and could therefore be considered as a rather poor window. The reason for this is currently still under investigation. There are many ways to create a BSF in the Si subcell. One of the ways employed in this dissertation, is by using a *p*-type boron diffusion at the rear of the Si subcell. In present day Si-PV, dielectric passivation of the rear surface has been shown to be more effective than a traditional dopant diffusion BSF [63]. This is the plan for future device iterations but was not employed within the work presented in this dissertation. The last critical aspect of the Si solar cell is the lifetime in the Si wafer. Due to grown-in and extrinsic defects which are activated during MOCVD growth of the III-V layers, the bulk lifetime can degrade resulting in reduced V_{OC} and, if bad enough, J_{SC}. SiN_x rear diffusion barriers and a prefabrication high temperature anneal, can eliminate these defects resulting the maintenance of high minority carrier lifetime throughout III-V growth. It has also been shown that this lifetime degradation can be recovered through subsequent hydride growth [64]. Various aspects of minority carrier lifetime evolution throughout III-V growth been explored by prior researchers in our group [64], our collaborators [65], as well as others in the III-V/Si community [66], [67].

CHAPTER 3:

GROWTH AND FABRICATION OF $GAAS_{0.75}P_{0.25}$/SI SOLAR CELLS

3.1. EPITAXY AND MOCVD

3.1.1. BASICS OF CRYSTAL STRUCTURE AND DEFECTS

“Epitaxy” comes from the Greek “epi” meaning above and “taxis” meaning “in an orderly manner.” This is one of the rare cases where the literal meaning of a word is the best way to describe it. Epitaxy is simply the deposition of atomic species on top of a substrate while maintaining crystallographic registry. To examine epitaxial growth techniques in more detail, one needs to first understand the basic crystal structure and crystalline defects. This section will begin with a brief discussion of crystallography, and then discuss further aspects of epitaxy that are necessary to understand the material throughout this dissertation. My intention is to make this section digestible for electrical engineers and device designers, only including the necessary information to understand the basics of epitaxy from a device design perspective.

3.1.1.1. CRYSTAL STRUCTURES

A crystal is simply a periodic arrangement of atoms. These repetitive patterns of atoms are dictated by the bonding arrangements and hybridization of the valence electrons in the constituent atoms. The smallest pattern that can be translated repeatedly to build the entire crystal is referred to as the crystal structure and is a common way to classify materials. There are nearly infinitely many possible crystal structures, and the atomic arrangements vary in complexity from a simple cubic to highly complex triclinic based structures. However, all crystal structures can be simplified down to one of the thirteen Bravais lattices, with each position in the lattice consisting of one or more atoms in the basis [68].

For this dissertation, we will focus on the two similar crystal structures for Si and III-AsP based materials both based on the face centered cubic (FCC) Bravais lattice and have 2 atoms in the basis. These crystal structures are diamond and zincblende for Si and

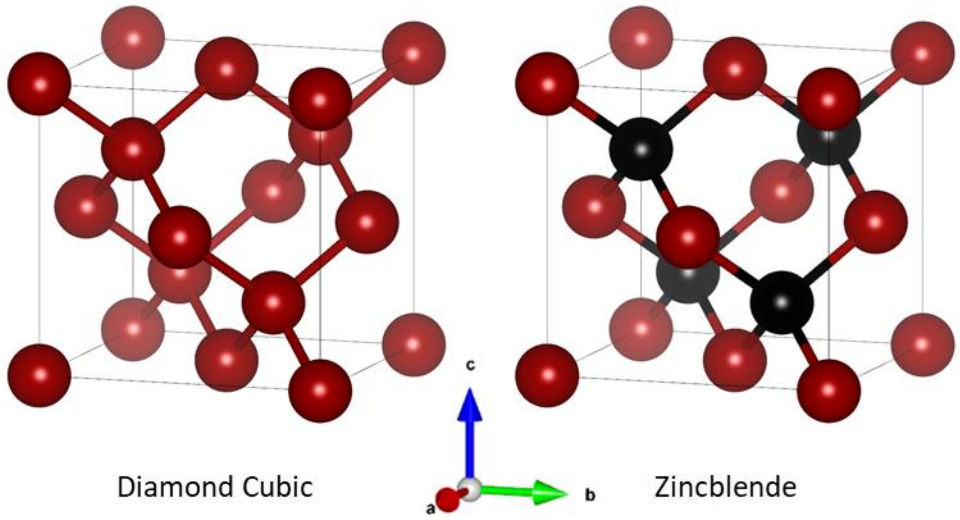

Figure 3.1 Schematic diagrams of diamond crystal structure (left) and zincblende crystal structures (right).

III-V materials, respectively, and are shown in Figure 3.1. Both crystal structures are based on tetrahedral bonding configurations and have a two-atom basis with atoms located at (0, 0, 0) and (¼, ¼, ¼). The difference between the two crystal structures is that the second atom in the case of zincblende is a different atomic species and therefore causes the crystal to possess reduced symmetry [69]. However, because both crystal structures are FCC and based on a tetrahedral bonding arrangement, it is possible to perform epitaxy with these slightly dissimilar crystal structures as will be discussed in further sections.

3.1.1.2. CRYSTAL DEFECTS

While crystals are supposed to be a perfect repeated arrangement of atoms without error, this is sadly not always the case. Various point defects (interstitials or vacancies) and extended defects (dislocations, stacking faults, antiphase domains) exist disrupting the periodicity of the crystal. A brief description of these defects is as follows [70].

Point defects such as vacancies and interstitial affect a single atom or lattice site. Vacancies are when an atom is missing from a lattice site; whereas interstitials are additional atoms in the crystal that do not sit on a lattice site. These defects, at times, can cluster together to create various point defect complexes. The arrangement of these vacancies and interstitials can change the behavior of the defect electronically.

Planar defects such as stacking faults and antiphase boundaries are extended defects that impact an entire atomic plane. Stacking faults are planar defects which break the stacking arrangement of the crystal. For example, in zincblende the proper stacking sequence is ABCABC. However, it is possible to satisfy bonding requirements and have a stacking sequence of ABCBA. So, if instead of the desired ABCABCABC, the crystal is stacked ABCA**BA**BC and a stacking fault is formed along the plane of the stacking error. This breaks the repetition of the crystal and the stacking fault occurs between the two letters denoted in bold above [71]. Antiphase boundaries, often present near polar/non-polar heterointerfaces, as discussed later in this section, are also planar crystalline defects. These arise when two crystal domains, which are not identical in polarity, are abutted next to each other. The anti-phase domains in the materials of interest are a result of atoms sitting on opposite lattice sites. For example, in "Ga-polar" GaAs, Ga is said to sit on the (0,0,0) site and As on the (¼, ¼, ¼) site. If the lattice sites are reversed, by say rotating the crystal 90 degrees, the resultant "As-polar" material is still a GaAs crystal with perfect registry. If two crystals of differing polarity meet, the bonding between them is not satisfied creating the planar defect known as an antiphase

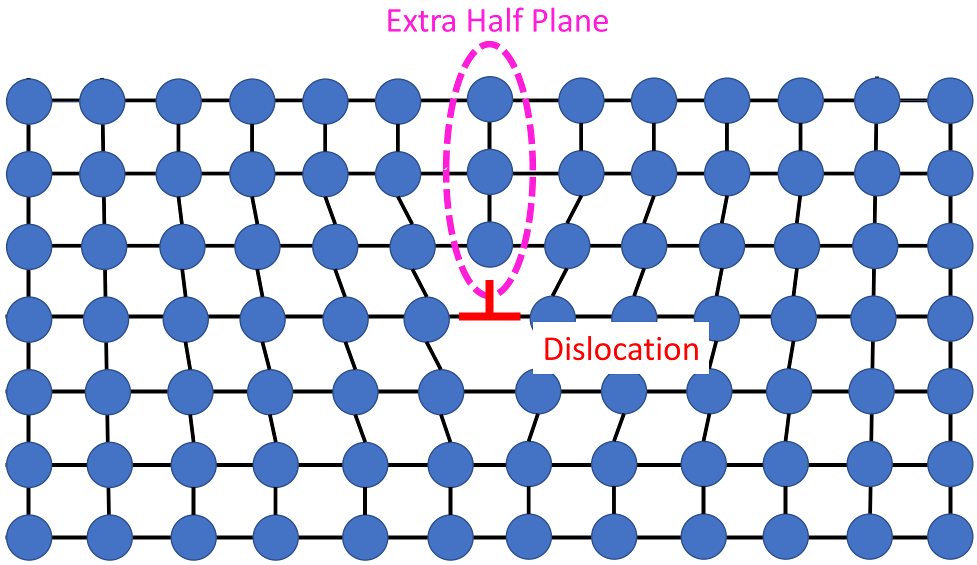

Figure 3.2 Schematic diagram of an edge type dislocation. The missing row of atoms runs in and out of the pageterminating the additional half plane.

boundary [72]. This is discussed in more detail in Section.3.1 as it relates to polar on non-polar heteroepitaxial growth.

Dislocations, which are discussed more in further sections, are probably the most important defect to understand in this dissertation. These are line defects that are essentially missing rows of atoms in a crystal as seen in Figure 3.2. These line defects are necessary to relieve strain in the crystal either due to attempted physical deformation like bending the material or, in the case of this work, strain introduced by lattice mismatched epitaxy. Dislocations can be classified into two types, screw and edge. Edge dislocations terminate an additional half plane of atoms as shown in Figure 3.2. These extra or missing half planes relieve strain in the direct orthogonal to the added or missing half plane. Screw-type dislocations are created by shearing a portion crystal by a single lattice site, and the screw type dislocation is formed at the termination of the shear. For the sake of simplicity, further discussion of dislocation in this section will primarily focus on edge-type dislocations as they are the primary strain relieving dislocation character in III-V films. It is important to note that the dislocations in III-V materials are of mixed character and contain segments which are partially edge-type and segments which are mostly screw-type.

One critical aspect of dislocations is that they must terminate at a surface and cannot just stop within the bulk. This is because, in the case of an edge dislocation, the half plane would not be entirely defined as it requires edges on all 4 sides. These defects therefore nucleate as dislocation “loops,” bordering the half plane which propagate down into the crystal from a free surface. This process thereby relieves strain. These existing dislocations can then move within a crystal to enable deformation of the crystal under stress. In the case of the materials of interest here, this is done by a process known as glide. For an edge type dislocation, this process can be thought of as an extension of the additional or missing half plane of atoms. This process continues to proceed along a crystallographic direction known as the glide plane at a velocity that depends upon the applied stress, temperature, and atomic bonding properties. Dislocations as they relate to the III-V materials of interest will be discussed in more detail in subsection 3.1.3.2.

3.1.2. EPITAXY BASICS

The discussion of epitaxy basics in this thesis is limited for the sake of brevity; however, it is necessary to at least explain the driving forces at play and to provide some degree of basic knowledge about film growth. In reality, the details provided here pale in comparison to the complexities of what is going on at the atomic scale, but it should at least provide the necessary intuition and knowledge to understand the subsequent chapters and to intuitively understand the challenges in III-V/Si heteroepitaxy.

Epitaxy relies on the transfer of a source material to the substrate through a mass transport process. The source material then condenses or adsorbs onto the surface before diffusing along the surface in order to find the appropriate lattice site. The driving force favoring the adsorption process is that the partial pressure of the source material must be higher than the vapor pressure of the compound trying to be deposited. Otherwise the competitive desorption process would be preferred and result in no film growth [69].

Once the atomic species is present on the surface, (then referred to as an adatom) a number of potential actions can happen. The adatom can be desorbed or released from

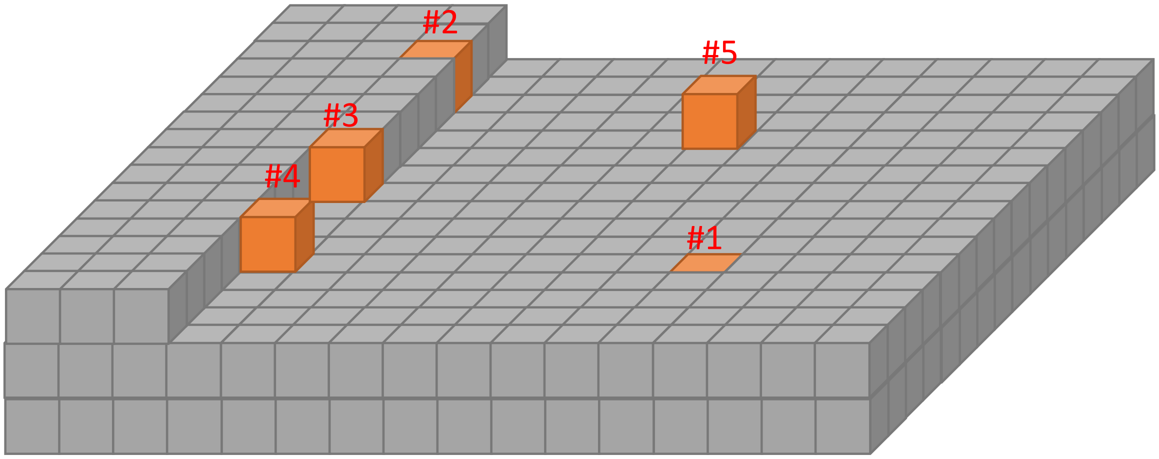

Figure 3.3 Kossel crystal representation of the various potential lattice site. Site 3 is known as a kink site is the most utilized as there are an equal number of bonded and un bonded sites.

the surface, diffuse and attach to an existing lattice site in a process called incorporation, or lastly, attach to other adatoms on the surface nucleating a new atomic layer. Depending on the temperature, vapor pressure and other growth conditions, these various processes can be suppressed or enhanced.

The incorporation process is especially interesting as adatoms do not have an equal probability of incorporating on every lattice site. The various lattice sites in the Kossel crystal model, a great over-simplification of the actual atomistic processes, are shown in Figure 3.3. The sites which are embedded within a flat surface (denoted as #1) are usually already filled as atoms are not likely to diffuse out of a lattice site with 5 adjacent filled lattice sites. In contrast, an adatom in site #5, which is only attached to the crystal via 1 adjacent lattice site, is not likely to remain bonded at that position. Instead, the thermal energy present within the system can break the bond and allow the adatom to diffuse around the surface until it finds a site with the lowest available energy state. The most probable site for incorporation is known as a kink site (#3). This has a near equal

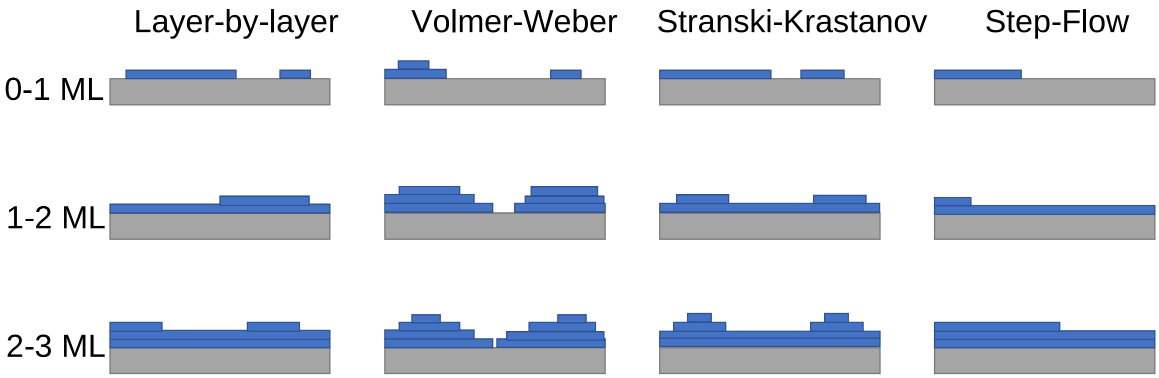

Figure 3.4 Schematic desicriptions of various epitaxial growth modes.

probability of holding the atom and allowing it to diffuse away. There is typically a large quantity of kink sites available and atoms will readily incorporate there creating an additional kink site along a step edge. This process continues until either the propagating kink site reaches another encroaching kink site, or the edge of the crystal.

Based on our ability to control competing processes on the surface, via control of temperature, elemental partial pressure, etc., the method by which the crystal grows and evolves can be altered. The common methods for crystal growth are detailed in Figure 3.4. The simplest method, layer-by-layer growth dictates that a complete atomic layer is completed before the clustering of adatoms and subsequent nucleation of another layer. This implies that the formation energy to nucleate new atomic layers is much higher than the energy required to diffuse to an existing kink site. Thus, the adatom diffusion length required is typically very long.

3-D island type growth, also known as Volmer-Weber (V-W) growth happens when the adatoms have much lower adatom mobility and shorter adatom diffusion lengths. Therefore, the adatoms would prefer to cluster together with nearest neighbor adatoms and form new atomic layers rather than to incorporate on existing layers that may be further from their initial position. Stranski-Krastanov growth is a similar method to V-W, but the initial atomic layer (or first few atomic layers), is grown in a layer-by-layer growth mode and the remainder of the film is grown in a V-W growth mode. This is often due to high compressive strain and is commonly used to make quantum dots.

The last growth mode is typically observed when using vicinal or offcut substrates. The offcut of the wafer towards a particular crystal direction creates numerous step edges on the surface. Adatoms prefer to incorporate along these step edges due to the high quantity of kink sites and therefore the step edges “flow” along the surface as the terraces elongate. This process only occurs if the adatom diffusion length is longer than the average terrace width. This is of course known as step flow growth and is generally the desired growth mode when using offcut wafers [73]. This growth mode usually results in very smooth epitaxial layers with low point defect densities.

3.1.3. CHALLENGES WITH HETEROEPITAXY IN THE III-V/SI SYSTEM

3.1.3.1. POLAR ON NON-POLAR HETEROEPITAXY

The challenges of polar on non-polar heteroepitaxy are best described by the review paper by Kroemer [72], and thus, for the sake of brevity, only a surface level understanding is presented here. As discussed in the above sections, Si and III-AsP materials have slightly different crystal structures which makes growth of III-V materials on Si difficult. This has been a long-explored problem both in the GaP/Si material system

[3], [5], [74], [75] of interest here as well as in GaAs on Ge [72], [76] and GaAs on Si [77]–[79].

The primary issue in polar/nonpolar heteroepitaxy arises with the formation of antiphase domains stemming from single atomic height steps. This can be simply explained in the diagram in the top of Figure 3.5. The crystal, although Ga initiated on all Si surfaces, does not line up in registry with the portion of the crystal grown on the step above or below it due to the lack of 90-degree rotational symmetry by the zincblende

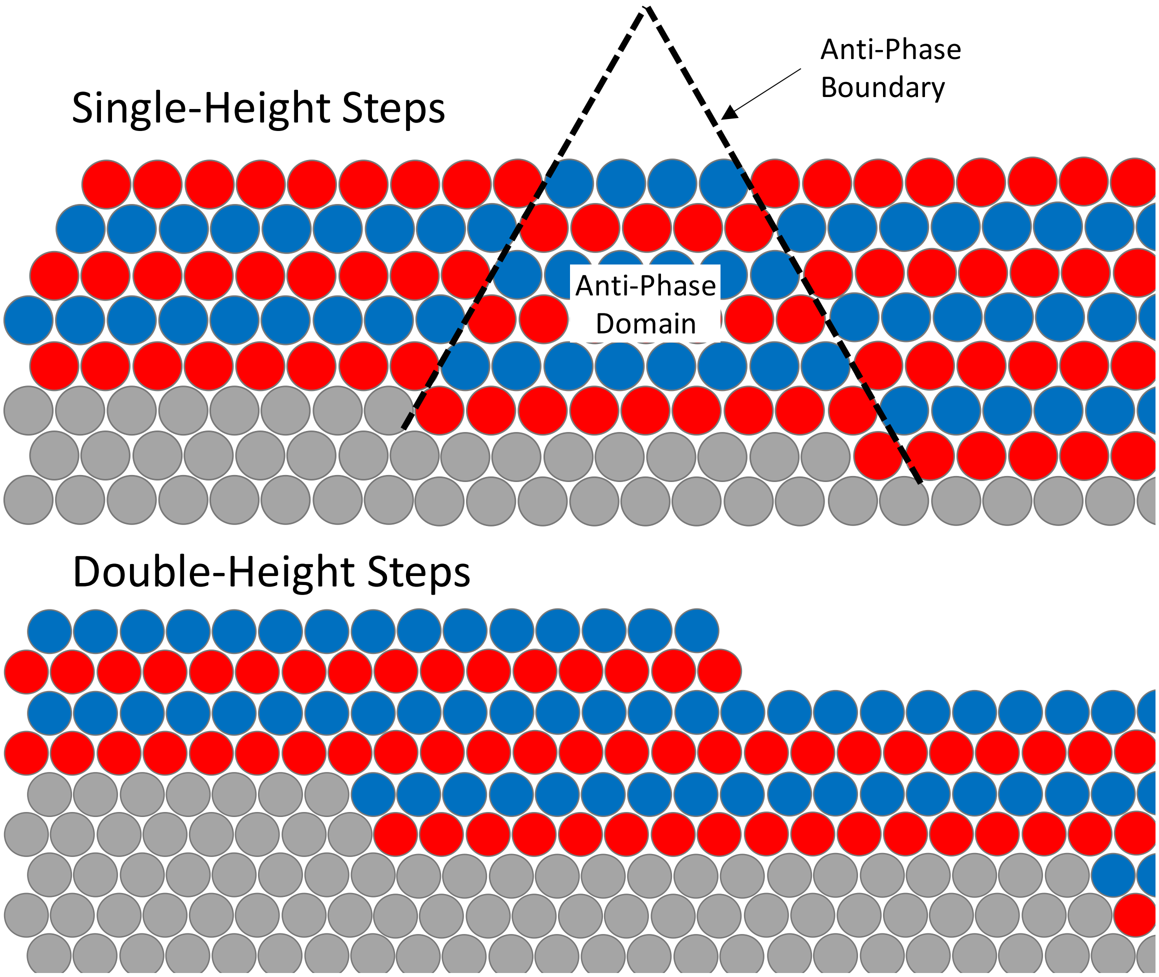

Figure 3.5 (Top) Schematic representation of the antiphase domains that form when single-height steps are present. (Bottom) Schematic representation of proper polar on non-polar heteroepitaxy due to the existence of double-height steps.

lattice. To solve this issue, an annealing step that reconstructs the surface to consist of only double-height steps is performed before the III-V layer is deposited on the Si. These double-height steps allow the crystals grown on different terraces to align in registry with each other. This is shown in bottom of Figure 3.5, and has been effectively demonstrated for both GaAs on Ge and GaP on Si. The formation of these double-height steps is a preferable surface reconstruction at elevated temperatures especially for offcut substrates. While the double-height steps can be created even for on axis wafers (due to slight atomic scale surface roughness), the presence of an offcut drastically reduces the temperature needed in order to promote complete double-height stepping. It is for this reason that the Si wafer can be annealed at temperatures of only ~700 °C under dilute SiH_4 flow rather than the >1100 °C needed for on-axis Si [77], [80]. The surface reconstruction into double-height steps is aided by the presence of atomic hydrogen supplied by the SiH_4 during the high temperature surface preparation [43], [81]. The additional Si adatoms are also likely beneficial in smoothing the surface and creating double-height steps.

3.1.3.2. METAMORPHIC GROWTH

As discussed in previous sections, $GaAs_{0.75}P_{0.25}$ is a near perfect E_g paring with Si thus maximizing the theoretical efficiency for the tandem cell. However, even beyond the general challenges of polar-on-nonpolar heteroepitaxy discussed in earlier subsections, $GaAs_{0.75}P_{0.25}$ is also not lattice matched to Si. Therefore, the alignment of the atoms for perfect crystal registry with the substrate induces large amounts of strain in the epitaxial film. This is shown on the left in Figure 3.6 with the film being pseudomorphically

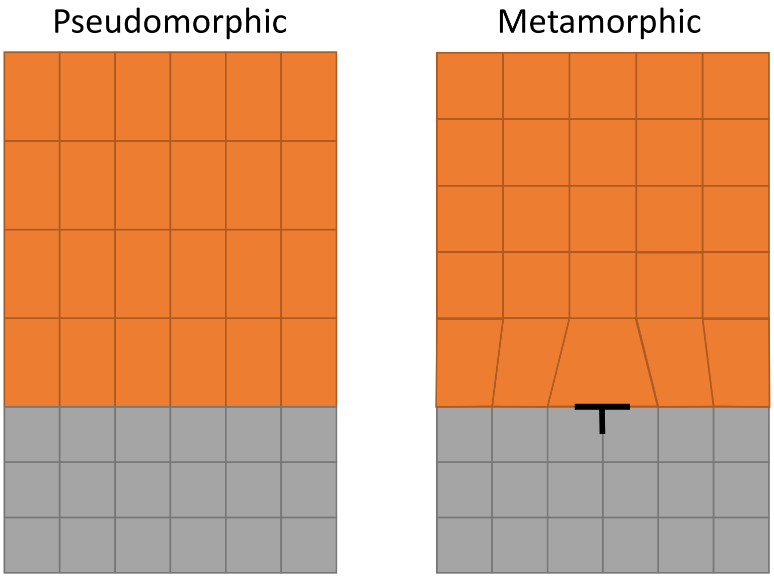

Figure 3.6 Schematic comparison of pseudomorphic and metamorphic films. Pseudomorphic films result in distorted crystals where the in- and out-of-plane lattice constants are different. Metamorphic growth results in fully relaxed films with equal in- and out-of-plane lattice constants through the creation of dislocations.

strained and the atoms maintaining registry with the substrate. This distorts the crystal making the out-of-plane and in-plane lattice constants different from the relaxed lattice constant. For a fully compressively strained film, the out-of-plane lattice constant is expanded, and the in-plane lattice constant is identical to the substrate. While maintaining pseudomorphic strain in thin lattice mismatched layers is possible, growing materials with the requisite thickness for complete light absorption would provide too much strain energy. This causes bonds to break generating dislocations (or missing rows of atoms) as described above and seen in the cartoon in Figure 3.6. This is known as metamorphic growth and is the necessary growth type to achieve layers thick enough to be effective solar absorbers. As more and more dislocations are generated, the film continues to relax

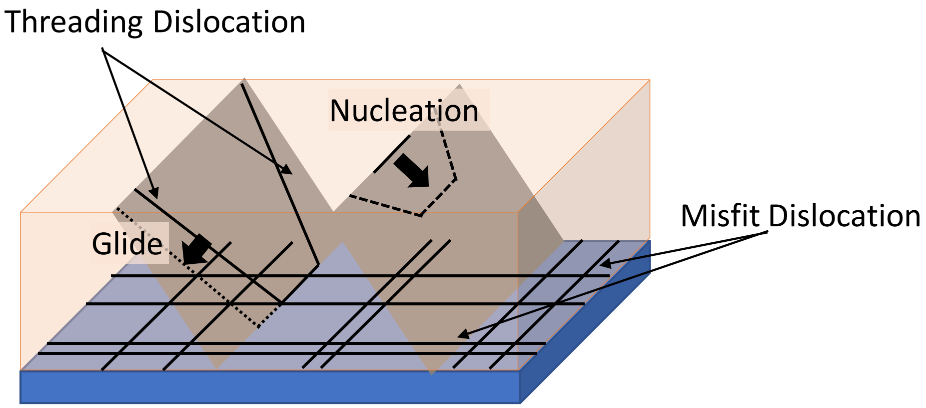

Figure 3.7 Schematic description of dislocation geometries in zincblende materials. The nucleation of new dislocation loops and glide of existing dislocation loops is shown.

with the in- and out-of-plane lattice constants trending towards the fully relaxed values [82].

While the Figure 3.6 shows only that these dislocations lie along the interface, dislocations must terminate at a surface rather than in the bulk of a crystal. The dislocation geometry in these III-V materials is shown in Figure 3.7. The two threading dislocations associated with every strain relieving misfit dislocation extend towards the surface and propagate through any active device layers and result in degradation of device performance metrics as discussed in detail in Chapters 5, 6 and 7. These threading dislocation segments are largely screw-type dislocations and non-strain relieving in nature [82], [83].

Because every misfit dislocation segment is terminated by two threading dislocation segments, the goal should be to relieve the maximum amount of strain with every single misfit dislocation to minimize the threading dislocation density (TDD). Elongation of the misfit dislocation (and therefore relaxation) is done through the dislocation glide process described earlier and shown for the case of dislocations in these materials in Figure 3.7. The misfit dislocation elongates and lays down a longer and longer misfit dislocation segment at the interface. This provides relaxation of the film without increasing the TDD and is therefore the desired process. Glide will begin to occur after the film is grown beyond critical thickness (i.e. the thickness where the forces on the dislocation outweigh the line tension of the atomic bonding) [84], [85]. Glide velocity can be modified by changing the temperature and/or the amount of stress, with higher temperatures and stresses providing faster glide [86]–[89].

If strain is introduced too quickly, (i.e. growing a highly lattice mismatched layer or growing with very high growth rates) the glide of existing dislocation loops is not sufficient to relieve the excess stress generated by the growing film [82], [90], [91]. Therefore, the formation of new dislocation loops is necessary to relax the film more

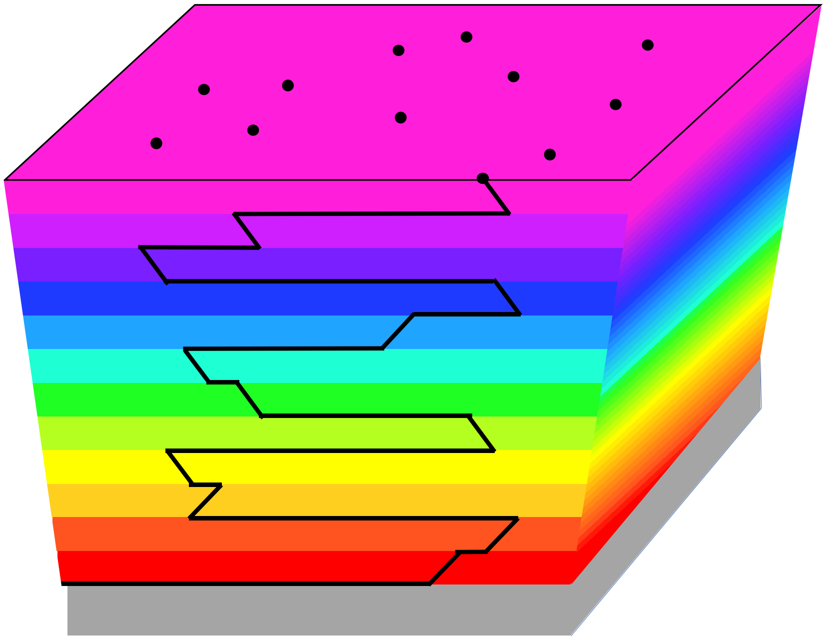

Figure 3.8 Schematic of a step graded buffer with a dislocation running through it. This structure slowly introduces strain in order to promote dislocation glide at each interface without excessive dislocation loop nucleation. The relative lattice constant at each step is given by the relative width of the layer showing a general increase in lattice constant at each step.

quickly. This is the precise phenomenon that must be avoided. This points to a sort of tradeoff between the desire to increase temperature and strain in order to promote high glide velocities, and the desire to keep these same values low to stay below the kinetic barrier for dislocation nucleation [92]. To partially mitigate this tradeoff, a series of thin, slightly lattice mismatched, layers are grown on top of each other slowly introducing more and more strain in a structure referred to as a step graded buffer (SGB) shown in Figure 3.8 [93]. The slower introduction of strain intends to keep strain energy in the film below the kinetic barrier for dislocation nucleation while providing additional interfaces and time for glide to occur. This enables the film to prefer glide as the mechanism for relaxation as opposed to the nucleation of new dislocation loops. SGBs have enabled very low TDDs ($\sim 10^5$ cm^{-2}) in numerous materials systems and is used in some of the highest performance multijunction III-V solar cells for space applications. It is of course also the strategy employed in the $GaAs_{0.75}P_{0.25}$/Si tandem solar cell where TDD control is very difficult due to the low native glide velocities of GaP [86], [88].

3.1.4. MOCVD BASICS

Metal organic chemical vapor deposition (MOCVD), also more accurately referred to as organometallic vapor phase epitaxy (OMVPE), is an epitaxy technique where some of the constituent elements of the desired film are delivered to the substrate via organometallic precursors. A simplistic diagram of an MOCVD reactor is provided in Figure 3.9. Precursors are delivered into the chamber by a carrier gas (usually N_2 or H_2) and the flow of the precursor and carrier gasses are controlled by mass flow controllers.

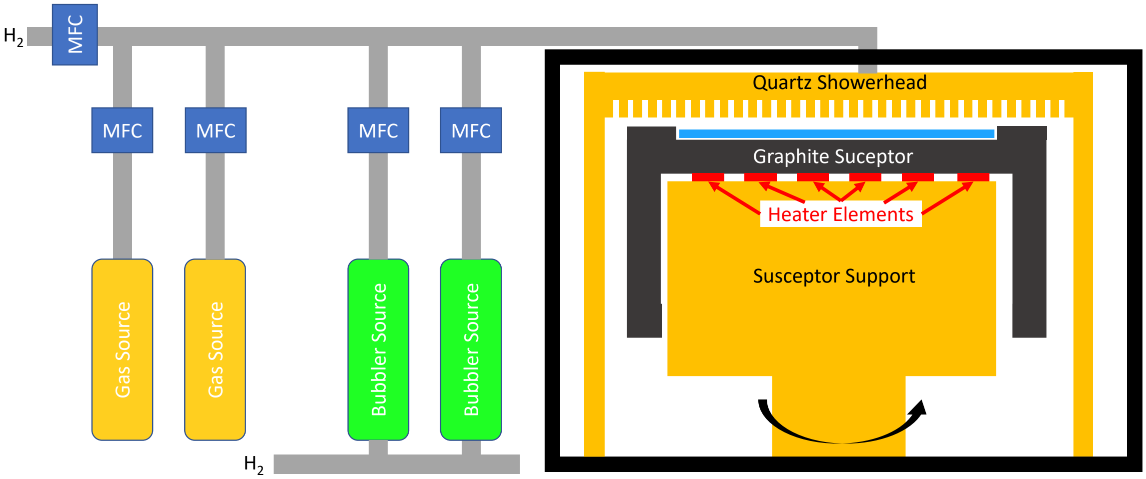

Figure 3.9 Simplistic schematic diagram of the close-coupled shower MOCVD reactor used in this work. H_2 is used as the carrier gas which flows through the bubbler sources in order to provide the precursor materials to the chamber. The source gasses mix in the quartz showerhead and are flowed across the wafer sitting atop the rotating and heated graphite susceptor.

This technique is usually performed at, or slightly below, atmospheric pressure in quartz lined chamber, as the precursors are often corrosive or toxic.

While MOCVD is a highly complex growth technique that has been extensively discussed in the text by Stringfellow [94], the simplified discussion in this dissertation will introduce some of the chemical precursors that deliver the constituent elements to the substrate and aspects of growth that must be considered and/or optimized.

The organometallic precursors used in this thesis for group-III elements are Trimethylgallium (TMGa), Trimethylaluminum (TMAl), Trimethylindium (TMIn), and in the case of low growth temperatures Triethylgallium (TEGa). All these precursors consist of a single central metallic atom and three organic compounds surrounding it. At elevated temperatures these organic molecules dissociate from the metal atom in a process referred to as cracking. This process provides the group-III elements to the substrate surface and leaves the organic molecules to be pumped out of the system.

These precursors are usually fully cracked at the typical growth temperatures and their incorporation is limited by the rate of thermal desorption of the adatoms from the surface.

The group-V precursors are usually hydride sources rather than organometallics including arsine (AsH_3), phosphine (PH_3), and for low temperatures Tertbutylphosphine (TBP). These precursors are not necessarily fully cracked at growth temperature especially in the case of PH_3. The more electronegative phosphorous atom holds more tightly to the atomic hydrogen than the bigger As atom in the case of AsH_3. With regards to layer composition this presents unique challenges especially in mixed group-V alloys such as $GaAs_{0.75}P_{0.25}$. Even at fixed group-V flows the composition can change substantially as a function of temperature. This makes precise targeting of composition very difficult and, in turn, current matching in III-V/Si tandem cells.

For dopant atoms, a number of different dopant sources are available including hydrides, organometallics, and even chloro-bromides. The common *p*-type dopant precursors in the $GaAs_yP_{1-y}$ alloys are diethylzinc and bromotrichloromethane ($CBrCl_3$) for Zn and C respectively. Zn is the typical dopant used in the cell growth (base and BSF) while C is used for ultra-high doping in tunnel junction layers. The *n*-type dopant precursors are Diethyl telluride (DETe) and Silane (SiH_4). Si is used for cell doping (emitter, window and cap layers), and the Te is used for high doping in the tunnel junction. Because not all of these dopant precursors have unity sticking coefficients or are fully cracked at growth temperature, dopant incorporation can change drastically with temperature and therefore substantial doping calibration growths are needed before device growth.

Beyond simply the precursors used, the input molar flow ratios of Group-III to Group-V precursors are critical to obtain films with low point defect densities. While intuitively one might think that a stochiometric ratio of group-V and group-III precursors would be needed, this is not the case. Instead films are typically grown in a group-V rich environment and the growth rate is solely determined by the group-III precursor flow rate. This is due in part to the preference for the group III elements to form droplets if the group V flux is not sufficient, and the incomplete cracking and low sticking coefficient of the group V elements [95]. Indeed, molar V:III flow ratios used in this work are all in excess of 100:1. When calibrating doping (at a fixed temperature) the molar flow of the dopant precursor is referenced to the group-III precursor. This way, if the growth rate is changed, the doping level can be adjusted accordingly.

3.2. POST EPITAXY DEVICE FABRICATION

3.2.1. TANDEM FABRICATION PROCESS FLOW

After the wafer is removed from the MOCVD reactor, numerous steps are needed to create electrical contact to the desired layers and to isolate individual test devices with specified dimensions. This section will first provide an overview of the device fabrication process as well as a few variants on this process that have been adapted to account for different epitaxial stacks and/or desired device functionality. The overall generalized device process flow for a III-V/Si tandem solar cell with a boron BSF Si subcell is shown in Figure 3.10. While certain groups of steps can be rearranged to suit the material stack, substrate, doping polarity etc., this entire process flow must be completed to ensure

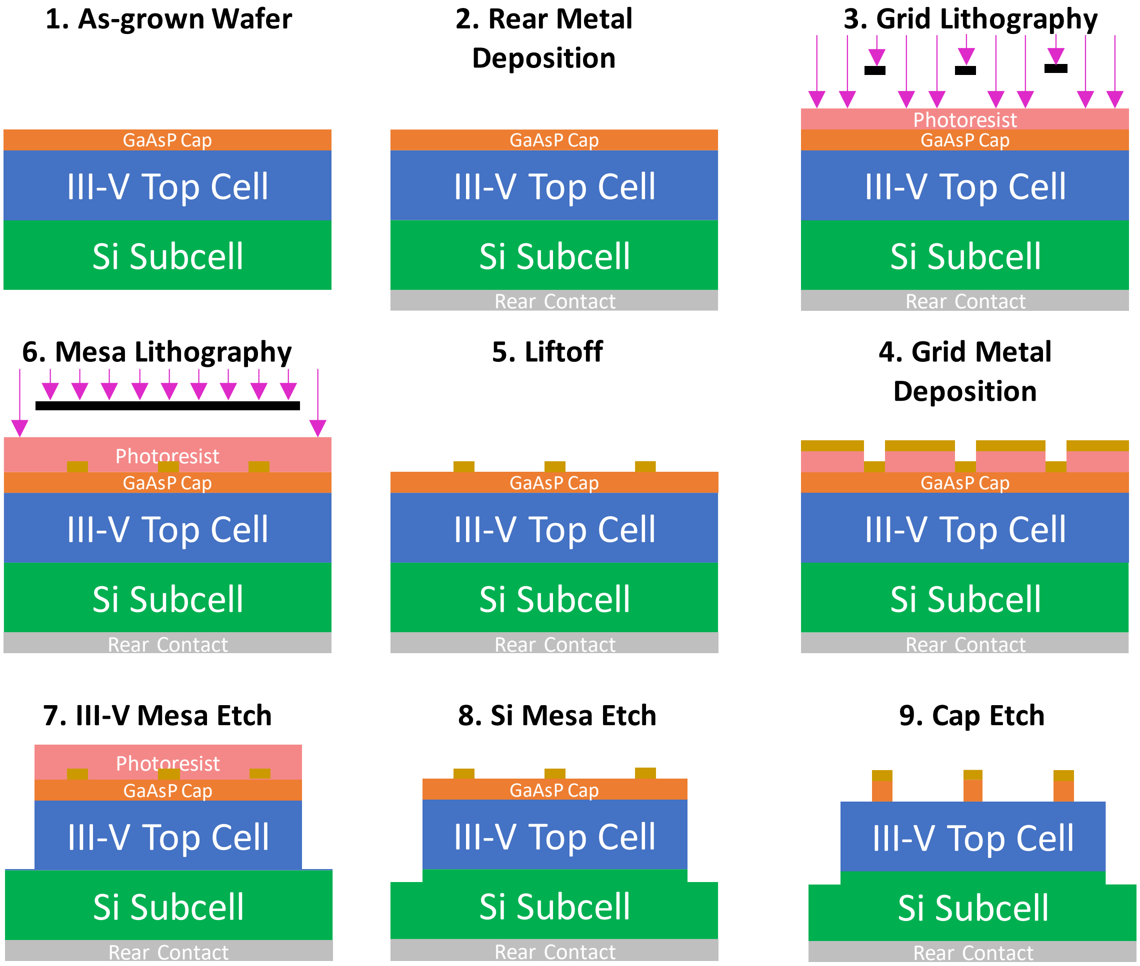

Figure 3.10 Simplified fabrication process flow for a GaAs$_{0.75}$P$_{0.25}$/Si tandem solar cell without and ARC.

electrical contact to both sides of the junction and proper device isolation. For the sake of this example, this initial section will be going through the fabrication process as it was originally intended, and comments will be made about the generalized order of the steps. Even this process can be done out of order with minimal repercussions, but in general should be performed in a manner similar to what is shown here.

First the wafer is prepared for the rear metallization. This is done by first spinning photo resist (usually AZ5214E for convenience) on the front side of the wafer, and hard

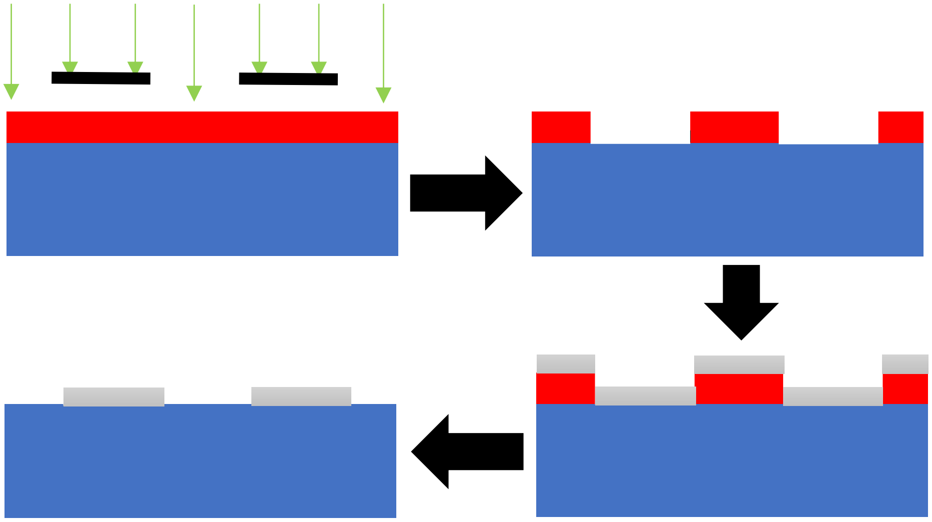

Figure 3.11 Schematic diagram of the liftoff process using negative resist.

baking the resist in order to protect the III-V layers from scratching or damage during handling. Special care is taken to avoid contamination of the rear surface using Teflon vacuum chucks which have been freshly cleaned. The native oxide on the Si wafer is then removed using 6:1 Deionized H_2O (DI) to Hydrofluoric Acid (HF) The rear metal stack (usually Al or Ag based) is deposited via E-beam evaporation. The resist is then removed using an acetone, methanol, and isopropyl alcohol rinse (AMI rinse). The wafer is then annealed at 400 °C for 5 min in the rapid thermal annealer (RTA) to produce rear ohmic contact.

Next the front grid patterning step is performed. This is a liftoff process as detailed in Figure 3.11. AZ5214E resist is spun on the front surface (epi-side) targeting a 1.7 µm resist thickness. This resist can act as both a positive or negative resist depending on bake and exposure conditions but is being used as a negative resist in this case. The wafer is then baked at 96 °C for 50 seconds to soft bake the resist. The front grid pattern consisting of numerous cells and test structures is then exposed, and the wafer is baked at 110 °C for 1 min during which the pattern becomes visible to the eye. After that, the wafer is then exposed to a flood illumination which acts to flip the tone of the resist to the desired negative tone. The wafer is developed in MF-319 TMAH-based developer to expose the pattern and reveal the semiconductor in places where metal will contact the semiconductor. Then an O_2 descum process using a low power O_2 plasma is used to remove any residual resist or residue in the resist openings.

The wafer is then prepped for grid metallization with an oxide etch (to remove the native oxides) consisting of 4:1 DI:HCl. This solution can also be substituted for 1:20 NH_4OH:DI which is preferable because it does not etch phosphide based materials (AlInP or GaInP). The metal used for N-type contacts is typically a NiGeAuNiAu stack. The exact mechanism for why this contact works is hotly debated, but most believe the Ge diffuses into the wafer and acts to create a tunneling-based ohmic contact. The top Ni supposedly acts as a diffusion barrier and the top Au is for added lateral conductivity and can be replaced with Ag for cost reduction. Upon removal from the evaporator, the wafer is soaked in acetone in order to remove the resist and liftoff unwanted metal. Sonication can be added to aid in metal removal. Carefully rinsing the wafers after removal from the metal filled solution is critical to ensure that metal flakes do not re-adhere to the semiconductor surface. After a thorough cleaning, the wafers are annealed in the RTA at 390 °C for 30 sec to produce ohmic contact.

The next step is patterning for the mesa etch. If using plasma etching (as discussed here) there is only 1 mask level needed. If wet chemistry is being used a two-step mesa etch which protects the sidewalls of the III-V during the mesa etch of the Si is used. The mesa pattern is generated using a 10 μm thick SPR220 resist. This is a positive resist that leaves plenty of thickness to protect the devices during plasma etching. Again, the pattern is developed in TMAH MF-319 developer. The resist profiles are measured using profilometry and reflectance spectroscopy.

The wafer is loaded into the ICP-RIE dry etching tool where a cyclic etching recipe of BCl_3/Ar is used to remove the III-V material. The plasma is struck for 30 seconds and then the sample is allowed to cool down for 15 seconds before starting again. This is done to prevent resist burning. The targeted depth is usually undershot for the first etching sequence to check etch rate and remaining resist thickness. The resist thickness is monitored via reflectometry, and the total resist thickness plus etch depth is measured using profilometry. The wafer is reloaded into the RIE-ICP and the target etch depth is set for ~10% greater than the expected III-V thickness. The etch rate decreases significantly upon arrival at the Si interface so over etching is allowable. Etch chemistry is then changed to CF_4 in order to etch the Si. A target depth of ~2 μm is used depending on the front diffusion profile. The resist is stripped off using an AMI rinse and the etch depth is verified using profilometry.

The last step in the device fabrication (excluding ARC deposition, which has not been done at OSU in my tenure) is the removal of the $GaAs_{0.75}P_{0.25}$ capping layer between the metal grid fingers. This cap layer is used to provide low ohmic contact resistance but if left between the grid fingers would parasitically absorb light before it can enter the top cell. The cap etch solution used is 2:1:40 $NH_4OH:H_2O_2$:DI. This etching solution is nearly perfectly selective to the $Al_{0.66}In_{0.34}P$ window layer and therefore minimizes over-etching.

Overall, this process isolates the devices and provides electrical contact to the front and back. Obviously, there is a great deal more nuance to this process than described here and, as mentioned, many different versions and adaptations of this process have been used during my tenure. For example, processing cells on a GaAs-based virtual substrate (as described in Chapter 6) requires the front grid contact to be performed before the rear contact. This is to ensure that the rear contact is not annealed. Additionally, a lateral conduction layer (LCL) contact can be made by first etching down to the corresponding layer in the epitaxial stack (usually through dry etching) and then depositing the contact in the desired region using a similar liftoff process to the grid metal process.

3.2.2. TECHNIQUE DESCRIPTIONS AND BACKGROUND

This section of the chapter will introduce in a bit more detail the various fabrication techniques used in this thesis. Further details of all of the techniques examined in this section can be found in the well-established texts on these topics [96], [97].

3.2.2.1. PHOTOLITHOGRAPHY

Photolithography processes begin with the use of a spin coater. This tool uses a vacuum to hold down the wafer while spinning the wafer in excess of 3000 RPM in order to evenly spread the photoresist. Photoresist is a liquid containing a photo-sensitive and sometimes thermally-sensitive polymer suspended in a solvent. Each photoresist has a unique spin speed vs. thickness curve and depending on the target thickness and uniformity the parameters on the spin coater are adjusted accordingly. The wafer is then placed on a hot plate in order to evaporate the excess solvent.

The photoresist is then exposed to UV light through a patterned mask. During this exposure, chemical changes to the photosensitive polymers occur. In the case of positive resists: “If it shows it goes.” This means that resist exposed to UV light will be removed when placed in the developer. In this case the UV light interacts with the photosensitive polymers to create localized regions of slightly acidic polymers. Positive resist is used to pattern the mesa etch step in the above process. These photo-acids created by UV exposure are then removed by the basic developer solution. In the case of negative resists, the polymer is crosslinked by the UV light creating resistance to chemical etching. Meaning the regions exposed to light remain unetched by the developer.

If a pattern must be aligned to the layer below it (as in the case of the mesa mask), contact aligners (Karl Suss MJB3 is my aligner of choice) have micrometer-based adjustments to rotate and translate either the sample or the mask. A microscope with varying objective is used to allow the user to manually move the wafer or mask to align features known as alignment marks to one another before exposure.

3.2.2.2. ELECTRON BEAM EVAPORATION

An electron beam evaporator is a high vacuum thermal deposition technique that utilizes a high energy electron beam in order to heat source material. This source material is evaporated, or sometimes sublimated, in order to coat a substrate, sample, etc. The electron beam is swept across the source material contained within a graphite or vitreous carbon crucible using electrically controlled magnetic fields. This allows for even heating of the source material. The crucible and water-cooled copper hearth act as the ground for these electrons and they dissipate their energy within the source material as heat. The source material can then be treated as a point source of flux and, due to the high vacuum nature and long mean free path of the atoms, the emitted flux travels undisturbed to coat the substrate. This point source results in a cosine flux distribution moving horizontally along the sample. For this reason, the samples are placed on a rotating turret that is shaped as a dome in order to maintain constant flux on all samples. A quartz crystal microbalance (QCM) is used monitor the thickness and deposition rate of the deposited material. This is used in a PID controlled feedback loop to change the current through the electron source filament thereby changing the current interacting with the source material. This feedback attempts to maintain a constant deposition rate. An electronically controlled shutter allows for degassing of source material before deposition on the sample surface to ensure clean interfaces.

3.2.2.3. ***REACTIVE-ION ETCHING / INDUCTIVELY COUPLED PLASMA***

Reactive ion etching (RIE) is a dry etching technique that is used to create anisotropic etch profiles. A radio frequency (RF) power supply is used in order to ionize the process gas and create a plasma. The plasma is attracted to the charge which builds up on the substrate. This creates a DC bias between the plasma and the substrate forcefully driving the ions to bombard the surface. These ions can etch chemically or even physically sputter away the sample.

In traditional RIE, increasing the power increases the DC bias between the plasma and substrate, increasing the etch rate. However, the increased DC bias begins to cause more crystalline damage from ion bombardment, placing limits on the achievable etch rates without causing excessive crystal damage. Therefore, a second RF power supply is used energize a coil around the chamber. The power supply increases the energy and density of the plasma. This means that at a still low DC bias, and therefore low damage, the etch rate can be increased due to the higher ion density of the plasma.

3.2.2.4. ***ATOMIC LAYER DEPOSITION***

Atomic layer deposition is a layer-by-layer chemical deposition technique performed at pressures slightly below atmosphere. N_2 is used as a carrier gas to bring the organometallic precursors into the chamber, where they react on the surface. ALD is a self-limiting reaction typically done at temperatures < 400 °C. Therefore, films are

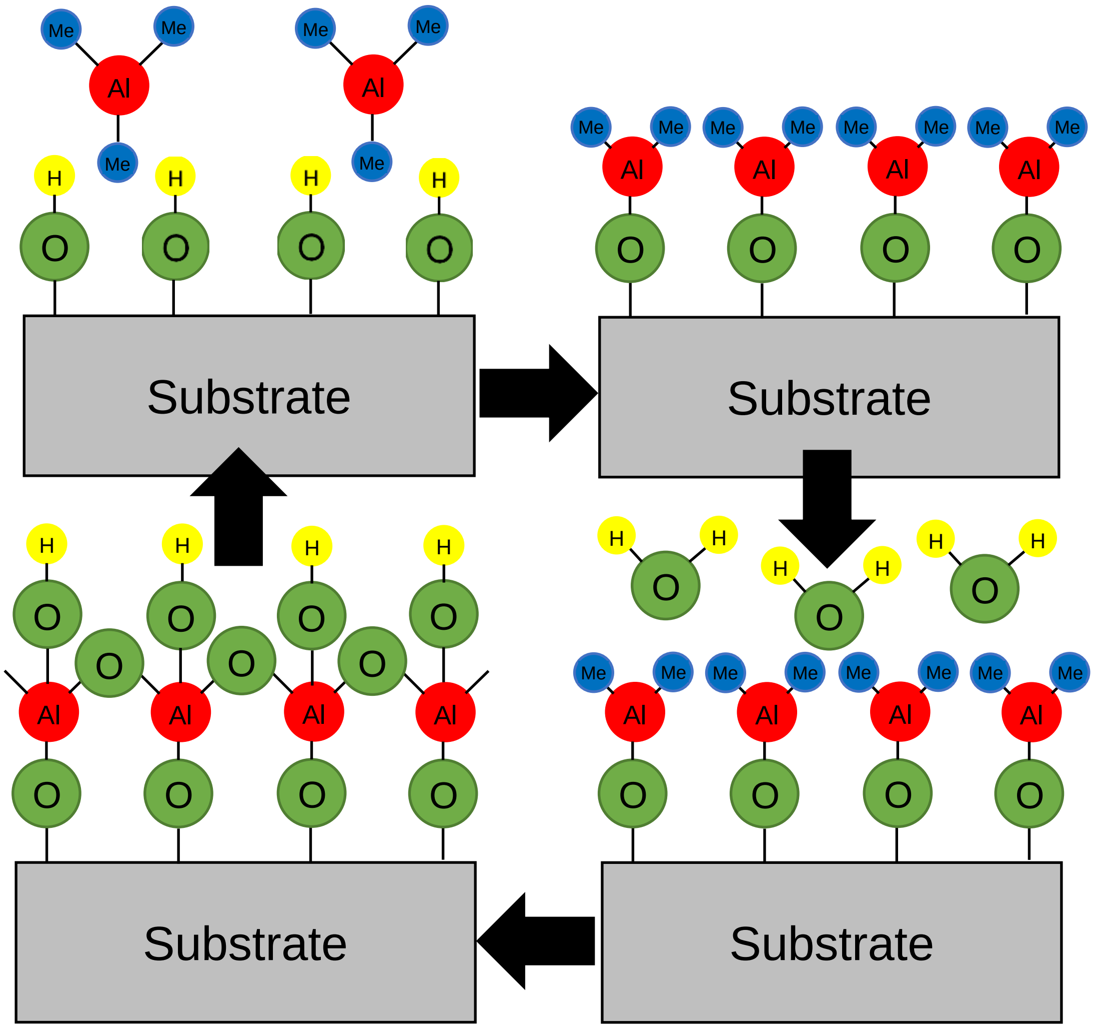

Figure 3.12 Step-by step diagram of the ALD self-limiting deposition process. Starting in the top left corner, the TMAl precursor is introduced into the chamber which reacts with hydroxyl groups absorbed on the surface. The TMAL removes the adsorbed Hydrogen and bonds to the O radical. The H_2O pulse (bottom right) strips off the methyl radicals creating methane and bonding hydroxyl groups to the surface again. The process then repeats.

typically amorphous rather than crystalline as in MOCVD. This section will specifically use the example of growing Al_2O_3 using trimethylaluminum (TMAl) and H_2O (Figure 3.12) as this was the material that was grown during the Rear-emitter/window study in Chapter 7.

The sample/substrate begins with a hydroxyl terminated surface from moisture adsorption. A small dose of TMAl is pulsed into the chamber. The TMAl reacts with the surface losing a methyl radical and attaching to the oxygen. The methyl radical bonds to the hydrogen radical and is pumped out of the chamber as methane. No matter how much additional TMAl is introduced into the chamber, once a single monolayer of TMAl bonds to the surface, the reaction stops. Next, a pulse of H_2O is introduced into the chamber. The moisture reacts with the remaining two methyl radicals removing them from the surface and creating methane. The available bonding sites are filled by oxygen and/or hydroxyl groups. These prepare the surface for the next ALD cycle starting again with TMAl. Monolayer level thickness control is therefore possible. Sometimes repeated pulses of TMAl can be used before beginning the cycle in order to remove organic compounds or native oxides from the surface. This can improve interfacial quality and alter the occupancy of surface defect states. This is sometimes known as a self-cleaning process, as was used in the Fermi level pinning exploration in Chapter 7.

3.2.2.5. SUPPLEMENTAL TECHNIQUES

Many additional fabrication techniques were used during my tenure at OSU. These include O_2 plasma etcher, rapid thermal annealer, profilometer, reflectometer, etc. For the sake of brevity, these very common fabrication and characterization techniques are not examined in detail herein.

3.3. CONCLUSIONS

Fabrication of a $GaAs_{0.75}P_{0.25}$/Si tandem solar cell relies on careful control of epitaxy and defects during growth, as well as numerous post growth fabrication steps. The defects associated with crystal growth include antiphase domains and dislocations which require careful control of the epitaxial process (temperatures, gas flows, substrate preparation, etc.), as well as intelligent strain management in order to reduce the quantity of crystalline defects that can degrade device performance. The post growth fabrication process relies on multiple lithography steps, metal deposition, and wet/dry chemical etching. All of these processes must be optimized in order to ensure that maximum power is extracted from the solar cell.

CHAPTER 4:

MATERIALS AND DEVICE CHARACTERIZATION TECHNIQUES

4.1. MATERIALS CHARACTERIZATION TECHNIQUES

The materials characterization techniques detailed in this section are used to determine composition, bandgap, and crystalline quality. This section will focus on a brief description of these techniques including x-ray diffraction, photoluminescence, and electron microscopy-based techniques.

4.1.1. HIGH RESOLUTION X-RAY DIFFRACTION

High resolution X-ray diffractometry (HRXRD) is a materials characterization technique that allows for measurement of crystal structure and lattice constants [98]. I have chosen to provide a more detailed description of this technique over the others in this section, as it is ubiquitous throughout semiconductor devices/epitaxy and entirely necessary to both characterize materials and calibrate epitaxial growth.

An x-ray source (usually made from copper) producing various x-ray wavelengths is excited using a high voltage power supply. These rays are columnated

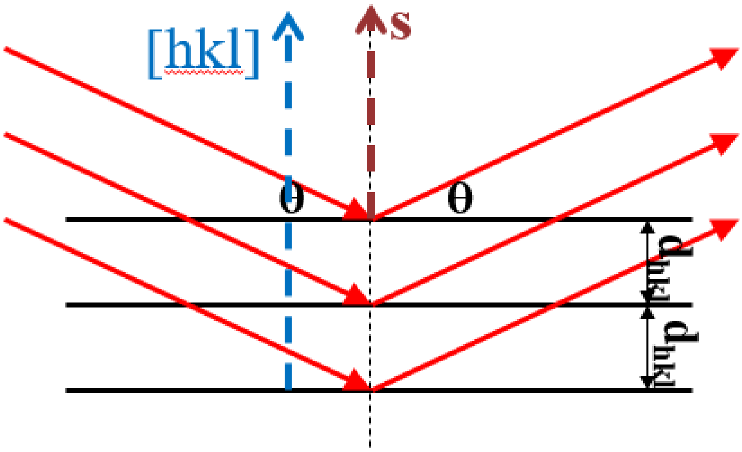

Figure 4.1 Schematic description of Bragg's law. S is the vector the that bisects the incoming and outgoing X-ray beams, and [hkl] is the vector normal to the plane of interest.

using either a channel cut crystal or, in the case of the Bede D1 HRXRD system at OSU, a max flux collimating optic. These x-rays are then put through a second channel cut crystal which acts as a monochromator in order to select only the Cu Kα-1 excitation. This newly columnated and monochromatic x-ray beam impinges on the surface of a sample and diffracts off the crystal planes according to Bragg's law: $n\lambda = 2d\sin(\Theta)$. This phenomenon is based off constructive interference effects resulting from diffraction off adjacent atomic planes as seen in Figure 4.1 [98]. Therefore, at the angle where Bragg's law is satisfied there will be a peak in the diffracted x-ray intensity. These x-rays are detected by a detector with a small slit on a movable arm where the angle between the arm and the incident x-ray source is known as 2θ. The angle between the beam and the surface of the sample is known as ω and the plane-to-surface angle is ϕ.

To measure information about the out-of-plane lattice constant for a single crystal, a symmetric ω-2θ scan is performed, meaning that $\omega = \theta$ and every 1° change in the 2θ angle the ω angle moves ½°. This case is shown in Figure 4.2a. A peak in intensity

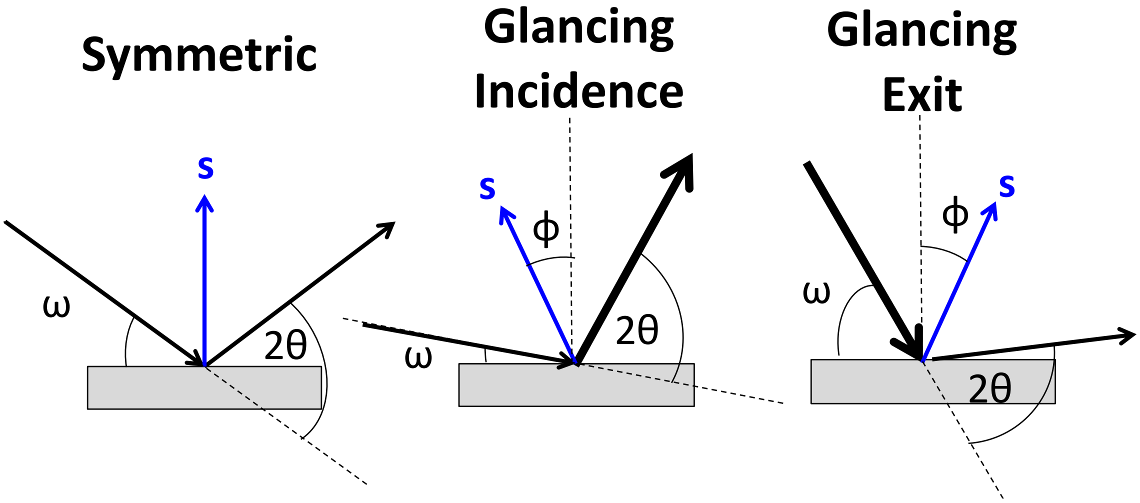

Figure 4.2 Different XRD scan geometries. Asymmetric scan geometries can be used to probe both in- and out-of-plane lattice constants.

will arise as the angular condition, θ, satisfies Bragg's law. This single scan can provide quantification of the out-of-plane lattice constant of a film; however, the lack of resolution in the 2θ axis, due to a finite width detector slit, causes a smearing of any peaks and makes peaks with similar angles difficult to resolve. To correct this, one last channel cut crystal is placed in front of the detector in order to have a much more well-defined 2-theta axis. In this way, this slit acts as a filter to reject all x-rays not entering the detector at the precise angle of interest. The addition of this sharp 2θ limitation is referred to as triple axis x-ray diffraction.

As was covered in the section in Chapter 3 on psuedomorphic vs. metamorphic growth, the lattice constant in the out-of-plane direction is not always equal to the lattice constant in the in-plane direction [99]. Therefore, the out-of-plane lattice constant provided by a symmetric triple axis x-ray diffraction scan is not sufficient to extract composition or stain state from a film, because a fully relaxed film with a given lattice constant could look identical to a pseudomorphically strained film with a smaller or bigger relaxed lattice constant. This means an asymmetric scan is necessary to probe both the in-plane and out-of-plane lattice constant. This can be done through either glancing incident or glancing exit geometries. The requirement that the vector normal to the plane of interest must bisect the incoming and outgoing rays must be satisfied as shown in Figure 4.2, as well as the obvious requirement of satisfying Bragg's law.

While these two scans provide all the necessary information to extract lattice constant in the fully strained and fully relaxed cases, partially relaxed films and nonidealities such as mosaicity and epitaxial tilt require reciprocal space maps (RSMs) to provide additional necessary information. Reciprocal space is simply a mathematical construct that turns an array of planes separated by distance (*d*) and plots it as a single point with a value of 1/d. Thus, a crystal can be defined by a 3-D array of points denoting every series of planes within a crystal with coordinates (Q_x, Q_y, Q_z). Looking along a single crystallographic direction, usually the <110> direction in the case of the materials in this thesis, we observe a 2D array of points corresponding to all of the planes which are in the (h,h,l) family of planes. Due to the mechanisms for diffraction of x-rays, not all these planes are allowable diffractions. For example, for the Zincblende structure, the diffraction rules state that a diffraction is not allowable if the indices of the planes are mixed odd and even numbers, say (1,1,2) for example. Strong diffractions occur in 2 instances: if all plane indices are odd ((1,1,5) for example), or if all plane indices are even and the sum of these indices is an even multiple of two ((2,2,4) for example). A weak diffraction peak, sometimes referred to as a superlattice peak, occurs when all indices are

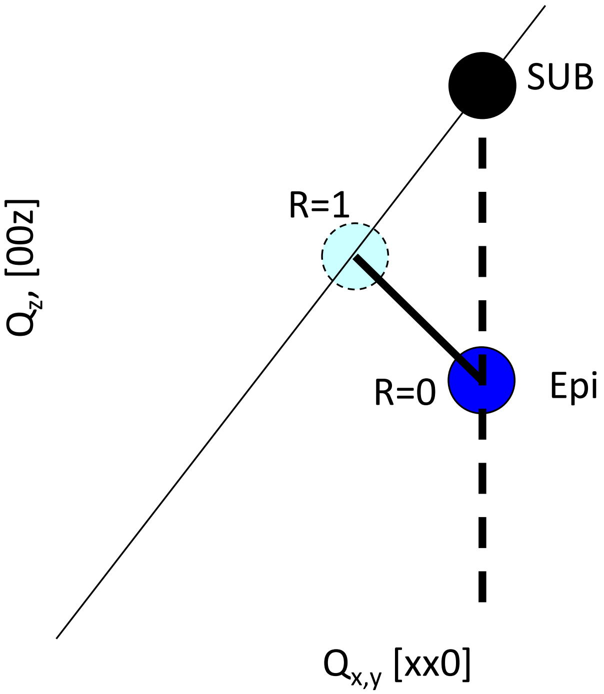

Figure 4.3 Mock reciprocal space map showing how the epilayer changes position in reciprocal space as the film relaxes.

even and the indices sum to an odd multiple of two ((2,2,6) for example). X-ray measurements in this thesis, focus on the strong diffraction conditions usually using the (2,2,4) asymmetric and the (0,0,4) symmetric diffraction conditions.

If we imagine a film with a slightly larger lattice constant is grown atop a substrate the reciprocal lattice point for the film will be slightly closer to the reciprocal lattice origin because the interplanar spacing (d) is larger. If the film is fully strained, the in-plane <1,1,0> direction lattice constant would be identical to the substate. Thus, meaning the epilayer reciprocal point has the same Q_x value as the substrate, but a different Q_z value. In the case of a fully relaxed film, the epilayer reciprocal lattice point lies along a line from the substrate to the reciprocal lattice origin. Varying degrees of

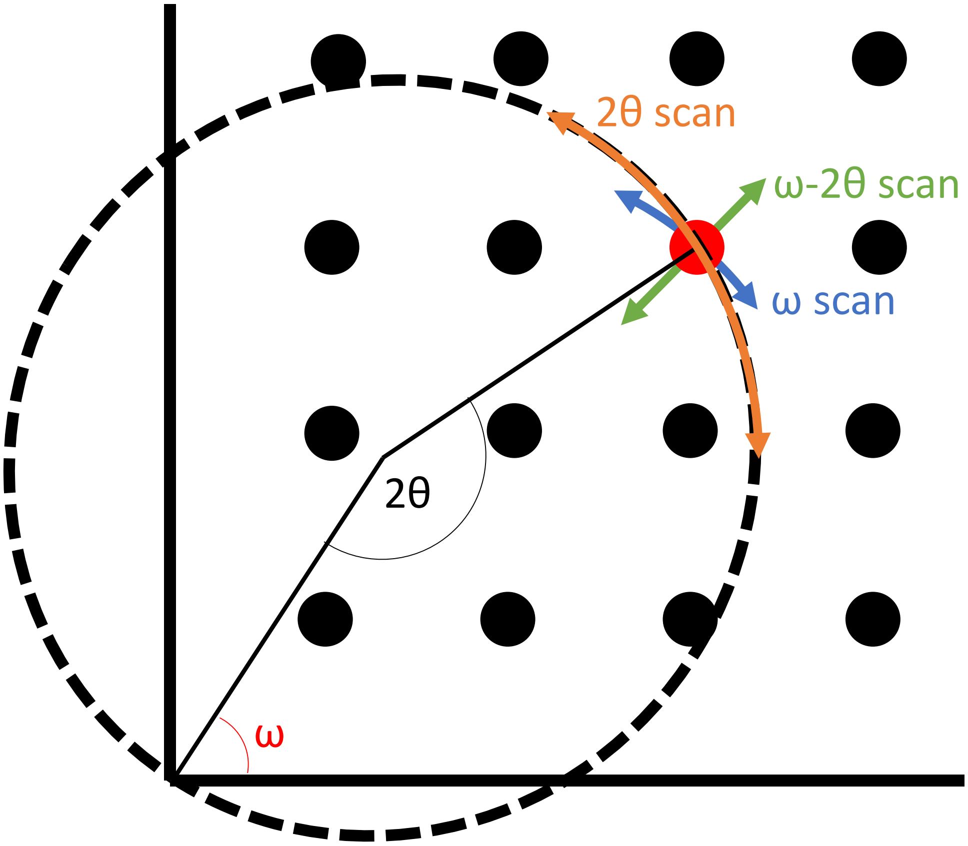

Figure 4.4 2D representation of reciprocal space and the Ewald's sphere. Diffraction occurs when the crystal is oriented so that a reciprocal lattice point intersects the Ewald's sphere. The common scan geometries used to probe the reciprocal lattice point are detailed.

relaxation causes the films reciprocal lattice point to move along the relaxation line shown in Figure 4.3.

In reciprocal space, Bragg's law is defined by a spherical shell known as Ewald's sphere. Along a single plane this is viewed as a circle and Bragg's law is satisfied when the circle attached to the reciprocal lattice origin, with radius 1/λ, intersects the reciprocal lattice point of interest seen in Figure 4.4. The crystal can be rotated by changing the incident x-ray angle (ω) to make the circle intersect the lattice point. The 2θ angle is therefore viewed as the angle created from the reciprocal lattice origin, to the center of

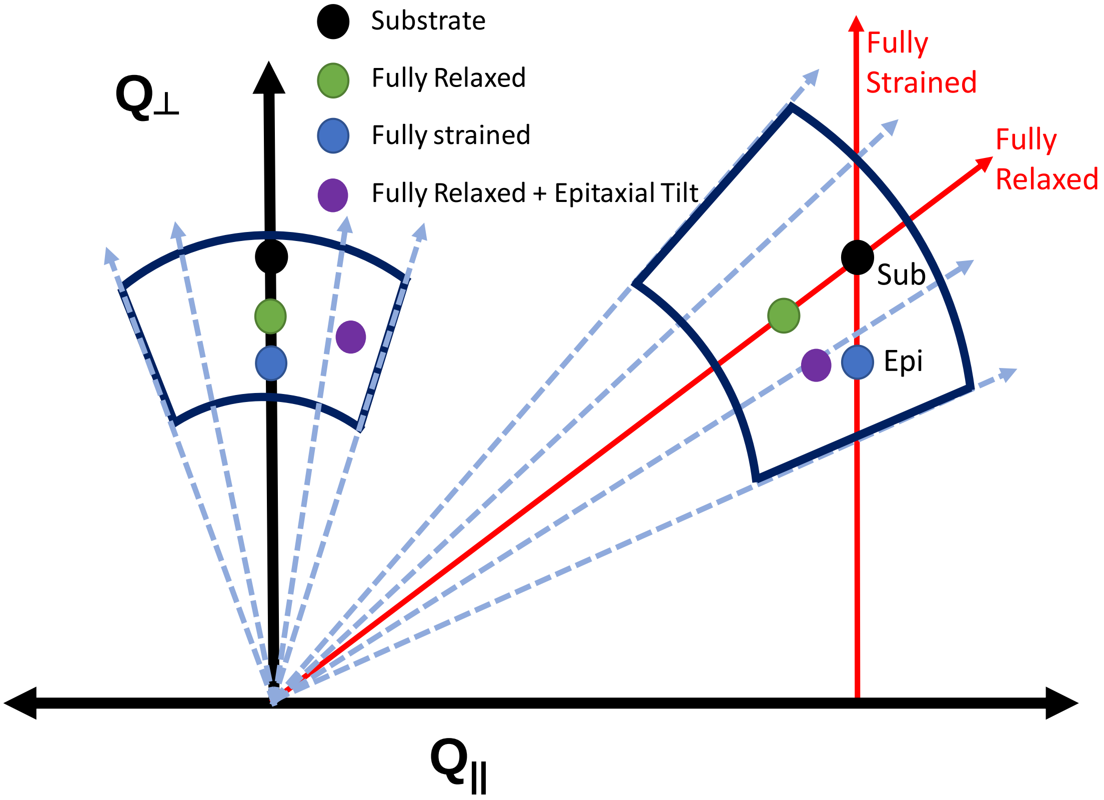

Figure 4.5 Mock reciprocal space maps for symmetric and asymmetric RSMs. This diagram details the impact of epitaxial tilt and strain on the position of fixed composition epilayers.

the Ewald's Sphere, and out to the reciprocal lattice point of interest as shown in Figure 4.4 with ω, ω-2θ, and 2θ scan geometries detailed as well. The ω-scan moves the crystal through the Ewald's sphere at a constant length arc around the reciprocal lattice origin, a 2θ scan moves the detector position along the Ewald's sphere, and the coupled ω-2θ scan moves along the line that intersects the reciprocal lattice origin.

Therefore, we can imagine performing numerous ω-2θ scans at various starting values of ω to map the area around a reciprocal lattice point. This is known as a reciprocal space map (RSM) and is shown in Figure 4.5. We can use the substrate as a reference position to remove error from stepper motor calibration and relax the necessity for perfect alignment. The relative peak location can then be used to extract in- and out-of-plane lattice constants individually. However, in the case of metamorphic materials grown on offcut substrates, epitaxial tilt can arise meaning that the crystal registry of the substrate is not parallel with the film. If only a single asymmetric RSM was used, the effects of strain and tilt can look very similar. Therefore, a second RSM using a symmetric diffraction condition can be used because tilt will show up strictly as a deviation in the Q_x direction. This epitaxial tilt of the film can be subtracted out from the asymmetric scan allowing for proper extraction of in- and out-of-plane lattice constant.

From these maps, composition and strain/relaxation can be extracted. First the in- ($a_{\parallel}$) and out-of-plane ($a_{\perp}$) lattice constants are extracted from the RSMs. The fully relaxed lattice constant is calculated using the Poisson ratio.

$$a_{relaxed} = \frac{1-\nu}{1+\nu} a_{\parallel} + \frac{2\nu}{1+\nu} a_{\perp} \qquad \text{Eq. 4.1}$$

From the relaxed lattice constant and in-plane lattice constant, percent relaxation can be calculated.

$$relaxation = \left[1 - \frac{a_{\parallel} - a_{relaxed}}{a_{sub} - a_{relaxed}}\right] * 100. \qquad \text{Eq. 4.2}$$

Lastly the composition of a ternary alloy can be calculated according to Vegard's law

$$x = (a_{relaxed} - a_2)/(a_1 - a_2) \qquad \text{Eq. 4.3}$$

where a_1 and a_2 are the lattice constants of the constituent binaries [99].

For additional information on XRD or RSMs see the text by Bowen et al. [98], the review paper by Fewster [100], or the more detailed write up in the thesis by Dr. Carrie Andre [26]. There are also a number of excellent visual resources such as the PPT from Dr. Speakman at MIT [101].

4.1.2. ATOMIC FORCE MICROSCOPY

Atomic Force Microscopy (AFM) is a scanning probe technique that is used to map the topography of a sample down to the < 1 nm scale. This can provide information about the epitaxial growth mode as discussed in Chapter 3. An AFM uses a piezoelectrically controlled cantilever to move a nearly atomically sharp tip around the sample. The forces acting on the cantilever by the surface atoms are measured. The cantilever continues to descend until the force of attraction by the nucleus of the surface atoms is balanced out by the repulsive force from the electron cloud. A laser reflected off the cantilever is used to measure the deflection of the cantilever at this point to determine the height of the sample pixel by pixel. The tip is scanned across the sample to map the surface over areas that range from 500 nm × 500 nm all the way to 20 μm × 20 μm.

4.1.3. PHOTOLUMINESCENCE

Photoluminescence (PL) is an optical characterization technique that can provide information about the bandgap energy and/or other optically active defect states within a material. A short wavelength, high intensity laser (488 nm is used at OSU) is shined onto a material, exciting electrons from the valance band to the conduction band. If the carriers combine via a radiative recombination process, there are photons emitted with energy roughly equivalent to the bandgap. A high-resolution spectrometer is used to capture this light and determine its relative intensity and wavelength. Often times these measurements are taken using a chopper and lock-in amplifier to improve the noise floor and filter out background light. At OSU, our PL system uses a single grating monochromator with a

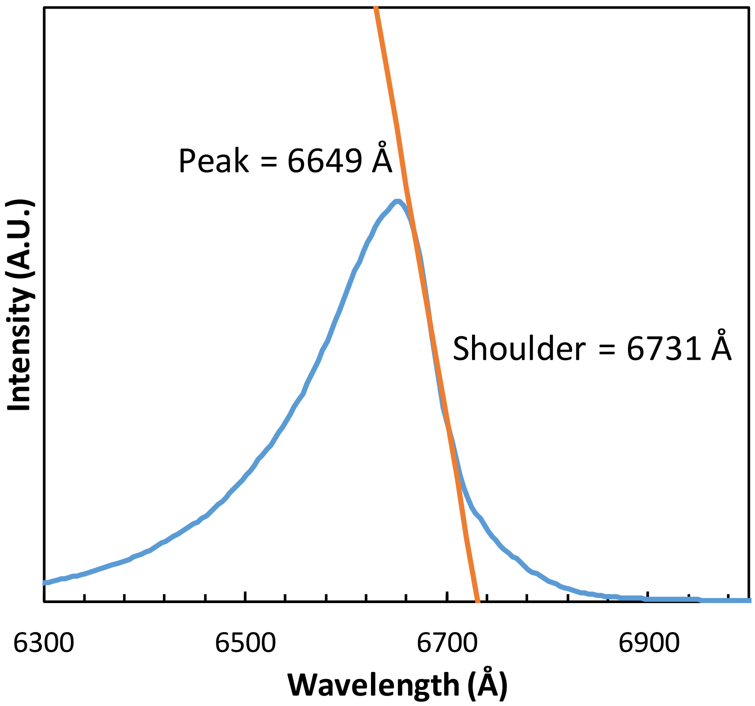

Figure 4.6 Example PL spectrum showing the extraction of Bandgap values. Bandgap is calculated as 12400/λ.

photon multiplier tube and a silicon detector to provide sensitivity to weak photoemission. An example PL scan is provided in Figure 4.6.

At OSU, we use two methods to glean bandgap information from this curve. The PL peak energy, as well as a linear fit to the long wavelength inflection point are determined from the curve. The PL peak position is not the band gap energy as the peak electron concentration does not reside directly at the conduction band edge due to the overlap of the density of states and the Fermi-Dirac probability function [102]. Therefore, the linear extrapolation of the longer wavelength inflection point provides a more accurate bandgap which closely aligns with the bandgap extracted from quantum efficiency measurements. However, changes in intensity can slightly change the value extracted from the linear fit due to challenges with curve fitting. This is the reason that a combination of PL peak position and shoulder position is used to verify the bandgap energy.

Increased radiative efficiency, the percent of minority carriers recombining through radiative processes, leads to brighter photoemission. Therefore, PL intensity measurements can provide generalized information about the quality of the material. While it cannot directly provide minority carrier lifetime information, generalized order of magnitude changes in PL intensity can point to higher quality material or improved minority carrier confinement. This intensity, for a diode is directly linked to the diode dark current with a brighter emission indicating a lower diode dark current.

4.1.4. ELECTRON CHANNELING CONTRAST IMAGING

Electron Channeling Contrast Imaging (ECCI) is a diffraction-based imaging technique performed in a scanning electron microscope (SEM) to quantify crystallographic defects such as stacking faults and dislocations. The disruption in the crystal lattice around defects, causes changes in the backscattered electron signal. The crystal must be rotated to satisfy a diffraction condition in order to promote electron channeling. These diffraction conditions can be seen visually in the SEM at low magnifications in a pattern known as the electron channeling pattern (ECP). An example ECP is shown in Figure 4.7. Zooming in on the edge of a Kikuchi band for a specific diffraction condition will reveal defects which perturb that particular set of planes. Therefore, imaging a particular direction of dislocations is possible by selecting a diffraction condition that satisfies the desired visibility criterion (i.e. the (220) condition).

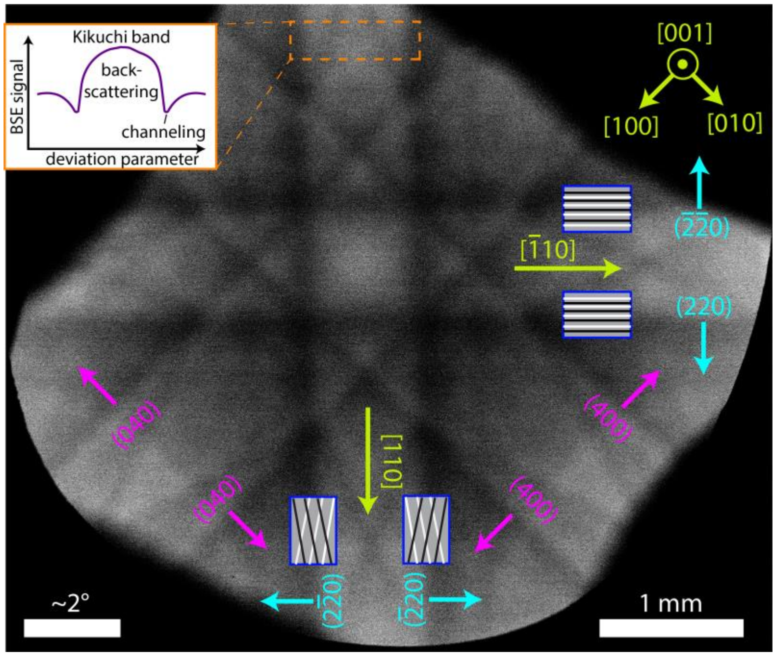

Figure 4.7 Electron channeling pattern of GaP/Si sample. Diffraction planes are indicated in teal and magenta. Depending on the diffraction condition selected different sets of defects can be viewed. Figure used with permission from Dr. Boyer.

All defects can be imaged by selecting a more ubiquitous family of diffraction conditions (i.e. the (400) condition).

An example of a (400) condition ECCI image on a thin GaP layer is shown in Figure 4.8. The misfit dislocations at the GaP/Si interface appear as bright or dark lines depending upon their Burgers vector. This imaging of misfit dislocation over such a large area is critical in understanding the dislocation glide and nucleation dynamics during growth. For thicker films, threading dislocations can be observed as bright-dark dipoles and counting these dipoles provides quantitative TDD information over large image areas. More details about this technique and its application to III-V on Si can be found in the literature by Carnevale et al. [103]–[105] and others [106].

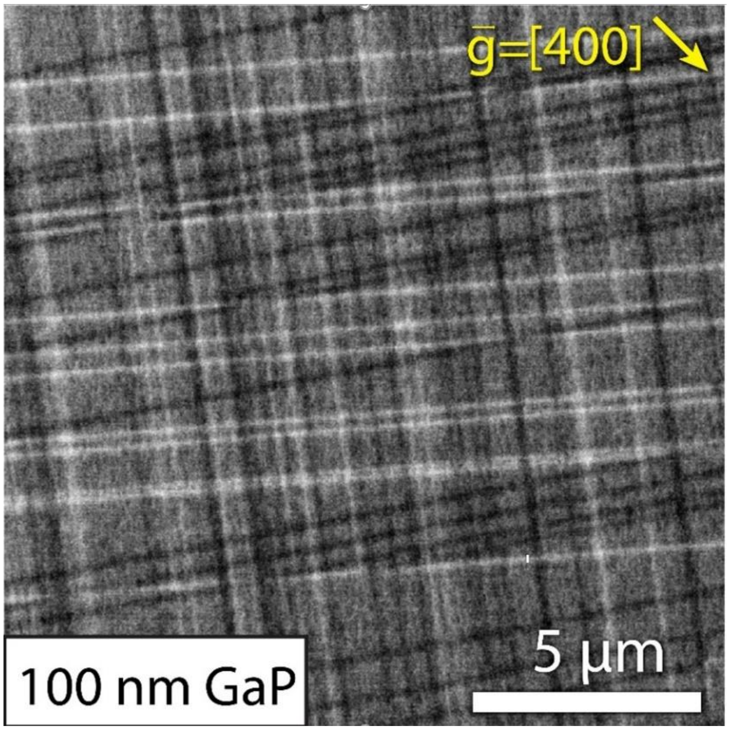

Figure 4.8 (400) condition ECCI image of a 100nm GaP layer on Si. The bright and dark lines are misfit dislocations that lie along the GaP/Si interface.

The non-destructive nature of ECCI, as opposed to traditional transmission electron microscopy (TEM) techniques or defect selective etching, is advantageous for rapid defect characterization over very large areas while maintaining high resolution. Oftentimes, mosaic images consisting of multiple SEM images can be used to image >10000 µm^2 areas. This provides greater accuracy in TDD extraction than plan view TEM or even dislocation delineation etching.

4.1.5. ELECTRON BEAM INDUCED CURRENT

Electron beam induced current (EBIC) is a materials characterization technique, that require a fabricated device with electrical contact to the semiconductor. The concept

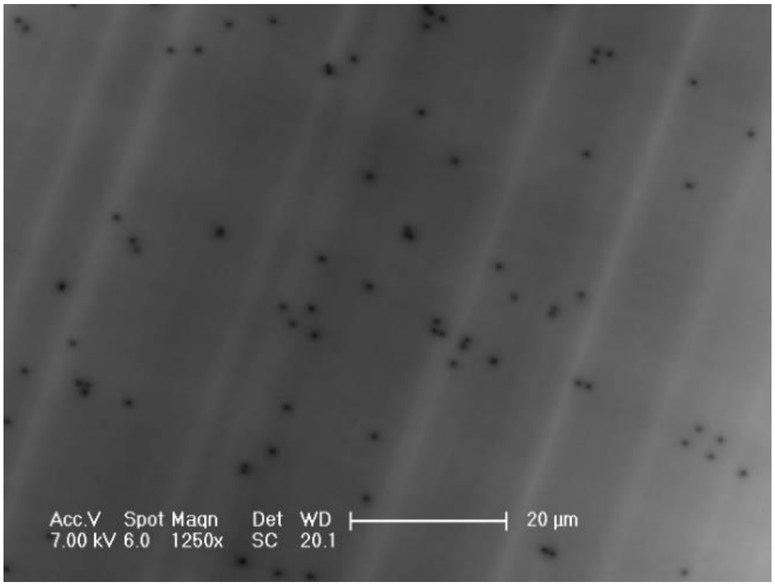

Figure 4.9 EBIC micrograph showing numerous recombination centers associated with dislocations in metamorphic $Ga_{0.64}In_{0.36}$ P solar cells.

is that electron-hole pairs are generated when the semiconductor material is struck by an electron beam. These electron-hole pairs are collected just as in the operation of a solar cell. In an ideal material, no matter where the beam is placed along the surface of a sample, the current should remain constant. However, in the presence of extended defects that act as Shockly-Read-Hall recombination centers, the current generated around this defect will be lower due to excess minority carrier recombination.

In this technique, the current is actively monitored by a transimpedance (current to voltage) amplifier, and the signal from this amplifier is overlaid with the beam position. Therefore, when the electron beam strikes a defective region of the crystal the current generated by the device will be lower showing up as a dark spot on the corresponding image created by the capture card. The dark spot density (DSD) can then be calculated and is usually treated as an acceptable analog to TDD. In terms of understanding the role of dislocations on device performance, EBIC (rather than ECCI) is often a more valuable technique. EBIC directly measures recombination activity rather than simply mapping perturbations in crystal structure. In devices, recombination is the more important metric and should therefore be preferred over a crystallographic measurement technique. An example EBIC image is given in Figure 4.9. While not performed in this dissertation, EBIC can also be used to extract minority carrier transport properties such as diffusion length. To learn more about both plan view and cross-sectional EBIC, the following references are quite useful [107]–[111].

4.2. DEVICE CHARACTERIZATION TECHNIQUES

This section focuses on device characterization technique that have been used to characterized solar cells in this dissertation. These include both *I-V* measurements, as well as spectrally resolved measurements such as quantum efficiency.

4.2.1. CURRENT-VOLTAGE MEASUREMENTS

A current voltage measurement (*I-V*) is a simple measurement that involves incrementing either the current or voltage being supplied to a device and observing the change in either the voltage or current respectively. This is done using a source measurement unit (SMU) which both supplies power and measures either current or voltage simultaneously. This is a very important measurement both in understanding the device physics at play and extracting critical solar cell metrics such as efficiency. Typically, the current values are normalized to the device area to produce a *J-V* measurement for more insight into device performance irrespective of area.

4.2.1.1. DARK *I-V* MEASUREMENTS

A dark *I-V* measurement is simply an *I-V* measurement performed in the absence of ambient light. This allows for extraction of critically important diode metrics which provide insight into the material quality and minority carrier lifetime. The diode *I-V* characteristics are typically viewed on a Log-*I* axis to observe the exponential nature of the I-V curve. An example of a dark *I-V* curve plotted on a log scale is give in Figure 4.10. Then, a double-diode model can be used to extract the physically relevant diode characteristics as discussed in Chapter 5.

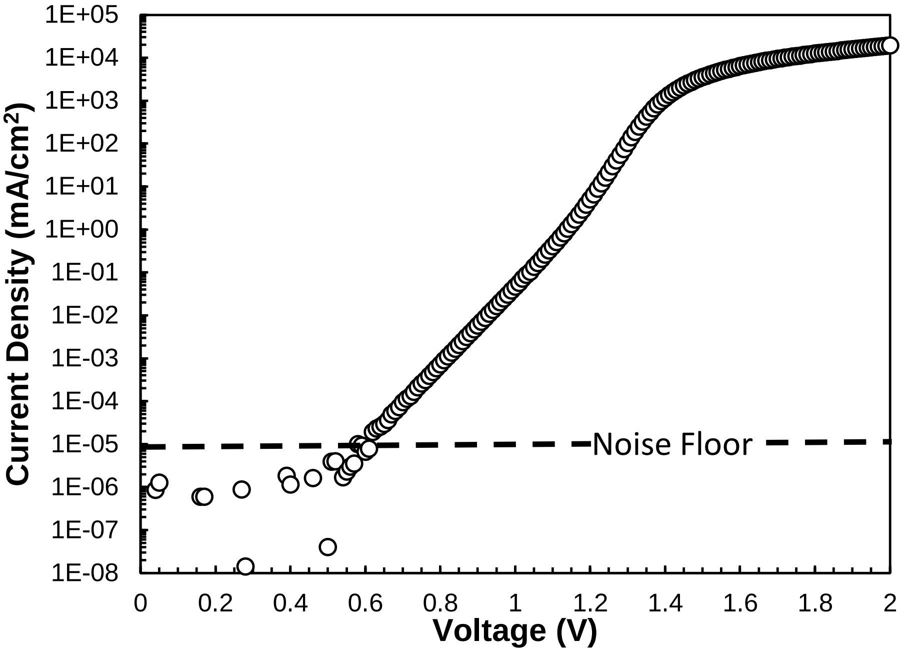

Figure 4.10 Example Dark-IV curve showing 3 regions of interest. The first linear section is J_{02} limited, the second linear region is J_{01} limited, before series resistance finally takes over.

4.2.1.2. ILLUMINATED I-V MEASUREMENTS

An Illuminated *I-V* (LIV) is typically performed under a solar simulator mimicking one of the standard solar spectra (AM1.5G or AM0). The voltage or current flowing through the device is controlled by the SMU even though the SMU is acting as a power sink rather than a power supply in this case. This measurement provides the useful cell metrics such as short circuit current (J_{SC}), open circuit voltage (V_{OC}), fill factor (FF), efficiency, etc. An example LIV measurement is given in Figure 4.11. It is critical that the solar simulator is calibrated properly to provide confidence in these metrics and to be able to compare results across research institutions. The solar simulator at OSU is a dual-zone simulator with 4 LED boost zones. These sources can be tuned in intensity to

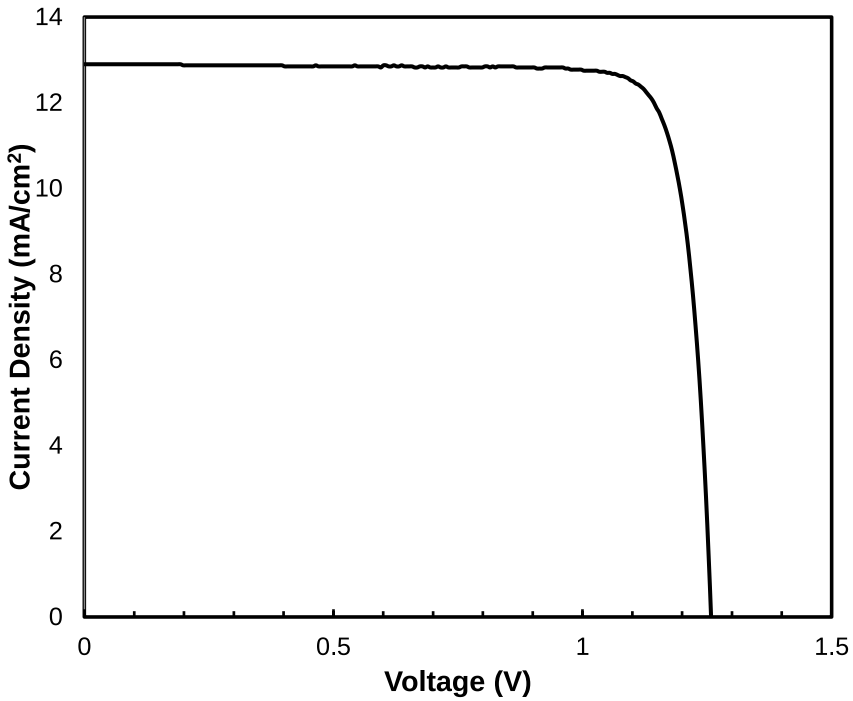

Figure 4.11 Example Illuminated *I-V* curve for a $GaAs_{0.75}P_{0.25}$ top cell under simulated AM1.5G solar spectrum.

accurately mimic the desired solar spectrum. The simulator is calibrated using multiple calibrated reference cells with different bandgaps, or in the case of recently, an NREL certified $GaAs_{0.75}P_{0.25}$ /Si tandem cell. This enables a semi-accurate spectral agreement with the desired standard spectrum; however, localized (nm by nm) deviations from the standard spectra are present. Therefore, certified measurement of efficiency is performed at a standardized laboratory such as the National Renewable Energy Laboratory (NREL), to accurately compare results across research groups and technologies. For more comprehensive reading on the standards and calibration procedures needed for accurate LIV measurements see the following references [112]–[115].

4.2.2. QUANTUM EFFICIENCY

4.2.2.1. BASIC CONCEPTS

Quantum efficiency is a measurement technique that provides spectrally resolved information about the photocurrent generated under light. External quantum efficiency is the ratio of electrons extracted from the device vs. the number of photons shined onto the device [50]. This measurement is done as a function of wavelength to describe how good or bad a solar cell is at collecting various wavelengths of light. An ideal EQE would be a value of 1 for wavelengths less than the absorption cutoff, and 0 for values greater than the absorption cutoff. Integrating the EQE as a function of wavelength multiplied by the spectrally resolved solar irradiance, provides the magnitude of the J_{SC} under a given spectrum.

$$J_{SC} = \mathrm{q} \int EQE(\lambda) * \Phi_{\mathrm{AM1.5G}}(\lambda)\, d\lambda. \qquad \text{Eq. 4.4}$$

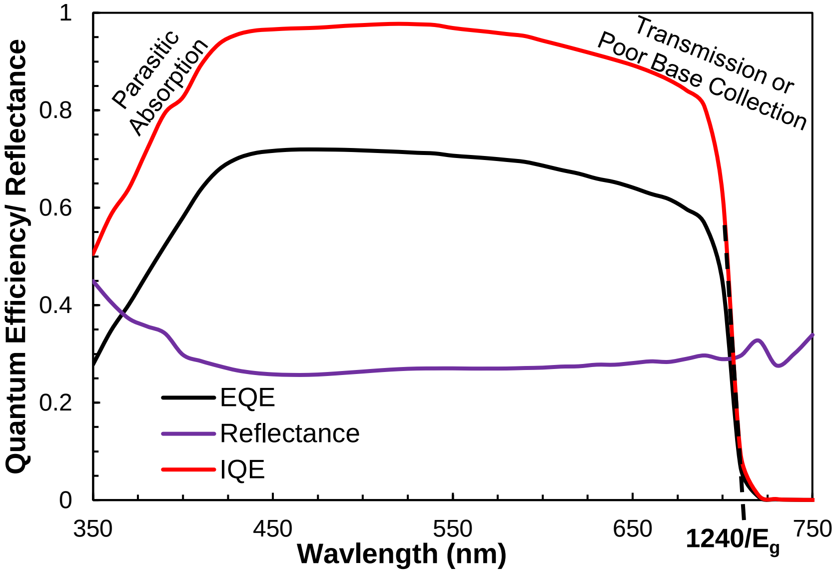

Figure 4.12 Example quantum efficiency and reflectance curves for a $GaAs_{0.75}P_{0.25}$ top cell. The roll off in short wavelength absorption is due to parasitic absorption, and the roll off at long wavelength is due to transmission and/or poor base collection.

Based on the cutoff wavelength the EQE curve can help to extract bandgap information from a solar cell by fitting the inflection point on the long wavelength side and seeing where it trends towards zero. While this value does not perfectly agree with the true bandgap of the material due to bandgap narrowing and/or incomplete absorption effects, it is in fact the more critical estimation of bandgap when designing current matched multijunction cells.

Oftentimes an even more insightful parameter for understanding the device physics at play in short circuit collection is the internal quantum efficiency (IQE). IQE is a reflectance normalized EQE. It effectively describes the following: “of the photons which entered the semiconductor, what fraction resulted in collected electrons.” Mathematically this concept can be expressed as

$$IQE = \frac{EQE}{1-R}. \qquad \text{Eq. 4.5}$$

This value provides more insight into the collection efficiency within the device, since it removes reflection as a variable. An example of EQE and IQE measurements are shown in Figure 4.12 for a $GaAs_{0.75}P_{0.25}$ top cell. Because different wavelengths of light are absorbed at different depths in the material, both EQE and IQE provide a sort of depth resolved understanding of collection efficiency. This led me to select, IQE as my measurement of choice to better understand collection dynamics in various types of solar cells during my tenure. In fact, the development of analytical modeling presented in Chapter 5 provided a great deal of insight into the transport parameters of the solar cells in this work.

4.2.2.2. QE MEASUREMENTS OF MULTIJUNCTION CELLS

While measurement of single junction solar cells is as simple as measuring the current output of the device and accurately knowing the input spectrum, multijunction solar cells require additional light and voltage bias in order to ensure that the subcell of interest is measured accurately. As discussed in Chapter 2, the current output of a multijunction solar cell is limited by the lowest current producing junction. When using a monochromatic source, all of the junctions except one would have no photocurrent preventing the generation of current from the multijunction device. To solve this, LEDs can be used to bias the other junctions with light much brighter than the monochromatic source. This makes the subcell of interest the current limiting subcell. However, this alone is not sufficient as the voltages produced by the other subcells will effectively bias the junction of interest in reverse bias at a value of (ΣV_{oc}). This is shown in the case of a dual junction solar cell in Figure 4.13. As a result, many artifacts could be present. First,

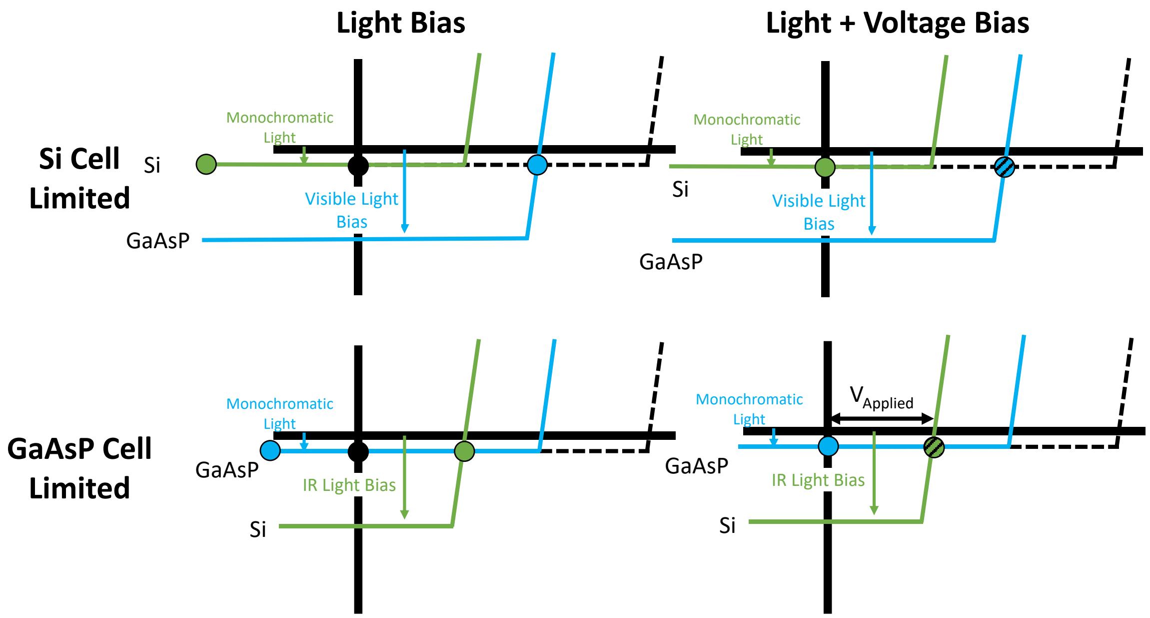

Figure 4.13 Schematic representation of light and voltage biasing for a $GaAs_{0.75}P_{0.25}$ /Si dual junction solar cell. The Light biasing is used to select the junction of interest and the voltage biasing is used to ensure that the junction is at zero bias.

the forward biased junctions will emit light which could potentially be absorbed by the junction of interest. This is known as luminescent coupling and results in a signal for a lower junction in the wavelength range expected for an upper junction. Second, it is important to measure the quantum efficiency at zero bias as voltage dependent collection efficiency can result in overestimation of the EQE if the subcell is measured in reverse bias. Lastly, low shunt resistance in a particular subcell can result in additional artifacts which may provide incorrect spectral response measurements. This is often seen in lattice latched triple junctions due to the low shunt resistance of the Ge subcell. In order to correct for these artifacts, it is necessary to apply a voltage to the overall device in order to ensure that the subcell of interest is under zero bias as seen in Figure 4.13. Further information on artifacts seen in the multijunction QE curve is given in the following reference [116]–[119].

4.2.2.3. OSU CUSTOM QE MEASUREMENT SETUP

In the QE system at OSU, the EQE is measured using a white light source, monochromator, chopper, filter wheel, microscope, calibrated detector, transimpedance amplifier, and a lock-in amplifier. First the detector is placed on the sample stage and the intensity of the source as a function of wavelength is measured. During this scan, a calibrated reference detector is placed after a beam splitter to provide a reference to correct for any temporal deviations in lamp intensity. Next, the sample is loaded onto the sample stage, probes landed on the device, and the source wavelength swept across the wavelengths of interest. The device is connected to the transimpedance amplifier which converts the current generated by the device into a voltage. Additionally, this amplifier allows us to filter out noise and provide bias to the cells in the case of multijunctions as discussed in the prior subsection. This voltage is passed into a lock-in amplifier, keyed to

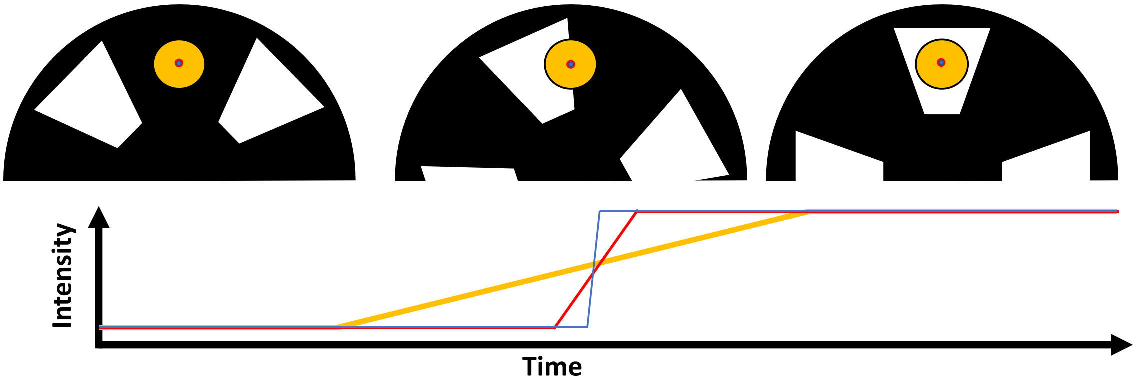

Figure 4.14 Qualitative description of why the chopper does not provide an ideal square wave. Due to this, the calculation of wave amplitude must be altered slightly from the standard Fourier transform of the square wave.

the frequency of the chopper, that extracts the first harmonic of the input wave. Three LEDs with wavelengths of 450 nm, 940 nm, and 600 nm are used in order to light bias multijunction solar cells. The voltage bias is achieved via the transimpedance amplifier, which has a voltage controller connected to a second series of probes attached to the device.

While a chopper should provide an ideal square wave signal, the beam does have a finite size and therefore results in a trapezoidal shaped wave. The reason for this is shown in Figure 4.14. The standard modulation factor relating the magnitude of the first harmonic measured by the lock-in amplifier to the amplitude of a square wave is given by the simple Fourier transform of a square wave ($\sqrt{2}/\pi$), and the value comes out to be 0.4502. However, as the diameter of the beam is increased and the waveform becomes more trapezoidal, the modulation factor decreases as more energy is contained within the lower frequency harmonics. The modulation factor for our chopper at a 3 mm diameter beam size is ~0.4378. These values have been obtained by numeric methods and are provided in the following reference [120].

EQE can then be calculated by determining the number of electrons (measured as current) and the flux entering the detector during the reference scan corrected by any deviation observed in the monitor detector from the earlier reference scan. Lastly, to calculate IQE, the reflected intensity of the sample as well as a calibrated mirror are measured as a function of wavelength. The reflectance can be calculated by creating a normalization factor using the calibrated mirror and applying this calibration factor to the reflected intensity from the sample.

4.2.3. SUNS J_{SC}-V_{OC}

Suns J_{SC}-V_{OC} is a method for recreating the diode dark *I-V* curve in the absence of series resistance and voltage dependent collection efficiency [121]. Instead of using an SMU to provide the power to the cell and measuring current vs. voltage, a light source with controllable intensity is used to provide power into the cell. For every light intensity the J_{SC} and V_{OC} are measured, and are plotted as an ordered pair (V_{OC}, J_{SC}). The light intensity is changed, and the next data point measured. At OSU, the tunable light source is a high-power white LED and can be tuned from very low intensity up to >1 sun intensity if the LED is placed very close to the device.

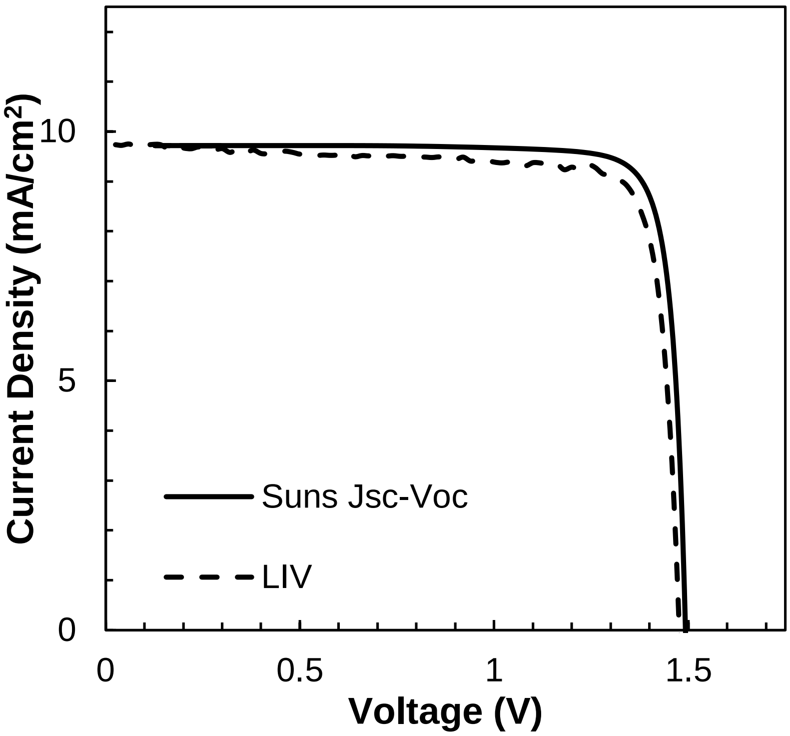

Figure 4.15 Example suns J_{sc}-V_{oc} measurement on a metamorphic $Ga_{0.64}In_{0.36}P$ cell. The removal of voltage dependent collection is evident in the Suns J_{sc}-V_{oc} measurement.

These Suns J_{SC}-V_{OC} measurements are often compared to LIV curves by flipping the diode curve and shifting it up by the value of J_{SC} as measured by LIV. Because the current is always measured at short circuit, this comparison removes the impact of voltage dependent collection efficiency discussed in more detail in Chapter 6. An example is shown in Figure 4.15 [122].

4.2.4. DIRECT VOLTAGE DEPENDENT COLLECTION MEASUREMENT

While the presence of VDC in single junction cells can typically be proven using Suns J_{SC}-V_{OC} measurements, it does not provide information about what wavelengths of light are being lost. Instead, to characterize the VDC, I have developed the numerical parameter, $F_{VDC}(\lambda)$, as the wavelength-resolved, normalized slope of the *I-V* curve near zero bias, $J(V \approx 0)$, in the absence of any discernable impact of non-infinite shunt resistance:

$$F_{VDC}(\lambda) \equiv \frac{\left[\frac{dJ(\lambda,V\approx 0)}{dV}\right]}{J(\lambda,V\approx 0)}. \qquad \text{Eq. 4.6}$$

$F_{VDC}(\lambda)$ effectively describes the fraction of photocurrent lost per volt, as a function of wavelength. By rearranging the above equation and integrating over the relevant illumination spectrum (AM1.5G/AM0), the slope of the LIV curve for a single junction cell can be analytically described by its EQE and F_{VDC}:

$$\frac{dJ(V\approx 0)}{dV} = \int_{\lambda=min}^{max} EQE(\lambda) \cdot \Phi_{\mathrm{AM1.5G}}(\lambda) \cdot F_{VDC}(\lambda) \cdot d\lambda. \qquad \text{Eq. 4.7}$$

To measure F_{VDC}, small spot, single wavelength illuminated *I-V* curves are collected. In the case of a tandem cell either a 940 nm or 450 nm LEDs can be used to provide the appropriate light biasing to measure the subcell of interest. While this measurement

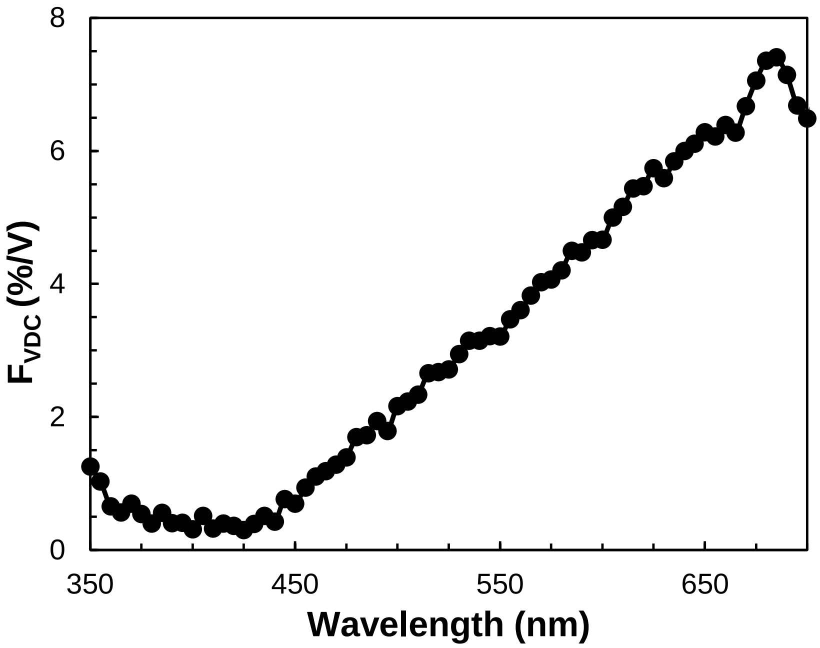

Figure 4.16 Example direct measurement of voltage dependent collection parameter.

provides similar insight to voltage dependent EQE measurements, it provides data at finer voltage steps to more accurately discern the impact of voltage on photocurrent than the traditionally larger voltage steps used in voltage dependent EQE measurements. Additionally, it directly measures the slope of an *I-V* curve, the metric of interest, rather than relying on just two current measurements at two significantly different voltages. An example VDC measurement of a $GaAs_{0.75}P_{0.25}$ top cell is shown in Figure 4.16.

This technique was developed during my tenure here, with groundwork from former postdoc Dr. Ratcliff to provide insight into the spectrally resolved nature of voltage dependent collection. If information is known about which wavelengths of light are being lost due to the application of voltage, insight into the physical mechanisms for this loss can be assessed. A simple model is presented in Chapter 5 to provide an understanding of the physical mechanism for the VDC.

4.3. CONCLUSIONS

There are a variety of materials and device characterization techniques used in this thesis. While each of these alone is powerful, correlation of materials properties to device performance is a critical corner stone of this work and is where these characterization techniques truly shine. The combination of all of these techniques helps to paint a picture of how materials properties correlate to transport properties and finally to device performance.

CHAPTER 5:

SOLAR CELL DEVICE MODELING

5.1. INTRODUCTION

Throughout this dissertation, I have employed analytical modeling to elucidate trends, quantitatively extract transport metrics, and to project solar cell performance as a function of defect densities. These models are fantastic for understanding the mathematical relationships in design choices and understanding tradeoffs present in cell design at the simplest level. I chose to focus on analytical models over computer aided design as they can provide greater insight into the underlying physics at play than numeric models. While at times these models may not capture all of the nuances, I believe that the intuition built using these models is paramount in designing devices and one of the primary reasons for the successes in this dissertation. The models used in this dissertation can be generally lumped into 5 primary areas:

1. Quantum Efficiency Modeling
2. Double Diode Modeling
3. Grid Metal Resistive Loss Modeling

4. Voltage Dependent Collection Modeling
5. TDD vs Performance Modeling

5.2. QUANTUM EFFICIENCY MODELING

5.2.1. APPROACH

As mentioned in Chapter 2, quantum efficiency can be modeled by the separately calculated collection probability and photogeneration as a function of position in the cell. This relationship is given in Equation 5.1.

$$IQE(\lambda) = \frac{\int f_c(x) * G(x,\lambda)dx}{\Phi(\lambda)} \qquad \text{Eq. 5.1}$$

Ultimately this equation reduces to the well-known Hovel's model [48], [123]; however, in my opinion, this approach provides greater flexibility where different methods for calculating either the photogeneration or collection probability can be employed depending on the structure and the relative importance of various optical and transport phenomena.

5.2.2. COLLECTION PROBABILITY MODELING

Collection probability in a given layer can be classified into one of 3 cases. First, collection probability in the depletion/space charge region is assumed to be unity due to the high electric field present in these regions. This large electric field quickly sweeps minority carriers out of this region well before any significant number of carriers can recombine. This assumption also is used in the Hovel's model [48], [123]. Second, collection probability in the un-depleted regions of the cell that are adjacent to the depletion region are calculated using Equation 5.2, formulated from the reciprocity theorem [124], [125]. In this case $x = 0$ is defined at the edge of the depletion region and the positive x direction is always moving away from the depletion region edge.

$$f_c(x) = \frac{D\cosh\left(\frac{W-x}{L_D}\right) + SL_D \sinh\left(\frac{W-x}{L_D}\right)}{D cosh\left(\frac{W}{L_D}\right) + SL_D \sinh\left(\frac{W}{L_D}\right)} \qquad \text{Eq. 5.2}$$

Here, D is the diffusivity of minority carriers, L_D is the minority carrier diffusion length, W is the width of the un-depleted/quasi-neutral region of interest, and S is the effective surface/interface recombination velocity with the adjacent layer at $x = W$. The last case is for layers like the window, where they are quasi-neutral but are not adjacent to the depletion region. In layers like this, Equation 5.3 provides forced continuity across the heterointerfaces to satisfy the reciprocity relationship.

$$f_c(x) = f_c(x = 0^-) * \frac{D\cosh\left(\frac{W-x}{L_D}\right) + SL_D \sinh\left(\frac{W-x}{L_D}\right)}{D cosh\left(\frac{W}{L_D}\right) + SL_D \sinh\left(\frac{W}{L_D}\right)} \qquad \text{Eq. 5.3}$$

Implementation of three cases for the various layers present in a typical III-V solar cell result in a piecewise collection probability with continuity at all interfaces as seen in Figure 5.1. In most cases, minority carrier generation and collection from the 2.05 eV bandgap $Ga_{0.63}In_{0.37}P$ BSF layer was ignored. This is because greater than 99.9% of photons with energy above 2.05 eV are absorbed within the preceding $GaAs_{0.75}P_{0.25}$ layers, eliminating any meaningful current contribution from the buried BSF layer.

The relative impact of surface and bulk recombination pathways is an important factor in determining the shape of the collection probability curve. If the collection is bulk limited (i.e. $S << D/L_D$) then the curve will decay exponentially as dictated by the

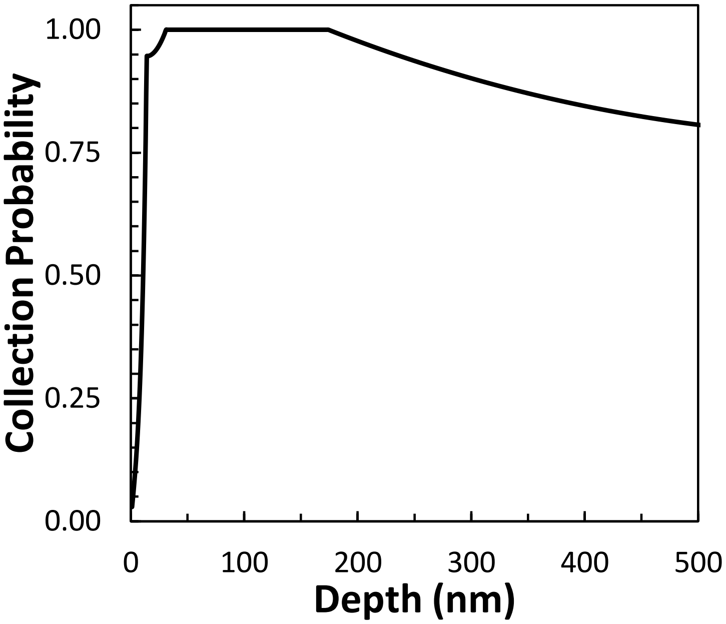

Figure 5.1 Piecewise continuous collection probability profile as a function of depth. The shar drop off at the front is the window layer, the next exponential increase is the un-depleted emitter, the flat unity collection region is the depletion region, and the exponentially decaying region is the un-depleted base.

cosh terms. If it is surface limited ($S >> D/L_D$) the curve will have a pseudolinear profile dictated by the sinh terms.

The impact of dopant grades and compositional grades in quasi-neutral regions result in the creation of electric fields (or effective electric fields in the case of a compositional grade) in the quasi-neutral regions. The diffusion length in discrete layers, $L_{D,}$ under weaker effective fields can be modified to an effective drift-diffusion length ($L_{D\text{-}D}$) according to Equation 5.4 [126].

$$L_{D-D} = \frac{L_D}{\sqrt{1+\left(\frac{\epsilon L_D}{2V_T}\right)^2}-\left(\frac{\epsilon L_D}{2V_T}\right)} \qquad \text{Eq. 5.4}$$

Equation 5.4 includes the average effective electric field acting on the minority carriers (ϵ), the thermal voltage (V_T), and the diffusion length (L_D). These electric fields also influence the surface or interface recombination velocity (SRV/IRV), S. This resultant effective IRV, S_{eff}, is then described by Equation 5.5 where S is the original SRV/IRV, μ_e is the carrier mobility, and ϵ is the electric field [127].

$$S_{eff} = S - \mu_e \cdot \epsilon \qquad \text{Eq. 5.5}$$

These modified transport parameters are then plugged into the equations dictating the piecewise collection probability profile. This approach of modifying the transport parameters due to an electric field was used in an early work during my Ph.D. tenure on graded window/emitter structures for $Ga_{0.51}In_{0.49}P$ cells not directly presented in this thesis [56].

5.2.3. PHOTOGENERATION PROFILES

5.2.3.1. INTERPOLATION OF OPTICAL CONSTANTS

Calculation of photogeneration vs. depth profiles relies on knowledge of material properties including the real and imaginary component of the index of refraction. These optical constants (*n* & *k*) used in the calculation of both internal reflectances and absorption calculations were interpolated according to a method developed by Lumb et al. [128], using previously reported critical points of the $GaAs_yP_{1-y}$ [129], $Ga_xIn_{1-x}P$ [130], and $Al_xIn_{1-x}P$ [131] materials systems and optical constants of the constituent binary and/or well-known ternary alloys [129], [132]–[135]. This interpolation procedure uses reports of how the critical points move with composition as well as a smooth interpolation of the data between these critical points. An example of the index of refraction of the $GaAs_yP_{1-y}$ material system as a function of composition is shown in

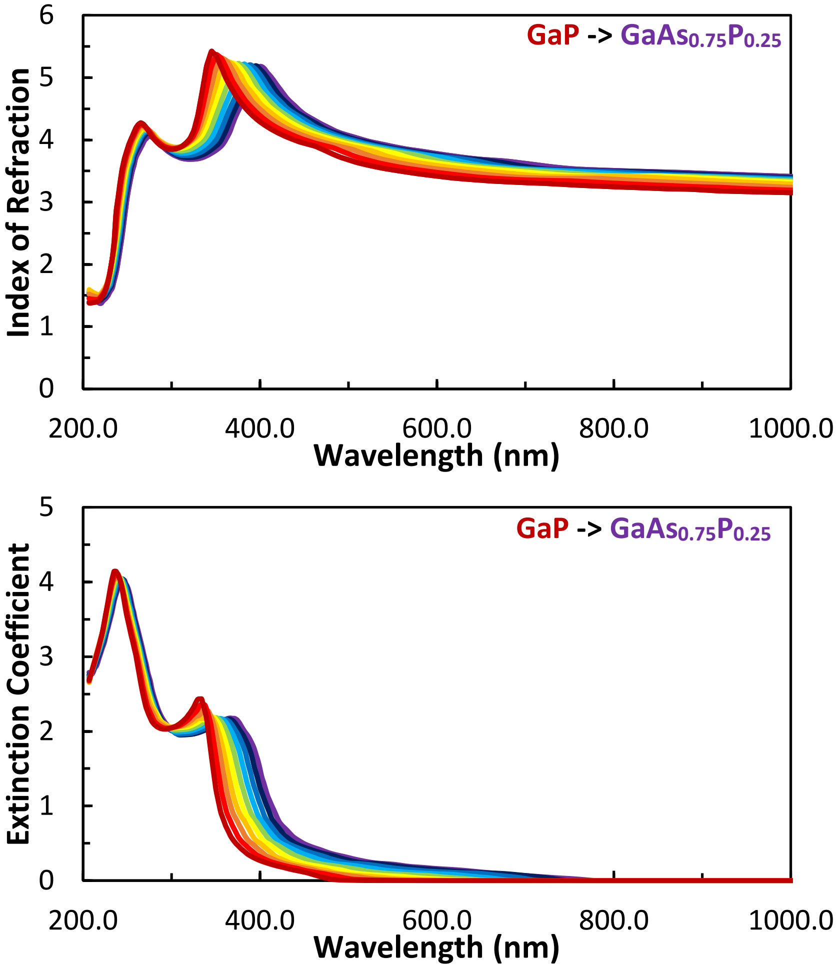

Figure 5.2 Index of refraction and extinction coefficient of numerous $GaAs_yP_{1-y}$ alloys from GaP (red) to $GaAs_{0.75}P_{0.25}$ (purple).

Figure 5.2. The optical constants of these alloys were then tuned according to empirical bandgaps and absorption edges to ensure realistic absorption coefficients near band edge (especially in the $GaAs_{0.75}P_{0.25}$ and $Al_{0.66}In_{0.34}P$ materials), based on methods presented by Kurtz et al. [136].

5.2.3.2. Photogeneration Without Second Pass Photons

Because the indices of refraction in the III-V materials of interest are so similar, the reflectances between these layers are usually small. This means that the flux reflected off a given interface and passed back through a material does not contribute significantly to the photogeneration and therefore IQE. In this case, a simple one pass Beer-Lambert law approach that removes flux reflected at interfaces was used. This strategy for the top layer in the solar cell with thickness W_1 is given by the Beer-Lambert law. In this case, Φ_0 is considered as the flux immediately after light has entered the semiconductor. This is the strategy used to model IQE because the front reflectance has already been normalized out.

$$G_1(x,\lambda) = \Phi_0(\lambda) * \alpha_1 * \exp(-\alpha_1 x) \quad | \quad 0 < x < W_1 \qquad \text{Eq. 5.6}$$

For the second layer, the incoming flux is modified by the absorption in the first layer, and the reflectance at the interface. This reflectance is small, ~1.3% AM1.5G

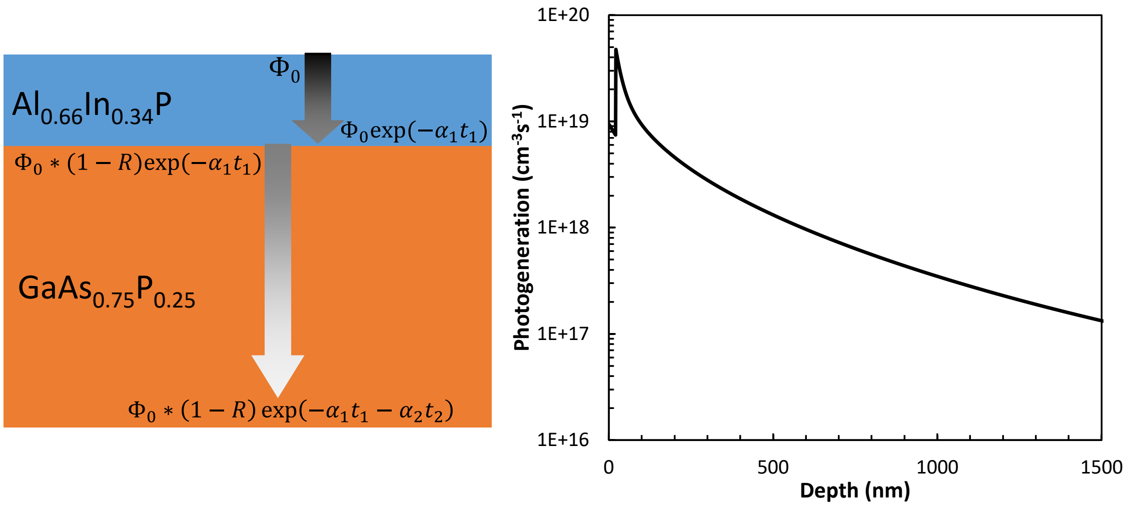

Figure 5.3 a) Schematic detailing the magnitude of the photon flux as a function of depth when not including a second photon pass. b) Example photogeneration as a function of depth for a white light source for a $GaAs_{0.75}P_{0.25}$ top cell.

average spectral reflectance at the $Al_{0.64}In_{0.36}P/GaAs_{0.75}P_{0.25}$ interface but should not be completely ignored. This flux is therefore removed from the flux entering the emitter.

$$G_1(x,\lambda) = \Phi(\mathrm{w}_1,\lambda) * (1 - R_{12}) * \alpha_2 * \exp(-\alpha_1 x) \quad | \quad 0 < x < W_2 \quad \text{Eq. 5.7}$$

This strategy is schematically detailed in Figure 5.3a with an example piecewise photogeneration vs depth profile in Figure 5.3b.

5.2.3.3. PHOTOGENERATION PROFILE INCLUDING SECOND PASS PHOTONS

The inclusion of internal reflectances is only necessary if there are optical structures that purposefully cause higher reflectance such as a distributed Bragg reflector or rear metal reflector. As such this approach is used in the section exploring the optically reflective structures in Chapter 7. The internal reflectances necessary to accurately calculate photogeneration rate in the active region of the cell can be determined via the transfer matrix method (TMM) [137]–[140], allowing for the calculation of the three key optical parameters: T_{Front}, the transmissivity of the layers above the regions of active collection; R_1, the reflectance at the front of the emitter layer with the front optical subsystem (S1); and R_2, the reflectance at the rear of the base layer with the rear optical subsystem (S2). S1 includes the window layer and the antireflection coating (ARC) layers, as detailed in further sections. S2 includes the BSF, tunnel junction interconnect, DBR layers, $GaAs_yP_{1-y}$ SGB, substrate and back metal (detailed in Figure 5.4).

Then using these critical reflectances/transmittances, the total photogeneration can be calculated as the sum of all photogeneration passes assuming totally incoherent reflectance (meaning no standing wave is formed). The first pass is calculated by

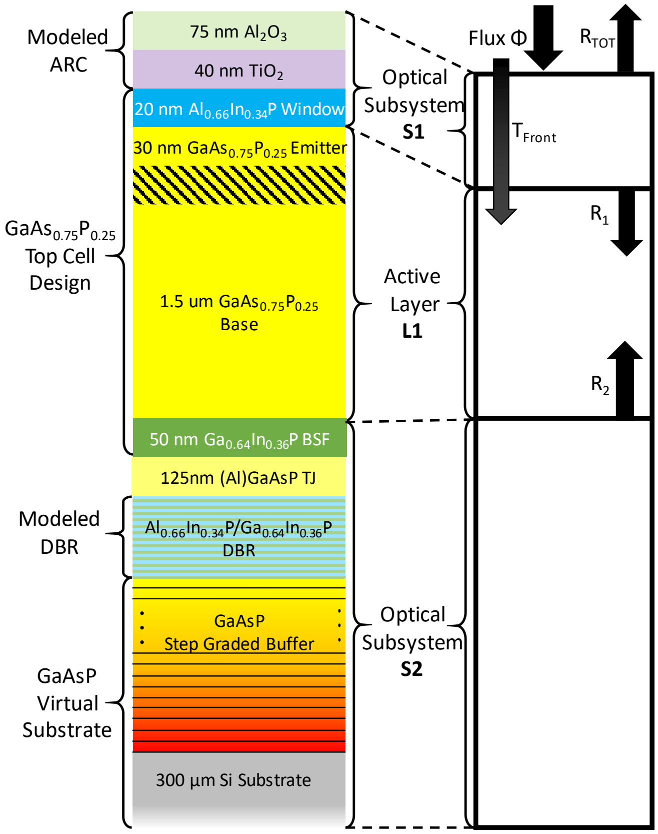

Figure 5.4 Schematic representation of the TMM approach allowing for the simplification of several complex optical layers into a single reflectance and transmittance.

Equation 5.8 where in this case Φ_0 is the flux before entering the emitter. Therefore $T_{front}(\lambda) * \Phi_0(\lambda)$ is the flux just after entering the region of active collection.

$$G_1(x,\lambda) = T_{front}(\lambda) * \Phi_0(\lambda) * \alpha * \exp\,(-\alpha x) \qquad \text{Eq. 5.8}$$

The second pass accounts for the absorption during the first pass and the reflectance at the back of the base with S2. In Equation 5.9 w is the thickness of the active region of collection (base + emitter).

$$G_2(x,\lambda) = T_{front}\;\Phi_0\exp(-\alpha w) * R_2\;\alpha\exp\,(-\alpha x) \qquad \text{Eq. 5.9}$$

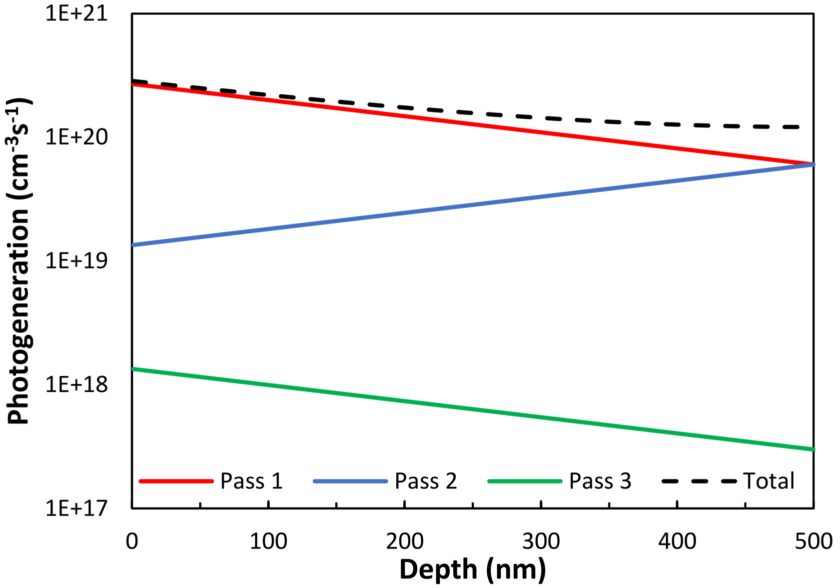

Figure 5.5 Photogeneration as a function of depth for a 500nm film illuminated with a monochromatic source.

The third pass includes the absorption losses from the first 2 passes plus the reflectance with the optical subsystem S1.

$$G_3(x,\lambda) = T_{front}\; R_2\Phi_0 \exp(-2\alpha w) * R_1\; \alpha \exp(-\alpha x) \qquad \text{Eq. 5.10}$$

This continues indefinitely for any number of optical passes. Realistically, if a proper ARC is designed, including flux beyond the second pass is not super impactful as R_1 should be very small making G_3 and subsequent passes negligible. This is shown in Figure 5.5 with the total photogeneration and photogenerations from each pass detailed. Additionally, including the T_{front} parameter, and excluding the window as an active collection layer makes this process more immediately amenable to the calculation of EQE rather than IQE. This can obviously be corrected by calculating the total structure reflectance (R_{front}) via the TMM and correcting the calculated EQE by this value to achieve IQE.

While this is a perfectly acceptable way to perform this calculation, I preferred to use an extension of the Hovel's model developed by Lumb et al. [141] in the actual simulation of the DBRs in Chapter 7 and the commensurate publication [142]. The only deviation from the model presented by Lumb is that instead of using $\Phi_0(1-R_1)$ as the incident flux to the active region of the cell, $\Phi_0(T_{Front})$ is used. This enables the model to account for absorption losses in layers prior to the emitter, including the window layer and modeled ARC layers. This model lumps together the two separately calculated photogeneration and collection probability terms as they often take similar mathematical forms. However, even with these algebraic simplifications, the equation is still prohibitively long to include here but is elegantly derived in the following reference [141].

Since the paper on the exploration of distributed Bragg reflectors was written, I have expanded the modeling capabilities already published to use a TMM based formulization for photogeneration in the active layer which uses an infinite series to sum the optical passes and accounts for coherent reflections. This technique is present in the holistic solar cell modeling code package presented in the Appendix.

5.3. DOUBLE DIODE MODEL

5.3.1. CONCEPT

The double diode model is a method of simulating or projecting the *I-V* curve of a solar cell using discrete circuit elements to account for the various physical transport phenomena within the cell. This can be done either in the illuminated condition to simulate the LIV curve or as a dark diode. The circuit schematic is shown in Figure 5.6. There are 2 parallel diodes (n=1 and n=2), a parallel resistor (R_{Shunt}), a series resistor (R_{series}) and in the illuminated case a parallel current source. All in all, this model can be used to analyze illuminated I-V curves but is especially valuable for the analysis of dark I-V measurements. This model does not account for the breakdown of the superposition of light and dark currents due to VDC but can still be valuable from a holistic device understanding such as the extraction of series and/or shunt resistances.

5.3.2. CIRCUIT LEVEL UNDERSTANDING

Beyond the current source and the $n = 1$ diode, all the other circuit elements are used to account for parasitic transport mechanisms. For example, the $n = 2$ diode

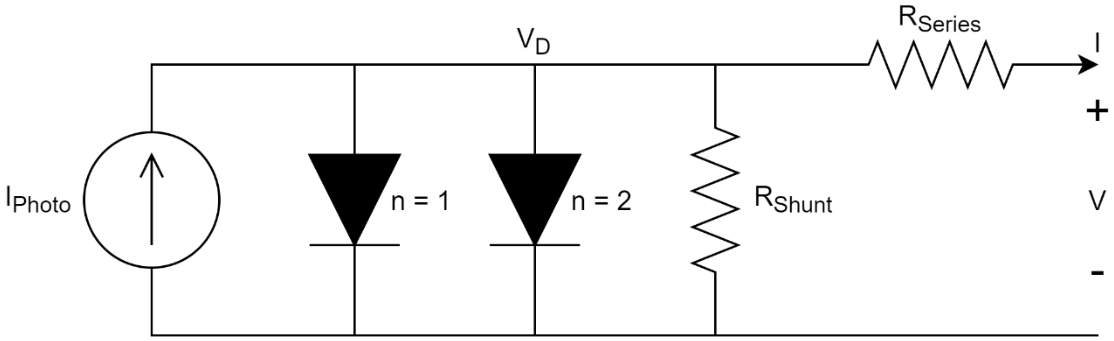

Figure 5.6 Double diode circuit model including parasitic diodes and resistances.

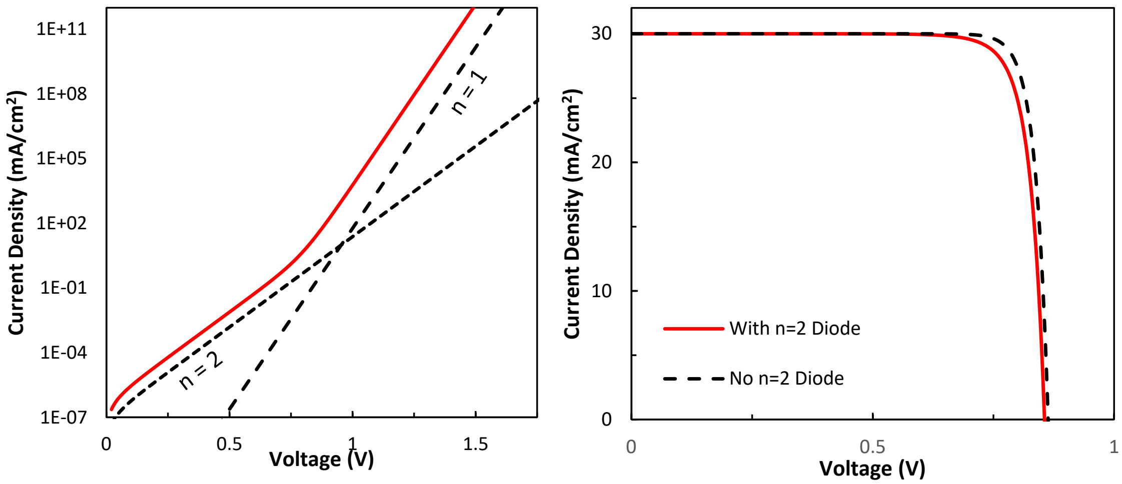

Figure 5.7 Simulation of the impact of the n=2 diode on the a) dark I-V curve and b) LIV curves.

discussed further in the next section has an ideality factor of ~2. This leads to a slower diode turn on and therefore a lower FF in the LIV curve. This diode is typically dominant at lower voltages or in highly defective materials. Eventually the $n = 1$ diode, due to its higher slope, will take over as seen in Figure 5.7a. If this transition is not done until voltages beyond V_{OC}, the diode is said to be limited by the $n = 2$ diode. This causes a reduction in V_{OC} as well as FF due to the majority of the current flowing through the parasitic diode rather than the desired $n = 1$ diode (Figure 5.7b).

The series resistor results in a voltage loss at voltages above the maximum power point in the illuminated I-V curve, but it does not impact the open circuit voltage (Figure 5.8a). This series resistance the dark I-V (log I vs. V plot) causes the current to roll off (Figure 5.8b) asymptotically approaching the current dictated by the series resistance. The shunt resistor (R_{Shunt}) also causes FF losses, but manifests itself as a slope of the LIV curve in the low voltage region of the curve (Figure 5.9a). In the dark I-V (Figure 5.9b), this also shows up in the low voltage region as a linear behavior before becoming

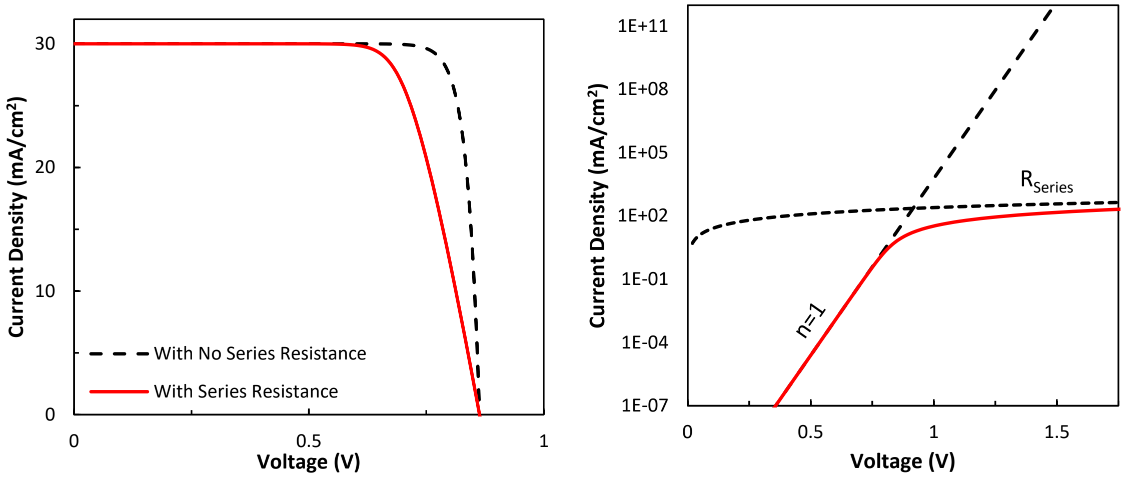

Figure 5.8 Simulation of the impact of series resistance on the a) LIV and b) dark I-V.

exponential. The ideal value for the R_{shunt} is ∞ ohm/cm^2, meaning that that resistive leakage path is an open circuit and no current flows through this pathway.

Obviously, as this model is effectively just a circuit, we can write an expression for the output current as a function input voltage using Kirchhoff's current law.

$$J = J_{photo} - J_{01} exp[\frac{q(V+JR_{series})}{kT}] - J_{02} exp[\frac{q(V+JR_{series})}{2kT}] - \frac{V+JR_{series}}{R_{shunt}} \quad \text{Eq. 5.11}$$

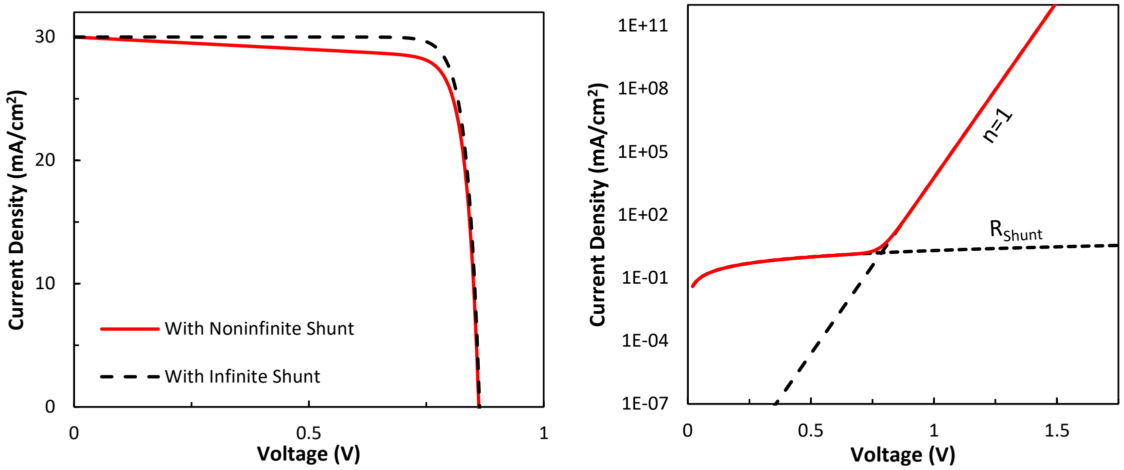

Figure 5.9 Simulation of the impact of shunt resistance on the a) LIV and b) dark I-V.

This is not analytically solvable due to the non-linear nature of the diode I-V curve, but the expression is numerically solvable via Newton's method or another numerical solving algorithm.

5.3.3. FROM CIRCUIT ELEMENT TO DEVICE PHYSICS

All the elements in the circuit model correspond to physically meaningful current flow processes within the cell. The first parallel diode is the traditional diffusion diode. The standard operation of this diode under forward bias is the result of injection of carriers from one side of the junction to the other and the diffusion of these now minority carriers away from the junction. This is dictated by ideal diode equation where J_{01} is the reverse saturation diode current and the ideality factor, *n*, is normally very close to 1.

$$J = J_{01}(\exp\left(\frac{qV}{nkT}\right) - 1) \qquad \text{Eq. 5.12}$$

J_{01} is dictated by the diffusion behavior of the minority carriers in the quasi-neutral region and is therefore the sum of the diffusion current from electrons in the p-type region ($J_{01,n}$) and holes in the n-type region ($J_{01,p}$). Usually, the more highly doped side of the junction (emitter) contributes very little current and thus this expression is often simplified to the form in Equation 5.13. This indicates that the diode dark current from this diode is dominated by the transport properties, dimensions, and doping levels in the base layer.

$$J_{01} = q * \frac{n_i^2}{N_A} * \frac{D}{L_D} * \frac{\frac{D}{L_D} sinh\left(\frac{W}{L_P}\right) + S_{eff} \cosh\left(\frac{W}{L_D}\right)}{\frac{D}{L_p} * \cosh\left(\frac{W}{L_D}\right) + S_{eff} * sinh\left(\frac{W}{L_D}\right)} \qquad \text{Eq. 5.13}$$

There are a few key tradeoffs that are important in terms of base layer design. First is that the dark current is approximately inversely proportional to the diffusion length and doping. This means the higher the diffusion length and the doping the lower the dark current. There is also a weak direct dependence on the width of the quasi-neutral region. These trends indicate that ideally a highly doped, long diffusion length, and thinner base layer is desired. We also notice that the second half of Equation 5.13 is very similar to the formula for collection probability. That is because they are both effectively generated from the derivative of the excess minority carrier concentration leading to the functional form seen here. Therefore, there is also a surface limited vs. bulk limited argument to be made just as in the collection probability calculation.

The n = 2 diode also known as the recombination-generation diode or the junction recombination diode, is a model for the recombination present in the depletion region when injecting carriers from one side to the other. The current is a result of recombination at defect states through the SRH process. Thus, the current assuming a worst case midgap defect state can be written as the recombination rate integrated over the width of the depletion region (W_{Dep}).

$$J_{02} = \int qU = q * \int \sigma v_{th} N_T n_i = \frac{q n_i W_{Dep}}{2\tau} \quad \text{Eq. 5.14}$$

The junction recombination current is therefore directly proportional to the width of the depletion region and intrinsic carrier concentration (n_i) and inversely proportional to the lifetime in the depletion region τ. Also, because the recombination is limited equally by the approach of the two carrier types in the case of a midgap state, the ideality factor, n, is roughly 2 when plugged into the ideal diode equation.

The series resistor is used to model majority carrier transport in the solar cell. This can be due to lateral current spreading and grid contacts as discussed in Section 5.4, as well as vertical conduction through layers in the device not intended for minority carrier collection. The shunt resistor is used to model ohmic leakage pathways in the solar cell. These could be caused by majority carrier conduction along extended defects such as dislocations or by sidewall surface conduction.

The current source is used to account for the short circuit photogenerated current due to illumination (J_{photo}). This effectively lumps all the physics and transport aspects of short circuit photocurrent, EQE, etc. (Section 5.2) into a single circuit element. Sometimes, this current source can be modified as a voltage dependent current source that depends on V_D to account for voltage dependent collection efficiency.

5.4. FRONT GRID LOSSES

A model which can properly calculate resistive and shadowing losses associated with the front grid is presented in the text by Green et al. [49]. This model is based off the concept that any grid design can be reduced to a unit cell with dimensions *A* and *B* as shown in Figure 5.10. The *A* dimension is the length of the busbar and the *B* dimension is the length of the grid fingers. The busbar is typically tapered with an average width of W_B. This is done to eliminate current crowding near the contact point. The width of the fingers, W_F, is defined by lithographical limitations, but in general thinner fingers are better as long as contact resistance is small. The distance between grid fingers, S, is a key parameter that is optimized based on the sheet resistance of the semiconductor.

The relative shadowing loss (P_{loss}/P_{tot}), P_{shadow}, is given by Equation 5.15, and is effectively a ratio of grid metal coverage to unit cell area.

$$P_{\text{shadow}} = \frac{W_B}{B} + \frac{W_F}{S} \qquad \text{Eq. 5.15}$$

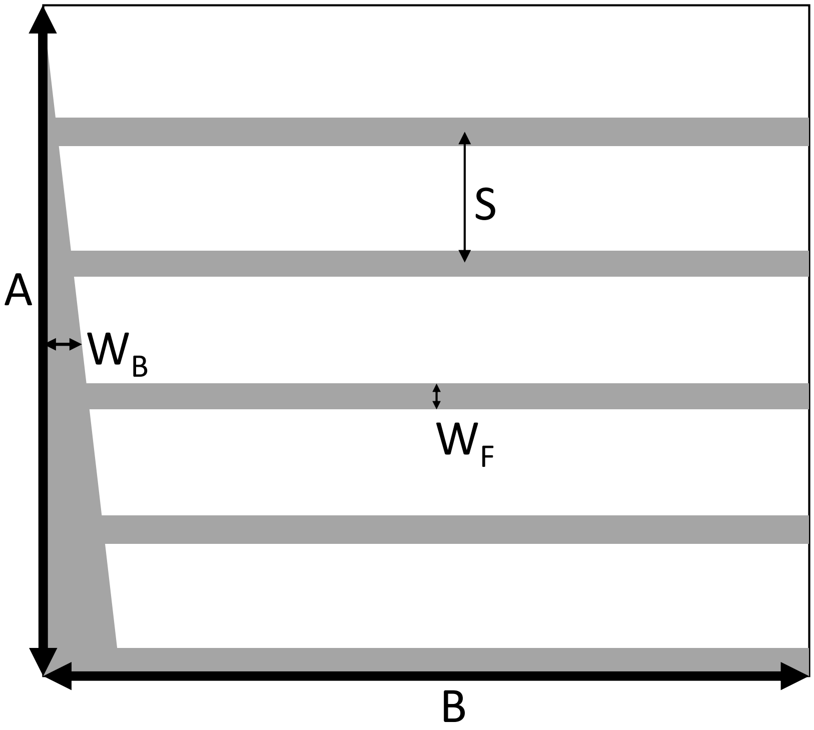

Figure 5.10 Schematic description of the unit cell grid design.

The relative resistive losses (P_{loss}/P_{tot}) can be split into 3 main components. The first losses are the lateral conduction losses in the semiconductor from photogenerated current between the grid fingers as dictated by Equation 5.16 where ρ_s is the sheet resistance of the top layer in the semiconductor stack.

$$P_{\mathrm{lat}} = \frac{\rho_s}{12}\frac{J_{\mathrm{mp}}}{V_{\mathrm{mp}}}S^2 \qquad \text{Eq. 5.16}$$

Second, is the contact resistance losses between the semiconductor and the metal. This calculation given in Equation 5.17 assumes that all the current is collected through the contact between the grid fingers and semiconductor with specific contact resistivity ρ_C.

$$P_{cont} = \rho_C\left(\frac{J_{\mathrm{mp}}}{V_{\mathrm{mp}}}\right)\frac{S}{W_F} \qquad \text{Eq. 5.17}$$

Lastly, Equation 5.18 is the relative conductive losses from current flowing through the grid fingers and busbar where ρ_{ms} is the sheet resistance of the metal.

$$P_{\text{grid}} = \frac{1}{3} B^2 \rho_{\text{ms}} \left(\frac{J_{\text{mp}}}{V_{\text{mp}}}\right) \frac{S}{W_F} + \frac{1}{4} A^2 B^2 \rho_{\text{ms}} \left(\frac{J_{\text{mp}}}{V_{\text{mp}}}\right) \frac{1}{W_B} \qquad \text{Eq. 5.18}$$

Overall, the series resistance of the grid can be extracted via Equation 5.19.

$$R_{series,Grid} = (P_{grid} + \mathrm{P}_{\text{cont}} + \mathrm{P}_{\text{lat}}) * \frac{V_{mp}}{J_{mp}} \qquad \text{Eq. 5.19}$$

These resistive losses can be balanced against the shadowing losses by equating the derivatives of these losses as a function of S and solving for where these are equivalent. The MATLAB code in the appendix can calculate the power losses from the shadowing and series resistance and can optimize the grid design for any given cell max power point and sheet resistance.

5.5. VOLTAGE DEPENDENT COLLECTION EFFICIENCY

To identify the underlying mechanism for a non-negligible VDC based on the measurement presented in Chapter 4, a simple analytical model can be used to fit the experimental results. VDC is commonly due to the modulation of the depletion region width in cases where the base diffusion length is shorter than the base width. Basically, as the top cell is biased the depletion region shrinks, thereby elongating the quasi-neutral base and reducing the likelihood of collecting deeply generated (i.e. long wavelength) minority carriers.

A simplistic collection probability (*CP*) model employing a semi-infinite base approximation (due to the expected low base diffusion length) can be used to account for the modulation of the depletion width.

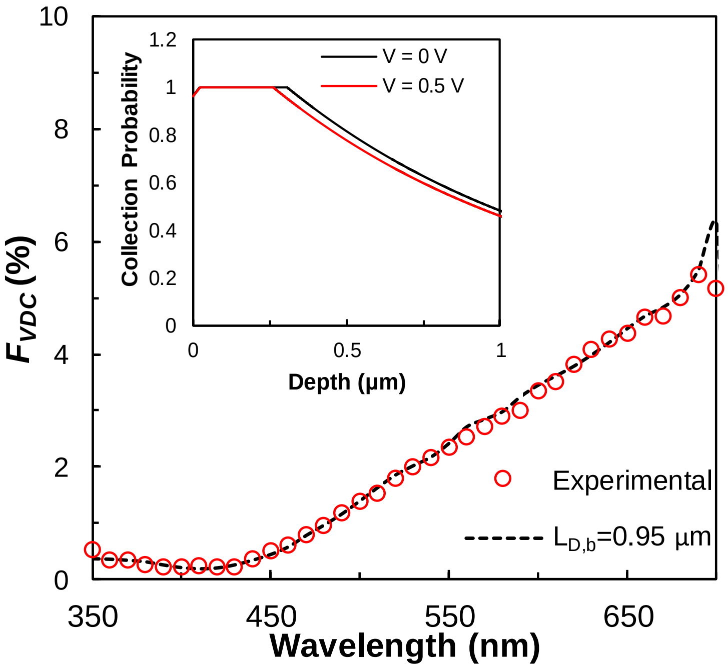

Figure 5.11 Wavelength-dependent VDC losses with modeled fit as a function of base diffusion length. The inset illustrates the reduction in collection probability attendant with the reduction in depletion region width at small forward bias.

$$f_c(x,V) = \begin{cases} \exp[-L_{D,e}(x_{dep,e} - x)] | & 0 < x < x_{dep,e} \\ 1 \quad | & x_{dep,e} < x < x_{dep,b} \\ \exp[-L_{D,b}(x_{dep,b} - x)] | & x_{dep,b} < x < W \end{cases} \qquad \text{Eq. 5.20}$$

Here $L_{D,e}$ and $L_{D,b}$ are the diffusion length of the emitter and base, respectively, $x_{dep,e}$ and $x_{dep,b}$ are the location of the edges of the depletion region on the emitter and base side, respectively, and W is the total width of the cell. The normalized wavelength-dependent photocurrent, $J(\lambda,V)$, can then be obtained from the collection probability, $CP(x,V)$, and the depth- and wavelength-dependent photogeneration rate, $G(x,\lambda)$

$$J(\lambda, V) = \int_0^W CP(x,V) \cdot G(x,\lambda)\, dx. \qquad \text{Eq. 5.21}$$

Simulating wavelength resolved current $J(\lambda,V)$ for the $GaAs_{0.75}P_{0.25}$ cell at both 0 V and a small forward bias, V_1 (0.5 V here), $F_{VDC}(\lambda)$ can then be determined by Equation 5.22.

$$F_{VDC}(\lambda) \approx \frac{\frac{J(V_1,\lambda) - J(0\,V,\lambda)}{V_1}}{J(0\,V,\lambda)} \qquad \text{Eq. 5.22}$$

This approach allows for calculation of the theoretical F_{VDC} parameter as a function of the relevant transport properties (i.e. diffusion lengths). An example of this fitting is shown in Figure 5.11. This model is used in this dissertation to understand VDC in tandem cells and to understand why or how TDD impacts VDC.

5.6. IMPACT OF THREADING DISLOCATION DENSITY ON DEVICE PERFORMANCE

The formalization of how dislocations are treated in solar cells was first presented by Yamaguchi et al. In this work, he treated threading dislocations as infinite SRH recombination sites, thereby reducing carrier lifetime and diffusion length. The dislocation limited diffusion length $L_{D,TDD}$ can be expressed as a geometrical argument assuming dislocations act as perfect carrier sinks. This model had been verified experimentally by both Yamaguchi et al. and Andre et al. [7]–[9].

$$L_{D_{TDD}} = \frac{2}{\sqrt{\pi^3 * \rho_{TD}}} \qquad \text{Eq. 5.23}$$

The total diffusion length in a material can therefore be expressed as an inverse summation of the constituent diffusion lengths as given by Equation 5.24 where $L_{D,Bulk}$ is the native diffusion length without dislocations.

$$\left(\frac{1}{L_{D,Tot}}\right)^2 = \left(\frac{1}{L_{D,Bulk}}\right)^2 + \left(\frac{1}{L_{D,TDD}}\right)^2 \qquad \text{Eq. 5.24}$$

It can be rationalized that the component of diffusion length (i.e. bulk or TDD limited) that is shorter will limit $L_{D,Tot}$.

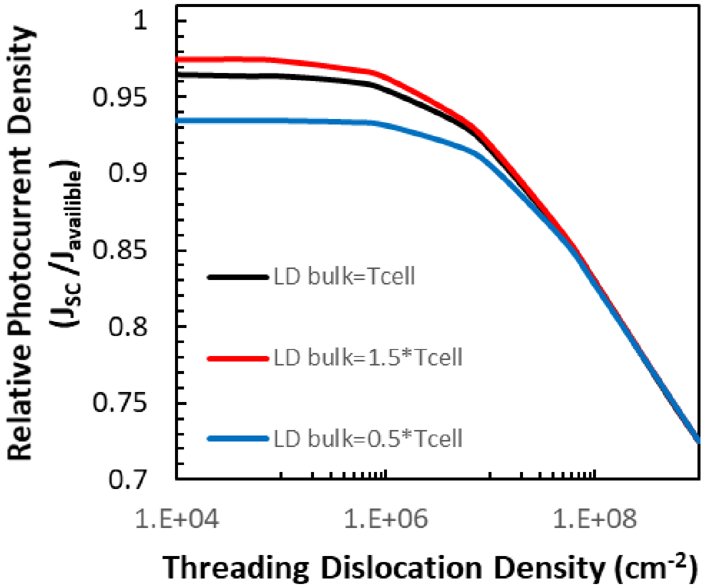

Figure 5.12 Relative photocurrent as a function of TDD for different bulk diffusion lengths.

This reduction in diffusion length, and therefore lifetime, results in reductions to both the V_{OC} and J_{SC}. Based on light and dark superposition, the photogenerated current can be treated separately from the diode *I-V* characteristics, as the impact of dislocations on each component are treated slightly differently. Beginning with the short circuit conditions, we can use these modified diffusion lengths in the quantum efficiency model presented in Section 5.2. Based on the Yamaguchi model understanding of the spatially resolved recombination associated with dislocations, the impact of elevated TDD on short circuit collection is limited to the quasi-neutral base layer. Intuitively this is because the native diffusion length in the emitter is already much shorter than the average spacing between threading dislocation segments. Therefore, these carriers will not have a high probability of interacting with the spatially localized recombination centers.

Figure 5.12 plots the normalized short circuit density (J_{SC} divided by the available photocurrent for that bandgap) of a simulated GaAs solar cell structure as a function of TDD for a few different bulk/native diffusion lengths. This simulation is done at a fixed base width and therefore does not give the ideal/optimized performance at every TDD. It does, however, provide an idea of how the native diffusion length affects the location of the roll off in J_{SC} and the peak in the undislocated case. The impact of TDD is rather small at a TDD of less than 10^6 cm^{-2}

Quantifying the impact of TDD on V_{OC} and *I-V* characteristics has been very thoroughly analyzed by Andre et al[7], [8]. Due to the defective nature of the semiconductors and the relatively wide bandgap of the $GaAs_{0.75}P_{0.25}$ material of interest, it is likely that the *I-V* curves will be dominated by junction recombination current, J_{02}, up to voltages exceeding V_{OC}. Recalling the formula for junction recombination current in Equation 5.25, it is observed that J_{02} is inversely proportional to the lifetime.

$$J_{02} = \frac{q n_i W_{Dep}}{2\tau_{tot}} \qquad \text{Eq. 5.25}$$

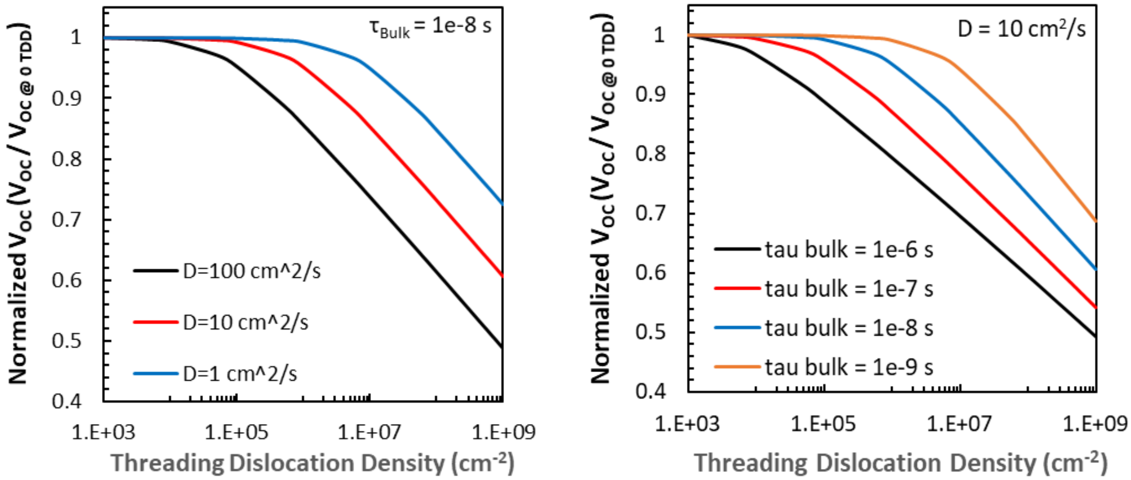

Figure 5.13 a) Normalized V_{OC} as a function of dislocation density for several diffusivities. b) Normalized V_{OC} as a function of TDD for various bulk/native lifetimes.

Using a similar treatment to that used in the diffusion length calculations above. The equation for the dislocation limited lifetime also is derived from the geometric argument used to determine the diffusion length [9]. Therefore, the equation for τ_{TDD} can be written as:

$$\tau_{TDD} = \frac{2}{\pi^3 * D * \rho_{TD}}, \qquad \text{Eq. 5.26}$$

where D is the minority carrier diffusivity. The total lifetime can be modeled as a reciprocal sum of dislocated and bulk/native lifetimes.

$$\frac{1}{\tau_{tot}} = \frac{1}{\tau_{TDD}} + \frac{1}{\tau_{Bulk}} \qquad \text{Eq. 5.27}$$

Plotted in Figure 5.13a is a calculation which assumes a 150 nm depletion width, and a 1×10^6 cm^{-3} intrinsic carrier concentration and plots normalized V_{OC} vs. TDD for a few different diffusivities of minority carriers. This directly shows the inverse relationship between diffusivity and V_{OC} that is unique to highly dislocated materials. Diffusivity changes the point by which the recombination associated with dislocations becomes dominant. This was the focus of the two critical works by Andre et al. that were both formative in my understanding of the impact of dislocations in devices [7], [8]. Figure 5.13b plots the normalized V_{OC} for different bulk/native lifetimes. Obviously, with reducing bulk lifetime the highest achievable V_{OC} goes down, but if the V_{OC} is normalized to the undislocated V_{OC}, we observe that the bulk lifetime also modifies the point by which the TDD begins to impact device performance. These parameters are therefore critical in determining the impact of TDD on device performance and can be manipulated with the intent of created TDD resilient designs as discussed in Chapter 7.

Calculation of the exact trend of FF as a function of TDD is a much more difficult calculation, but a few key aspects of this parameter should be considered. First is VDC. As discussed in the prior section, as base diffusion length becomes much shorter than the metallurgical width of the base (due to high TDD) the effect of small changes to the depletion region width due to bias begins to strongly impact photocurrent. Therefore, our traditionally assumed voltage independent photocurrent (i.e. superposition) breaks down and calculation of said LIV curves becomes increasingly difficult. However, the above model is a reasonable place to start to predict the impact of TDD on FF. Secondly, the J_{02} recombination current traditionally results in a loss of fill factor and this will get stronger as J_{02} becomes more dominant. Both, effects will result in reduced FF and their exact magnitude must be determined experimentally for any degree of certainty.

CHAPTER 6:

DEVELOPMENT OF FRONT-EMITTER GAAS$_{0.75}$P$_{0.25}$ TOP CELLS

The initial demonstration of GaAs$_{0.75}$P$_{0.25}$ /Si tandem cells by our group in 2013 was far from optimal and had not undergone significant cell design or growth optimization. Thus, opportunities for immediate efficiency improvements were available in this area. A number of strategies were explored that spanned generations of both material quality and device design. Initially cell development on GaAs-based virtual substrates (VS) allowed for rapid and forward-looking optimization (Section 6.1). The transition of this improved design to a high-TDD Si-based platform allowed for both a retention of the improvements made to the short wavelength response, but also an improved quantitative understanding of the role of dislocations in cell performance (Section 6.2). Once, the Si-based VS was improved through the details presented in Chapter 8, development on the new low-TDD VS presented unique challenges in both short and length wavelength response as well as FF. Intelligent design, and modeling were used to mitigate these issues ultimately resulting in cells that outperformed cells initially grown on the GaAs-based VS (section 6.3).

6.1. FORWARD-LOOKING TOP CELL DEVELOPMENT

As discussed in the prior chapters, elevated quantities of threading dislocations, which stem from the difficulties with metamorphic and heteroepitaxial growth of III-V materials on a Si substrate, cause a reduction in the diffusion length and minority carrier lifetime[7]–[9]. This degradation in transport properties creates a difficult problem in terms of cell design where, as defect density is continually reduced, the optimal design will change significantly. This is especially problematic when defect densities are rapidly reducing as they have over my tenure at OSU and as discussed in more detail in Chapter 8. Thus, a method for deconvoluting the impact of excess TDD on cell performance is necessary to both inform technology potential and device modeling, as well as to allow efforts on other subcomponents to continue in parallel. In this spirit, the use of a VS with TDD similar to technology targets is an ideal platform to begin cell development efforts.

In order to achieve a lower TDD VS, tensile-graded *p*-type $GaAs_yP_{1-y}/GaAs$ VS (GaAs-Based VS) with TDD ~ $1\text{-}2\times10^6$ cm^{-2}, as measured by electron channeling contrast imaging [103], [104] were used. The native oxide was thermally desorbed under AsH_3 flow at 650°C directly prior to growth. The buffers were grown with an average grading rate of 0.2% misfit/µm (4.5 at.% As per µm) using steps of 0.04% misfit/step (1.0 at.% As). The layers in the step graded buffer were ~200 nm thick with an ~500 nm terminal layer, for a total of 26 layers. This strategy of achieving the target lattice constant (shown in Figure 6.1) allows for improved defect control when compared to $GaAs_yP_{1-y}/GaP/Si$ (Si-based VS), therefore resulting in lower TDD. Due to the fully relaxed nature of the VS, no additional dislocation motion is expected within the cell

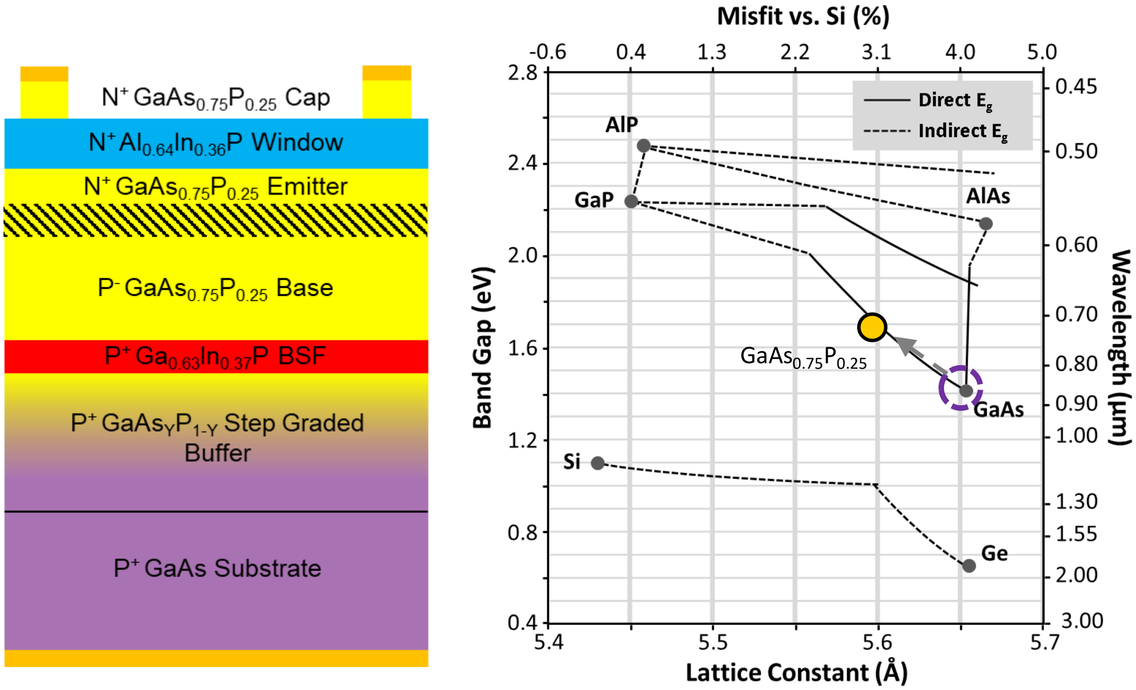

Figure 6.1 Structure and E_g-lattice constant diagram showing the alternate pathway to the $GaAs_{0.75}P_{0.25}$ lattice constant.

layers. Thus, top cells grown on either a GaAs-based VS, used here, or the more traditional Si-based VS should only contain threading dislocation segments and not misfit dislocation segments. It is therefore assumed that the dislocations in both cases should act similarly, even though one is grown on a compressive SGB and the other is growth on a tensile SGB, because the threading segments are largely not strain relieving. Additionally, the $GaAs_yP_{1-y}$/GaAs VS provides a similar optical environment to that present in the $GaAs_{0.75}P_{0.25}$/Si tandem, where all in-band transmitted photons ($\lambda <$ ~720 nm) are absorbed by subsequent semiconductor layers and no substantial rear reflection is present.

Isotype test devices were fabricated using standard lithographic and fabrication techniques described in Chapter 3. The cell design iterations are detailed in Table 6.1.

Table 6.1 Device design parameters for the three $GaAs_{0.75}P_{0.25}$ cell iterations. Key changes from the prior generation are indicated in italics, while nominal values (where they differed from actual) are indicated in parentheses.

Layer	**TC-1**	**TC-2**	**TC-3**
Window (n-$Al_{0.66}In_{0.36}P$)	14(20) nm 1(5)$\times 10^{18}$ cm^{-3}	14(20) nm 1(5)$\times 10^{18}$ cm^{-3}	*20 nm* *5×10^{18} cm^{-3}*
Emitter (n- $GaAs_{0.75}P_{0.25}$)	50 nm 2×10^{18} cm^{-3}	*30 nm* *1×10^{18} cm^{-3}*	30 nm 1×10^{18} cm^{-3}
Base (p- $GaAs_{0.75}P_{0.25}$)	1.50 μm 2×10^{17} cm^{-3}	*1.75 μm* *1×10^{17} cm^{-3}*	*1.50 μm* 1×10^{17} cm^{-3}
BSF (p-$Ga_{0.65}In_{0.34}P$)	50 nm 3×10^{18} cm^{-3}	50 nm 3×10^{18} cm^{-3}	50 nm 3×10^{18} cm^{-3}

Intended targets which differed from achieved values are placed in parenthesis and values which differed from the prior generation are denoted in italics.

The results of these top cell optimization efforts are detailed in Figure 6.2 and Figure 6.3 and Table 6.2. TCAD modeling of the original device structure, TC-1, suggested that the emitter was too thick and too highly doped, leading to excessive recombination within this layer and a commensurate reduction in both J_{SC} and V_{OC} [11]. Additionally, at least based on the available optical properties at the time, the models indicated that a slight increase in base thickness and commensurate reduction in doping could provide a small increase in J_{SC}. Indeed, as a result of this change, the TC-2 design yielded a significant increase in short wavelength response over TC-1, observed in both EQE below 525 nm and the notable improvement in all relevant performance metrics, especially J_{SC} and FF.

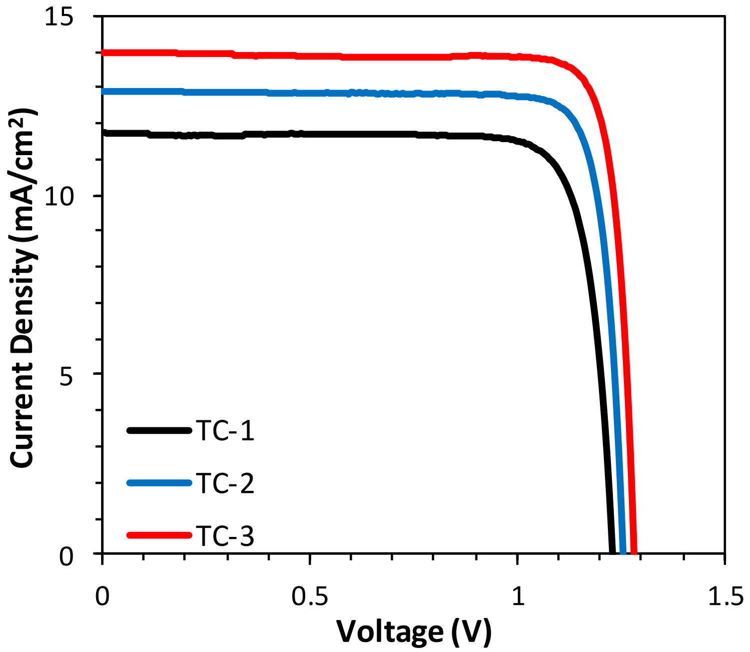

Figure 6.2 Illuminated I-V curves of the $GaAs_{0.75}P_{0.25}$ isotype cells demonstrating a clear current and voltage improvement over the initial device.

Table 6.2 Isotype top cell performance metrics extracted from AM1.5G illuminated current-voltage measurements in Figure 6.2.

Metric	TC-1	TC-2	TC-3
VOC [V]	1.232	1.250	1.284
WOC [V]	0.49	0.47	0.44
JSC [mA/cm2]	11.7	12.9	14.0
FF [%]	82.2	85.2	86.0
ηAM1.5G [%]	11.8	13.7	15.5

The second iteration of this design effort (TC-2 to TC-3) primarily served to correct for a miscalibration of the window layer. Due to an incorrect calculation of growth rate and dopant flows, the window layers in the TC-1 and TC-2 samples were thinner than intended (~14 nm) and heavily compensated due to excess Si dopant species, yielding an actual carrier concentration of $N_D \approx 1\times10^{18}$ cm^{-3}, 5× lower than the nominal target. The excessively thin window layer and under-doping combined to result in

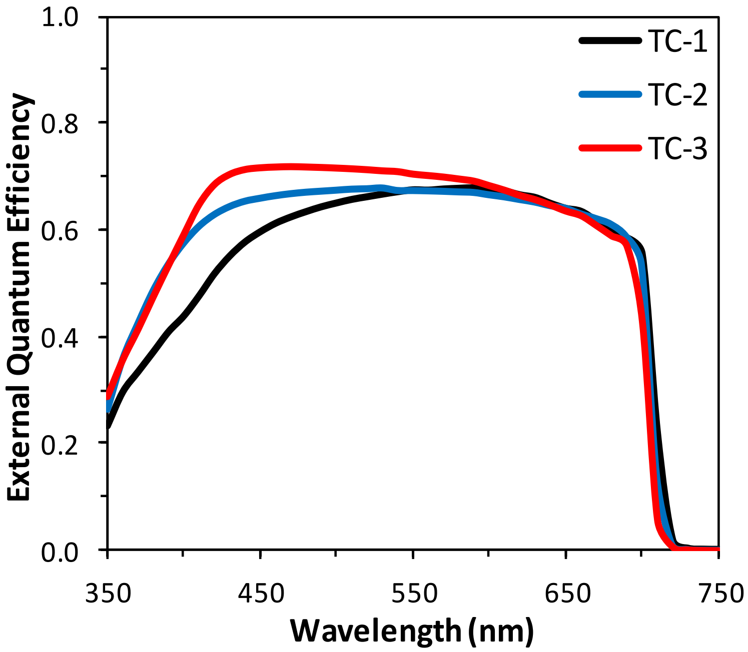

Figure 6.3 EQE results from ~1.72 eV $GaAs_{0.75}P_{0.25}$ top cell isotype cell showing the improvements to the short wavelength response commensurate with the changes to the emitter and window layers.

insufficient surface passivation, allowing depletion from the native $Al_{0.66}In_{0.36}P$ surface to extend into the emitter, increasing the effective interface recombination velocity at the window/emitter interface. Increased window thickness and doping reduces the impact of the surface depletion, thereby improving the collection probability in the emitter and improving the short wavelength response, as clearly seen in the TC-3 EQE. This particular discovery of a poorly passivating window will be further discussed in Chapter 7 as it pertains to defect resilient rear-emitter cells [15]. Ultimately these improvements to the cell design also resulted in meaningful improvements to all three key performance metrics, especially V_{OC} and J_{SC}. Overall, an increase in AM1.5G efficiency (sans ARC) of nearly 4% absolute (versus TC-1) was achieved. All in all, this top cell is sufficient to enable nearly 30% conversion efficiency for a $GaAs_{0.75}P_{0.25}$/Si tandem solar cell.

6.2. *TOP CELLS AT ELEVATED TDD*

Beyond optimizations to the cell structure, a quantitative understanding of the role of TDD on cell performance must be established to guide design optimization efforts as the material quality is continuously improved. As a point of direct comparison, the final top cell design (TC-3) was grown on a high-TDD (~2×10^7 cm^{-2}) Si-based VS produced on a *p*-type Si wafer. Rear contact to the $GaAs_{0.75}P_{0.25}$ cell was made to the SGB, which, in this case, is doubling as a lateral conduction layer. The results of these cells are presented in Figure 6.4 and Figure 6.5 and detailed in Table 6.3. While the IQE remains high in the short wavelength region of the cell, the long wavelength response suffers with

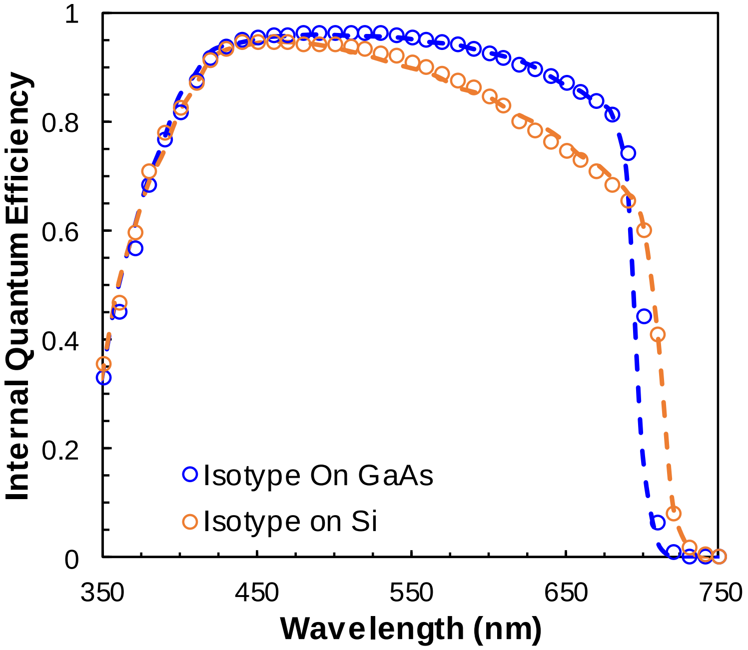

Figure 6.4 Experimental and Modeled IQE data for the TC-3 design grown on the low-TDD GaAs-based VS and the high-TDD Si-based VS.

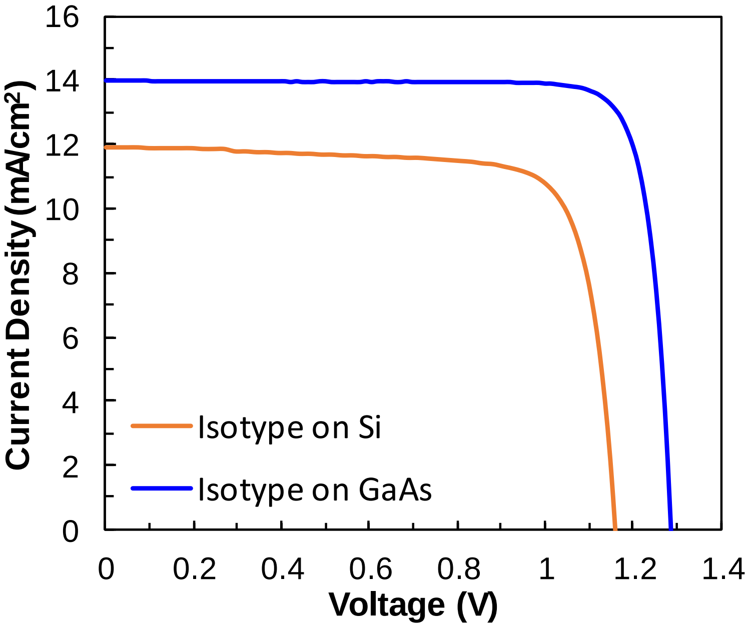

Figure 6.5 AM1.5G illuminated I-V curves for the TC-3 GaAs0.75P0.25 design grown on the low-TDD GaAs-based VS and the high-TDD Si-based VS.

Table 6.3 Performance metrics for TC-3 Cell designs grown on GaAs- and Si-based VS.

Performance Metric	**GaAs-Based VS**	**Si-Based VS**	**Difference**
V_{OC}	1.284 V	1.160 V	-124mV
J_{SC}	14.0 mA/cm^2	11.9 mA/cm^2	-2.1 mA/cm^2
Fill Factor	86.0 %	79.2 %	-6.8 %

a 10-15% absolute loss in IQE over the 550 nm to 700 nm wavelength range. A ~4.5% absolute efficiency loss is the $GaAs_{0.75}P_{0.25}$ cell for a ~10× increase in TDD highlights the immense impact TDD has on cell performance as well as the necessity for TDD specific cell design in order to extract maximum performance for a given material quality.

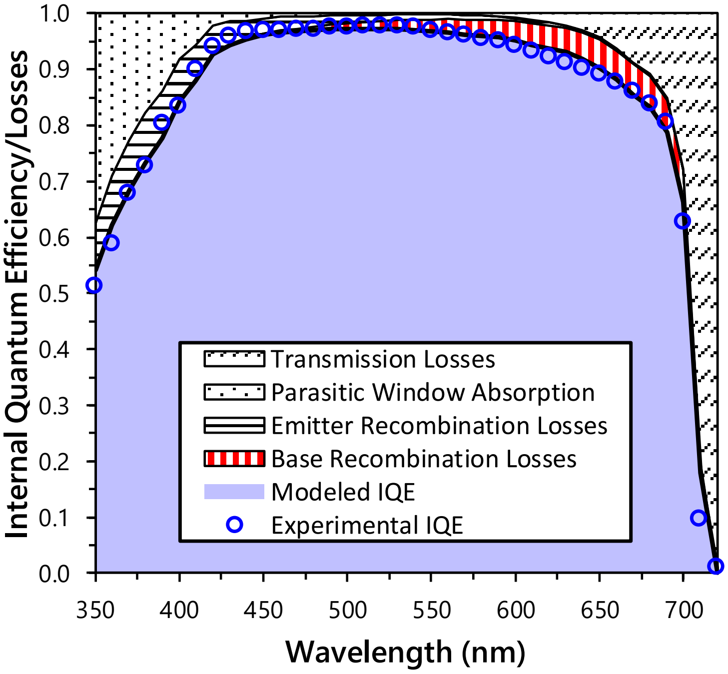

Figure 6.6 Loss analysis of the TC-3 cell grown on the GaAs-based, 2×10^{6} cm^{-2} TDD VS revealing the recombination loss present in the base layer.

To better understand the specific impact of TDD in these devices, their experimental IQE curves were fit using the analytical IQE model described in Chapter 5 with results overlaid in Figure 6.4. Beyond allowing for extraction of relevant transport properties (done in detail in Chapter 7.3), modeling allows for the determination of the sources and magnitudes of current losses within different regions of the cell structure, including transmission, parasitic absorption, and recombination, which can then be directly related to the overall cell J_{SC} and measured TDD. Plots detailing these losses are shown in Figure 6.6 and Figure 6.7 for the cells on the GaAs-based and Si-based VS respectively. The critical result of such an analysis is the quantification of the recombination losses in the base due to the elevated TDD. This is done by first modeling the IQE curve and then one by one making transport and optical properties ideal. The

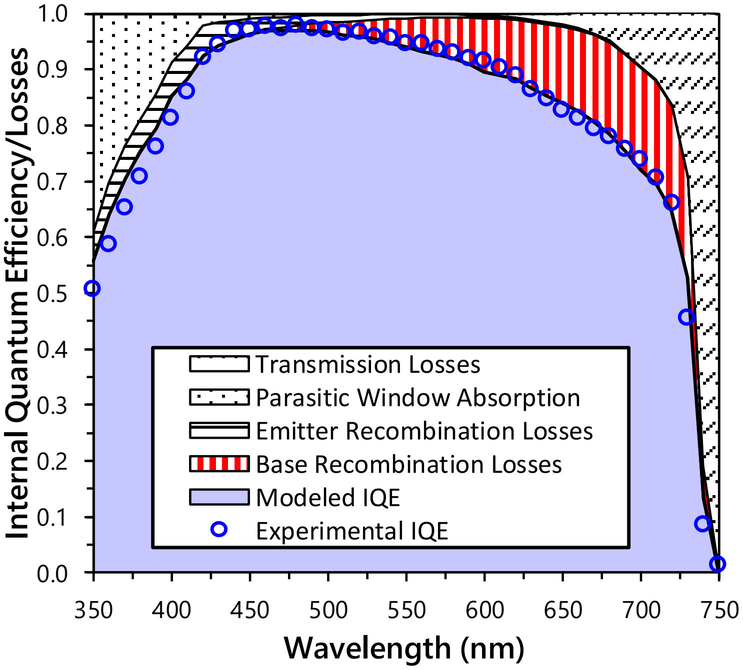

Figure 6.7 Loss analysis of the TC-3 cell grown on the Si-based, 2×10^{7} cm^{-2} TDD VS revealing the recombination loss present in the base layer.

deltas between the curves allow for the quantification of the losses. The additional 10× increase in TDD results in a 1.06 mA/cm^{2} increase in base recombination losses under AM1.5G. The emitter recombination losses are effectively identical between the two devices and can therefore be identified as independent of TDD. This is expected due to the low native diffusion length of the 1×10^{18} cm^{-3} doped $GaAs_{0.75}P_{0.25}$ in comparison to the predicted TDD limited diffusion length (~1 μm). The lifetime and/or diffusion length in the emitter layer is likely limited by radiative recombination, point defects or point defect complexes associated with high Si doping [143], [144].

Additionally, to elucidate the impact of TDD on V_{OC}, Figure 6.8 presents E_g - V_{OC} offset (W_{OC}) values extracted from the samples in this study, as well an intermediate TDD value from the literature (grown via MBE, but with a similar device structure), plotted

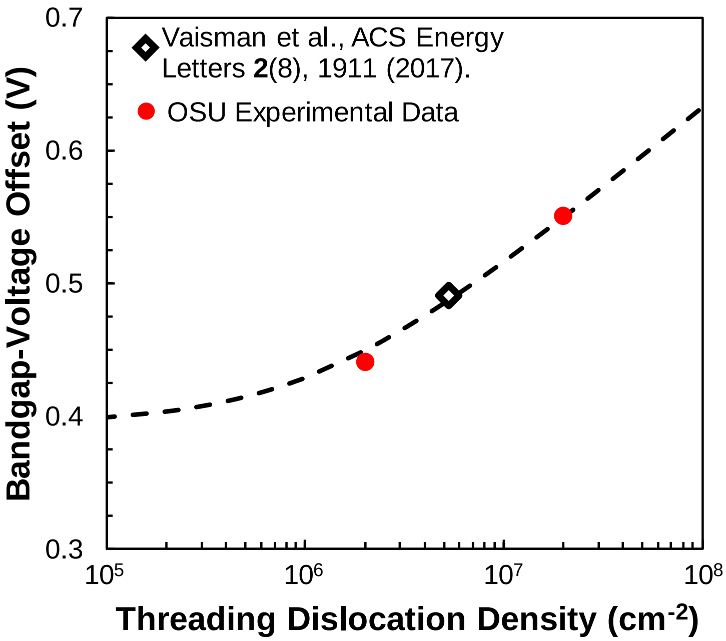

Figure 6.8 E_g-V_{OC} offset (W_{OC}) versus TDD trend extracted from available experimental data and intermediate result from literature.

against TDD. W_{OC} is often used as a metric for material quality with a value of 0.4 V being indicative of exceptional material quality [52]. The E_g used in this calculation were extracted from a linear fit of the near band edge region of the reported EQE curve. The dashed line represents a fit to these values using the model by Yamaguchi et al. (and expanded/verified by Andre et al.) [7]–[9], allowing for the extraction of V_{OC} as a function of TDD. It was assumed that the bulk/non-dislocated lifetime would result in a W_{OC} of ~0.4 V. Coupling both of the IQE loss and W_{OC} analyses establishes a strong quantitative understanding of the performance of the $GaAs_{0.75}P_{0.25}$ cell as a function of TDD and helps guide continuing development to take advantage of improving metamorphic III-V material quality going forward.

6.3. DEVELOPMENT OF GAAS$_{0.75}$P$_{0.25}$ CELLS ON REDUCED TDD GAAS$_{Y}$P$_{1-Y}$/SI VIRTUAL SUBSTRATES

6.3.1. CHALLENGES ENCOUNTERED WITH NEW SI-BASED VIRTUAL SUBSTRATES

While the interpolative models above provide a robust theoretical understanding of the role that dislocations play in cell performance and design, these models do not successfully capture additional nuance in growth differences between the GaAs-based VS used to achieve the forward-looking 1-2×10^{6} cm^{-2} TDD target and the desired Si-based VS which is critical for application in the eventual tandem device. Despite recent advances that enabled a ~5-10× reduction in TDD down to 3×10^{6} cm^{-2} discussed further

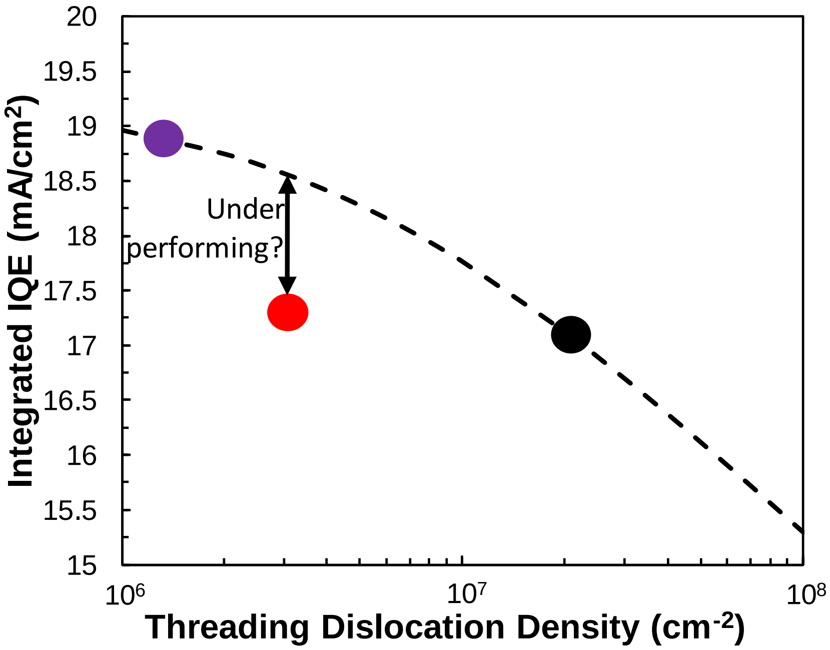

Figure 6.9 Modeled integrated IQE as a function of TDD from the results in section 6.2. Cells grown on Si-based VS with reduced TDD significantly underperformed their expected performance from the above modeling.

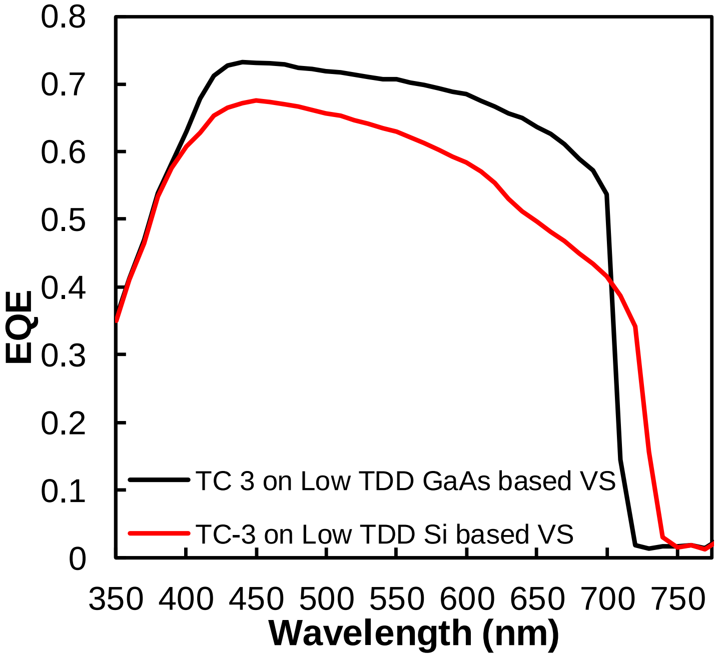

Figure 6.10 TC-3 Cell designs grown on two VS with similar TDD significant deviation from the expected results is shown in the cell grown on the recently developed Low-TDD VS on Si.

in Chapter 8 [145], the expected increase in performance commensurate with such a reduction in TDD was not initially present. This is shown in Figure 6.9 where it is clear that the short circuit of a cell grown on a 3×10^{6} cm^{-2} TDD VS is drastically underperforming the expected values from interpolative modeling. The methods for this interpolative modeling are discussed in more depth in Chapter 5 and 7 [142].

As eluded to, initial attempts at $GaAs_{0.75}P_{0.25}$ cell growth on these new low-TDD Si-based VS resulted in poor performance, even worse than the prior growths on the High-TDD Si-based VS shown in Figure 6.4 and Figure 6.5, even though TDD was measured by ECCI to be ~3-5×10^{6} cm^{-2} or ~4× lower. The EQE of this initial device with the same TC-3 cell structure is presented in Figure 6.10 in comparison to the TC-3 cell grown on the low-TDD GaAs-based VS with TDD of 1-2×10^{6} cm^{-2}. Both short and long wavelength significantly lag the aspirational values provided by the TC-3 structure grown on the GaAs-based VS. The slight difference in TDD between these two devices is nowhere near substantial enough to explain such drastic degradation, especially in the short wavelength region where the EQE was shown to be agnostic to TDD.

Thus, it was proposed that innate differences between the VS on GaAs and the recently developed low-TDD VS on Si must be the root cause of the poor device performance. One such difference in these VSs were the wafer offcut. Changing the offcut can result in changes to both dopant incorporation and surface growth kinetics which impact optimal growth conditions. The offcut for the Si substrates used for the new VS was 2° vs. previous growths on Si which utilized 4° offcut substrates. Thus, modifications to both growth conditions and device design were required to recover the expected performance as detailed over the next few pages

6.3.2. RECOVERING SHORT WAVELENGTH COLLECTION

Initial focus of this focused $GaAs_{0.75}P_{0.25}$ cell development effort was on recovering short wavelength response of the cells on the new low-TDD Si-based VS. The details of samples in this study are shown in Table 6.4. Separately-produced doping calibration samples showed that emitter dopant incorporation was ~3-4× higher as

Table 6.4 Detailed structures of the attempt to recover short wavelength performance after transition to the recently developed low-TDD Si-based VS.

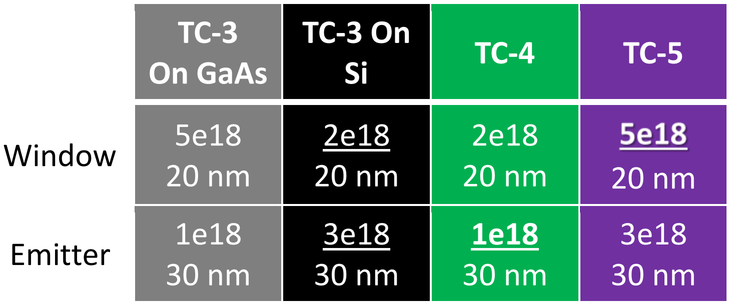

	TC-3 On GaAs	TC-3 On Si	TC-4	TC-5
Window	5e18 20 nm	2e18 20 nm	2e18 20 nm	**5e18** 20 nm
Emitter	1e18 30 nm	3e18 30 nm	**1e18** 30 nm	3e18 30 nm

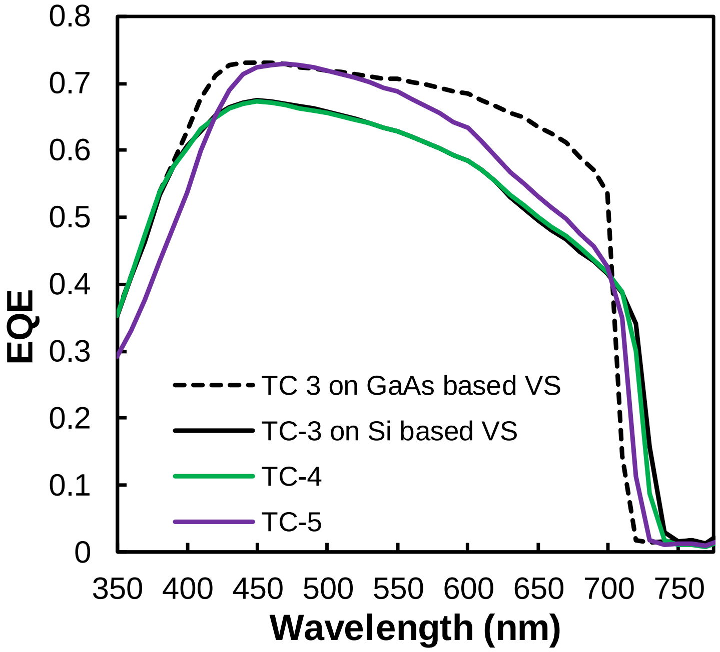

Figure 6.11 Top cell development efforts to improve short wavelength response in cells grown on the recently developed low-TDD VS on Si.

measured by Hall effect than as intended in these devices, and the window doping value as measured by Hall effect was low by ~2× likely due to amphoteric compensation stemming from overdoping. Thus, subsequent cells were grown in which the emitter and window dopant flows were reduced to target the correct doping values; however, there was no substantial improvement in short wavelength response between TC-3 on Si and TC-4, as seen in Figure 6.11. However, based on other work in this dissertation on the critical role of window doping and thickness on device performance (Chapter 7) [15], the window thickness was increased to 30 nm due to suspicions that 20 nm was not sufficient to contain surface depletion due to surface Fermi level pinning unless the window doping was > 5×10^{18} cm^{-3} [146], which is near the amphoteric limit in $Al_{0.66}In_{0.34}P$. This design change enabled substantial broadband EQE improvements indicating an improved collection efficiency in the emitter layer thus further validating the surface depletion theory elaborated on in Chapter 7.2. There is a slight reduction in EQE at wavelengths shorter than 450 nm due to increased absorption in the window layer as well as changes to the reflectivity, but the potential for fine tuning of the window thickness and doping is indeed possible.

Upon analysis of some of these devices by ECCI, shallow misfit dislocations were observed such as in the correlative ECCI and EBIC images in Figure 6.12. Based upon the sharpness of these misfits observed after removing the $GaAs_{0.75}P_{0.25}$ cap layer, it is most likely that these dislocations are present at the $GaAs_{0.75}P_{0.25}/Al_{0.65}In_{0.35}P$ interface [103]. EBIC shows dark lines which correlate with the misfit dislocations indicating that these misfit dislocations are acting as localized Shockley-Read-Hall recombination

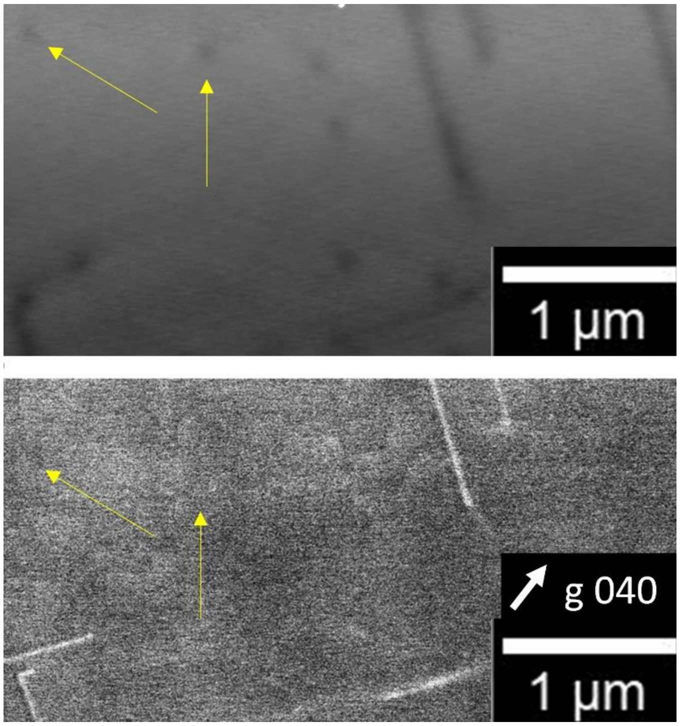

Figure 6.12 Correlative a) EBIC and b) ECCI images of the TC-3 design showing misfit dislocations acting as recombination centers. Yellow arrows indicate recombination centers which do not correlate with threading dislocations identified via ECCI.

centers [108]. The surface depletion induced electric field which extends into the emitter in the TC-3 and TC-4 devices drags holes against this defective interface. Thus, a pathway for further improvement for perfect lattice matching between the window and emitter materials is necessary. It is also important to note that even after adjusting emitter and window properties, the cells still greatly lag behind the expected values given from the interpolative modeling in Figure 6.9.

6.3.3. ANALYSIS OF VOLTAGE LOSSES

Beyond the short circuit response, the V_{OC} is also lagging behind the expected values from the interpolative exploration vs TDD in section 6.2 by > 50 mV. Cells on the Low-TDD Si-based VS peaked at only 1.19 V, when cells on a GaAs-based VS had V_{OC} as high as 1.28 V. W_{OC} values of various growths with similar cell designs used to attempt to debug this problem are shown in Figure 6.13 plotted with the dark spot density (DSD) as given by EBIC. Interestingly, a significant quantity of dark spots that do not correlate with threading dislocations as imaged by ECCI are observed, as indicated by the yellow arrows in Figure 6.12. A fit to the experimental data of W_{OC} vs DSD was performed according to the Yamaguchi model [9] in Figure 6.13 using intrinsic carrier concentration from Vurgaftman et al. [147], τ_{bulk} and diffusivity values that realistically constrain the curve to $W_{OC} > 0.38$ V, and the estimated diffusivity of electrons from an interpolation of majority carrier mobilities of the constituent binaries.

This result shows that while traditionally it is assumed that dark spots in EBIC are often due to threading dislocations, other spatially localized defects such as point defect clusters can act similarly to dislocations with regard to their impact on V_{OC}. Additionally,

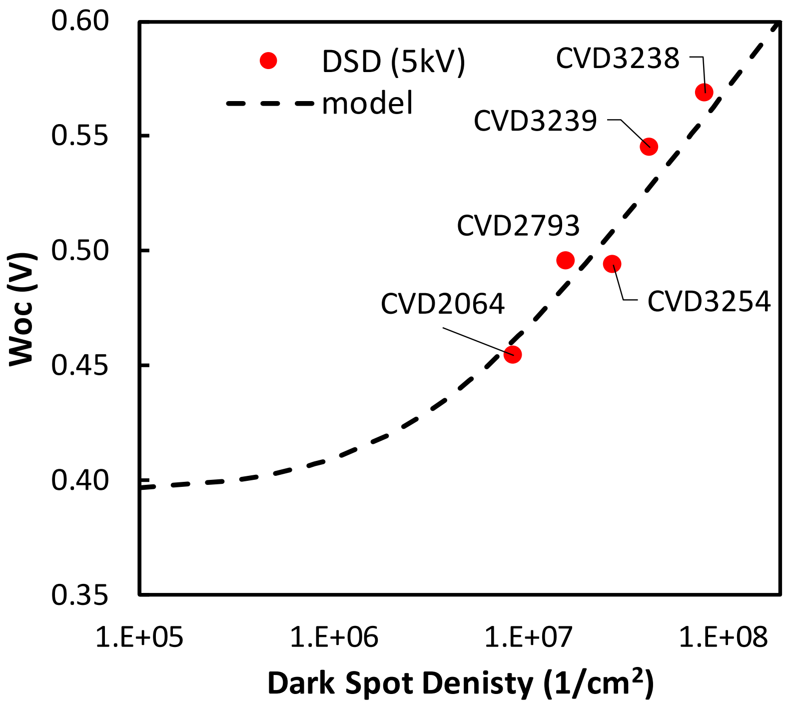

Figure 6.13 Bandgap-voltage offset (W_{OC}) plotted as a function of dark spot density. Fitting to experimental data was performed using the Yamaguchi model using realistic materials parameters constraining $W_{OC} > 0.38$V and D=55 cm^2/s.

the strong agreement of the fit to predicted theory indicates that it is indeed dark spots in EBIC which appear to be the important metric which dictates cell voltage rather than TDD as measured by ECCI. This is intuitive as EBIC directly measures recombination activity whereas ECCI specifically observes extended crystalline defects [109].

6.3.4. IMPROVING LONG WAVELENGTH RESPONSE AND FILL FACTOR

With this realization that transport metrics may be limited by excess quantities of point defect clusters or other defects, an investigation of growth conditions was

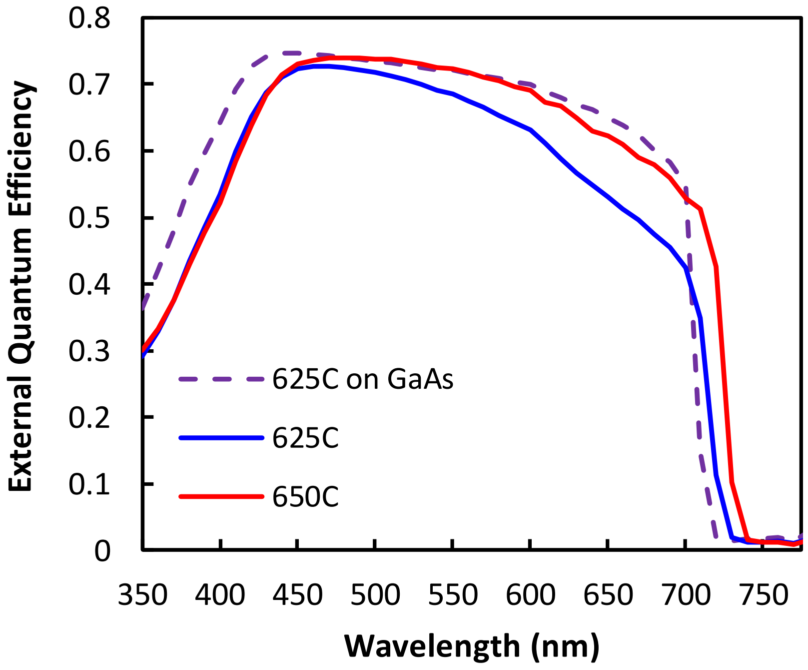

Figure 6.14. EQE highlighting the impact of growth temperature on long wavelength collection.

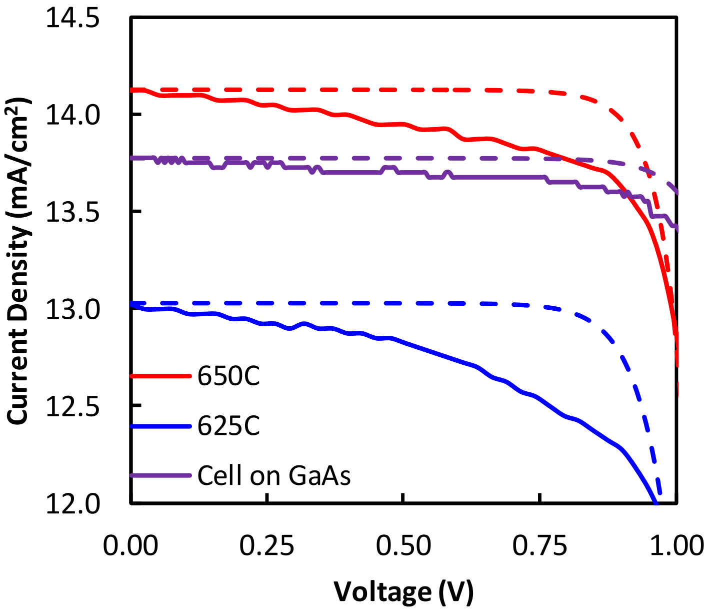

Figure 6.15 Zoomed in LIV curves of the samples in the growth temperature dependent study. Dashed lines are suns JSC-VOC measurements. The flatness of the Suns J_{SC}-V_{OC} curves in comparison to the LIV indicates voltage dependent collection efficiency.

performed with the hope of removing growth condition-related defects and commensurately improving the base diffusion length and long wavelength collection. Cell growth temperature was increased to 650^{o} C while correcting for changes in cracking efficiency of group V and dopant precursors to ensure that doping and composition of all layers were not altered significantly. This change in growth temperature drastically improved the EQE especially in the long wavelength dominated by base collection as seen in Figure 6.14. This indicates a reduction in point defect recombination centers ostensibly due to more ideal growth conditions as the TDD was not observed to be significantly altered.

In spite of these impressive results, nearly matching the J_{SC} of the TC-3 cell on GaAs, the zoomed in LIV shown in Figure 6.15 shows significant fill factor losses due to a shunt-like behavior of the I-V curve even at the increased growth temperature. Suns

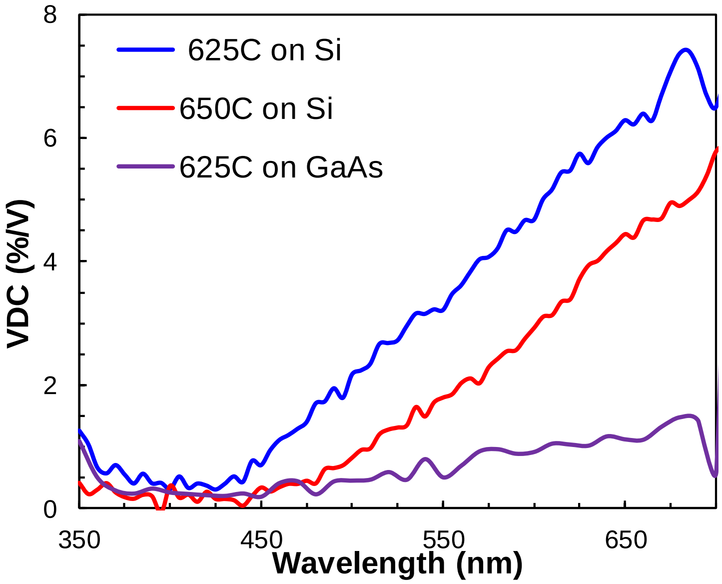

Figure 6.16 Voltage dependent collection measurements which identifies long wavelength photons as the primary source of the voltage dependent collection efficiency.

Jsc-Voc measurements indicate that this is not a typical ohmic shunt behavior such as in the standard double-diode model and rather voltage dependent collection efficiency (VDC). While the VDC is significantly reduced over the device grown at 625 °C, the 650 °C device still loses ~0.5mA/cm^2 in current density near max power point, resulting in a ~1-2% absolute reduction in FF.

To understand more about the origin of the VDC losses, the spectrally resolved VDC measurement discussed in more detail in Chapter 4 was performed. These results are given in Figure 6.16 and show clearly that long wavelength photons are more likely to be lost with the application of forward bias. This result points to loss of photogenerated carriers deep within the base layer being the primary source of the VDC. This is ostensibly due to low base diffusion length; however, recent results not included here may point to sidewall recombination as a potential additional culprit.

For this reason, the dopant grade structure detailed in Figure 6.17a was designed. The dopant grade creates a built-in electric field which acts on photogenerated electrons in the base dragging them towards the depletion region. This is shown in the approximate band diagram in Figure 6.17b. As mentioned in Chapter 5, this modifies the effective diffusion length for these carriers and enables higher collection probability throughout the base layer [56]. However, typically in cells with dopant grades, increased J_{01} dark current due to an effective shortening of the diffusion length seen by carriers emitted across the junction (i.e. carriers which are part of the dark current component) is observed [51]. These electrons emitted into the base by the emitter are traveling in the opposite direction as the photogenerated carriers being collected. Thus, there is a trade-off present

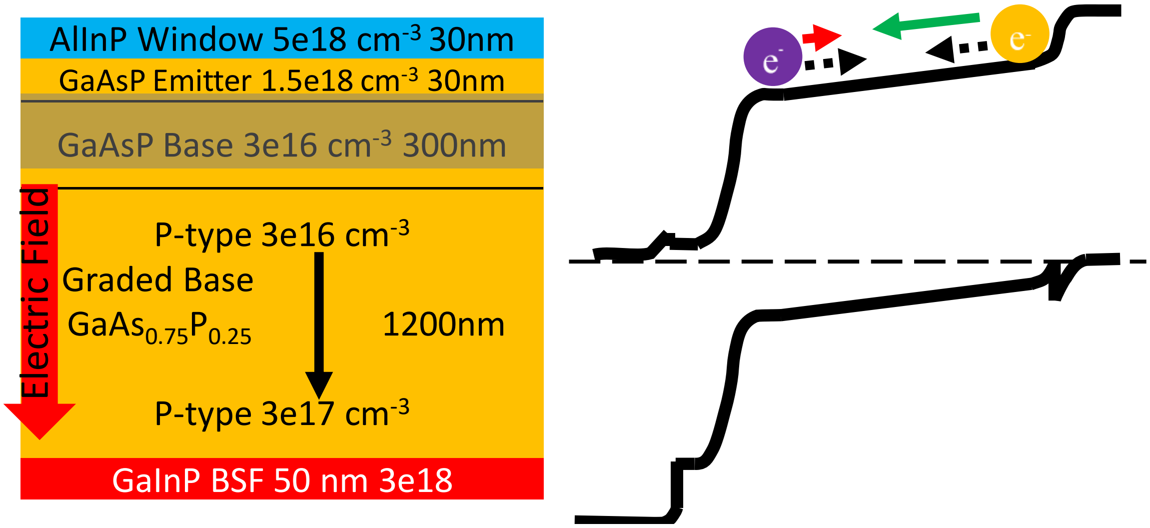

Figure 6.17 a) structure diagram for the graded doping base design. The electric field pulls electrons towards the depletion region aiding collection. b) Qualitative Band diagram showing the built-in field in the base layer. The electric field present positively affects the diffusion length of photogenerated carriers (Yellow), but negatively impacts the diffusion length of electrons which are emitted across the junction (purple) thereby increasing diode dark current in J_{01} limited solar cells.

with the application of a dopant grade that limits its usefulness in more traditional applications.

However, due to the unique J_{02}-limited nature of the GaAs$_{0.75}$P$_{0.25}$ top cell, the J_{01} diode dark current is effectively inconsequential in the I-V characteristics at voltages below V_{OC}. This is counter to the case of many III-V cells lattice matched to GaAs that are strongly J_{01} limited due to low defect populations. Recalling the formula for J_{02} where a direct relation between depletion width and dark current density is observed, it is imperative to maintain the same depletion width and material quality if the same dark currents are to be maintained after the application of a dopant grade. It is for this reason that a 300 nm region of material was left without a dopant grade as to not change the depletion region, thereby keeping J_{02} the same as in prior designs. This sort of achieves

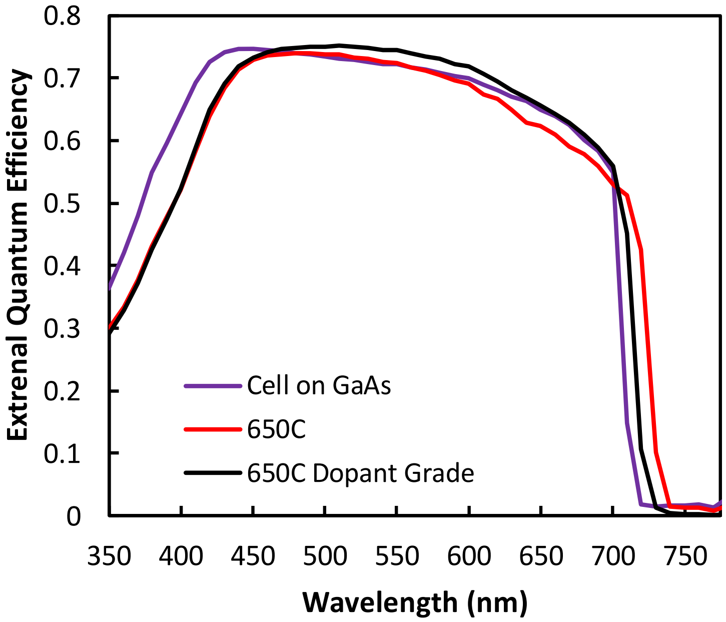

Figure 6.18 EQE of the dopant grade cell compared to the TC-3 cell grown on GaAs-based VS and the cell without the dopant grade grown at the improved growth conditions (650 C).

the best of both worlds, identical diode dark current, and enhanced short circuit collection and *hopefully* a reduction in VDC.

A fabricated device based on the structure in Figure 6.17a (referred to as the dopant grade cell) was grown using the improved growth conditions (650 °C) and were compared with the TC-3 device on GaAs and a cell without the dopant grade (650 °C Cell). EQE results shown in Figure 6.18 indicate even further improved collection over the 650 °C cell to levels greater than the TC-3 cell on GaAs. This is a remarkable achievement as the cell with the doping grade still possesses a TDD that is ~2-3× higher than the cell on GaAs. LIV results in Figure 6.19a show the commensurate increase in J_{SC} and a significant reduction in the shunt-like losses, seemingly due to a reduction in VDC. While there is a slight increase in V_{OC}, this is due to slight differences in the E_G (seen in Figure 6.18), as the calculated W_{OC} is nearly identical between the two cells grown on Si.

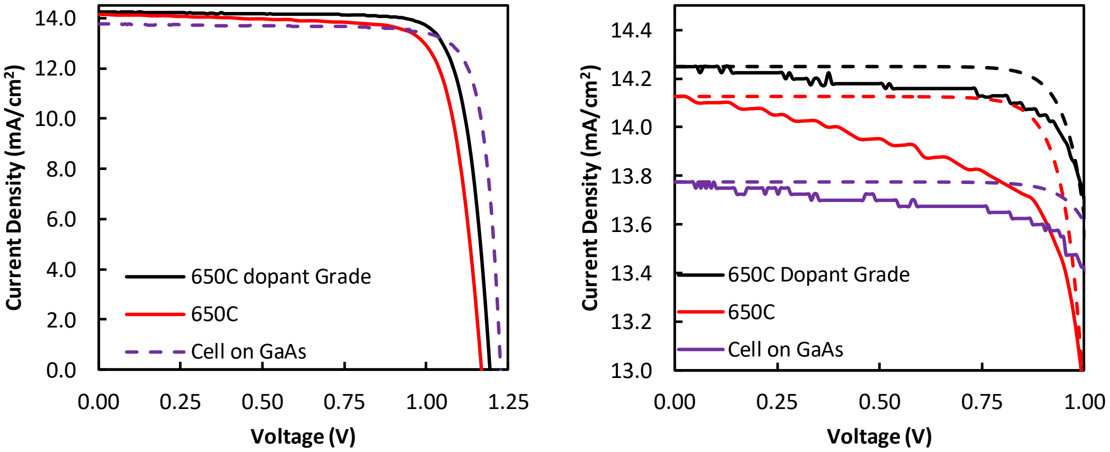

Figure 6.19 a) LIV of the dopant grade cell compared to the TC-3 cell on GaAs as well as a cell grown at identical growth conditions without a dopant grade (650 °C cell). b) A zoomed in inset of the LIV curves in a) showing the reduction in VDC with the application of the dopant grade.

The zoomed in region of this graph shown in Figure 6.19b with Suns-J_{SC}-V_{OC} measurements indicated in dashed lines show the VDC was reduced through the application of the dopant grade down to levels that are on par with the cell grown on the GaAs-based VS. This cell already possessed an impressive 86% FF so matching the shunt like losses is a critical step towards high tandem FFs. With these increases in FF and J_{SC}, this cell, with the addition of an ARC is expected to outperform the highest performing GaAs$_{0.75}$P$_{0.25}$ cell on Si reported to date. This previous record cell was reported by Fan et al. at UIUC grown by MBE and using a PIN cell design which strongly aids short circuit collection [25]. The PIN design *does* increase the depletion width in contrast to this strategy and therefore adversely affects V_{OC} by increasing junction recombination current J_{02}. It is for this reason why a dopant grade is preferable over the PIN design.

6.4. CONCLUSIONS

The development of high performance $GaAs_{0.75}P_{0.25}$ top cells is obviously of utmost importance in improving $GaAs_{0.75}P_{0.25}$/Si tandem efficiency. Thus, in the initial stages of dissertation research, forward looking cell optimization on low-TDD, GaAs-based VS provided an excellent methodology to focus on mechanisms which dominate short wavelength collection. These identified issues with over doping of the emitter, and subsequently issues with the window which were strongly limiting short wavelength collection. Transitioning this improved design to a higher-TDD (2×10^{7} cm^{-2}) Si platform, coupled with analytical modeling, allowed for a robust quantitative understanding of the impact of TDD on both transport properties and cell performance. Further modeling of these samples and detailed metrics about cell performance and design are presented in Chapter 7.3 when exploring DBR structures [142].

As TDD was reduced though the efforts detailed in Chapter 8 [145], further exploration of long wavelength collection, growth conditions, and voltage dependent collection was performed. The final design, using graded p-type doping in the base to aid collection, has enabled efficiencies which are on par with the best cells demonstrated on the GaAs-based VS ($1\text{-}2\times10^{6}$ cm^{-2}), and is projected to outperform the best reported $GaAs_{0.75}P_{0.25}$ cells on Si with the application of an ARC.

CHAPTER 7:

TOWARDS TDD TOLERANT CELL DESIGNS

7.1. OVERVIEW

Over the course of my tenure at OSU, I have focused on two potential strategies that were aimed at mitigating the performance losses associated with TDD. As mentioned in prior chapters, the reduction in minority carrier diffusion length and lifetime placed difficult constraints on the cell design and ultimately limits BOTH V_{OC} and J_{SC} to values which are less than desirable for enabling maximum tandem cell efficiency. Thus, it is worthwhile to explore new cell architectures and design implements, which provide a degree of tolerance to the performance degradation associated with elevated TDD. The first method explored, the rear-emitter solar cell, focuses primarily on improving open circuit voltage through an enhancement in minority carrier lifetime and a commensurate reduction in diode dark current. This work was the first primary project in this research and really served as a steppingstone in the scientific understanding and research methodology enveloped by this dissertation. The second method explored was the use of a distributed Bragg reflector in order to enhance the optical length of the solar cell, while maintaining an electrically short device. The concept here was to hopefully eliminate the tradeoffs between optical path length and carrier collection efficiency.

7.2. REAR-EMITTER SOLAR CELLS

The rear-emitter solar cell schematically depicted in Figure 7.b, was explored extensively as a method to improve the V_{OC} of the $GaAs_{0.75}P_{0.25}$ top cell even at elevated TDD. This concept was brought about by the desire to utilize an *n*-type base while maintaining the necessary *n-on-p* device polarity for application in a $GaAs_{0.75}P_{0.25}/Si$ tandem cell. This section first begins with a background on why changing from an n^+/p diode such as in the standard front-emitter design (Figure 7.1a) to a n/p^+ diode, as in the rear-emitter solar cell should, in theory, provide enhanced voltage at a given threading dislocation density. Then, as a part of the development efforts associated with the

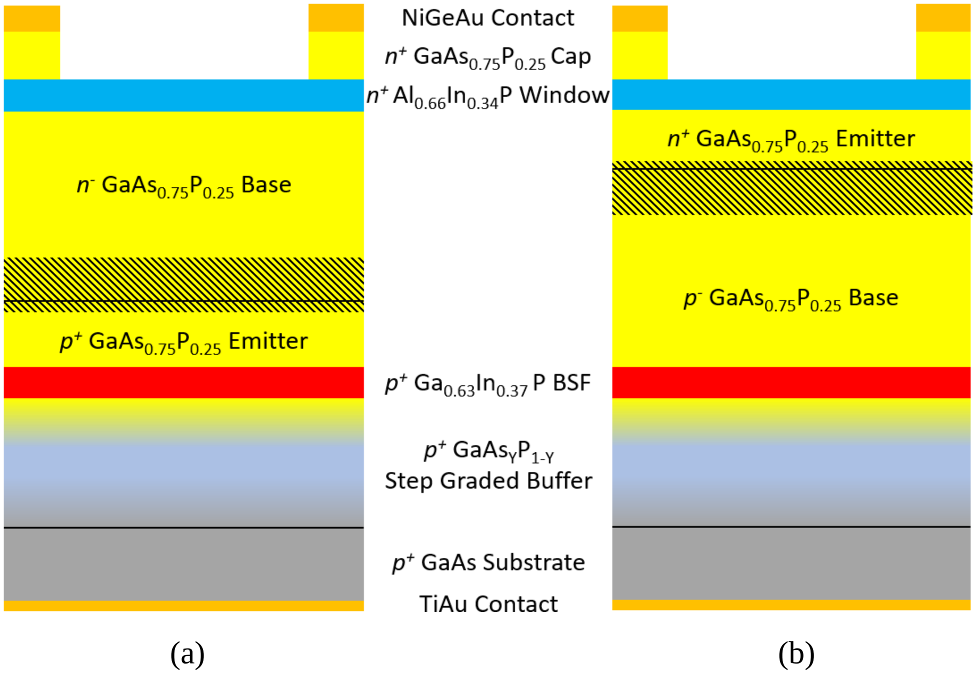

Figure 7.1 Device schematics for (a) rear- and (b) front-emitter devices investigated in this work. The hatched regions indicate the approximate location of the depletion region.

realization of these devices, critical aspects associated with the passivating role of the $Al_{0.66}In_{0.34}$ P window layer are presented which enabled a ~2x increase in conversion efficiency for the rear emitter design. Then a comparison of rear- and front- emitter solar cells and analysis of the recombination current and V_{OC} behaviors is presented proving the potential of such a design in improving V_{OC}. Finally, the work explores the broader impact of this design on carrier collection and photocurrent behavior, with pathways for future implementation discussed.

7.2.1. THEORY AND CONCEPT

Because threading dislocations act as spatially localized recombination centers, when the TDD is beyond some critical value (around 10^5 cm^{-2} for *p*-type GaAs) [7], [8], the minority carrier diffusion length, and thus lifetime, becomes statistically limited by the spacing between threading dislocation segments [9]. Assuming a uniform distribution of threading segments, the lifetime associated with recombination at these defects, τ_{TDD}, can be described by

$$\tau_{TDD} = \frac{4}{\pi^3 D \rho_{TD}}, \qquad \text{Eq. 7.28}$$

where *D* is the minority carrier diffusivity and ρ_{TD} is the TDD [9]. Note the inverse relationship of lifetime and diffusivity that arises from the spatially-localized nature of the recombination mechanism. Intuitively, slower diffusion of carriers to these recombination sites leads to longer lifetimes. Therefore, lower diffusivity in materials that are limited by a significant quantity of threading dislocations could be advantageous in certain cases where the dislocation limited lifetime itself is the singular limiting factor (such as for V_{OC} in higher bandgap materials, as will now be described).

Due to the *combined* effect of a wide bandgap and the defective nature of the metamorphic $GaAs_{0.75}P_{0.25}$ top cells of interest here, the depletion region recombination current (J_{02}) is expected to be the dominant component of the total dark diode current (i.e. much larger than the J_{01} saturation current component) and must be minimized in order to maximize the V_{OC}. While this goes counter to many lattice-matched materials such as GaAs and $Ga_{0.51}In_{0.49}P$, where the dark I-V characteristics are typically limited by saturation current component (J_{01}), J_{02} limited behavior has been shown to be the case for metamorphic GaAs when appreciable TDD is present [7]. This is expected to be even more likely for $GaAs_{0.75}P_{0.25}$ given its larger 1.7 eV bandgap, and thus smaller (versus GaAs) intrinsic carrier density, n_i. Because J_{01} scales with n_i^2, $GaAs_{0.75}P_{0.25}$ will exhibit an even larger discrepancy between J_{01} and J_{02} than similarly defective GaAs. J_{02} is given by Equation 7.2

$$J_{02} = \frac{q * W_d * n_i}{2 * \tau_{dep}}, \qquad \text{Eq. 7.1}$$

where, W_d is the width of the depletion region, $\tau_{dep}$is the Shockley-Read-Hall lifetime in the depletion region, and n_i is the intrinsic carrier concentration [148]. As a result of the inverse proportionality between J_{02} and τ_{dep}, low carrier lifetime in the depletion region is the primary factor contributing to increased J_{02}, and thus lower V_{OC}.

The depletion region in a typical asymmetrically-doped homojunction solar cell exists mostly within the lower-doped side of the metallurgical junction (i.e. the base). Therefore, the J_{02} component attributed to the base, or $J_{02,b}$, will dominate the total depletion recombination current. Furthermore, because the arrival rate of minority carriers from the base to the spatially-localized threading dislocations will ultimately be the rate limiting process for recombination within the depletion region, the lateral diffusivity (versus vertical drift) of these carriers will largely dictate the magnitude of the junction recombination current. Hence, the specific minority carrier type in the base—electron for a *p*-type base or hole for an *n*-type base—is an important parameter. From Equation 7.1, a lower minority carrier diffusivity in the base will improve carrier lifetimes (τ_{TDD}) and therefore reduce junction recombination current in materials whose lifetime is limited by the presence of excess TDD. This reduction in J_{02} should improve V_{OC} in diodes that are, of course, junction recombination limited to voltages at or beyond V_{OC}.

As noted above, this phenomenon has been previously shown to dictate V_{OC} for GaAs solar cells with low but non-negligible TDD values; and due to the lower value of n_i for 1.7 eV bandgap $GaAs_{0.75}P_{0.25}$ this would intuitively be expected to be more dominant here. While a more in-depth discussion of this formative work is presented in Chapter 5, it is instructive to briefly review the result from Andre et al. here to gain context for the subsequent metamorphic $GaAs_{0.75}P_{0.25}$ analysis. The aforementioned work focused on GaAs grown on strain-relaxed $Si_{1-x}Ge_x$ buffers (on Si). In this system it was shown that when the TDD was greater than ~10^5 cm^{-2}, p^+/n GaAs junctions exhibited longer base minority carrier lifetimes and thus higher V_{OC} than for GaAs n^+/p junctions [7], [8]. This effect was attributed to the reduced junction recombination current (J_{02}) of the p^+/n polarity cell. Ultimately, the 11× difference in minority carrier diffusivity between electrons and holes in GaAs results in an ~100 mV V_{OC} advantage for p^+/n cells versus n^+/p cells at a TDD ≈ 1-2×10^6 cm^{-2} [7]. Here, because the ideal 1.7 eV bandgap top junction composition ($GaAs_{0.75}P_{0.25}$) is expected to behave similarly to the GaAs binary alloy, it is likely that this alloy will have somewhat similar transport properties. Therefore, the implementation of a p^+/n configuration for a metamorphic $GaAs_{0.75}P_{0.25}$ cell, where the majority of the depletion region is located within the *n*-type base, may also yield improved V_{OC} at realistic TDD values of >10^5 cm^{-2}.

However, design flexibility for the $GaAs_{0.75}P_{0.25}$ top cell within the overall $GaAs_{0.75}P_{0.25}$/Si tandem structure, of course the ultimate goal, is limited by the large valence band offset ($\Delta E_V \approx 1.0$ eV) at the GaP/Si interface [149]. This effectively mandates the use of *n*-on-*p* subcell polarities. Additionally, *n*-type ohmic contacts tend to provide superior specific contact resistivity versus *p*-type for III-V semiconductors. This, combined with the fact that lower front-side sheet resistance, can be more readily obtained with an *n*-on-*p* polarity given the generally lower resistivity for equal carrier concentrations for *n*-type material versus *p*-type results in lower series resistance losses and therefore greater potential fill factors.

In order to achieve the potentially desirable n-type base polarity, while still maintaining the requisite n-on-p structure, a “rear-emitter” (or rear-junction) design can be used. In this case, the thin p+-doped (“emitter”) side of the junction is buried beneath the thicker, lightly-doped n-type “base.” This naming convention was chosen to be in agreement with the naming convention of bipolar junction transistors where irrespective of doping type the emitter is always dictated as the higher doped side of the junction.

This convention is sometimes ignored within the PV community, so this work is keen to note the technical accuracy.

In addition to possibly providing longer minority carrier lifetimes and higher V_{OC}, as just described, the thick n-type base layer now on the front side should provide even lower sheet resistance and better current spreading than the common front-side thin emitter variants. A lower sheet resistance should then allow for reduced metal coverage and potentially higher FF when using an optimal grid design. In fact, this design concept has already been implemented for several dislocation-free materials, including Si [150], lattice-matched $Ga_{0.51}In_{0.49}P$ [151], and GaAs [152], and such advantages were indeed observed. However, the mechanisms for V_{OC} improvement in these technologies rely solely on a necessary reduction in the reverse saturation component (J_{01}) of the dark current, whereas for the case of the dislocated $GaAs_{0.75}P_{0.25}$ alloys of interest here, a reduction in junction recombination current (J_{02}) is likely necessary to improve V_{OC}.

7.2.2. THE CRITICAL ROLE OF THE $AL_{0.66}IN_{0.34}P$ WINDOW

Three generations of rear-emitter $GaAs_{0.75}P_{0.25}$ cells were fabricated, the structures of which are detailed in Table 7.1. The only nominal differences between the three structures are the thicknesses and doping concentrations of the *n*-type $Al_{0.64}In_{0.36}P$ window layers, with all other parameters held constant. Comparisons of the internal quantum efficiency (IQE) of these structures are presented in Figure 7.2. Unexpectedly, Device-1 exhibited substantially lower J_{SC} and IQE than was expected from both analytical and TCAD modeling. Upon adjusting the doping of the window from Device-1 to Device-2 a large improvement in IQE was observed. The increase in window thickness

Table 7.1 Device structure descriptions for the devices used to study the role of the $Al_{0.66}In_{0.34}P$ window on rear-emitter cell performance.

Device	**Layer**	**Thickness (nm)**	**N_A or N_D (cm^{-3})**
Device-1	*n-Window*	*14*	1×10^{18}
	n-Base	1250	1×10^{17}
	p-Emitter	50	1×10^{18}
	p-BSF	50	2×10^{18}
Device-2	*n-Window*	*20*	5×10^{18}
	n-Base	1250	1×10^{17}
	p-Emitter	50	1×10^{18}
	p-BSF	50	2×10^{18}
Device-3	*n-Window*	*50*	5×10^{18}
	n-Base	1250	1×10^{17}
	p-Emitter	50	1×10^{18}
	p-BSF	50	2×10^{18}

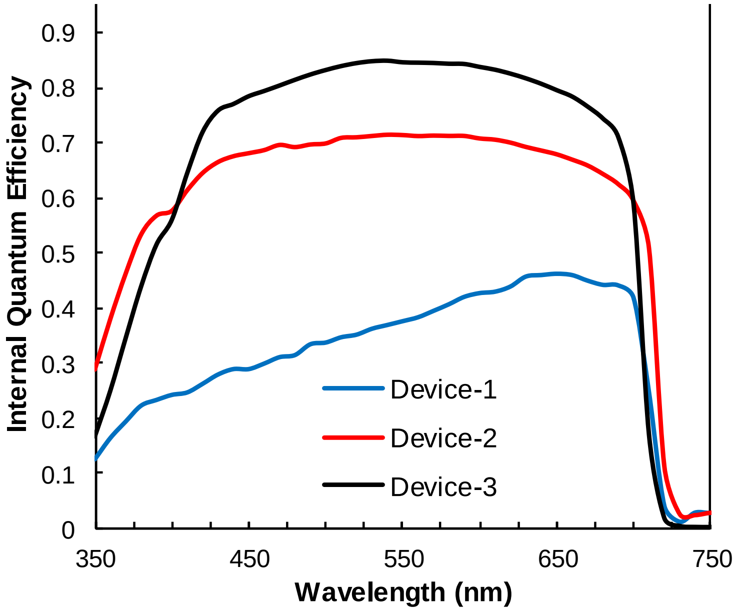

Figure 7.2. Internal quantum efficiency of as grown devices. Thicker and more highly doped windows provide higher IQE response well beyond the band edge of $Al_{0.64}In_{0.36}P$.

and doping between Device-1 and Device-2 resulted in an approximate AM1.5G current improvement of 8.1 mA/cm^{-3}, calculated from the integrated IQE. This observed improvement occurs counter to the intuition that the thicker, more parasitically absorbing window would reduce the short wavelength collection and thus overall current. However, the thicker window results in a broadband IQE improvement beyond the absorption edge of $Al_{0.64}In_{0.36}P$, indicating that the carrier collection efficiency in the layer adjacent to the window, the base in this case, must be improved via changes to the window. There is even further improvement moving to Device-3, which possesses a much thicker, and likely more parasitically absorbing, 50 nm window, showing that even the 20 nm window in Device-2 may still be non-ideal.

Note that illuminated I-V measurements and EQE are not presented here due to their tendency to somewhat obfuscate the underlying trends. That is, since changes in window thickness strongly impacts short wavelength reflectance, the differences between the devices do not appear to be as significant or as systematic as they do when examining IQE, which removes this effect. Nonetheless, it is relevant to note that the V_{OC} of the champion devices were found to vary between 1.27 V and 1.30 V, commensurate with changes in J_{SC} observed from EQE/IQE measurements, and also slight differences in bandgap. Because the photocurrent values in these rear-emitter devices are predominantly generated within a single layer (i.e. the thick front-side absorber/base), understanding the limiting mechanisms in this device is simpler than in front-emitter structures where photocurrent is contributed by multiple regions within the cell (i.e. emitter, space-charge region, and base). The rather clear linear nature of the IQE profile of Device-1 suggests that collection is likely limited by the interface recombination velocity (IRV) at the window/base interface [48]. This effect can be seen through the modeling sensitivity analysis presented in Figure 7.3, where the black curves represent the situation where the window/base IRV is the dominant mechanism limiting the collection probability within the device. These calculations were performed using the models described in Chapter 5. A drastic reduction in IQE is observed as the result of either an increase in window/base IRV or decrease in base/absorber minority carrier diffusion length, L_D. However, it is the high window/base IRV (> 5×10^4 cm/s) case that produces a pseudolinear response between 425 nm and 600 nm, consistent with the IQE of Device-1. Conversely, if the base/absorber diffusion length is instead reduced, with IRV maintained at a reasonable value (here, 2000 cm/s), the device maintains a much flatter response across the same spectral range.

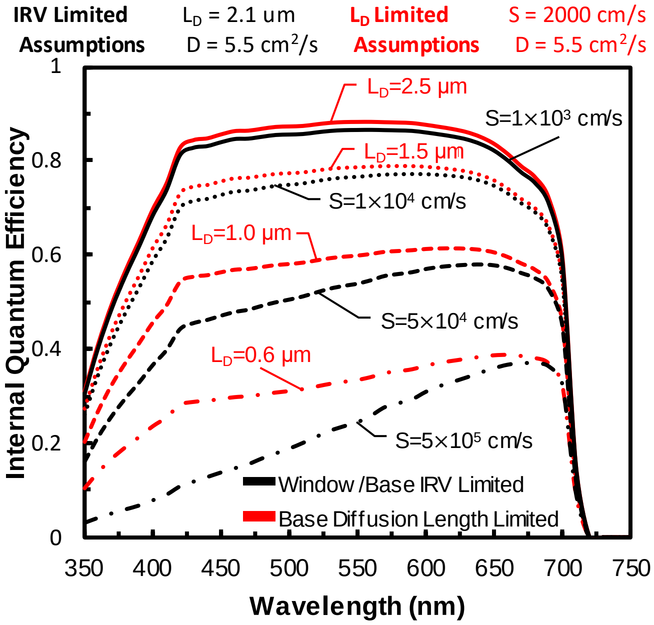

Figure 7.3. IQE modeling sensitivity analysis for a window/base interface recombination limited case (black) and a base diffusion length limited case (red). Notice that the IRV limited case results in a steeper and near linear response between 425 nm and 650 nm when compared to the flatter response provided by the diffusion length limited case. The IRV limited case more accurately describes the shape of the IQE of Device-1.

Based upon this sensitivity analysis, the shape of the experimental data from Device-1 cannot be adequately fit by a diffusion length limited collection profile and is much more effectively fit with the case of a limiting window/base IRV. Although one would not intuitively expect that changing the window thickness or doping would affect the diffusion length of the base layer, (and thus the collection probability within the base) the fact that the devices considered here all possess nominally identical interfaces (i.e. the same material transition process) and base layers suggests otherwise.

Therefore, working on the hypothesis that changes in window/base IRV are indeed likely responsible for the drastic change in cell performance associated with changes to the window parameters, surface Fermi level pinning was considered to be a plausible mechanism to explain the elevated recombination activity. Surface depletion commonly occurs at III-V surfaces due to Fermi level pinning if a sufficiently high density of surface defect states are present [153]–[157]. As previously noted, this is effectively the main reason that window layers are used. Of course, Fermi level pinning is also just as likely to occur at the surface of the window layer, or at the unpassivated air/$Al_{0.64}In_{0.36}P$ interface here. Because the exact surface Fermi level pinning energy for $Al_{0.64}In_{0.36}P$ is not known, the pinning level was assumed to be near the middle of the bandgap, as commonly observed and/or assumed for other III-V materials [155], [156], [158], and band diagrams were calculated for the front side of all three devices, presented in Figure 7.4.

In the Device-1 case (Figure 7.4a) the surface depletion is found to extend well into the *n*-$GaAs_{0.75}P_{0.25}$ base layer. The resulting electric field attracts minority carrier holes to the window/base interface, where recombination is significantly more likely, even if the native IRV is relatively low (but non-zero). Thus, the *effective* IRV at the $Al_{0.64}In_{0.36}P/GaAs_{0.75}P_{0.25}$ interface increases, regardless of the epitaxial quality between the two layers. Such a surface depletion induced window/base interfacial recombination effect was previously theorized by Gee et al. in front-emitter GaAs solar cells with AlGaAs windows [159]. Conversely, in the Device-3 structure (Figure 7.4c) the surface

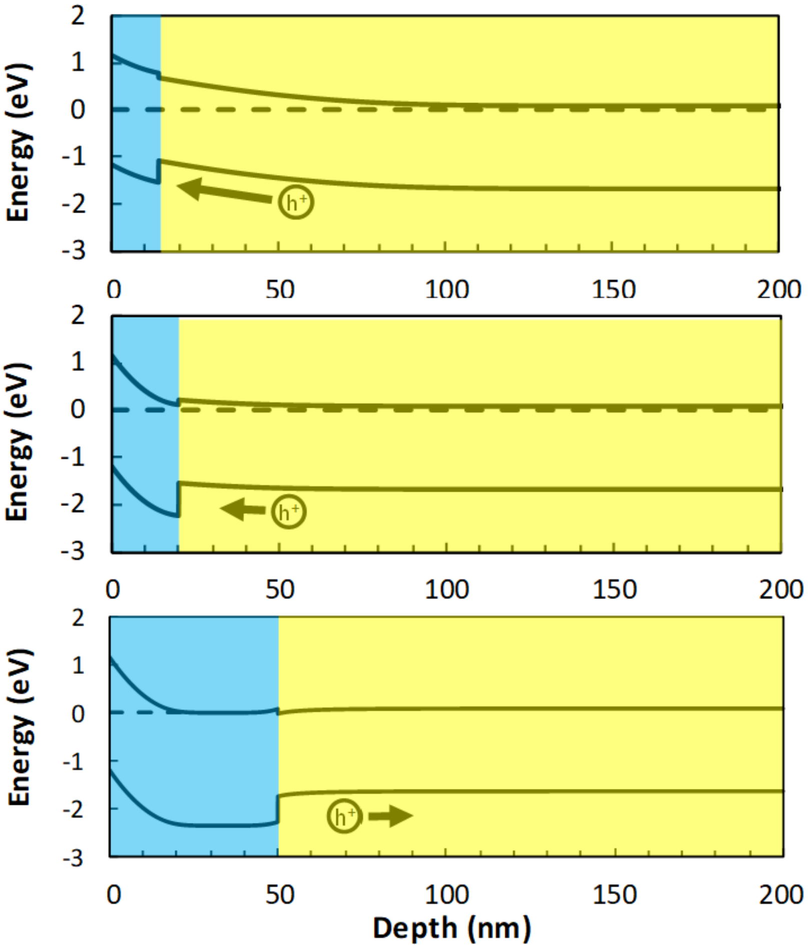

Figure 7.4. Band modeling of the window/base interface for a) Device-1, b) Device-2, and c) Device-3 assuming midgap surface fermi level pinning. Notice that the surface depletion extends into the base in both the Device-1 and Device-2 case but is completely contained in the case of Device-3. This surface depletion pulls minority carrier holes up against the $Al_{0.66}In_{0.34}P/ GaAs_{0.75}P_{0.25}$ interface causing elevated interfacial recombination.

depletion is fully contained within the window and does not reach the base layer, thus providing no window/base recombination enhancement. In this case, the intrinsically low IRV afforded by the high heteroepitaxial quality between the $Al_{0.64}In_{0.36}P$ and $GaAs_{0.75}P_{0.25}$ is maintained.

Device-2 (Figure 7.4b) brings with it a much greater level of uncertainty. While initial band diagram modeling does suggest a slight extension of the surface depletion into the base, the field appears to be very small. Therefore, strong conclusions about whether this device is limited by the surface depletion induced window/base interfacial recombination cannot be made without further analysis. Recalling the sensitivity analysis in Figure 7.3, we find that either IRV or diffusion length limited cases can provide very similar profiles in the performance range exhibited by Device-2, complicating the analysis of this device.

To gain additional insight into the limiting mechanism(s) in Device-2, Al_2O_3 was deposited onto the device surface by atomic layer deposition (ALD) with the intent to change the surface chemistry and monitor the impact on IQE. Ideally, this should alter the Fermi pinning level energy and/or occupation at the air/$Al_{0.64}In_{0.36}P$ interface and change the surface pinning energy and depth of the surface depletion. Although Al_2O_3 is commonly used to *passivate* such surface defects, here no attempt at optimization was made and only a standard deposition process was used under the expectation that true passivation would not be achieved, and that even potentially worsened pinning could result. IQE results from this study are shown in Figure 7.5.

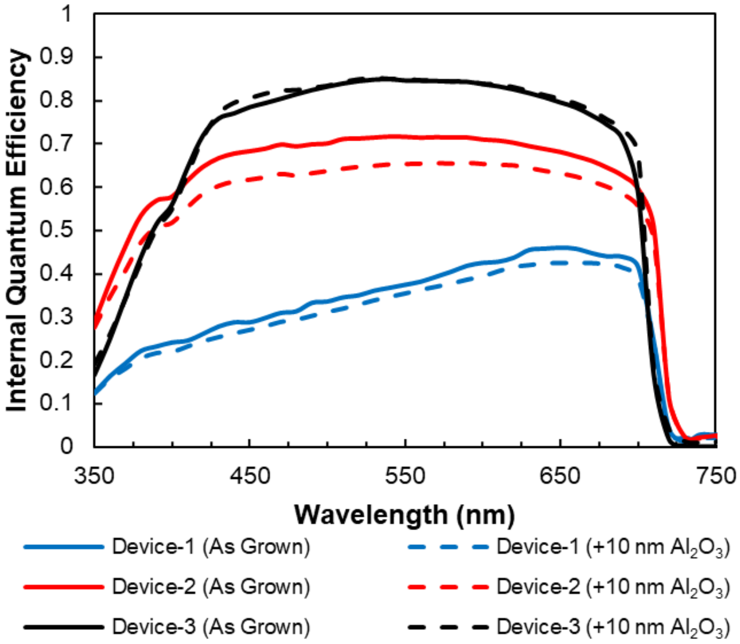

Figure 7.5 IQE curves for as grown and post ALD cells. Devices-1 & 2 exhibit reduced performance after ALD treatment while Device-3 is unchanged.

The Device-1 and Device-2 cells were found to exhibit reduced IQE performance after the Al_2O_3 deposition, indicating worsened pinning, ostensibly due to changes in the surface chemistry creating defect states. This would effectively increase the depth of the surface depletion resulting in further penetration into the base layer, causing enhanced window/base interfacial recombination. Device-3, on the other hand, does not change, indicating that the window layer in this device is sufficiently thick and/or doped highly enough to still fully contain the larger depletion field. Ultimately, with respect to Device-2, these results are consistent with the IRV-limited mechanism. Additionally, it is important to note that Device-2 exhibits a larger change in IQE performance after ALD Al_2O_3 than Device-1. This is likely because the surface depletion is only just beginning to extend into the base in the unadulterated Device-2, resulting in a relatively weak residual field. As such, even slight changes to the surface pinning level can thereby cause large

Table7.2 Transport parameters used in modeling of devices in the window thickness/doping study.

Layer	L_D (cm)	D (cm^2/s)	Effective IRV or SRV (cm/s)
Window	5.1×10^{-7}	0.26	[a]1.0×10^6
Base	2.1×10^{-4}	5.5	[b]Variable
Emitter	1.7×10^{-6}	15	[c]5.0×10^2

[a] Window/Air SRV is held constant

[b] Base/window IRV assumed to be 2000 cm/s for the as grown case of Device-3, then used as a fitting parameter for the remainder of devices

[c] Emitter/BSF effective IRV is held constant

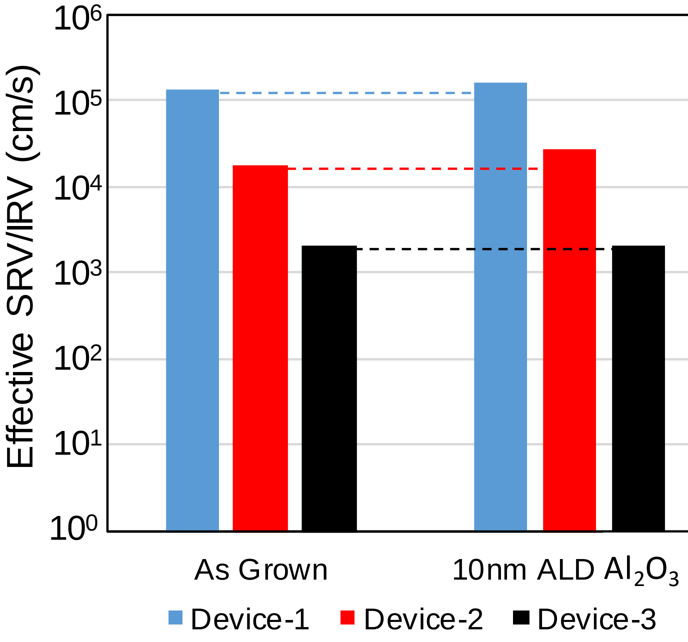

Figure 7.6 Model extracted effective window/base IRV. Window/base IRV changes by nearly two orders of magnitude with changes to window thickness and doping and is increased slightly with the addition of ALD Al_2O_3 for the case of Devices 1 and 2.

relative changes to the effective IRV at the window/base interface due to the rapidly changing strength of electric field at this interface. Interestingly, this result suggests that the original Device-2 is potentially close to completely containing the surface depletion.

Using the constants shown in Table7.2, fits to the as grown and Al_2O_3-coated samples allow for the extraction of the effective window/base IRV, as presented in Figure

7.6. First, initial extraction of base diffusion length must be performed by determining and fixing a baseline window/base IRV—that is, the native IRV within a device with collection probability that is limited only by base diffusion length, L_D. Using Device-3 for this purpose, the window/base IRV was assumed to be of moderate quality at 2000 cm/s, or slightly greater than reported values for GaAs/$Al_{0.51}In_{0.49}P$ [160], since no intentional growth study on interfacial quality has been performed to date. Using these assumptions, the diffusion length in Device-3 was extracted to be 2.1 μm. Even with this assumed moderate interface quality, the device is still strongly diffusion length-limited, as indicated by the 13.5× larger diffusion velocity, D/L_D, (>26000 cm/s) compared to the effective surface recombination velocity (2000 cm/s). This extracted base diffusion length was then used in the fitting of the remainder of the devices, using the window/base IRV as the sole fitting parameter. Note that these extracted IRV values assume flat band conditions near the interface and is a measure of the role of both interfacial quality and the associated field assisted interfacial recombination. High quality fits to experimental data were achieved, with maximum root mean squared deviations of only 1.6%.

Based on the extracted window/base effective IRV values shown in Figure 7.6, two key aspects of this phenomenon are further reinforced. First, the effective IRV at the window/base interface can change by at least two orders of magnitude (300×) solely due to changes to the window thickness and doping. Second, the addition of ALD Al_2O_3 slightly increases the effective window/base IRV for cases where the surface depletion is not fully contained within the window (Device-1 and 2) and is unchanged for cases where the window is sufficiently doped and thick enough to contain the surface depletion.

Since the window is traditionally treated as a parasitic absorber, where photons that are absorbed are lost to recombination (i.e. a dead layer), understanding the limits of window thickness are important toward efforts of simultaneous maximization of window transparency and collection of the short wavelength photons, which we now recognize are at odds with each other. If the surface depletion is contained within the window layer it should not impact carrier collection in the base layers. Therefore, the depth of the surface depletion provides the fundamental limit on the window thickness.

The depth of the surface depletion is dependent on two key factors: the doping concentration (N_D) and the energy at which the Fermi level is pinned at the surface ($E_C - E_{Pin}$). Figure 7.7 plots surface depletion as a function of doping for various E_{Pin} values calculated using a non-abrupt depletion approximation, which includes Debye spreading [161], [162]. This is simply approximated as the nominal depletion region width, assuming abrupt depletion, W_D, summed with the additional Debye length term, λ_D, which accounts for a gradual end to the depletion region. Equation 7.3 details this approach, where Φ_B is the difference in Fermi level energies between its pinned location at the surface ($E_C - E_{Pin}$) and its neutral location in a bulk layer ($E_C - E_F$), ε_s is the permittivity, and N_D is the dopant concentration.

$$x_d \approx \sqrt{\frac{2\epsilon_s \Phi_B}{q N_D}} + \sqrt{\frac{2\epsilon_s k_B T}{q^2 N_D}} = W_D + \lambda_D \qquad \text{eq. 7.2}$$

Figure 7.7 shows that if the pinning level, E_{pin}, at the air/ $Al_{0.64}In_{0.36}P$ surface can be reduced through passivation of surface states, requirements on window thickness can be reduced, thereby improving optical transparency of the parasitic window layer. To maximize transparency, while maintaining the desired passivating quality, the optimal

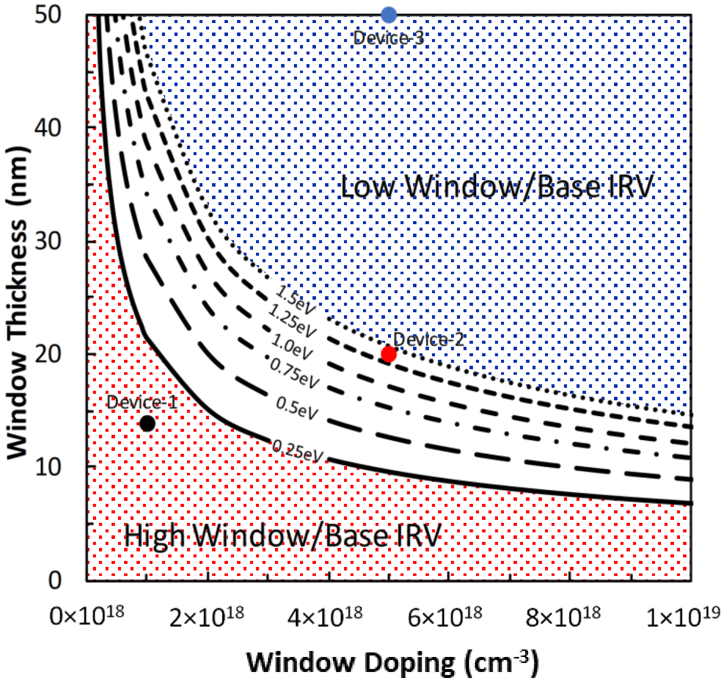

Figure 7.7 Theoretical necessary window thickness as a function of doping for various surface Fermi pinning energy levels (E_{Pin}) where E_{Pin} is defined as the difference between the conduction band and the Fermi level at the surface. Data points indicate experimental devices.

window thickness should be set to slightly larger than the depth of the surface depletion. Therefore, ultimate limits on the window thickness rely on a knowledge of the exact surface Fermi pinning level in $Al_{0.64}In_{0.36}P$, as well as the maximum obtainable *n*-type doping in $Al_{0.64}In_{0.36}P$. Plotting the devices from this experiment, as done in Figure 7.7, we see that Device-1 is indeed limited by surface depletion enhanced window/base IRV, Device-2 devices falls within a grey area, and Device-3 lies above all the curves and is therefore safe from this surface depletion induced effect. Because the ALD Al_2O_3 experiment confirmed that Device-2 is indeed limited by the enhanced IRV mechanism, the location of the surface pinning level can be estimated to lie deeper than 1.25 eV from the conduction band edge. This localizes the pinning level to the bottom half of the

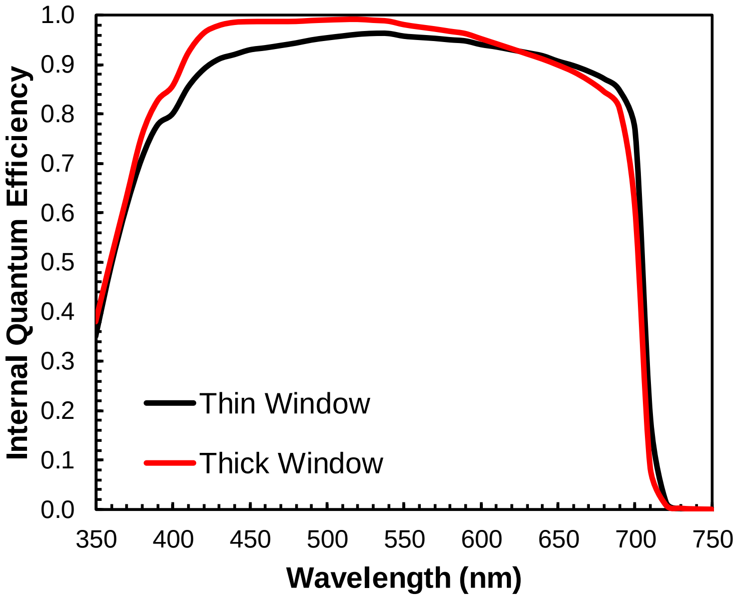

Figure 7.8 IQE comparison of front emitter devices with different window thickness and doping. While the effect of the $Al_{0.66}In_{0.34}P$ window parameters remain, the magnitude of this effect is drastically reduced when compared to the same design change in the rear-emitter structure.

bandgap. It is likely that this level is located close to the $E_C - 1.25$ eV level since Device-2 is very sensitive to changes in surface pinning energy, but it is difficult to estimate its exact position based on the available data alone.

As a slight extension of this exploration of surface Fermi level pinning on window design in $GaAs_{0.75}P_{0.25}$ cells, a similar study was performed on standard front-emitter cells as discussed in Section 6.1 going from the TC-2 design to the TC-3 design. The IQE data is repeated in Figure 7.8. A similar broadband increase to the IQE was observed, however the effect was markedly smaller. This is primarily for 2 reasons. First, the more lightly doped base layer in the rear-emitter design allows the surface depletion to penetrate deeper into the region of active collection. This causes a larger region of enhanced recombination near the front of the cell detrimentally impacting collection. Secondly, the layer adjacent to the window in the front-emitter design (the emitter) is

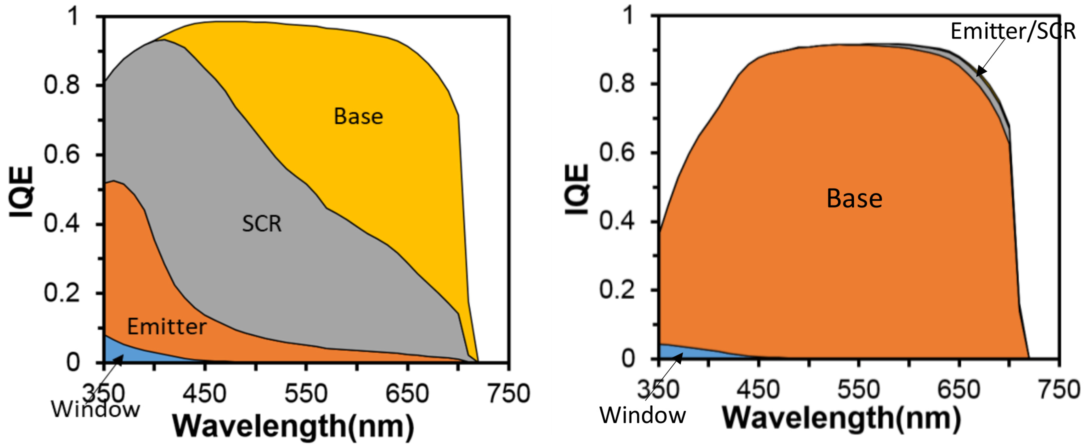

Figure 7.9 Component IQE plots for Rear- and Front emitter devices. In the rear-emitter design the vast majority of the photocurrent is generated in the layer adjacent to the window, while in the front-emitter design, only a small percentage of the total photo current is generated in the emitter

much thinner than the layer adjacent to the window in the rear-emitter design (the base). Thus, in the front emitter, only a small fraction of the total photocurrent is generated in this layer and therefore at risk of recombining at that front interface. This can be visualized by the component IQE plots in Figure 7.9. The shaded regions indicate the portion of the quantum efficiency curve generated in each layer based on device modeling described in Chapter 5. The depletion region, in this case, can be considered as a buffer or isolation layer which protects photogenerated minority carriers in the base from interacting with the high IRV interface. This is an important advantage of front emitter designs in the case of unavoidably high Window/absorber IRVs.

To summarize, this work has identified a dramatic sensitivity to window doping and thickness, while identifying surface Fermi level pinning at the window/air interface as the key factor limiting the minimum thickness/doping in the window layer. The surface depletion induced by this Fermi level pinning can cause anomalously high effective IRV at the window/base interface if the resultant field is allowed to extend into the base layer. While this has been demonstrated on this particular metamorphic $GaAs_{0.75}P_{0.25}$ material system, this surface Fermi level pinning effect should hold true across various III-V cell materials. Calculations have shown the necessary window thickness/doping to contain this surface depletion depends heavily on the actual surface Fermi pinning level. Based upon this work, the surface Fermi level pinning energy is estimated to be ≥1.25 eV away from the conduction band (i.e. within the bottom half of the bandgap). Additional quantification of the surface pinning energy is required to understand the theoretical quantitative limits on window thickness and doping. Nominally, if the density of defect states at the window layer surface can be reduced or passivated, restrictions on the necessary doping/thickness can be relaxed due to the resulting reduction and/or elimination of the surface pinning effect. This would have the impact of improving short wavelength collection in rear-emitter cells. Lastly, a similar study on front emitter cells has confirmed that this effect is indeed present in these devices; however, at a much-reduced magnitude due to the isolation of a larger number of photogenerated carriers protected from the interface with the enhanced IRV.

7.2.3. REAR- VS. FRONT- EMITTER COMPARISON

After initial exploration of the rear-emitter device, specifically the role of the $Al_{0.66}In_{0.34}P$ window as described in the previous section, Device-3 from the exploration above was compared to a front-emitter cell with nominally identical doping, and similar thicknesses of the layers. These structures are detailed in Table 7.3. This direct comparison was done to validate the theory and concept of the rear-emitter cell detailed

Table 7.3 Device structure details for the comparison of rear- and front-emitter.

Device	Base	Emitter	Window	BSF
Front-emitter	1.25 µm 1×10^{17} cm^{-3}	30 nm 1×10^{18} cm^{-3}	50 nm 5×10^{18} cm^{-3}	50 nm 5×10^{18} cm^{-3}
Rear-emitter	1.25 µm 1×10^{17} cm^{-3}	50 nn 1×10^{18} cm^{-3}	50 nm 5×10^{18} cm^{-3}	50 nm 5×10^{18} cm^{-3}

in Section 7.2.1. As a slight refresher, the rear-emitter cell was theorized to provide lower dark current densities and therefore higher voltages than the front-emitter design.

Thus, the dark I-V characteristics of these diodes were measured and are presented in Figure 7.10. A double-diode model was used to fit the data for the voltage region from 0.7 V to 2.0 V and extract relevant metrics (J_{01}, J_{02}, n_2, and R_{series}), shown in Table 7.4 [163]. The data below 0.7 V was excluded due to the high noise levels produced by the source-measurement unit in these low-current regimes. Shunt resistance was ignored (due to the exponential nature of the dark I-V curves above 0.7 V) and n_1 was set to 1, with all other values serving as fit parameters. Including shunt resistance terms without accurate low voltage I-V data can lead to inaccurate parameter extraction and thus was not included in the fitting. Assuming linear superposition of dark and light currents (based on spectrum-integrated EQE), the difference in the V_{OC} implied from dark I-V of the rear-emitter (1.29 V) and front-emitter (1.23 V) devices is ~60 mV. This trend agrees with the expected reduction in junction recombination current given by the theory in Section 7.2.1. However, quantum efficiency curves (Figure 7.12) for the two designs indicate a slight difference in bandgap (i.e. composition), with rear-and front-emitter bandgaps of 1.74 eV and 1.72 eV, respectively, which must be accounted for when comparing dark I-V characteristics. Therefore, it is necessary to normalize the J_{02} and J_{01} extracted values of this cell by a slight change in the intrinsic carrier concentration.

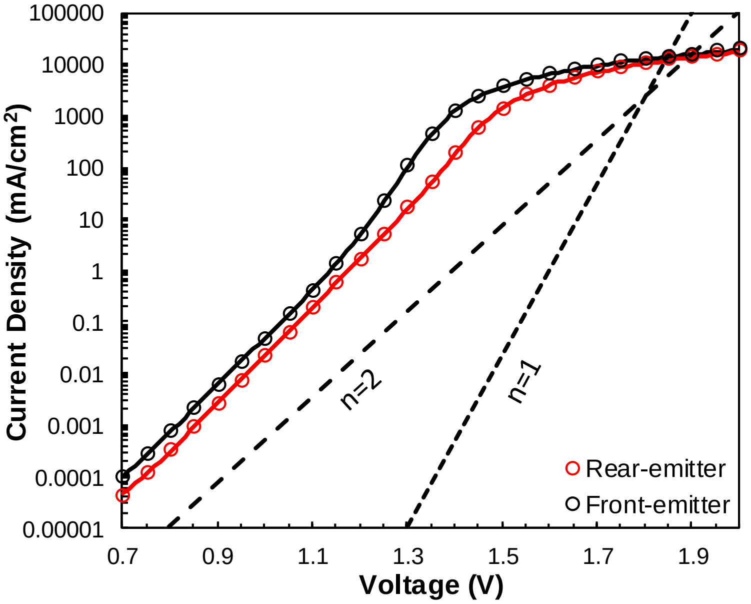

Figure 7.10 Dark I-V measurements for front and rear-emitter devices, the rear-emitter device exhibits a ~60 mV higher implied V_{OC} than the front-emitter device. Open circles indicate experimental data and solid lines indicate double-diode model fits. Reference lines for n=1 and n=2 are shown as black dashes.

Table 7.4 Extracted parameters from Double-diode Model for rear- and front-emitter devices.

Device	**J_{02} (A/cm^2)**	**n_2**	**J_{01} (A/cm^2)**	**n_1**	**R_{SER} (Ω-cm^2)**
Front-emitter	4.31×10^{-14}	1.88	8.00×10^{-24}	1	0.0298
Rear-emitter	8.97×10^{-15} ($1.32\text{x}10^{-14}$)	1.81	2.02×10^{-25} (4.36×10^{-25})	1	0.0268

These factors are 2.16x and 1.47x for J_{01} and J_{02} respectively due to the n_i and n_i^2 dependencies. The rear-emitter bandgap normalized values are given in parenthesis in Table 7.4.

Base and emitter doping magnitudes for the front- and rear- emitter device designs were nominally identical, allowing direct comparison between the two device structures. Both devices exhibit n_2 values approaching 2 (1.88 and 1.81 for the front- and rear-emitter designs, respectively), as expected for a material dominated by recombination current within the depletion region (i.e. due to elevated TDD and wider bandgap).

Recalling that the relationship between the J_{02} dark current term and carrier lifetime is described by Equation 7.2, where the lifetime in the depletion region shares an inverse relationship with the dark current density, allows a comparison between the lifetime in the two samples. Using the experimentally determined and bandgap normalized J_{02} dark current densities (see Table 7.4), the rear-emitter device was determined to possess a 3.3× longer effective minority carrier lifetime in the depletion region than the front-emitter cell. This difference is much larger than what may be expected from any small differences in TDD between the two device structures (i.e. within the low uncertainty afforded by the ECCI-based dislocation counting). As such, it is deemed significant and attributable to the apparently improved tolerance of the *n*-type base design to threading dislocation-mediated depletion region recombination from the perspective of V_{OC}. This is analogous to a similar result from Andre *et al.* [7] who demonstrated an 11× lifetime improvement in *n*-type metamorphic GaAs over *p*-type at the same TDD. It is expected that the lifetime improvement is smaller in $GaAs_{0.75}P_{0.25}$, because the electron and hole diffusivities are expected to be more similar than in pure GaAs [147].

Additionally, it is consistent with prior literature on rear-heterojunction $Ga_{0.51}In_{0.49}P$ cells, [151] that there is a large (18.3×) reduction in J_{01} associated with the switch to a rear-emitter geometry and an *n*-type base. While it was expected that the $GaAs_{0.75}P_{0.25}$ cells would be solely limited by J_{02} recombination current, there does appears to be some contribution from J_{01} in the front-emitter structure, as seen by the change in slope from n = 1.88 to n = 1 (upward turn) in the dark I-V curve at ~1.2 V before the clear onset of series resistance. This feature is not clearly observed in the rear-emitter structure, but careful derivative analysis does reveal a very slight increase in slope at ~1.35 V, commensurate with the beginning of a transition to J_{01} dominated behavior. This derivative plot was then used as fitting aid to assist in a more accurate extraction of J_{01} from the rear-emitter cell.

The relative impacts of the changes in J_{01} and J_{02} can be observed by first calculating the implied V_{OC} using only the bandgap normalized J_{02} diode parameters. From this calculation, there is a ~13 mV improvement in bandgap normalized implied V_{OC}. The addition of the J_{01} components in the diode results in an additional ~18mV improvement in bandgap normalized implied V_{OC}. Using these extracted improvements to the bandgap normalized V_{oc} dark I-V estimates a 31 mV improvement in the *bandgap-*V_{OC} offset ($W_{OC} = E_g/q - V_{OC}$) for the rear-emitter structure. Although absolute conclusions about the physical mechanisms driving the reduction in J_{01} are more difficult to make due to its larger uncertainties in fitting and key physical parameters, such as diffusivity, diffusion length, and surface recombination velocities, it is worthwhile to attempt to understand the difference in transport in the quasi-neutral regions of the diodes. Based on the reciprocity between excess minority carrier density and collection probability [125], additional information can be extracted from modeling of quantum efficiency curves, as presented below.

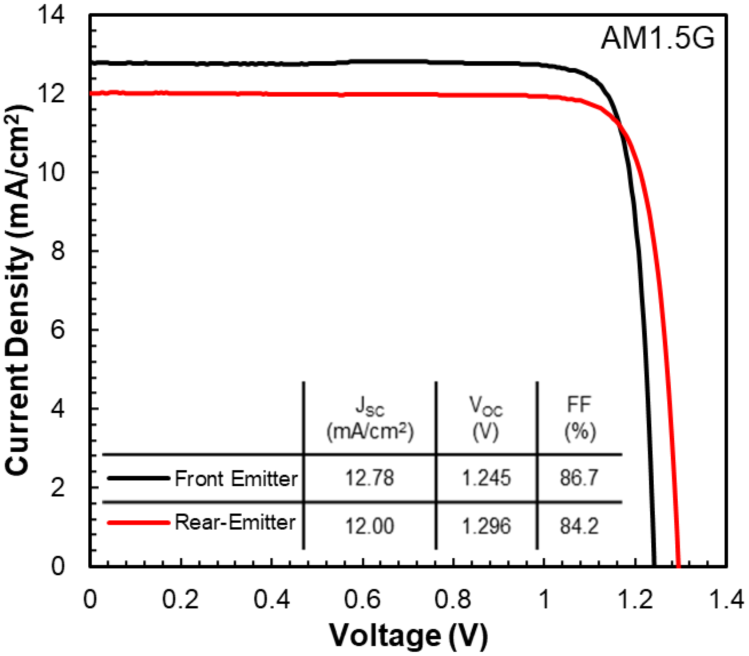

Figure 7.11 Illuminated I-V measurements for front and rear-emitter devices, the rear-emitter device exhibits a ~50 mV higher V_{OC} than the front-emitter device.

Representative LIV under simulated AM1.5G for both device structures is presented in Figure 7.11, with extracted performance metrics given in the inset. There are two key results to examine here. First, the V_{OC} of the rear-emitter device is ~50 mV higher than the front-emitter device, in general agreement with the 60 mV change in implied V_{OC} from the dark I-V results. Additionally due to the slight bandgap difference mentioned previously, the *bandgap*-V_{OC} offset ($W_{OC} = E_g/q - V_{OC}$) is a more appropriate metric for comparison. The W_{OC} for the front- and rear-emitter devices are 0.475 V and 0.445 V, respectively, revealing a 30 mV advantage for the rear-emitter design over the front-emitter design for the present TDD, in strong agreement with the 31 mV estimated from dark I-V, this result confirms the positive effect of the rear emitter n/p^+ design for the voltage output of the $GaAs_{0.75}P_{0.25}$ cell.

The second key result is with regard to the J_{SC}. We observe that the J_{SC} of the rear-emitter device is roughly 6.5% lower than that of the front emitter device. It must be noted that the rear-emitter device structure has not been optimized to improve current collection. Nevertheless, it is still important to understand how this structure impacts the short circuit collection dynamics, since this may provide further insight into fundamental transport differences between the quasi neutral regions of the structures, as well as suggest pathways to optimize current collection.

IQE curves for the front- and rear-emitter devices are shown in Figure 7.12. The immediate conclusion to be made based on these results is that the rear-emitter design exhibits reduced current collection across the entire relevant spectrum versus the traditional front-emitter device, consistent with the reduced J_{SC}. However, to better understand the transport properties in both structures with respect to the design rationale

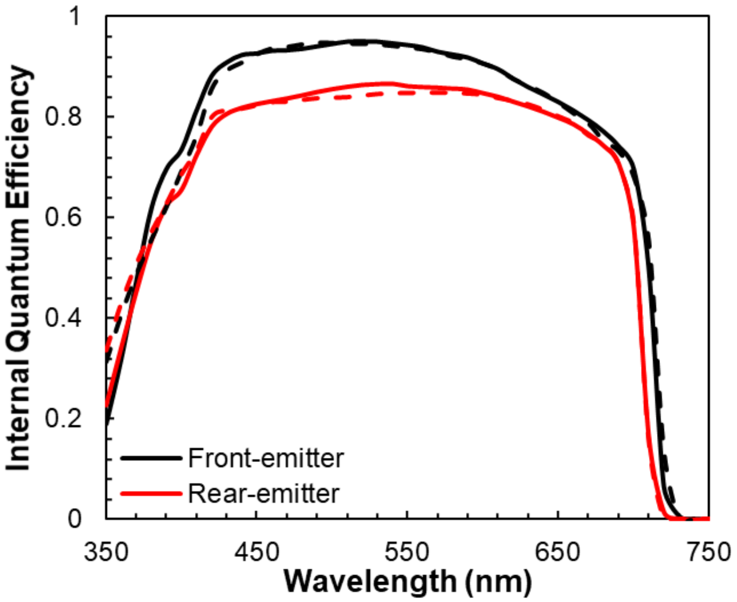

Figure 7.12 Internal quantum efficiency for rear- and front-emitter cells. Dashed lines indicated modeled fits of the experimental data.

Table 7.5 Modeling extracted transport parameters for rear- and front-emitter designs

Device	**Layer**	**L_D (cm)**	**D (cm^2/s)**	**SRV or IRV (cm/s)**
Front-Emitter	Window[a]	5.1×10^{-7}	0.26	1.0×10^{6}
	Emitter[b]	2.3×10^{-6}	3.17	5.0×10^{2}
	Base[b]	***1.3×10^{-4}***	54.6	5.0×10^{2}
Rear-Emitter	Window[a]	5.1×10^{-7}	0.26	1.0×10^{6}
	Base[c]	***1.8×10^{-4}***	7.12	5.0×10^{2}
	Emitter[c]	3.0×10^{-5}	18.1	5.0×10^{2}

[a] SRV for window rows indicate Window/Air interface.
[b] IRV in front-emitter device indicates Base/BSF and Window/Emitter interfaces.
[c] IRV in rear-emitter device indicates Base/Window and Emitter/BSF interfaces.

discussed herein, the analytical IQE model described in Chapter 5 was used to fit the experimental IQE data. Table 7.5 provides the extracted transport parameters. Except in the case of the window/air interface, surface and interface recombination velocities (SRV, IRV) were assumed to be relatively low based on the superior quality of fit given by the bulk recombination limited case, where $D/L_D >> S$. The air/$Al_{0.66}In_{0.34}P$ SRV was set to 1×10^{6} cm/s, in line with typical III-V SRV values [164]. The assumed value for the $Al_{0.66}In_{0.34}P/GaAs_{0.75}P_{0.25}$ and $GaAs_{0.75}P_{0.25}/Ga_{0.64}In_{0.36}P$ IRVs was selected to be 5×10^{2} cm/s, in line with those reported for GaAs/ $Al_{0.66}In_{0.34}P$ and even higher than $GaAs/Ga_{0.51}In_{0.49}P$ [160]. It should be noted that because the diffusion velocity D/L_D in these layers range from 4×10^{4} cm/s to 1.3×10^{6} cm/s, the resultant fits are essentially insensitive to the IRV parameter until it reaches ~1×10^{4} cm/s which is expected to be too large for a high quality III-V As/P interface which is not exacerbated by surface depletion.

The total diffusion length for minority carriers in the *un-depleted* base region, $L_{D_{TOT}}$, extracted from the model can be described by contributions from both the bulk, dislocation-free diffusion length ($L_{D_{BULK}}$) and the dislocation-limited diffusion length ($L_{D_{TDD}}$) [9],

$$\frac{1}{L_{D_{TOT}}^2} = \frac{1}{L_{D_{TDD}}^2} + \frac{1}{L_{D_{BULK}}^2}. \qquad \text{eq. 7.4}$$

The dislocation-limited component of the total base diffusion length ($L_{D_{TDD}}$) is dictated by the spacing between threading segments. This is formalized in the Yamaguchi model (re stated in equation 7.5), yielding $L_{D_{TDD}}$ for the measured dislocation density (2×10^6 cm^{-2}) of 2.5 µm:

$$L_{D_{TDD}} = \frac{2}{\sqrt{\pi^3 * (\rho_{TD})}}. \qquad \text{eq. 7.5}$$

As presented in Table 7.5, the model-extracted $L_{D_{TOT}}$ values for the front- and rear- emitter devices are 1.3 µm and 1.8 µm, respectively. It should be noted that there are multiple sources of uncertainty in the diffusion lengths extracted from modeling, including the specific optical parameters used, assumptions made within the model itself, and error in the experimental data to which the models were fit. The resultant uncertainty in the final computed values is difficult to estimate without having more definitive numbers for any of these inputs with which to compare, but the results obtained are within reason, based on the experimental results. More importantly, the modeling was performed in a consistent manner in order to ensure comparability between the different device structures and enable its use in understanding the impact of material quality and transport properties. Nonetheless, to examine the significance of the relative differences in diffusion lengths determined via the modeling, a test simulation of the rear emitter structure with a 1.3 µm base diffusion length (versus 1.8 µm) was performed, which yielded a current loss of 2.05 mA/cm^2 in AM1.5G-integrated IQE. Such a large difference highlights the sensitivity of this parameter and would be clearly observable in the experimental data, if uncertainty in this parameter had been an issue.

It is also important to note that these values are less than $L_{D_{TDD}}$by 30% to 60%, indicating that the diffusion length is potentially not entirely limited by the dislocation spacing. Most likely this is the result of some population of point defects (or other form of bulk recombination) not associated with the spatially-localized recombination at threading dislocation segments. Indeed, careful optimization of the growth conditions for the GaAs$_{0.75}$P$_{0.25}$ cell material has not yet been performed.

Based on the measured dislocation densities and equations 7.4 and 7.5 above, approximations for both minority electron and hole diffusion lengths in the un-depleted base, $L_{D_{BULK}}$, can be made. By this analysis, $L_{D_{BULK}}$ of the minority carriers is found to be 2.6 µm in the rear-emitter design (holes) and 1.5 µm in the front-emitter design (electrons) for the same 2×10^6 cm^{-2} TDD. The reason for the longer bulk hole diffusion length is not fully understood at this point but could be a result of differences in the recombination properties (e.g. trap energy levels, capture cross sections, charge states, etc.) of the dislocations and/or bulk point defects in the *n*- and *p*-type materials. Regardless of the fundamental reason, a longer bulk diffusion length in the *n*-type base is in agreement with the sizeable reduction in J_{01} current observed in the dark I-V and is then likely even more important at dislocation densities below 10^6 cm^{-2}.

Finally, it is revealing to further explore important intrinsic differences between the rear- and front-emitter designs with respect to short circuit carrier collection. Figure

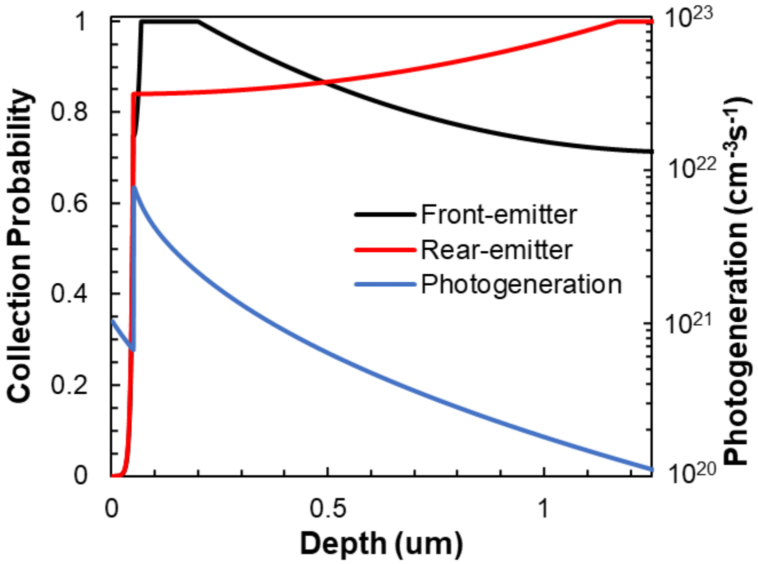

Figure 7.13 Nominal collection probability and photogeneration rate profiles for the front- and rear-emitter designs. Higher regions of collection probability near the front of the cell leads to improved IQE for the front-emitter design.

7.13 plots the modeled collection probabilities of both designs along with the photogeneration rate as a function of depth using the parameters extracted from the experimental data. Notice that the region of maximum collection probability for the front-emitter design resides near the front of the cell, coincident with the maximum photogeneration rate. This leads to the observed short wavelength IQE advantage for the front-emitter device exhibited in Figure 7.12. Conversely, the maximum collection probability for the rear-emitter design lies near the back side of the device, indicating that it should enable improved collection at longer wavelengths. However, because the photogeneration rate in this region is at a minimum, the advantage is likely to be markedly smaller than the shorter-wavelength enhancement exhibited by the front-emitter design. Nonetheless, neither of these devices have undergone significant optimization and are therefore not indicative of their nominal potentials. Further development of a more optimized rear-emitter structure could allow for improved short-wavelength response due to its longer base diffusion length.

This work successfully demonstrated prototype n/p^+ rear-emitter $GaAs_{0.75}P_{0.25}$ cells, which exhibited a 30 mV improvement in W_{OC} over a conventional n^+/p front-emitter design at the same TDD value of 2×10^6 cm^{-2}. The improved W_{OC} of the rear-emitter structure was shown to be the result of a 3.3× reduction in the bandgap normalized J_{02} current term as well as a ~18× reduction in the bandgap normalized J_{01} current term. Each of these improvements account for roughly half of the demonstrated improvement in dark *I-V* determined, bandgap-normalized, V_{OC}. The reduction in J_{01} is less understood and is likely due to differences in the recombination processes in the n- and p-type bases seen by the differences in the diffusion lengths extracted from QE. The reduction in J_{02} can be attributed to an improvement in carrier lifetime in the depletion region due to the lower diffusivity of the minority carrier holes in the n-type base, over electrons in a p-type base theorized in equation (1). It should be noted that this design is not limited to the III-V/Si tandem system investigated herein, and indeed could be beneficial overall if two major criteria are met: (a) the minority carrier lifetime is limited by spatially-localized defects, such as threading dislocations, and (b) there is a significant difference in minority carrier electron and hole diffusivities. Further work is necessary to optimize the collection probability profiles in the rear-emitter design to improve $J_{SC,}$ but initial results are promising for application in III-V/Si tandems and other systems limited by non-negligible TDD.

7.3. DISTRIBUTED BRAGG REFLECTORS

While the above strategy focuses on the transport of the underlying diode in order to combat high TDD, this strategy focused on using optical structures in order to combat the deleterious effects of TDD. Work in this section was the result of a combination of a question posed during my candidacy exam, and the COVID-19 pandemic, which removed me from all laboratory activity for ~3 months. The question posed during my candidacy exam in Fall of 2019 was to assess the efficacy of DBRs in $GaAs_{0.75}P_{0.25}$/Si tandem cells and see what potential efficiency gains could be made. While this question resulted in a nice initial exploration more than sufficient for the candidacy examination, there were still holes in the logic and assumptions, which were suboptimal. In Spring 2020, during the Covid-19 pandemic, I had the opportunity to take off my experimentalist hat and put on my theorist hat, albeit just for a short time. Time for a combination of deep thought and Matlab modeling allowed me to flush out the initial exploration that I performed to satisfy the candidacy exam requirements and turn it into what a reviewer noted as a "*sound and well-presented methodology of developing this DBR structure*." This is a paper I am particularly proud of, as it was truly an idea which I personally took from concept through to a paper filled with impactful results with very little oversight.

7.3.1. DBRS IN SOLAR CELLS

The use of epitaxially-integrated distributed Bragg reflectors (DBRs) within III-V multijunction solar cells, typically situated behind subcells with low minority carrier diffusion lengths, is a well-demonstrated method for improving J_{SC} and resilience against various types of crystalline defects (i.e. radiation induced defects, extended defects, etc.)[165]–[171]. In such a structure, the DBR acts as a band reject filter, reflecting wavelengths near the absorption edge of the overlying cell back into the active region of the device while maintaining optical transparency to the longer wavelength photons intended for the subsequent underlying subcells. With this increase in the optical pathlength, a thinner absorber can then be employed, nominally reducing the impact of short minority carrier diffusion lengths. Thus, cell architectures where elevated quantities of threading dislocations result in short diffusion lengths with respect to the physical base thickness, such as in metamorphic III-V top cells in monolithic, epitaxially-integrated III-V/Si tandem solar cells (e.g. $GaAs_{0.75}P_{0.25}$/Si), may find particular benefit from the application of DBRs. This strategy has been previously employed in III-V solar cells for space applications to improve radiation hardness, an analogous case to the low base diffusion lengths caused by elevated TDD. However, the direct application of DBRs to mitigate the impact of elevated threading dislocation densities (TDD) in Si based tandems has yet to be explored.

This work presents the design of $GaAs_{0.75}P_{0.25}$ top cells incorporating DBRs that are realistically constrained by the $GaAs_{0.75}P_{0.25}$/Si materials system and lattice constant. This is performed through the development and application of experimentally-informed analytical modeling. By using existing experimental data obtained from measured $GaAs_{0.75}P_{0.25}$/Si tandem cells that currently do not benefit from DBRs, both the potential efficacy of a DBR in improving the J_{SC} of a $GaAs_{0.75}P_{0.25}$ top cell across a range of TDD values, and the interplay between TDD and optimal base/absorber layer design, can be quantified. This analysis is performed under the hypothesis that, in essence, DBRs should allow for J_{SC} values equivalent to that of a cell with lower TDD, thereby creating an "effective TDD" that is lower than the measured TDD. It is presented herein that indeed this is the case, with a practically achievable DBR structure capable of providing a near 2× reduction in effective TDD.

7.3.2. METHODS

In this work modeling of EQE and IQE allow for both the extraction of transport properties, such as diffusion length, from existing cells, and the projection of cell performance as a function of transport properties and cell design. -In this work we employ a model that relies on two approaches: the optical modeling of internal and external reflectances and the calculation of carrier collection efficiency.

The internal reflectances necessary to accurately calculate photogeneration rate in the active region of the cell were determined via the transfer matrix method (TMM) [137]–[140], allowing for the calculation of the three key optical parameters: T_{Front}, the transmissivity of the layers above the regions of active collection; R_1, the reflectance at the front of the emitter layer with the front optical subsystem (S1); and R_2, the reflectance at the rear of the base layer with the rear optical subsystem (S2). S1 includes the window layer and the optional modeled antireflection coating (ARC) layers, as detailed in further sections. S2 includes the BSF, tunnel junction interconnect (if present), DBR layers (if present), $GaAs_yP_{1-y}$ SGB, substrate and back metal (detailed in Figure 7.14).

Optical constants used in the TMM reflectance and photogeneration calculations were interpolated according to Lumb et al., [128] using previously reported critical points of the $GaAs_yP_{1-y}$,[129] $Ga_xIn_{1-x}P$,[130] and $Al_xIn_{1-x}P$[131] materials systems and optical constants of the constituent binary and/or well-known ternary alloys [129], [132]–[135].

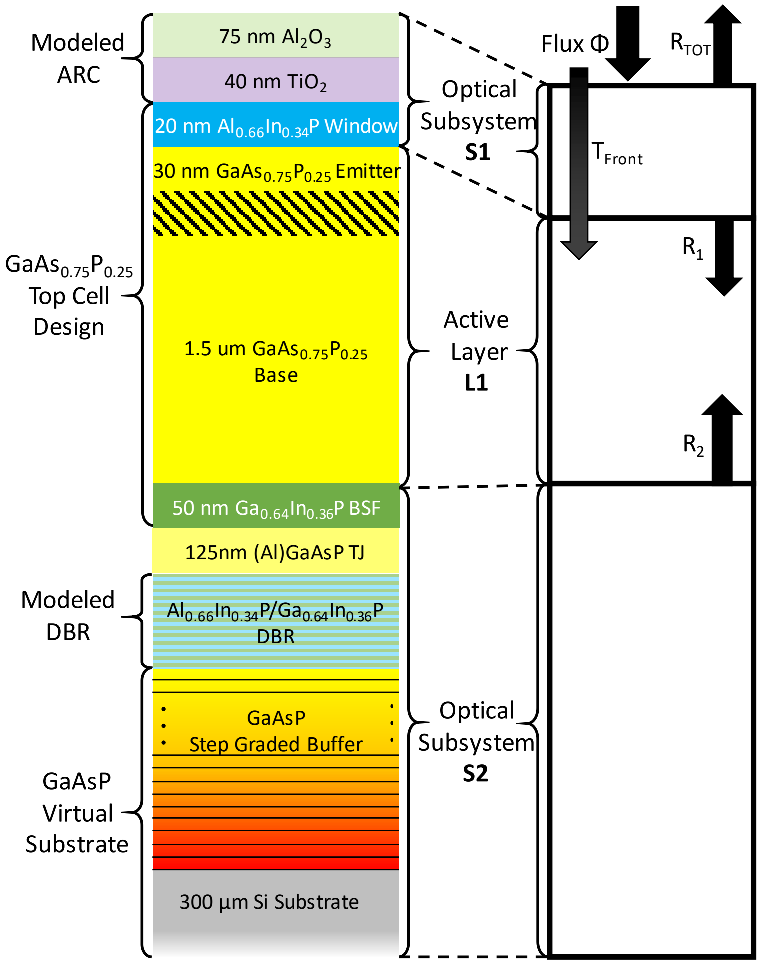

Figure 7.14 Schematic representation of the $GaAs_{0.75}P_{0.25}$ top cell on the high TDD $GaAs_{0.75}P_{0.25}$ virtual substrate. Also depicted is the location of modeled optical structures (ARC and DBR) as they are used in the modeling exploration.

The optical constants of these alloys were tuned according to empirical bandgaps and absorption edges to ensure realistic absorption coefficients near band edge in the $GaAs_{0.75}P_{0.25}$ and $Al_{0.66}In_{0.34}P$ materials, based on methods presented by Kurtz et al. [136].

In order to simplify the analysis, reflections R1 and R2 were assumed to be incoherent. To reduce any error created by this assumption, Al_2O_3/TiO_x bilayer ARCs were also simulated during the predictive modeling of cells with rear reflectors, enabling $R_1 < 3\%$ in the wavelength regions of interest. Thus, the magnitude of the standing wave created by coherent reflections is small and not a significant source of error, as discussed by Lumb et al. [141]. This assumption significantly reduces the computational complexity of subsequent photogenerated carrier collection. R_{Tot}, used in the calculation of IQE, is calculated from the Fresnel coefficients extracted from the scattering matrix of the entire optical system.

The calculation of EQE uses a modified Hovel's model [48], [123] that has been extended to account for incoherent reflectance at the rear and front of the cell. This was first formalized in another work by Lumb et al. [141]. The only deviation from the original model is that instead of using $\Phi_0(1\text{-}R_1)$ as the incident flux to the active region of the cell, where Φ_0 is the AM1.5G flux, $\Phi_0(T_{Front})$ is used. This enables the model to account for absorption losses in layers prior to the emitter, including the window layer and modeled ARC layers. Subsequent calculation of IQE was performed by first calculating EQE via the above approach and then correcting by the total front surface reflectance, R_{Tot}, extracted via the TMM:

$$\mathrm{IQE} = \frac{\mathrm{EQE}}{1-\mathrm{R_{Tot}}} \qquad \text{eq. 7.6}$$

7.3.3. DESIGNING AN ENHANCED BANDWIDTH DBR

To achieve a high peak reflectance and a bandwidth that spans the entire region of significant transmission (500-720 nm), the two materials with the largest difference in index of refraction over the wavelengths of interest should be selected. Nevertheless, to ensure that the target DBR is practical for implementation in a real device, certain

Table 7.6 Interpolated optical parameters for available materials for DBRs.

Material	**Index of Refraction @ 600 nm**	**Index of Refraction @ 700 nm**	**Direct E_g Absorption edge [nm]**
$GaAs_{0.75}P_{0.25}$	3.78	3.63	721
$AlAs_{0.74}P_{0.26}$	3.09	3.01	398
$Ga_{0.64}In_{0.36}P$	3.53	3.33	605
$Al_{0.66}In_{0.34}P$	3.06	2.96	452

constraints were placed upon the design. First, the total DBR thickness must be kept low (< 3 μm). Because of the mismatch in thermal expansion coefficients between the III-V epitaxial layers and the Si substrate, excess III-V thickness can lead to epitaxial cracking or strong wafer bowing. The 3 μm constraint was used based on a maximum total epitaxial thickness limit of 8 μm, which we have experimentally observed to be the point where unavoidable epilayer cracking occurs. Therefore, with a ~1.5 μm thick cell and a 3.5 μm thick SGB (1% misfit/μm), that leaves only 3 μm in which to implement a DBR. Second, the addition of the DBR must not further increase the TDD and thus must be grown internally lattice-matched to the $GaAs_{0.75}P_{0.25}$ top cell and terminal $GaAs_yP_{1-y}$ SGB composition. However, the availability of III-AsP materials that fit this constraint is limited, with only four III-AsP ternary alloys feasible (listed in Table 7.6). This is further constrained by the requirement that the DBR layers be transparent to the flux transmitted by thin $GaAs_{0.75}P_{0.25}$ layers (Figure 7.15). Because it would absorb the near band edge flux intended for reflection, this constraint effectively eliminates the use of $GaAs_{0.75}P_{0.25}$ as a constituent DBR material. Therefore, $Ga_{0.64}In_{0.36}P$ and $Al_{0.66}In_{0.34}P$ are left as the most promising candidates given their relatively wide E_g and largest available delta in refractive index.

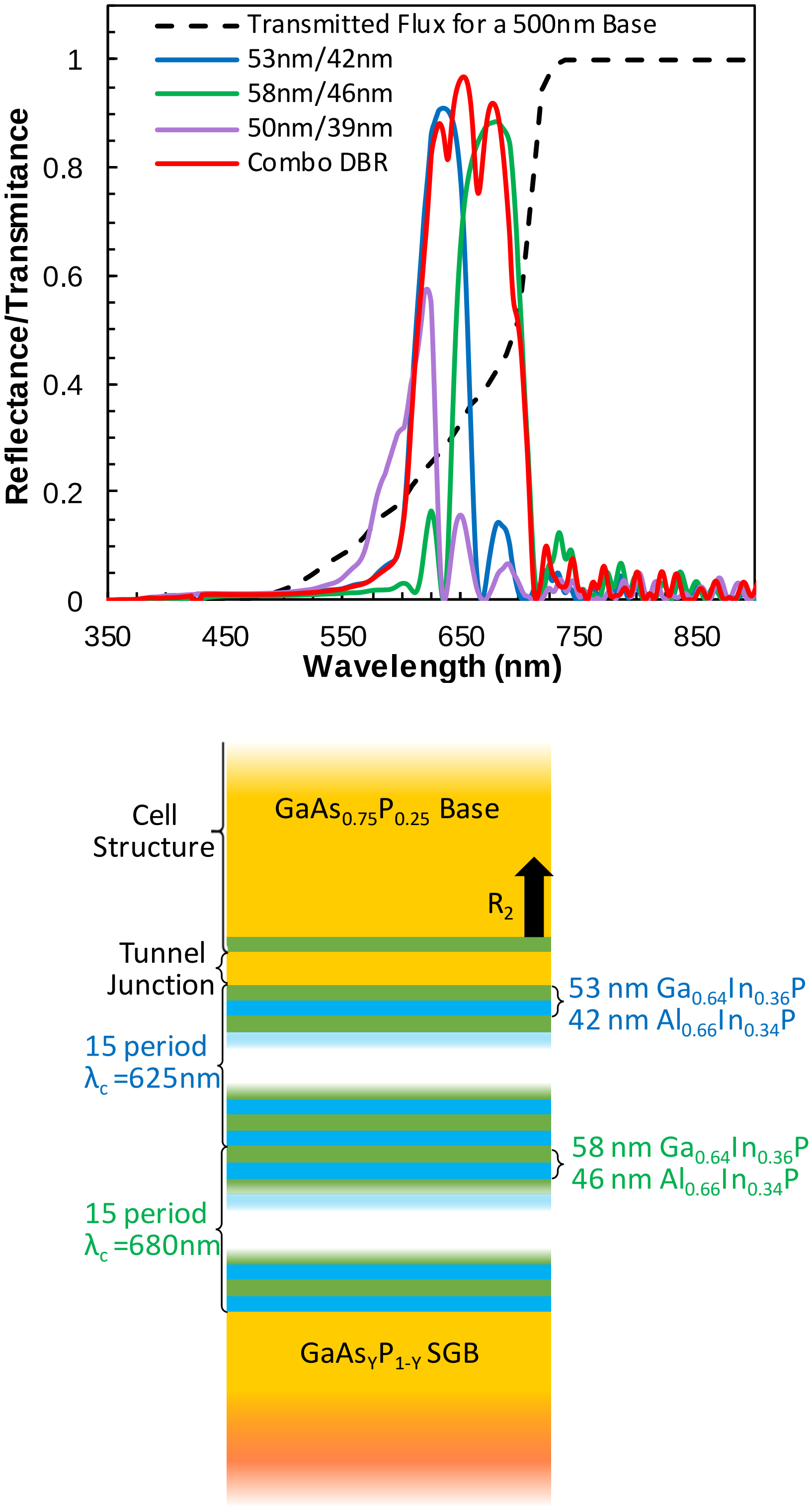

Figure 7.15 a) Reflectance (R_2) of the single wavelength and combo-DBR structures b) Schematic of the combo-DBR structure.

15-period $Al_{0.66}In_{0.34}P/Ga_{0.64}In_{0.36}P$ DBRs were simulated, with center wavelengths of 575 nm, 625 nm, and 680 nm in an attempt to span the region of flux transmission from a 500 nm thick $GaAs_{0.75}P_{0.25}$ base, seen in Figure 7.15a. The simulated DBRs were placed behind the $(Al)GaAs_{0.75}P_{0.25}$ tunnel junction so that they could be *n*-type doped; *n*-type polarity allows for higher doping and mobility, reducing the resistivity of the DBR layers. The reflectance R_2 was calculated using the TMM to quantify the added internal reflectance. While the DBRs that exhibited longer center wavelengths (625 nm and 680 nm) maintained high peak reflectance, the bandwidth (as measured by full width at half max) was only ~50 nm. This is insufficient to span the entire wavelength region of interest. Additionally, the DBR with the shortest central wavelength (575 nm) did not make an effective reflector due to strong absorption of < 600 nm photons by the $Ga_{0.64}In_{0.36}P$ layers (2.05 eV bandgap). It should be noted that alloying Al with $Ga_{0.64}In_{0.36}P$ or $GaAs_{0.75}P_{0.25}$ can raise the direct E_g of the material, thereby reducing parasitic absorption, while maintaining nearly the same lattice constant. However, due to the added uncertainty in optical constants and additional growth complexity of the quaternary $Al_z(Ga_xIn_{1-x})_{1-z}P$ and $Al_xGa_{1-x}As_yP_{1-y}$ alloys, this avenue was not explored in the present work.

Even excluding the capability of reflecting photon flux with wavelengths shorter than 600 nm for the sake of this initial investigation, it is clear that single central wavelength $Al_{0.66}In_{0.34}P/Ga_{0.64}In_{0.36}P$ DBR structures do not possess sufficient bandwidth to provide significant reflectance across the entire 600-720 nm band of transmitted flux (Figure 7.15a). To combat this issue, prior DBR studies for solar applications have used combination DBR (combo-DBR) structures that combine two or more DBRs together for improved bandwidth [172]. This approach is taken in this work, combining two DBRs with central wavelengths of 680 nm and 625 nm in an architecture detailed in Figure 7.15b. The results of this DBR (Figure 7.15a) demonstrate that indeed this structure acts as a sort of superposition of the two DBR structures leading to high reflectance (>70%) across the 600-720nm wavelength band. The central wavelength values for the individual DBRs (625 and 680 nm) were chosen based on a coarse optimization (20-30 nm central wavelength steps) of total reflected flux and are thus likely far from optimal. However, analysis of such a structure provides insight into the potential efficacy DBRs may have in improving performance at various TDD values.

Although a $GaAs_{0.75}P_{0.25}$ top cell with elevated TDD is expected to be the current-limiting subcell by a great margin, assuming a well-designed Si bottom cell, any reflectance in the spectrum intended for the Si bottom cell is a loss mechanism that must still be considered. Reflectance losses in this wavelength band from the introduction of the combo-DBR total 0.26 mA/cm^2, assuming a 100% Si IQE from 720 nm to 950 nm. While this current loss is certainly not negligible, the combo-DBR can likely be redesigned in a manner that further minimizes these reflectance losses. Ultimately, the aim of this particular work is not to design the best possible DBR, but rather to provide a methodology and initial simulation framework to warrant its further experimental exploration.

7.3.4. QUANTIFYING THE IMPACT OF TDD ON J_{SC}

To extract the necessary transport parameters to explore the efficacy of the epitaxial DBR as a function of TDD, the measured IQE curves for the higher-TDD (2×10^{7} cm^{-2}) and lower-TDD (2×10^{6} cm^{-2}) cells were fit using the IQE model described in Chapter 5. This is similar to the analysis done in Chapter 6 but is presented in a slightly different manner here. The experimental data and modeled fits are reiterated in Figure 7.16. Extracted base and emitter diffusion lengths and assumed IRVs are presented in Table 7.7.

Analysis of the experimental IQE curves confirm the expected reduction of the base diffusion length by the observed reduction in long wavelength response. Base diffusion lengths (L_D) of 1.90 μm and 0.825 μm were extracted for the low-TDD and higher-TDD samples respectively. It is critical to note that the emitter diffusion lengths are effectively unchanged by the different TDD values due to the already short values

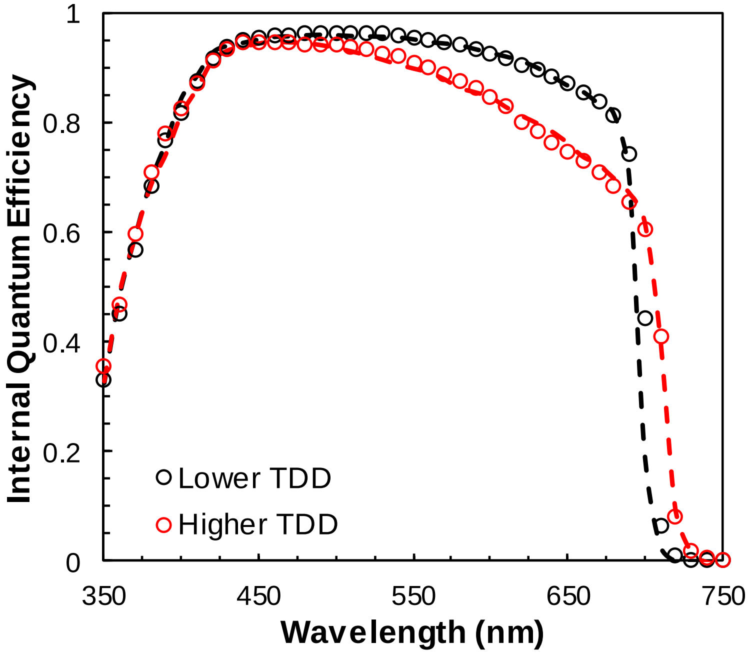

Figure 7.16 Modeled fits to experimental IQE curves which both serve to verify the accuracy of the model and to extract base diffusion length for 2 different TDDs.

Table 7.7 Extracted diffusion lengths from IQE modeling for cells with different TDDs.

Device	Layer	L_D (cm)	D (cm^2/s)	SRV or IRV (cm/s)
Lower TDD	Base	1.9×10^{-4}	54.57	1000
	Emitter	2.25×10^{-6}	3.17	1000
Higher TDD	Base	8.25×10^{-5}	54.57	1000
	Emitter	2.35×10^{-6}	3.17	1000

induced by the higher doping concentration. That is to say, photogenerated minority carriers in the emitter are unlikely to interact with threading dislocations before recombining through other processes.

To quantify the role that elevated TDD has on the short circuit carrier collection dynamics in $GaAs_{0.75}P_{0.25}$ cells and to provide TDD dependent base transport properties, the extracted diffusion lengths were fit to the Yamaguchi model (Figure 7.17):[9].

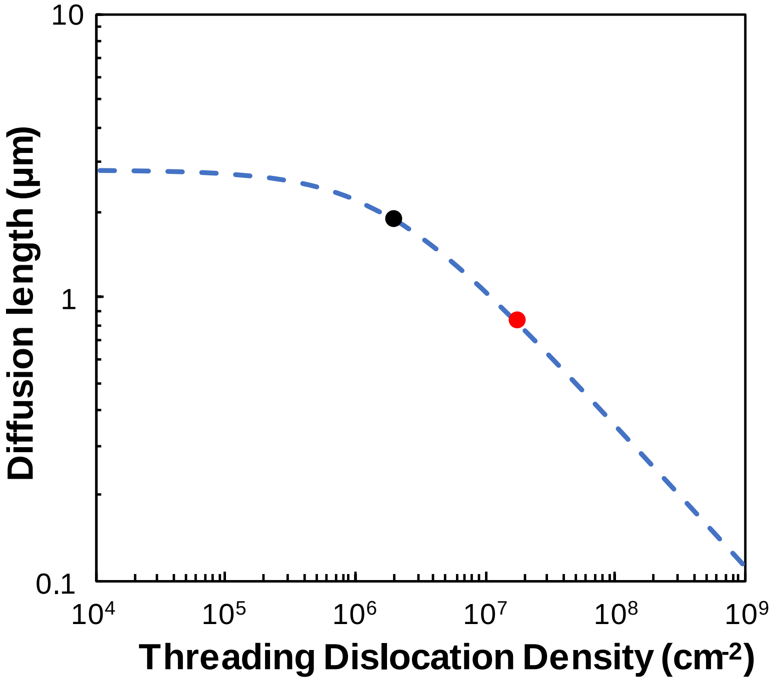

Figure 7.17 Analytical extraction of base L_D as a function of TDD for $GaAs_{0.75}P_{0.25}$ top cells.

$$\frac{1}{L_D^2} = \frac{1}{L^2{}_{D_{Bulk}}} + \frac{\pi^3(TDD)}{4}\,. \qquad \text{eq. 7.7}$$

Here, L_D is the effective diffusion length and $L_{D,bulk}$ is the ideal diffusion length if no dislocations were present. While only two experimental data points for two different TDD values are in hand at present, the strong alignment seen in Fig. 3b does appear to validate this simple model in providing a reasonable methodology for reliably interpolating and/or extrapolating the impact of dislocations on short circuit carrier collection from a limited experimental data set.

Finally, for the sake of simplicity, it is also assumed that diodes with the realistically achievable TDD range explored in this study (1×10^6 cm^{-2} to 1×10^8 cm^{-2}) are likely limited by the depletion region recombination current (J_{02}) due to the relatively wide bandgap (1.72 eV) and defective nature of the top cell [14]. Depletion region recombination current is independent of the base width, meaning that, to first order, the metallurgical base width (W_B) does not impact the I-V characteristics. Additionally, while the work by Yamaguchi et al. in the GaAs material system simulated trends with base doping using empirical fits to prior reports of diffusion length and mobility [9], the lack of similar datasets for $GaAs_{0.75}P_{0.25}$ makes such analysis impossible at present. Therefore, changes to doping were not explored and the primary cell design variable considered in the exploration of DBR structures is W_B.

7.3.5. QUANTIFYING THE IMPACT OF A DBR ON J_{SC}

To truly assess the efficacy of a DBR on cell performance (i.e. J_{SC}), the optimal base design with a DBR must be compared to the optimal base design without one.

Otherwise, these comparisons may be misleading and would overestimate, or underestimate, the effectiveness of such optical structures depending on base thickness. While it would be nearly impossible to perform experimental demonstrations of numerous base widths at every TDD, simulation enables us to examine the role of TDD on DBR performance enhancement. Thus, the $GaAs_{0.75}P_{0.25}$ top cell J_{SC}, calculated by integrating EQE over the AM1.5G spectrum, with the addition of a 45 nm/75 nm TiO_x/Al_2O_3 ARC to suppress coherent reflectance effects, was simulated as a function of W_B using the transport properties from both the lower-TDD and higher-TDD experimental cells (Figure 7.18). In addition to simulating devices without a reflector and with the combo-DBR, an ideal long pass mirror (R = 100% for all wavelengths less than 720 nm and R = 0% for wavelengths longer than 720 nm) was placed behind the cell at the position of R_2 in Figure 7.14. This is, of course, a purely hypothetical construct, as

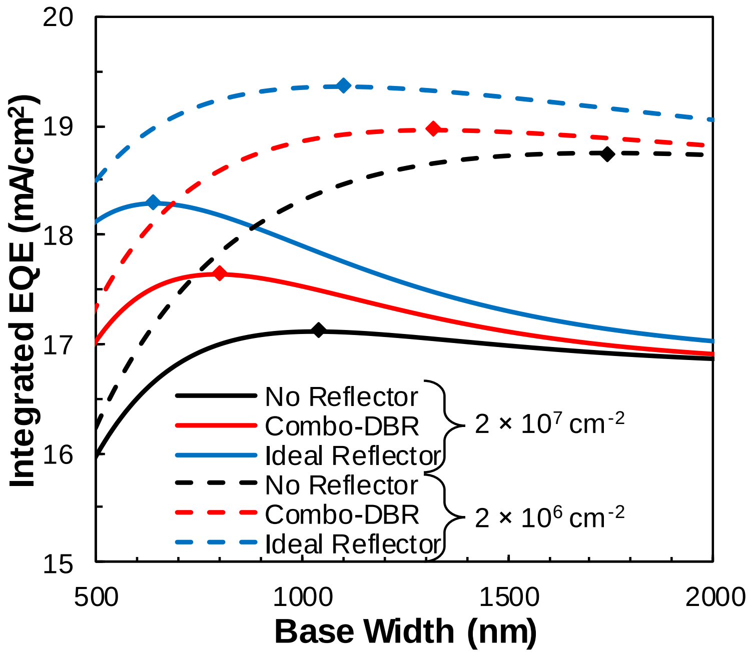

Figure 7.18 Simulated integrated EQE of $GaAs_{0.75}P_{0.25}$ cell designs with a combo-DBR, an ideal reflector, and without any reflector. This simulation was performed at the two experimentally demonstrated TDDs.

there is no method to epitaxially integrate an ideal 100% in-band reflector while maintaining the high transmissivity required in the spectrum intended for the Si bottom cell. However, analysis of this ideal case provides an upper limit to the potential gains enabled by a DBR behind the $GaAs_{0.75}P_{0.25}$ cell.

On first analysis of Figure 7.18, there are two strong trends observed by the addition of a rear reflector. First, the maximum obtainable J_{SC} is improved, as hypothesized. Second, the base width that provides optimal short circuit performance is significantly reduced. These results can be rationalized by the tradeoffs present between optical absorption and collection probability. If the optical path length is improved through the use of a DBR, the base can be made much thinner, thereby improving the diffusion length to base width ratio (L_D/W_B). A higher L_D/W_B improves the probability of collecting a photogenerated carrier and thereby increases the current for a constant photogeneration rate. While the general shortening of the base, and the improvement in optimal J_{SC} are present at both 2×10^7 cm^{-2} and 2×10^6 cm^{-2} TDD, the optimal base designs are quite different.

At a TDD of 2×10^7 cm^{-2} (solid lines in Figure 7.18), the combo-DBR provides a short circuit current improvement of 0.51 mA/cm^2 with a 240 nm reduction in ideal base length. The ideal reflector places a ceiling on the improvement given by a rear reflector for this TDD at 1.17 mA/cm^2 and enables a 400 nm base width reduction. While such a direct comparison of the combo-DBR to the ideal reflector is not necessarily a fair comparison, as an ideal reflector is indeed not realistic, it does elucidate the fact that there are areas for improvement in the design of the relatively unoptimized combo-DBR.

To examine this, the EQE of the 3 cells with optimal base designs (denoted by the diamonds) were compared (Figure 7. 19a). The combo-DBR indeed improves the long wavelength response of the cell with a near superposition of the shape of the DBR, on top of the existing EQE curve. However, the lack of reflection in the 500 nm to 600 nm wavelength band maintains a high degree of transmissivity in that wavelength regime as the base is thinned. As such, the ideal base width for the combo-DBR device is ~20% longer than with the ideal reflector. If a DBR with broadband response expanded to cover the 500-600 nm wavelength range could be designed, it would significantly improve the DBR efficacy at elevated TDDs leading to current improvements approaching values provided by the ideal reflector (1.17 mA/cm^2). While this would indeed be a challenge given the limited materials availability, the quaternary $Al_xGa_{1-x}As_yP_{1-y}$ and $Al_z(Ga_xIn_{1-x})_{1-z}P$ alloys, which possess greater than the necessary 2.2 eV direct E_g needed to minimize absorption, may provide a pathway. However, uncertainty in the optical data of these alloys prevented the exploration of these materials in this work. Even with the non-idealities in the DBR design used in this work the application of this design in a $GaAs_{0.75}P_{0.25}$/Si tandem cell could result in AM1.5G absolute efficiency improvements of 0.7%, using V_{OC} and fill factors from the authors' previous $GaAs_{0.75}P_{0.25}$/Si tandem reports [12]. With improved reflectance response in the 500-600 nm wavelength range, the absolute efficiency improvement could approach an aspirational value of nearly 1.6%.

In the lower-TDD case (dashed lines in Figure 7.18), the combo DBR provides a 0.22 mA/cm^2 improvement with a 420 nm base width reduction, while the ideal reflector provides a 0.61 mA/cm^2 J_{SC} improvement and a 640 nm base width reduction. The DBR would result in a ~0.3% absolute efficiency improvement, assuming a 1.8 V V_{OC} and 83%

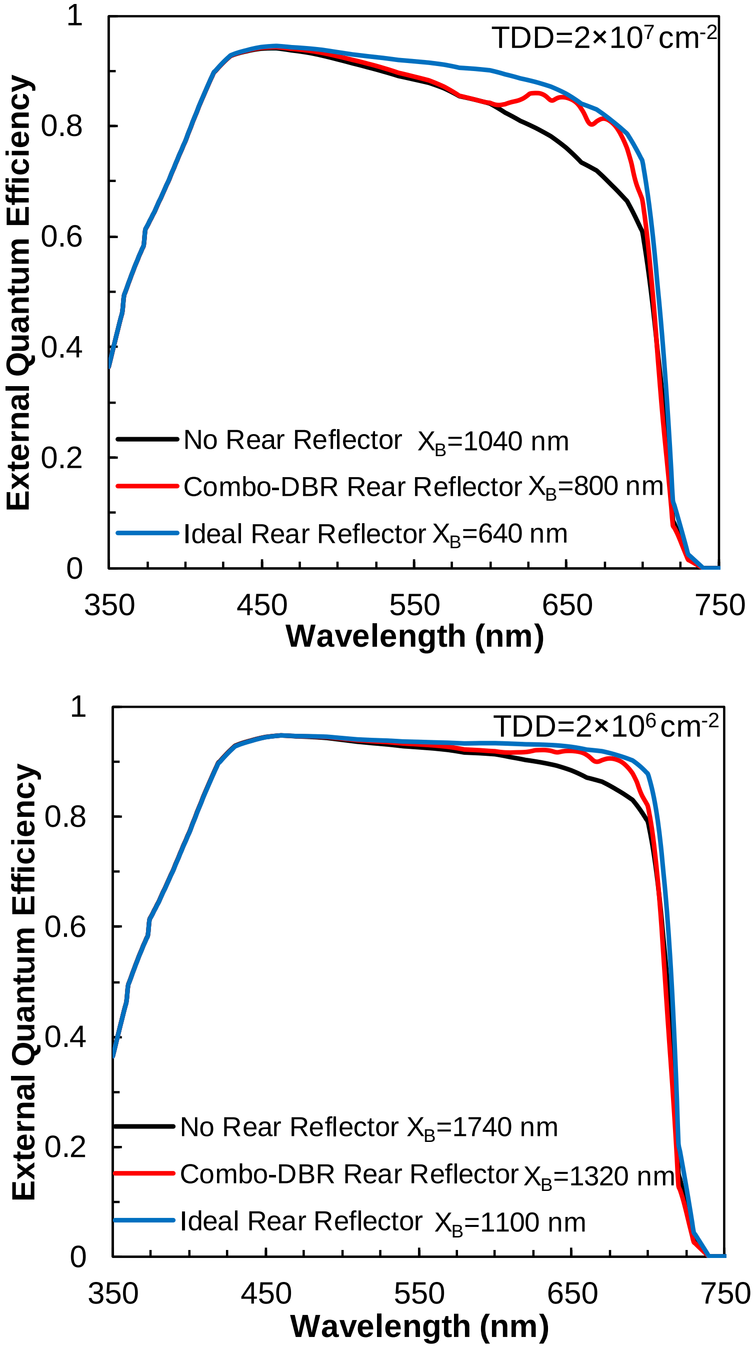

Figure 7. 19 a) EQE Simulations for $GaAs_{0.75}P_{0.25}$ cells at a constant TDD = 2×10^{7} cm^{-2} value comparing use of a combo-DBR, an ideal reflector, and without any reflector, with the base thickness optimized for each case. b) Similar EQE simulations as b except at a lower TDD value of 2×10^{6} cm^{-2}.

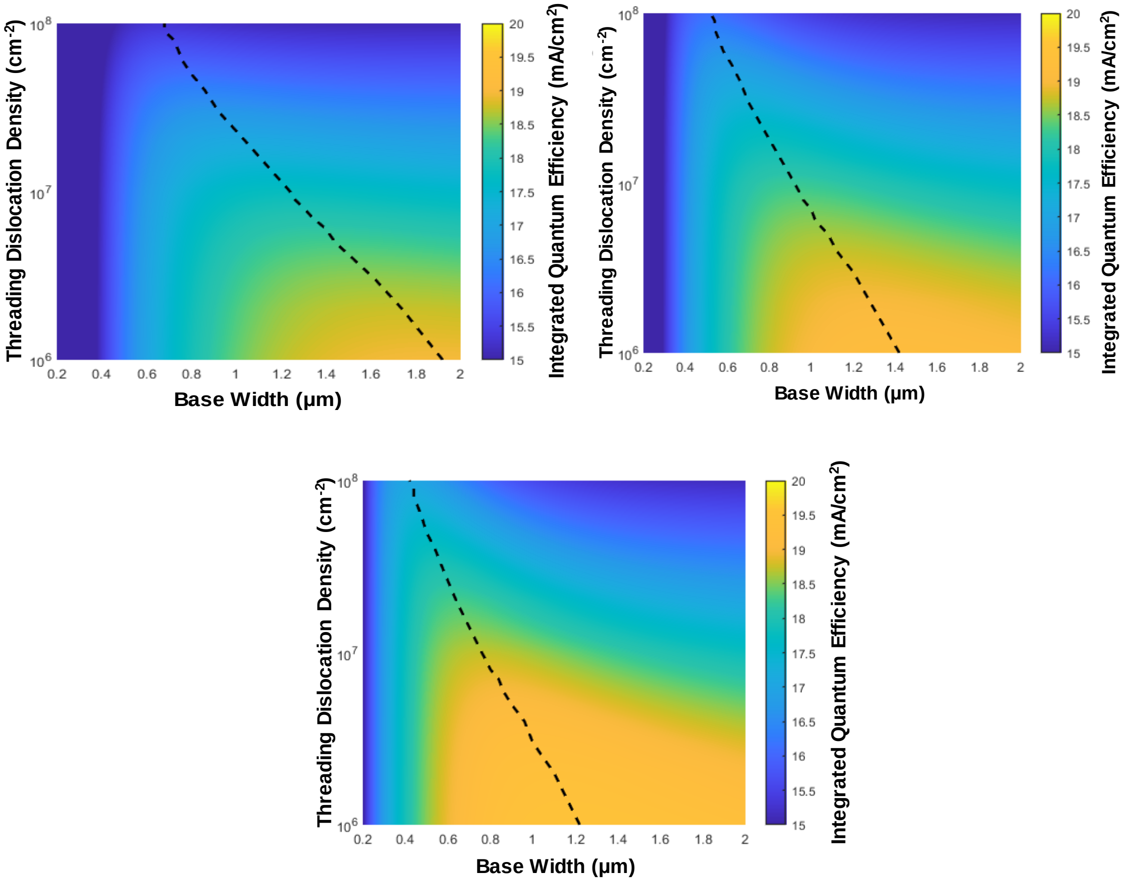

Figure 7.20 a) Simulated integrated EQE as a function of TDD and base width for a $GaAs_{0.75}P_{0.25}$ cell with no rear reflector. Dashed lines show the optimal base width as a function of TDD. b) Simulated integrated EQE as a function of TDD and base width for a $GaAs_{0.75}P_{0.25}$ cell with a combination DBR. Dashed lines show the optimal base width as a function of TDD. c) Simulated integrated EQE as a function of TDD and base width for a $GaAs_{0.75}P_{0.25}$ cell with an ideal reflector. Dashed lines show the optimal base width as a function of TDD.

fill factor (FF) with an absolute efficiency improvement ceiling of 0.91%. These V_{OC} and FF values were conservative estimates based on the authors' previous reports of $GaAs_{0.75}P_{0.25}$ top cells at this TDD [11], [12], [14] and simulation of the optimal Si bottom cell design. These analyses of potential efficiency improvements are conservative as it doesn't include optimizations to doping profiles or emitter design, which have the potential to improve V_{OC}, especially in the case of reduced base width.

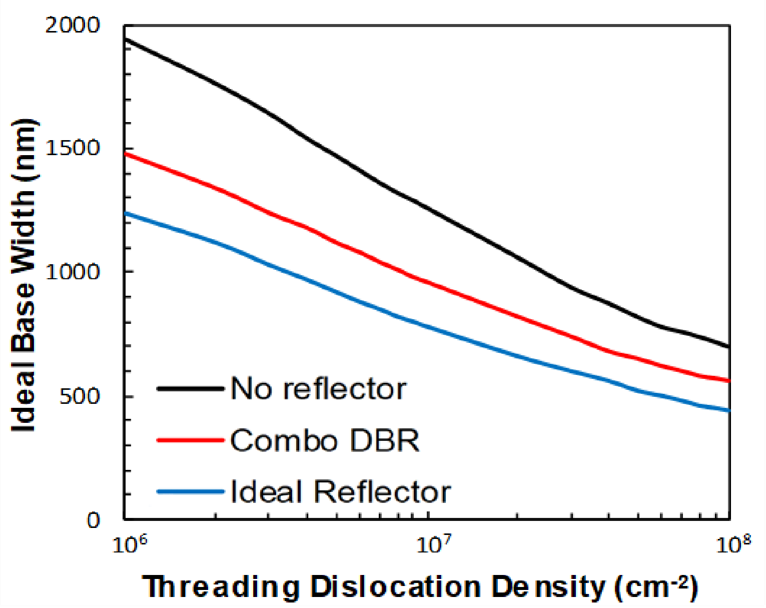

Figure 7.21 Optimal base width as a function of TDD for cell designs with a combo-DBR, an ideal reflector, and without any reflector.

To provide better insight into the efficacy of a DBR as a general function of TDD, cells with no reflector (Figure 7.20a), combo-DBR (Figure 7.20b), and an ideal reflector (Figure 7.20c) were simulated using TDD dependent transport properties and a range of W_B, thereby enabling extraction of optimal performance and design as a function of both TDD and base design. The dashed lines indicate the ideal base width for each TDD value, providing the TDD-specific optimal design. The intuitive basis for the shape of the contour plots in Figure 7.20 again details the tradeoff between optical absorption and carrier collection. This phenomenon is observed with the region to the left of the dashed line (thinner than ideal base), where transmission is too high, and to the right (thicker than ideal base) where insufficient L_D yields reduced collection probability. The optimal W_B are plotted as a function of TDD (Figure 7.21). Just as observed in the discrete TDD points explored previously, the optimal base width is significantly reduced with elevated

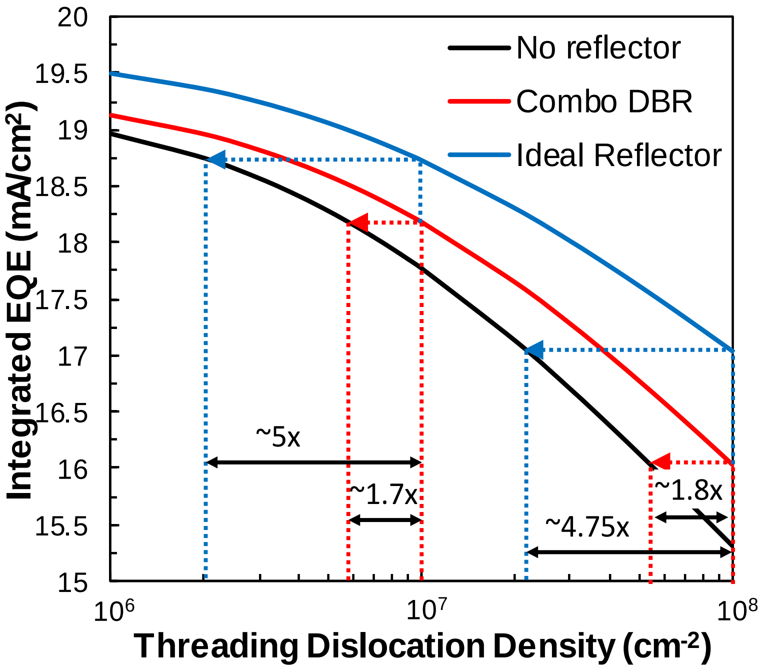

Figure 7.22 Simulated maximum achievable integrated EQE as a function of TDD for cell designs with a combo-DBR, an ideal reflector, and without any reflector. Arrows are drawn to indicate the effective reduction in TDD.

TDD and the addition of a rear reflector. It is interesting to note that the percent reduction in W_B between the optimal design without a reflector and with a reflector is nearly constant as a function of TDD with the ideal reflector allowing a 36-38% reduction in W_B and the combo DBR allowing a 20-24% reduction.

With the optimal base width at every TDD in hand, the performance of cells with these optimized designs as a function of TDD can be plotted, providing a convenient direct comparison of performance improvement with the addition of a realistic DBR or an idealized rear reflector (Figure 7.22). This figure can be used to roughly estimate the defect mitigation of the DBR, quantified as an equivalent reduction in TDD (i.e. the reduction of TDD necessary to achieve the same J_{SC} without a rear reflector). The equivalent TDD reduction of ~1.8× provided by the DBR clearly demonstrates that this design is an effective way to provide a significant degree of resilience to elevated TDD. Notably, the ideal reflector provides an aspirational effective TDD reduction of nearly 5×, which points to the potential of the DBR as an extremely effective method to mitigate the impact of elevated TDD if the combo-DBR design could be improved in the 500-600 nm wavelength band, as discussed previously.

7.4. CONCLUSIONS

With the glaring challenge of TDD induced performance losses being the primary limiter of $GaAs_{0.75}P_{0.25}$/Si tandem solar cells at present, methods to reduce the impact of the resident TDD on maximum achievable device performance is paramount to achieve the highest efficiencies. The methods explored in this chapter provide methods to improve BOTH critical device performance metrics, J_{SC} and V_{OC}. Additionally, these strategies were explored with a forward-looking lens, looking at lower values of residual TDD than is currently available on the Si platform and quantifying how TDD directly impacts optimal cell design (for the case of the DBR). While challenges remain to implement the DBR experimentally and to improve the J_{SC} of the rear-emitter design, the progress made during my tenure at OSU amounts to critical advances towards the ultimate goal of TDD resilient and/or defect tolerant designs necessary to achieve >30% efficient tandems. Beyond the scope of $GaAs_{0.75}P_{0.25}$/Si tandems, the work in this chapter maintains broad applicability to many III-V materials systems especially in the case of metamorphic materials systems.

CHAPTER 8:

TOWARDS LOW TDD GAAS$_{0.75}$P$_{0.25}$/SI VIRTUAL SUBSTRATES

8.1. INTRODUCTION

As discussed extensively thus far, reducing the residual TDD in the GaAs$_{0.75}$P$_{0.25}$ top cell is *the* critical step of materials improvement towards achieving high efficiency GaAs$_{0.75}$P$_{0.25}$/Si tandems and ultimately breaking the single junction efficiency barrier. Dislocations are line defects or missing rows of atoms that act as the mechanism for strain relief in lattice mismatched epitaxial growth. Thus, a certain quantity of dislocations is necessary in order to relax lattice mismatched epitaxial layers. However, minimizing excess TDD in these films is required as TDD strongly reduces optoelectronic device performance. A more rigorous discussion on fundamentals of dislocation formation and motion is found in Chapter 3, with discussion of their direct impact on solar cell performance discussed in Chapter 5,6, and 7. This work occurred in parallel with that which has been described here in prior chapters, and thus its implementation for future solar cell applications is part of ongoing and near-term future work.

The work presented in this chapter was a collaborative effort within our research group, but was primarily a joint effort between Dr. Jacob Boyer and myself. This chapter serves to act as a summary of the immense technical depth and exploration present in both the papers and dissertation by Dr. Boyer. Instead of a rigorous deep dive into the materials science, this chapter will only focus on the results of epitaxial design changes that had a meaningful impact on residual TDD in both GaP and $GaAs_yP_{1-y}$ layers. This will hopefully simplify the discussion surrounding this very complex materials growth problem, and allow for a more approachable understanding for those in the electrical engineering and device design disciplines.

It will begin with a general outline of the epitaxial growth process, and identification of critical variables present in the growth of $GaAs_yP_{1-y}$ virtual substrates. Then focus on key areas that enabled critical reductions in TDD, ultimately resulting in TDD of ~3×10^6 cm^{-2} in Si-based $GaAs_{0.75}P_{0.25}$ virtual substrates, nearly 10× lower than the state of the art at the beginning of my Ph.D. tenure.

8.2. OUTLINE OF THE $GaAs_{0.75}P_{0.25}$ VIRTUAL SUBSTRATE GROWTH PROCESS

A generalized flowchart of the $GaAs_{0.75}P_{0.25}$ growth process is shown in Figure 8.. The growth process begins with a rigorously cleaned and nearly atomically smooth offcut Si wafer. Offcuts typically range from 2°-6° towards the nearest <111>. This wafer is chemically cleaned with an $HF\rightarrow H_2SO_4:H_2O_2\rightarrow HF$ process that leaves a hydrogen terminated surface and minimal organic content on the surface. The wafer is then loaded in to the MOCVD where any residual oxide is removed at 750 °C under a dilute SiH_4 flow to promote double height stepping (necessary to minimize antiphase domains as

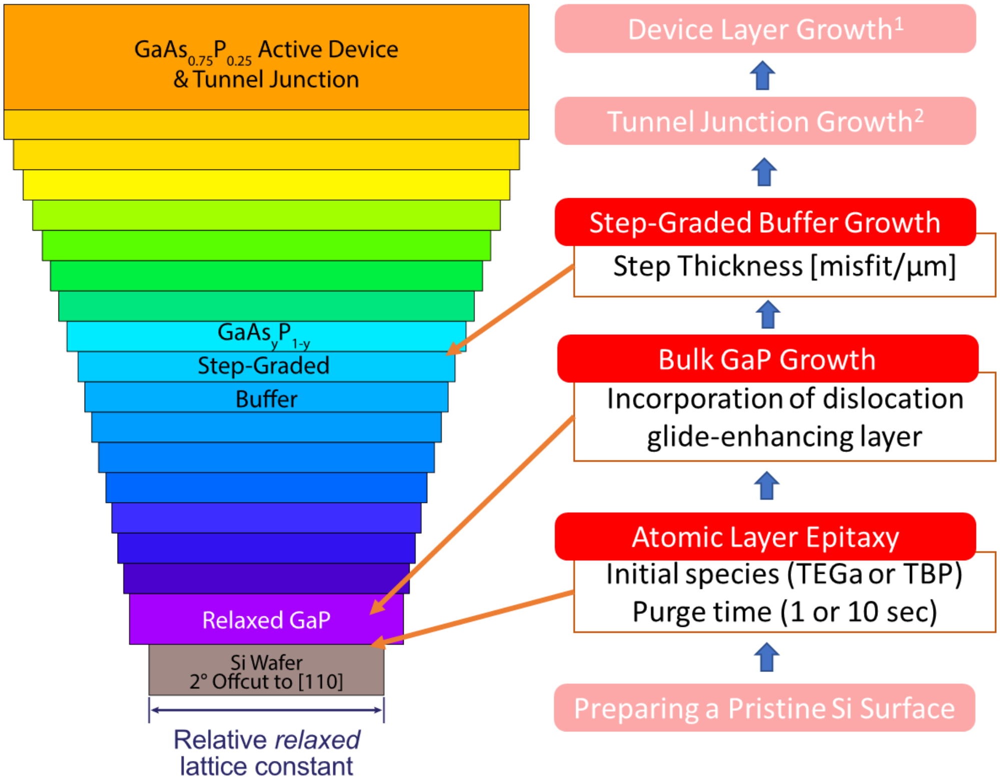

Figure 8.1 Schematic identifying the steps and critical variable for the growth of the GaAs$_{0.75}$P$_{0.25}$ virtual substrate. Figure used with permission from Dr. Boyer.

discussed in Chapter 3). The additional Si adatoms and atomic hydrogen is theorized to promote the double height step surface reconstruction [43], [74], [80].

The Si wafer temperature is then reduced to ~450 °C in order to grow the GaP seed layer via a technique called atomic layer epitaxy. Atomic layer epitaxy (referred to as migration enhanced epitaxy in MBE) [75], [173]–[175] is a similar concept to atomic layer deposition (discussed very briefly in Chapter 3) except the reaction is not self-limiting. Still, it follows the same principle where one precursor is pulsed into the chamber, allowed to react, then pumped out. This is followed by the same procedure for the second precursor. The precursors used in the ALE growth of GaP are Triethylgallium

(TEGa) and Tertbutylphosphine (TBP). The sequencing, pulse time, and purge time are critical in determining the epitaxial quality of the GaP seed layer.

Next wafer temperature is increased to between 550-700 °C where the remainder of the GaP nucleation layer is grown. The dislocation dynamics are sensitive to the growth temperature during this step and has been an area of exploration especially by the group at UIUC [176], [177]. This layer ranges from 30 nm to 100 nm with recent results finding that growing thinner may help to protect the reactor from contamination in subsequent growths. The initial GaP/Si template growth is very sensitive to the Si surface quality and cleanliness, which is disrupted by residual Group V elements in the chamber during oxide desorption. Therefore, a Si coating growth is performed in between GaP nucleation template growths to bury residual Group V elements. These thin GaP/Si templates are then removed from the MOCVD and left in an inert environment.

Using a different susceptor and glassware, to maintain the clean environment for the GaP nucleation process, the thin GaP templates are loaded back into the reactor where subsequent bulk GaP growth takes place. Total GaP thickness is usually targeted around 500 nm to ensure the film is mostly relaxed and that minimal further dislocation evolution at the GaP/Si interface is necessary during the step graded buffer (SGB) growth. Dislocation dynamics during this portion of the growth are highly critical as slow glide velocity and/or rampant nucleation are the primary causes of high residual TDD in the $GaAs_{0.75}P_{0.25}$ top cell [86]–[88], [145]. TDDs in excess of 4×10^{7} cm^{-2} were common at the beginning of my tenure and reduction down to 2×10^{6} cm^{-2} was achieved through careful epitaxial design and the implementation of a superlattice structure to enhance glide velocity discussed later in this chapter [145].

Lastly the $GaAs_yP_{1-y}$ step graded buffer (SGB) is grown. This structure uses discrete layers with 3.5 at.% As steps in order to slowly transition the lattice constant to that of the desired $GaAs_{0.75}P_{0.25}$ alloy. The SGB is terminated with a thicker terminal layer slightly overshot in composition (77 at.% As) in order to promote complete relaxation. The most critical design aspect of the $GaAs_yP_{1-y}$ SGB is to minimize thickness without increasing the TDD. Therefore, the highest possible grading rate (denoted in % misfit/μm) that does not result in increased TDD should be used. After the terminal layer of the SGB the entire stack can be treated as a virtual substrate where no further dislocation evolution or film relaxation is expected during subsequent top cell or tunnel junction growth.

8.3. OPTIMIZATION OF THE ALE NUCLEATION LAYER

A schematic detailing of the ALE growth process is shown in Figure 8.2. Over the many years of research on MOCVD-grown GaP layers on Si at OSU, many knobs have been tuned with respect to the ALE parameters: temperature, dose, etc. [3], [178]. Fine tuning of most of these parameters resulted in very minor changes to TDD, and TDD below 10^7 cm^{-2} was not achievable at thicknesses significantly beyond critical thickness (>50 nm). However, two critical variables had been overlooked until recently: the purge time in between precursor pulses and the initial precursor species. These variables ended up having a tremendous impact on the dislocation population and dislocation glide/nucleation dynamics.

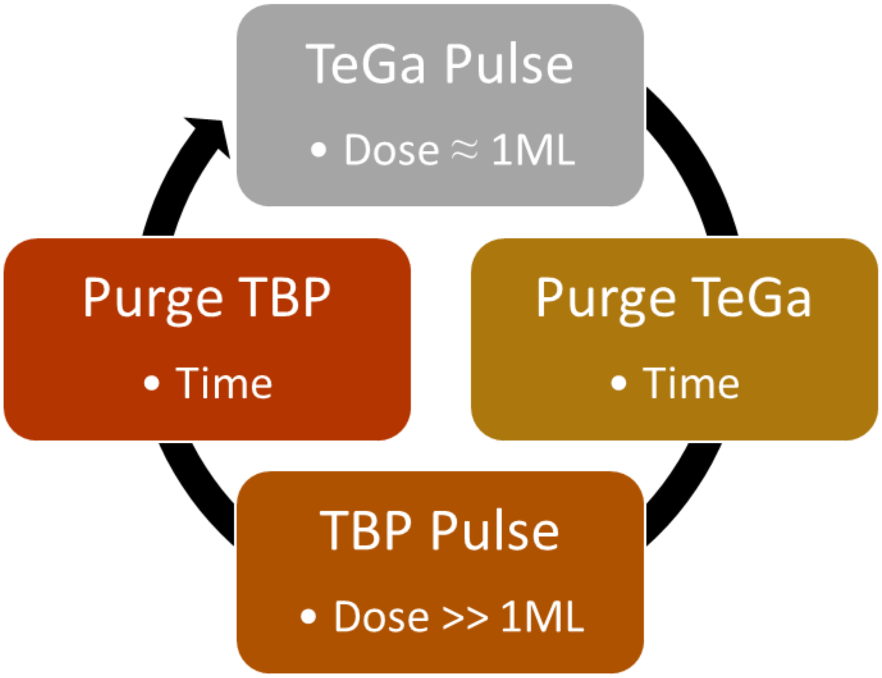

Figure 8.2 Flow chart detailing the GaP ALE growth process with critical variable of the steps listed in bullets.

Figure 8.3 shows ECCI images which detail the changes made to the ALE process for a 100 nm thick GaP layer grown on Si in order to observe the dislocation population. The legacy recipe used a Ga-first precursor sequence with a 1 sec purge time. Increasing the purge time to 10 sec resulted in a substantial increase in misfit dislocation length indicating improved glide velocities as well as a substantial reduction in dislocation nucleation rate. This change resulted in a ~5× reduction in TDD in thin 100 nm layers. This drastic reduction in TDD and change in dislocation population distribution is ostensibly due to improved seed layer quality and a reduction of what seemed to be a break down in layer by layer growth during the ALE growth. The excess concentrations of residual precursor remaining in the chamber probably allowed for parasitic precursor reactions and subsequent nonideal GaP growth. Increasing the purge time allowed for

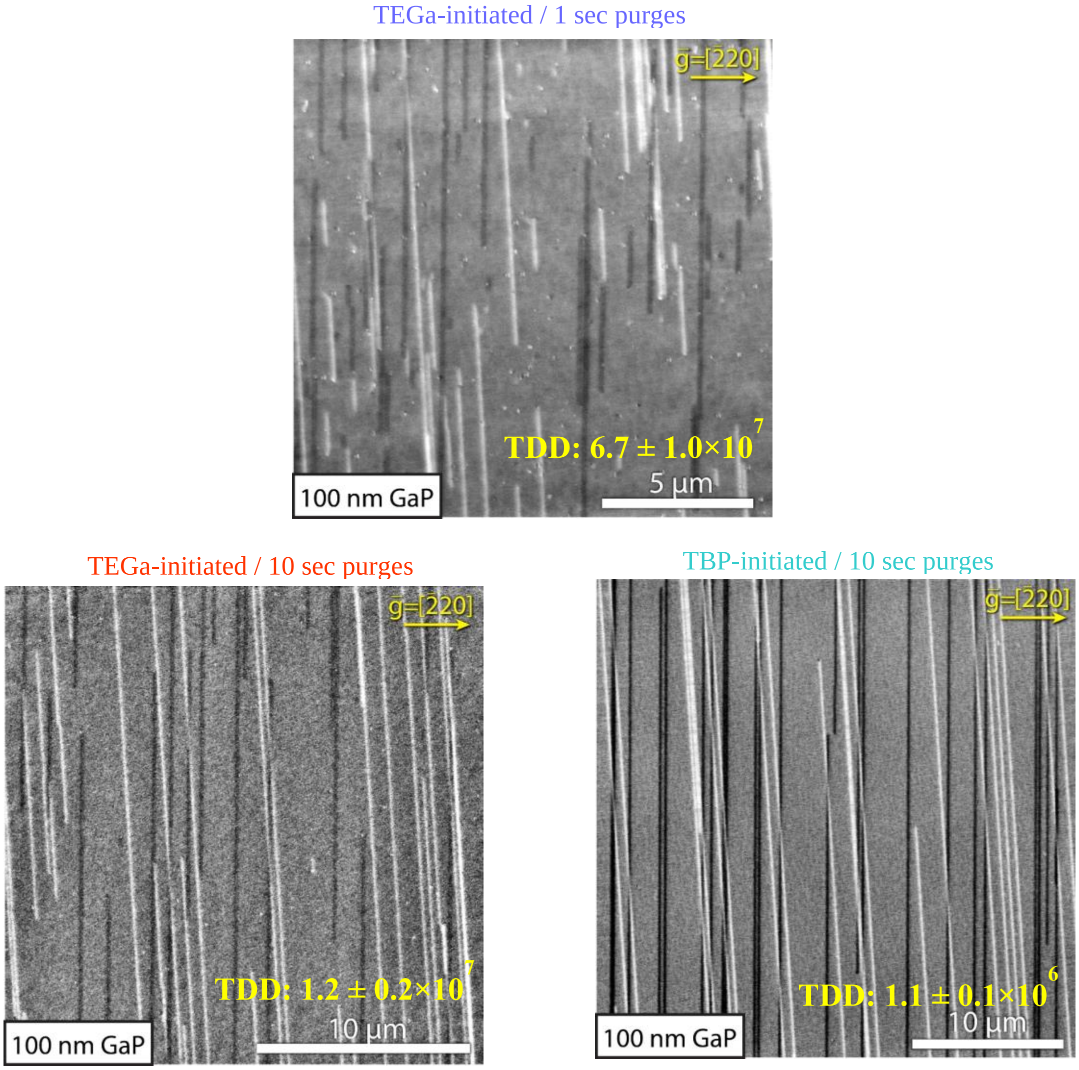

Figure 8.3 ECCI micrographs of MD content in 100 nm GaP/Si films, comparing (a) TEGa-initiated / 1 sec purge time, (b) TEGa-initiated / 10 sec purge time, and (c) TBP-initiated / 10 sec purge time. ECCI micrographs used with permission from Dr. Boyer.

proper removal of the prior precursor species and a return to proper ALE type growth modes. In hindsight, this was an obvious oversight as the pump/flow rates never could have removed the residual precursor in the 1 second time allotted.

The second change was a switch in the initial precursor from TEGa to TBP resulting in an additional 10× reduction in TDD. The mechanism for why this was so effective is less clear as etch pit measurements indicate that the films are still Ga polar which means that the initial species on the Si surface is still Ga. Therefore, it is possible that the initial TBP pulse may be acting to remove contaminants or residual native oxide similar to self-cleaning processes in ALD [179], [180]. This has not been confirmed, but this epitaxial design change clearly made a meaningful impact on initial film quality and reduced the quantity of pyramidal stacking faults. Nonetheless it resulted in TDD of ~1×10^6 cm^{-2} in 100 nm thick GaP layers, an impressive reduction from the 6×10^7 cm^{-2} starting point from the legacy process.

8.4. REDUCTION OF TDD IN BULK GAP GROWTH

While the above TDD reduction in thin 100 nm GaP films was an encouraging and necessary breakthrough, it did not entirely solve the issue of elevated TDD in fully relaxed GaP films. The necessary thicker GaP overgrowth still resulted in nearly identical

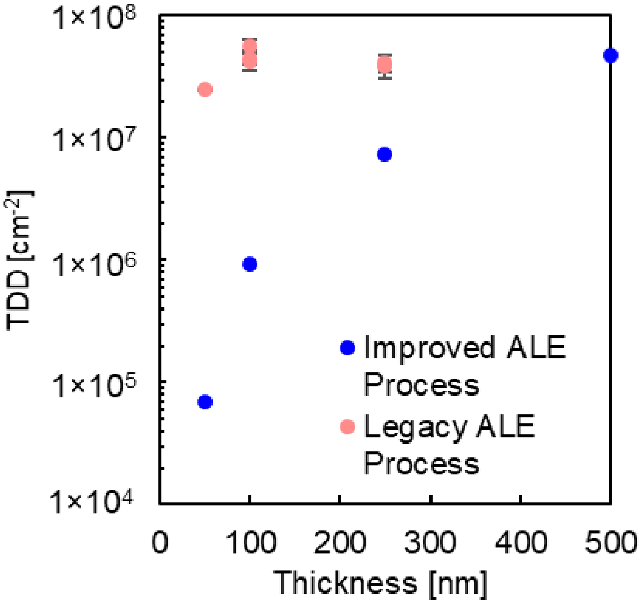

Figure 8.4 Comparison of TDD as a function of thickness between the legacy ALE nucleation process and the improved process. Figure used with permission from Dr. Boyer.

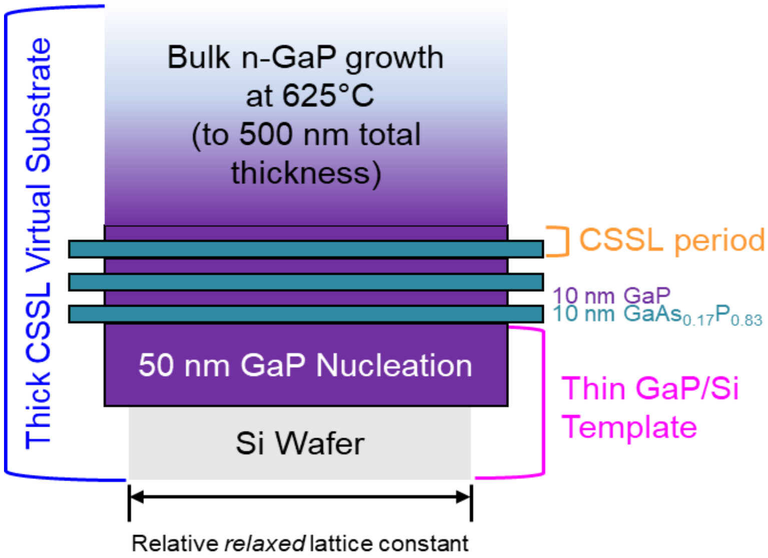

Figure 8.5 Schematic diagram of the CSS structure. Approximate lattice constant differences (not to scale) are depicted with the width of each material layer. Figure used with permission from Dr. Boyer.

TDD to the legacy process at >3×10^7 cm^{-2}. This is shown in the TDD vs thickness plot in Figure 8.4. This continued nucleation during subsequent overgrowth points to low glide velocities in the GaP layers. The continued nucleation indicates that the rate of removal of excess stress is not fast enough with the reduced population of dislocations (i.e. lower TDD). Therefore, the film nucleates new dislocation loops in order to make up for this deficiency. This indicates that the glide velocities of the dislocation loops are clearly not high enough to remove the stress without nucleating new dislocation loops. A method is needed for increasing the glide velocities of the existing dislocation population so the nucleation of new dislocations can be suppressed.

A glide-enhancing superlattice structure was used in order to hopefully increase glide velocities and thus aid in removal of excess stress without additional nucleation. This structure is detailed in Figure 8.5. This compressively strained superlattice layer (CSS) was placed just after the onset of dislocation nucleation at 50 nm from the GaP/Si

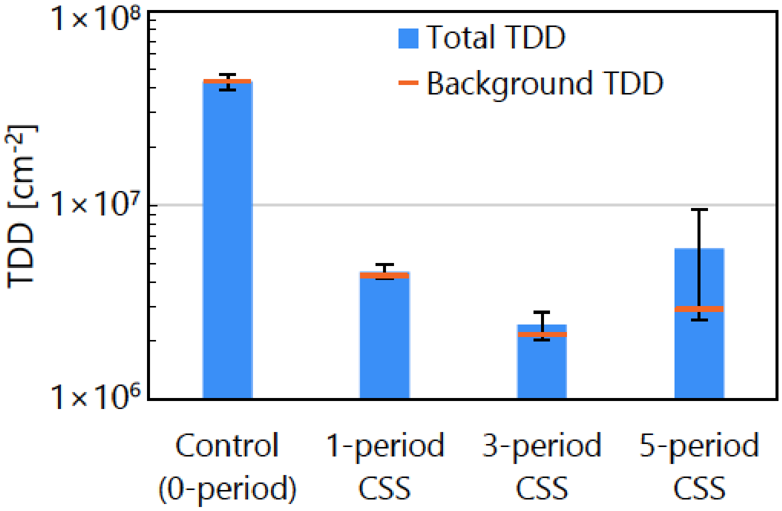

Figure 8.6 Total TDD and background TDD extracted from ECCI micrographs for all CSS structures and control. Figures used with permission from Dr. Boyer.

interface. The larger lattice constant of the $GaAs_{0.17}P_{0.83}$ layers in the super lattice create regions of high localized strain, but the total strain energy in the film remains low because the $GaAs_{0.17}P_{0.83}$ layers are thin (below critical thickness). Stepping back to GaP, rather than growing thick layers of $GaAs_{0.17}P_{0.83}$, this maintains a lower degree of excess stress and therefore keeps the total strain energy lower than the kinetic barrier for rapid nucleation. However, it is theorized that the regions of localized strain act to increase glide velocity because the local driving force for glide in these regions is enhanced. $GaAs_{0.17}P_{0.83}$ was chosen as the composition in the super lattice because it is the lowest feasible AsH_3 flow at the desired growth temperature of 600 °C.

CSS structures with 1×, 3×, and 5× periods were explored, followed by a n-type GaP overgrowth to 500 nm total III-V thickness. Additionally, these were compared to a control sample of 500 nm GaP with no CSS grown on the same 50 nm thin GaP templates fabricated using the improved ALE process. Results of this study are shown in

Figure 8.6 and are immediately impressive. Even with the addition of a single period of $GaAs_{0.17}P_{0.83}$ the TDD was reduced with TDD down to 5×10^{6} cm^{-2}. Moving to 3 periods, a minimum in TDD of ~2×10^{6} cm^{-2} was achieved. Increasing further to 5 periods saw an increase in total TDD caused mainly by an increase in pileup density. The reason for these pileups is still under exploration and further examination of this structure can be seen in the papers and thesis by Dr. Jacob Boyer. Nonetheless, the above results in this section and the prior, have enabled a ~20× reduction in TDD down to extraordinary values, as low as ~2×10^{6} cm^{-2} for fully relaxed n-type GaP films on Si.

8.5. REALIZATION OF LOW TDD $GAAS_{0.75}P_{0.25}$ VIRTUAL SUBSTRATES

After optimization of the GaP nucleation layer and subsequent overgrowth, the SGB was explored with a primary focus on thickness reduction and optical transparency. The SGB in the legacy virtual substrate was grown at a grading rate of ~0.5% misfit/μm. All SGBs in this study are grown with 22 individual steps separated by 3.5 at% As. The growth temperature starts at 725 °C but is reduced to 675 °C at the ~50% As step. This was done historically to reduce observed dislocation pileups. The terminal layer at 77% As is grown thicker (500 nm) in order to promote complete relaxation.

The legacy SGB resulted in a thickness of ~6 μm and an entire 2J epitaxial stack thickness exceeding 8 μm. These thicknesses led to a large degree of wafer bowing and epitaxial cracking during post-growth fabrication due to the mismatch in thermal expansion coefficients between the substrate and III-V epilayers [181], [182].

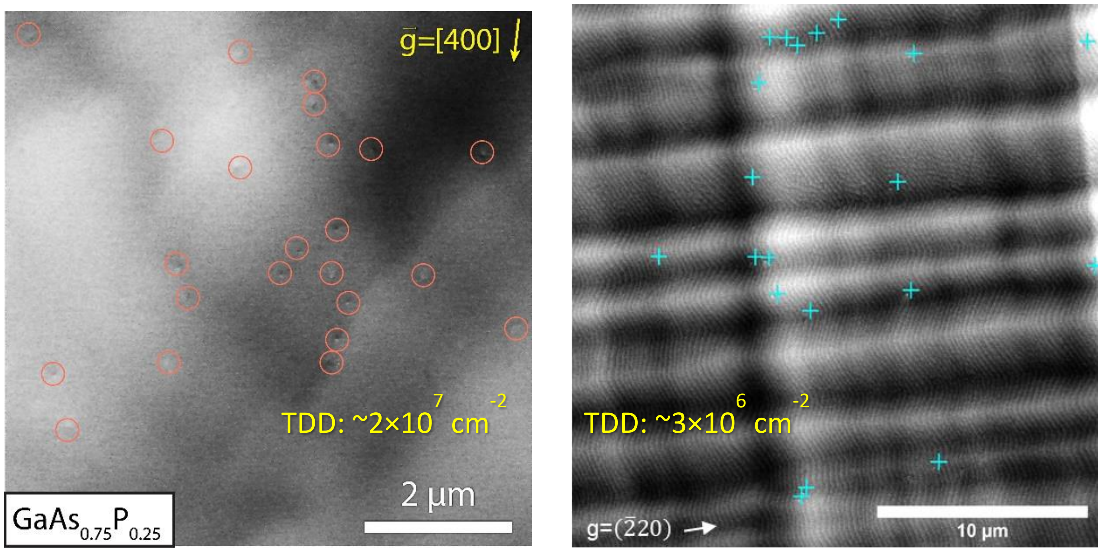

Figure 8.7 a) ECCI micrograph of legacy $GaAs_{0.75}P_{0.25}$ virtual substrate with a TDD of $>2x10^7$ cm^{-2}. (b) TDD of improved $GaAs_{0.75}P_{0.25}$ virtual substrate with TDD of $3x10^6$ cm^{-2} while even reducing the total thickness by 50%.

After improving the GaP layer, the SGB grading rate was increased to 1 % misfit/μm and the TDD remained low and nearly constant with respect to the TDD in the GaP layer. Total TDD after SGB, TJ, and cell growth only increased to $\sim 3\times10^6$ cm^{-2}. The result is shown in Figure 8.7b with the legacy $GaAs_{0.75}P_{0.25}$ virtual substrate in Figure 8.7a. The improvement to both TDD (note the scale bars) and improved surface morphology are evident from these images.

Additionally, due to the constraints placed on the $GaAs_{0.75}P_{0.25}$ top cell by elevated TDD (even at values as low as 3×10^6 cm^{-2}), the transmission of in-band photons out of the back of the $GaAs_{0.75}P_{0.25}$ top cell is significant. The SGB with its minimum Eg of 1.7 eV therefore absorbs some of the transmitted photons with energy greater than ~1.7 eV. To combat this, ~15% Al was added to each of the last 5 layers of the SGB allowing for increased transparency. This strategy is shown in Figure 8.8. While the calculated E_g profile in Figure 8.8 [147] is less absorptive than the standard SGB, the

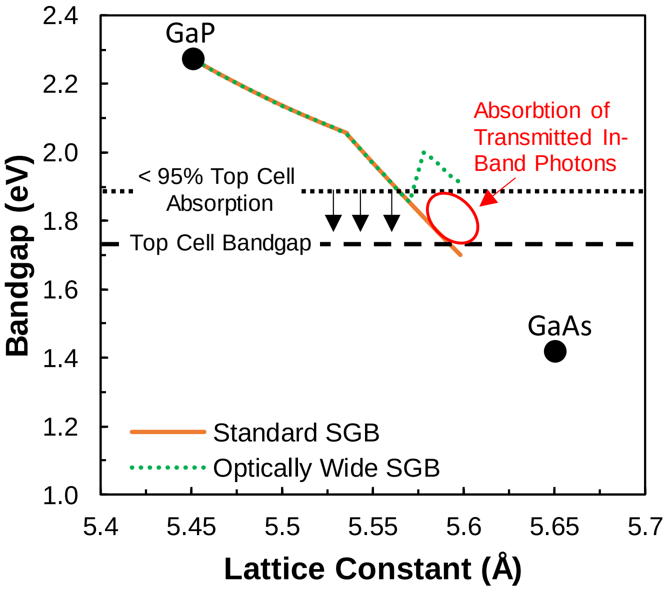

Figure 8.8 Bandgap vs lattice constant chart showing the design of an optically wide SGB. While a standard SGB should be transparent to all out of band flux, the $GaAs_{0.75}P_{0.25}$ cell is not thick enough to absorb all of the in band flux. Thus, previously the $GaAs_yP_{1-y}$ SGB was aborbing photons which could have been absorbed by a Si bottom cell.

abrupt jump in the E_g may cause a slight increase in reflectance. These should be much smaller than the gains afforded by the wider E_g. Future designs should make use of even higher transparency SGBs with smooth E_g profiles to minimize reflections. The addition of Al to the last few layer of the buffer did not result in a measurable increase in TDD.

8.6. CONCLUSIONS

Overall, a ~20× reduction in TDD in the GaP nucleation layer was achieved by altering critical parameters in the ALE seed layer growth, and by adding the CSS after 50 nm of GaP growth enhancing glide velocities to avoid rampant dislocation nucleation. With these impressive reductions in TDD, the $GaAs_yP_{1-y}$ SGB was optimized removing >2 μm of unnecessary III-V material and improving optical transparency for photons with energies >1.7 eV that are transmitted through the $GaAs_{0.75}P_{0.25}$ top cell. These should enable more mechanically robust and higher performance $GaAs_{0.75}P_{0.25}$/Si tandem cells. This work is nothing short of revolutionary for the monolithically integrated III-V/Si tandem cell community. These are the lowest reported TDDs for n-type $GaAs_{0.75}P_{0.25}$ virtual substrates and have the potential to unlock efficiencies well beyond single junction Si.

CHAPTER 9:

GAAS$_{0.75}$P$_{0.25}$ SI TANDEM CELL DEVELOPMENT

9.1. INTRODUCTION

Throughout my tenure at OSU I have produced four GaAs$_{0.75}$P$_{0.25}$/Si tandem solar cell generations (Gen-2 through Gen-5), each with increasing efficiencies and embodying various design improvements detailed throughout this dissertation. This chapter will briefly go through the lineage of these devices showing the pathway from the 13.3% device up to the now 23.4%, world record tandem solar cell. A summary of the results of these efforts are detailed in Figure 9.1. Due to the chronological nature of the improvements, it is not worth going into excruciating detail on the earlier device generations, but it is still worthwhile to introduce the devices to explore the lineage and design pathways of going from 13.3% to 23.4%.

I am keen to note that these efficiency improvements were largely achieved with no meaningful improvement in TDD as the advancements in Chapter 8 and the dopant grade cell in Chapter 6 have yet to be employed in a tandem cell. Integrating these recent advancements provides a realistic near-term pathway to >27% tandem solar cells. Lastly,

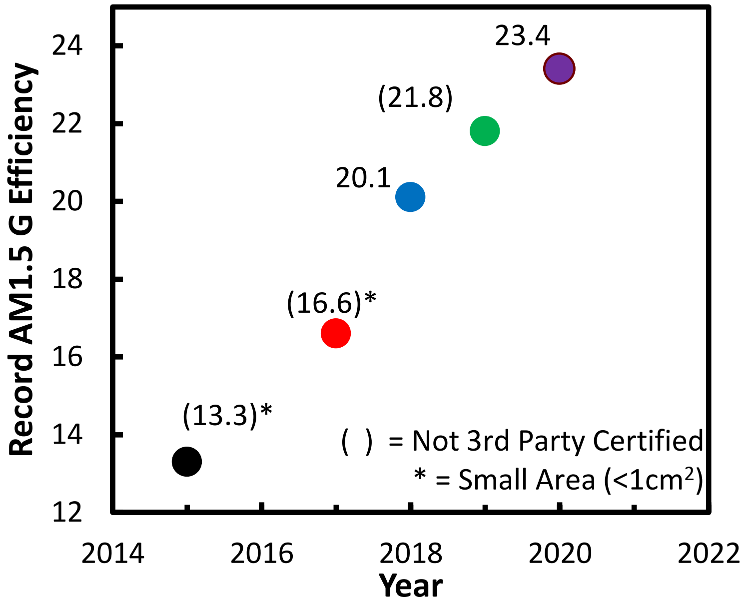

Figure 9.1 $GaAs_{0.75}P_{0.25}/Si$ tandem efficiency over the last 5 years.

this chapter will explore via modeling the pathway to >30% efficiency as a function of TDD to better understand the potential of this technology moving forward.

9.2. GENERATIONAL IMPROVEMENTS

9.2.1. GEN-2 DEVICE

Before I arrived at OSU, the group, led by Grassman et al. [178], [183], had demonstrated a tandem solar cell with an efficiency of 13.3% measured in house. This Gen-1 device had not received any significant optimization of the top cell (TC-1 design) and relied on an in-situ grown Si bottom cell without a BSF. It also employed a rather marginal tunnel junction interconnect whereby numerous devices across wafer did not satisfy peak tunneling current requirements.

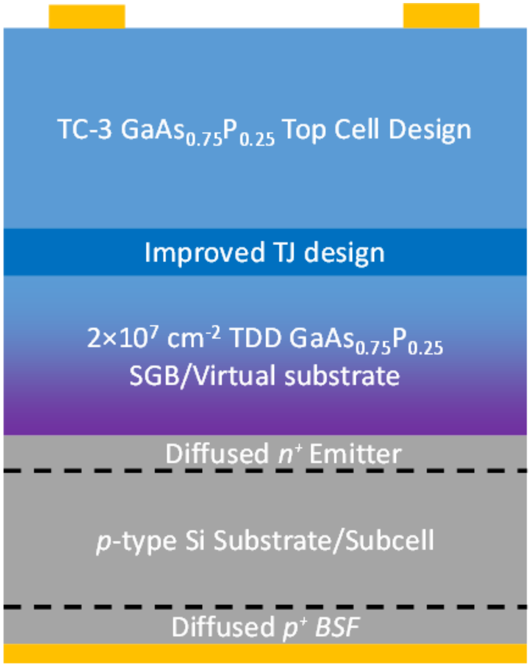

Figure 9.2 Gen-2 cell design which used an ex-situ Si bottom cell with front and rear diffusion.

The Gen-2 device attempted to correct these issues by implementing the TC-3 top cell design (Chapter 6), the newly designed tunnel junction (as detailed in the publications [184], [185] and dissertation by Chmielewski [62]), and an ex-situ produced Si bottom cell provided by our collaborators at the University of New South Wales (UNSW). This new Si bottom cell employed a B-diffused BSF and P-diffused emitter as detailed in the structure in Figure 9.2. This cell was fabricated using a small area device mesa (4 mm^2) with a ~8% metal coverage. This cell used the same virtual substrate as the Gen-1 device and possessed a TDD in excess of 2x10^7 cm^{-2}. Therefore, these improvements were primarily due to improvements in cell design rather than material quality.

The LIV and EQE results of the Gen-2 cell are presented in Figure 9.3. The improvement in the J_{sc} was due to substantial improvements in the short wavelength

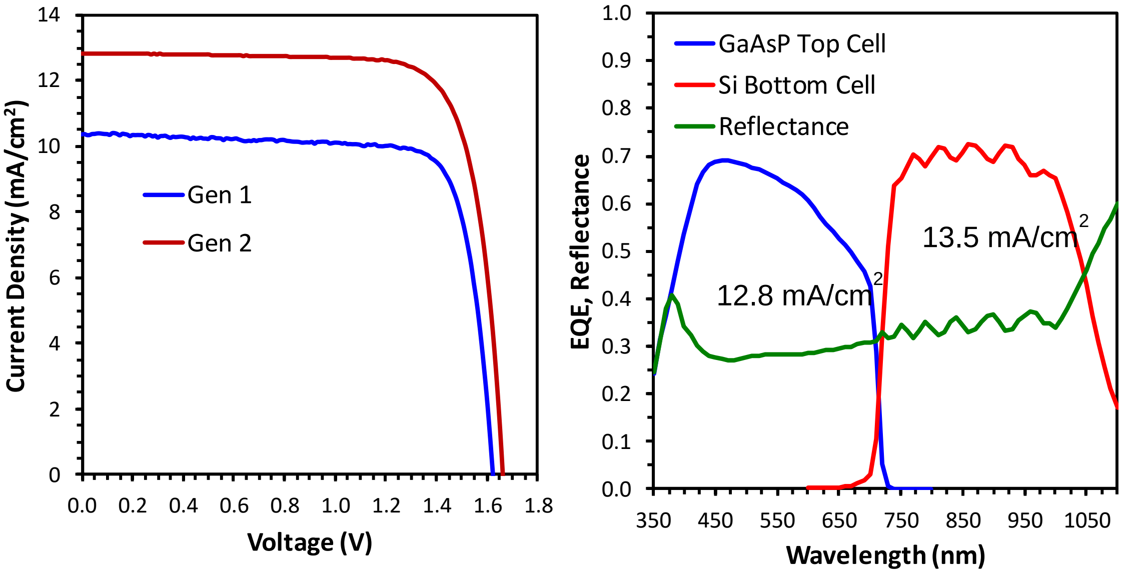

Figure 9.3 a) LIV and b) EQE of the Gen-1 and Gen-2 $GaAs_{0.75}P_{0.25}$/Si tandem cell.

response in the $GaAs_{0.75}P_{0.25}$ top cell (discussed in Chapter 6), as well as the long wavelength response in the Si bottom cell, commensurate with the improvements to both subcells. However, the fatal flaw of this cell is the lack of ARC which significantly limits the current and ultimately resulted in an efficiency of only 16.6%. The efficiency projected with a 5% spectral weighted reflectance (SWR) ARC is ~21.5%.

9.2.2. GEN-3 DEVICE

The Gen-3 device was frankly an “accidental” world record solar cell. It was intended as material for our collaborators, SolAero Technologies, to practice fabricating devices for future device iterations. They were able to produce much larger device areas (4 cm^2) with lower front grid shadowing (~4%) due to thicker front grid metal and a well-developed full wafer processing flow as opposed to the 4 mm^2 test cells produced at OSU. As we did not expect much performance from this initial process development

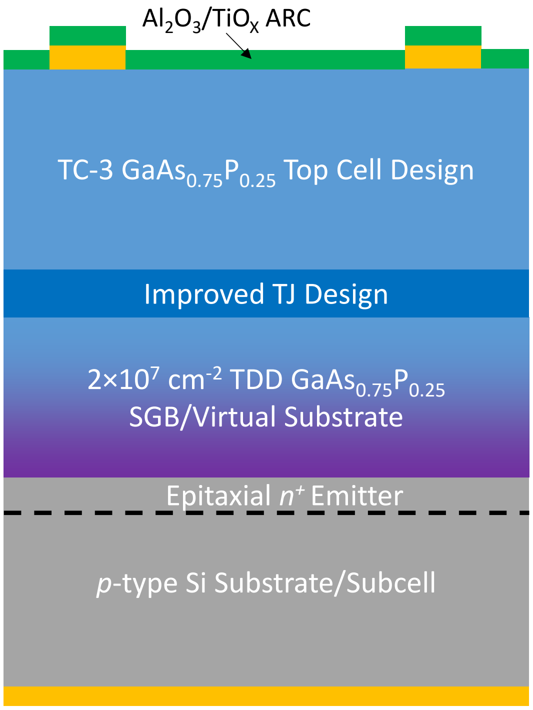

Figure 9.4 Structure of the Gen-3 $GaAs_{0.75}P_{0.25}$/Si tandem cell, which employed an Al_2O_3/TiO_x ARC.

endeavor, the structure was therefore simply an in-situ grown Si bottom cell (90 nm of epitaxial n-type Si on top of a *p*-type Si wafer) with the TC-3 $GaAs_{0.75}P_{0.25}$ top cell design (Figure 9.4). This design also employed no real improvements to material quality with TDD still more than 2×10^7 cm^{-2}.

There was however an Al_2O_3/TiO_x ARC with a 7.8 % SWR. While this is not an exceptionally good SWR, it did provide a very large boost in J_{SC} over the Gen-2 device (2.14 mA/cm^2). This ultimately led to a 20.1% efficiency for a 4 cm^2 device as verified by NREL (Figure 9.5a). This at the time beat out the 19.7% efficient 3-junction GaInP/GaAs/Si solar cell by Feifel et al. [43], and was the first entry for monolithic III-V/Si 2-junction cells into the solar cell efficiency record tables published by Green et al. [2].

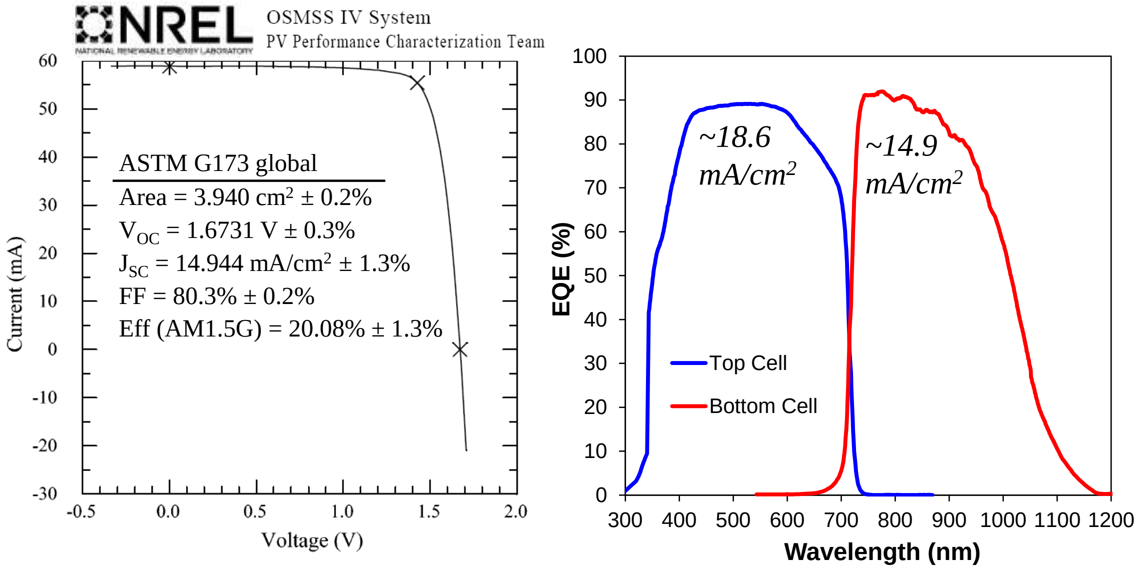

Figure 9.5 a)LIV and b) EQE measurements of the Gen-3 $GaAs_{0.75}P_{0.25}$ cell resulting in the first NREL-certified III-V/Si cell with an AM1.5G conversion efficiency over 20%.

The quantum efficiency measurements (Figure 9.5b) indicate bottom cell limited performance by ~3.7 mA/cm^2, as a result of no BSF in the in-situ grown Si bottom cell. This caused the device to be Si bottom cell limited by a substantial margin. The addition of a BSF was therefore an obvious place for further improvement in future device iterations.

9.2.3. GEN-4 DEVICE

The Gen-4 device (Figure 9.6) was very similar to the Gen-3 Device except it included an ex-situ produced Si BSF. The ex-situ produced Si bottom cell improved the J_{SC} by 1.7 mA/cm^2; however, the fill factor was reduced by ~2% absolute. The added BSF did improve the long wavelength response in the Si bottom cell as seen in Figure 9.7b, but the lack of rear texture, and an overly deep rear diffusion still limited the performance of the tandem cell. To combat this, the ARC was specifically tuned to boost

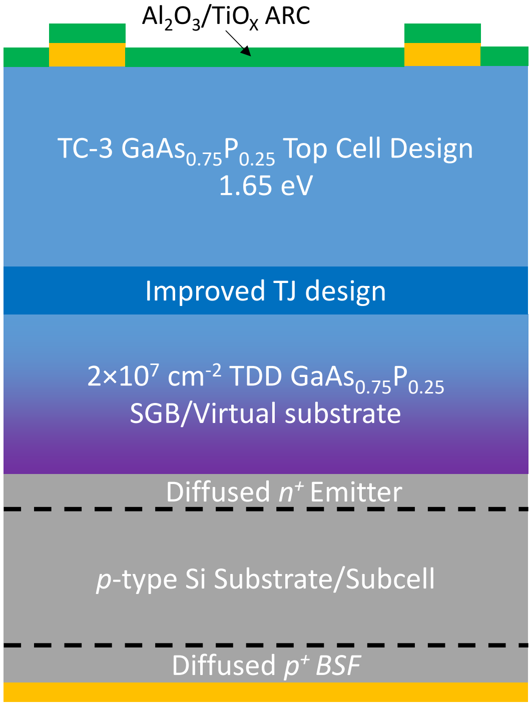

Figure 9.6 Structure of the Gen-4 $GaAs_{0.75}P_{0.25}$/Si tandem solar cell. This cell combined the efficiency improvements from the ex-situ Si bottom cell and the Al_2O_3/TiO_x ARC.

the current in the bottom cell rather than to minimize SWR. This resulted in a slightly improved to 6.8% SWR, but an overall reduction in the EQE of the $GaAs_{0.75}P_{0.25}$ top cell even though the $GaAs_{0.75}P_{0.25}$ cell IQEs between Gen-2 and -3 were identical.

The largest pitfall in this device was the bandgap of the $GaAs_{0.75}P_{0.25}$ top cell. Due to changes in wafer offcut, variation in temperature across different susceptors, etc. the bandgap of the $GaAs_{0.75}P_{0.25}$ top cell (1.65 eV) was lower than the intended 1.72 eV. This resulted in not only overfilling the top cell more than intended, but also a reduction in the expected V_{OC} by nearly 70 mV. This was partially mitigated by designing the ARC to minimize reflectance in the wavelength region of the Si subcell rather than designing for minimum broadband reflectance. However, the loss in voltage was ultimately a strong

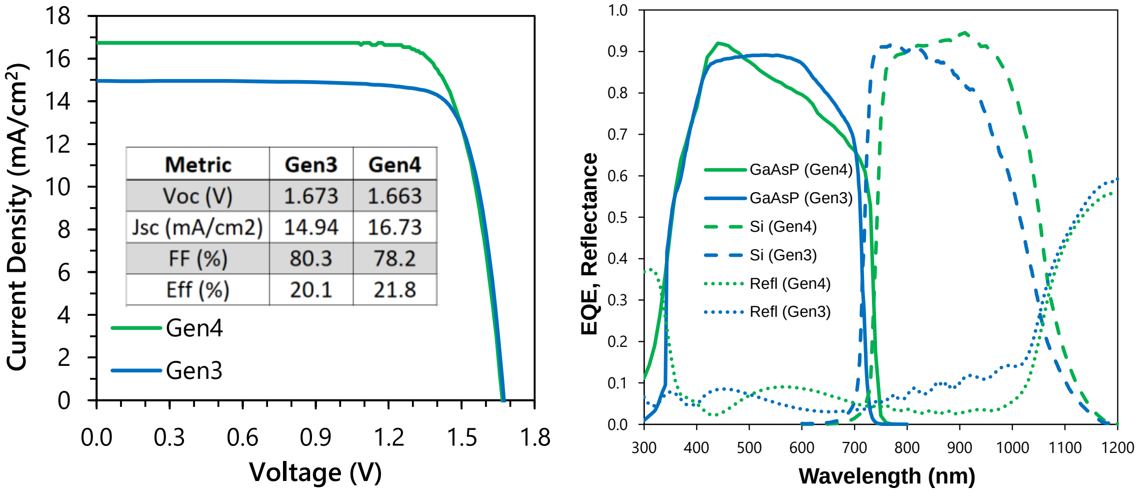

Figure 9.7 a) LIV and b) EQE/Reflectance measurements of the Gen-4 GaAs$_{0.75}$P$_{0.25}$/Si tandem Solar Cell. I slightly low bandgap of 1.65eV resulted in a lower V_{OC} than expected.

limiter of performance. Based on the IQE, this cell was projected to be a ~24% efficient device if properly current matched.

9.2.4. GEN-5 DEVICE

The Gen -5 device (Figure 9.8) is, at the time of writing, the 2 junction III-V/Si tandem cell efficiency verified world record with an AM1.5G efficiency of 23.4%. Comparisons will be made to the Gen-1 device, noting that the Gen-5 device is truly the culmination of the advancements made in the early part of my Ph.D. work, and, for the most part, is the proper integration of all of the advances that really should have been included in Gen-2 through Gen-4. Each of these cells had significant limitations due project planning, underperforming Si bottom cells, missed bandgap targets, etc. While this device is indeed still not the perfect integration of the optimal subcells at this time, the more in-depth analysis of this device will hopefully provide a nice summary of all of the advancements made from the start of my Ph.D. to now.

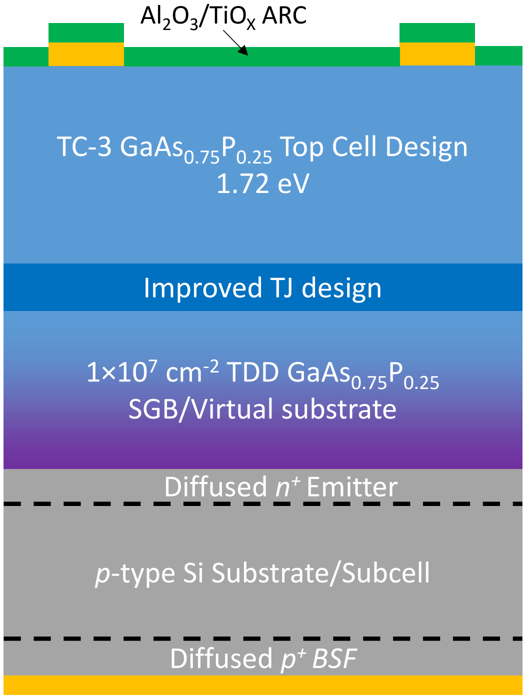

Figure 9.8 Structure of the Gen-5 $GaAs_{0.75}P_{0.25}$/Si tandem solar cell which primarily served to correct the top cell bandgap/composition.

Figure 9.9 presents LIV and EQE/IQE results for the Gen-5 $GaAs_{0.75}P_{0.25}$/Si tandem solar cell; extracted performance metrics are given in Table 9.. This cell generation employing an ex-situ produced Si subcell with B-diffused BSF, an Al_2O_3/TiO_x ARC, and TC-3 $GaAs_{0.75}P_{0.25}$ top cell, yielded considerable quantitative improvements to both V_{OC} and J_{SC} over the prior generations, especially Gen-1. While the addition of an ARC can account for a significant portion of the overall difference between the two design generations, especially in terms of J_{SC}, the holistic improvement is highlighted by comparison of the Gen-5 device with the ARC-projected LIV curve and performance metrics for the Gen-1 device, as provided in Figure 9.9a and Table 9.1. This projection assumes a spectral weighted reflectance (SWR) of 5%, which is readily achievable with an optimized ARC design, but notably better than what was implemented on the Gen-5

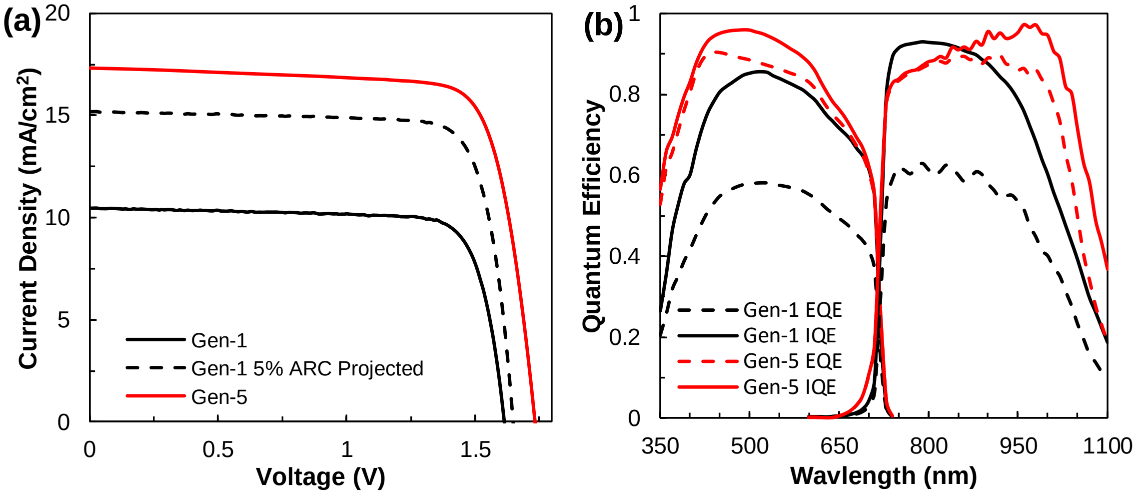

Figure 9.9 a) LIV of champion Gen-5 $GaAs_{0.75}P_{0.25}$/Si tandem solar cells. The ARC-projected (dashed line) Gen-1 curve was calculated assuming a 5% flat, broad-band reflectance, with the curve shifted to the new J_{SC} based on superposition of light and dark currents. b) EQE and IQE of the same Gen-1 and Gen-5 cells.

Table 9.1. AM1.5G LIV and integrated quantum efficiency metrics for the Gen-1 and Gen-5 tandem cells.

Sample	**J_{SC} (mA/cm^2)**	**V_{OC} (V)**	**FF (%)**	**$\eta_{AM1.5G}$ (%)**	**$J_{EQE,GaAsP}$ (mA/cm^{-2})**	**$J_{EQE,Si}$ (mA/cm^2)**
Gen-1	10.5	1.62	79.3	13.4	10.9	10.7
Gen-1*	15.2	1.65	79.8	20.0	15.2	15.5
Gen-5	17.3	1.73	77.7	23.4	17.1	17.1

**Projected metrics with implementation of a 5% SWR ARC.*

cell (7.6% SWR). Comparing the projected current-voltage (I-V) curve of the Gen-1 device to that of the Gen-5 device, improvements of +1.9 mA/cm^2 in J_{SC} and +80 mV in V_{OC} are observed.

These gains can be attributed to a combination of the improvements in the prior tandem generations including the redesign TC-3 $GaAs_{0.75}P_{0.25}$ top cell and the implementation of a B-diffused BSF. The form the BSF in the Si bottom cell is somewhat offset however by a reduction in bottom cell short wavelength (λ < 800 nm) response due to the inclusion of an overly deep front diffused emitter, which was introduced intentionally to attempt to block the recombination active GaP-Si interface [186]. However, the deeper than intended depth of this diffusion exposed additional photogenerated carriers to the higher non-radiative recombination rates within the highly doped emitter. The improvements to the top cell are mainly the result of a slight 2× reduction in TDD enabled by the improved GaP MEE conditions discussed in Chapter 8 along with the front-side window/emitter redesign discussed in Chapter 6.1. This design however still possessed a TDD of $\sim 1\times10^{7}$ cm^{-2} as the CSS (presented in Chapter 8) has yet to be implemented.

Nevertheless, in spite of these overall improvements, a surprising reduction of the FF is also observed. At first glance it appears to be due to a loss that is shunt-like in nature, based on the negative slope of the LIV between V = 0 and the maximum power point. To help explain and quantify this loss, an effective shunt resistance was extracted by fitting the Gen-5 LIV to an illuminated double-diode model, shown in Figure 9.10a, yielding an effective parallel resistance, R_{par}, of 2.25 kΩ-cm^2. While this may be an overly simplistic analysis — this is not a single junction cell and thus rigorous fitting requires a more complex model — it does provide a comparative metric to assess FF losses. For example, if R_{par} is increased to a sufficiently high value to effectively remove the shunt-like behavior, shown in Figure 9.10a for 1 MΩ-cm^2, a 3.3% absolute FF difference between the original and shunt-free traces is revealed. However, dark *I-V* measurements of the tandem device, shown in the Figure 9.10a inset, as well as a single-junction isotype top cell structure grown on the same $GaAs_{0.75}P_{0.25}$/Si virtual substrate

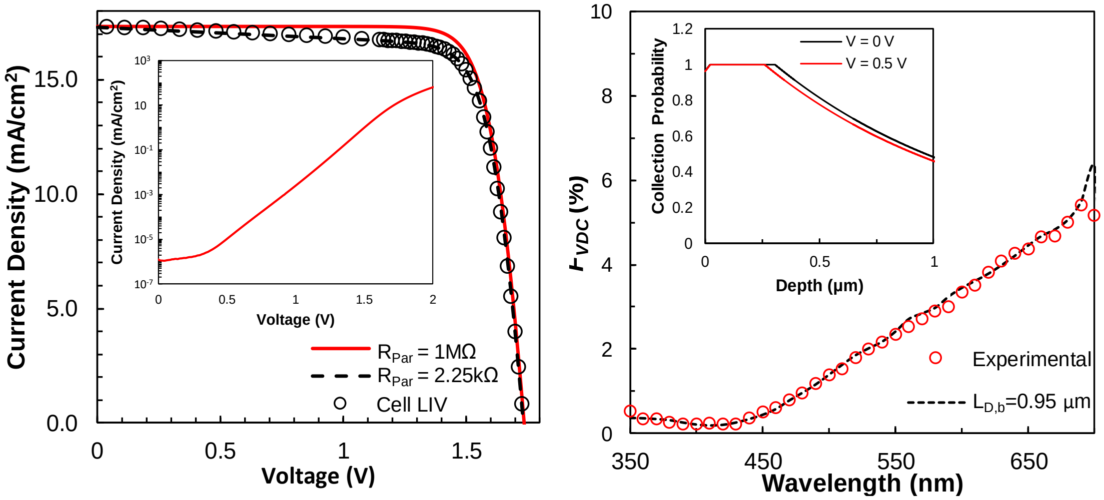

Figure 9.10 a) Comparison of Gen-5 LIV (and double-diode model fit) with and without apparent shunt loss. (b) Wavelength-dependent VDC losses with modeled fits/projections as a function of base diffusion length. The inset illustrates the reduction in collection probability attendant with the reduction in depletion region width at small forward bias.

(not shown), do not actually exhibit any significant shunt loss. Furthermore, prior generations (Gen-1,Gen-3 and Gen-4) all possessed bottom cell limited I-V characteristics and no significant shunt-like behavior was observed [12]. Therefore, a more likely source of the shunt-like losses is voltage dependent collection efficiency (VDC) in the $GaAs_{0.75}P_{0.25}$ top cell, rather than a more traditional shunt resistance.

Therefore, measurements of the VDC were made according to the method detailed in Chapter 4. As a refresher, $F_{VDC}(\lambda)$ effectively describes the fraction of photocurrent lost per volt, as a function of wavelength. By multiplying this parameter by EQE and integrating over the relevant illumination spectrum (here, AM1.5G), the slope of the LIV curve for a single junction cell can be analytically described by its EQE and F_{VDC}.

$$\frac{dJ(V\approx 0)}{dV} = \int_{\lambda=min}^{max} EQE(\lambda)\cdot\Phi_{\mathrm{AM1.5G}}(\lambda)\cdot F_{VDC}(\lambda)\cdot d\lambda \qquad \text{Eq. 9.1}$$

While the Gen-5 tandem is near current-matched at short circuit bias (0 V), any significant reduction in photocurrent in either of the sub cells would result in that subcell being the current-limiting junction. Therefore, any change in voltage across the tandem is roughly equivalent to the voltage drop across the current-limiting subcell. Thus, it is reasonable to assume that the analysis, derived for single junction cells, still holds true for this particular tandem cell.

The results of this measurement for the Gen-5 tandem are provided in Figure 9.10b. A clear trend of increasing F_{VDC} as a function of wavelength is observed, indicating that the collection efficiency of long wavelength photogenerated carriers is more strongly impacted by changes in cell voltage than it is for the short wavelength photogenerated carriers. By employing Equation 9.1, along with the $F_{VDC}(\lambda)$ curves from Figure 9.10b and the $GaAs_{0.75}P_{0.25}$ top cell EQE curves from Figure 9.9b, we can recover the slope of the AM1.5G LIV curve (recalling the assumption that all voltage is dropped across the $GaAs_{0.75}P_{0.25}$ subcell). Using this technique, an AM1.5G LIV slope of -0.480 mA/V was determined, in excellent agreement with that observed in the AM1.5G LIV (-0.484 mA/V). This result provides confidence in the validity of this non-standard characterization method and further supports the conclusion that the shunt-like slope in the I-V curve is due to top cell VDC and not an ohmic shunt resistance.

To further verify this analysis, as well as identify the underlying mechanism for a non-negligible F_{VDC} the analytical model discussed in Chapter 5 was employed. VDC in these cells is expected to be due to the modulation of the depletion region width in cases where the base diffusion length is shorter than the base width. Basically, as the top cell is biased the depletion region shrinks, thereby elongating the base (shown in Figure 9.10b inset) and reducing the likelihood of collecting deeply generated (i.e. long wavelength) photocarriers. This effect is seen qualitatively in Figure 9.10b with the F_{VDC} parameter increasing as a function of wavelength. Shown in Figure 9.10b as the black dashed line, the experimental data (red circles) is most adequately fit using a $L_{D,b}$ of 950 nm. This value is very similar to the TDD-limited diffusion length predicted by the Yamaguchi model [9], which, at a TDD of $1\text{-}2\times10^{7}$ cm^{-2}, is 1.14 – 0.80 μm. As such, we can conclude that the results of the F_{VDC} measurement, and the FF loss itself, are entirely consistent with the existence of VDC resulting from TDD induced reductions to the minority carrier diffusion length in the metamorphic (TDD = 1×10^{7} cm^{-2}) $GaAs_{0.75}P_{0.25}$ top cell.

Beyond the FF losses related to the metamorphic $GaAs_{0.75}P_{0.25}$ top cell, which can be improved through intelligent cell design (e.g. base layer optimization) and improvements to material quality (i.e. lower TDD, longer diffusion length), the ARC employed in the Gen-5 cell was still far from ideal, with a high SWR of 7.6%. Although SWR is a common metric used for characterizing and/or designing ARCs, this particular Al_2O_3/TiO_x bilayer structure was intentionally designed to correct for slight subcell current mismatch; establishing nearly perfect subcell current matching (as seen in Figure 9.9 and Table 9.1) to ensure maximum performance from the overall tandem device. Therefore, optimal ARC design will continue to change as subcells are further improved through structure optimization and/or TDD reduction; average reflectance will thus also improve as the subcells themselves are more closely current-matched. Regardless, the

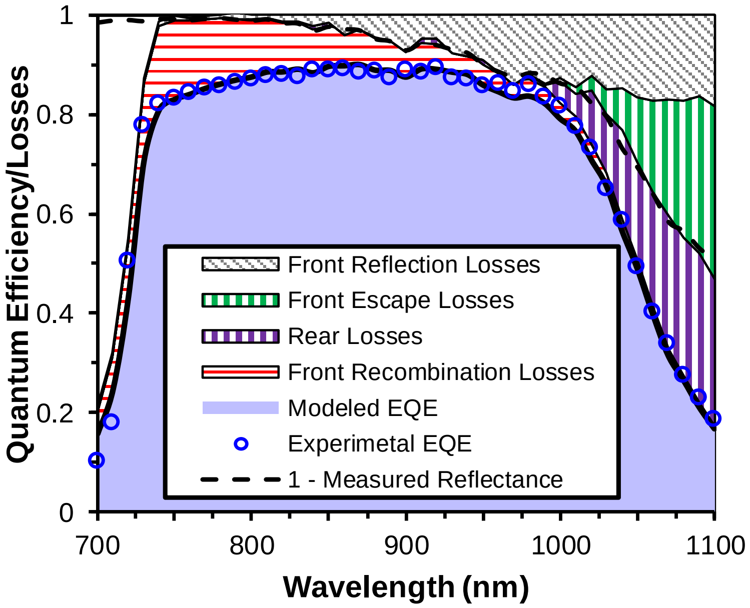

Figure 9.11 Loss modeling of the Si subcell elucidating 3 primary losses related to Si subcell design.

Al_2O_3/TiO_x combination is also not optimal, and moving to SiO_2/TiO_x or MgF/ZnS would provide further improvement in ARC performance.

Beyond the clear necessity for TDD reduction in the $GaAs_{0.75}P_{0.25}$ top cell, there is still significant room for improvement within the Si bottom cell. The Si subcell employed in this tandem did not possess any rear surface texture or light trapping, preventing optimal collection of long-wavelength photons. Additionally, an overly deep emitter diffusion profile resulted in sub-par short wavelength response. Loss analysis for the Si bottom cell was calculated by collaborators at UNSW using a combination of SunSolve from PV Lighthouse [187] for optical effects and PC1D [188] for electrical effects. SunSolve was used to calculate the optical absorption in the tandem cell from the experimental reflectance profile using a two-step method that separates the front escape losses, stemming from reflectance at the rear surface, from the reflectance due to the bulk materials and ARC. Absorption in the Si bottom cell can then be calculated by

Table 9.2 AM1.5G detailed current loss in the Si subcell.

Metric	Current/Current Loss ≤ 1100 nm (mA/cm^2)
Integrated Experimental EQE	17.0
Modeled EQE	17.0
Front Recombination	-1.3
Rear Losses	-1.1
Front Escape Losses	-0.8
Front Reflectance Losses	-1.5

subtracting the absorption in the top ARC and III-V layers from the absorption in the full tandem cell calculated above. The absorption in the III-V layers was determined using interpolated III-V optical data [21], [131]–[134], [189] according to the method by Lumb et al. [128].

The transport losses were then determined using simulations of the Si subcell structure using the transport modeling softwarePC1D. PC1D is a drift-diffusion solver whose roots are based in the equations and models presented in Chapter 5. With the determined optical properties of the cell, and the measured EQE as inputs, the front junction depth, as well as the front and rear surface recombination velocities, were used to fit the EQE. The bulk lifetime was set to 1 ms, as measured in other samples, and was not adjusted in the fitting since the collection efficiency is effectively insensitive to changes in such high lifetimes. The best fit to the data was found for a front junction depth of 4.1 μm with a peak doping of 2×10^{20} cm^{-3}, but with unphysical front and rear surface recombination velocities of zero. The insensitivity of the simulation to the front surface recombination velocity is a result of the very deep and heavy, Auger limited emitter diffusion profile that was used to attempt to mitigate the impact of the recombination active GaP-Si interface [186]. The expected rear recombination losses are masked by the much larger front recombination loss. The extension of this loss to very long wavelengths makes such an extraction difficult. As such, we grouped both rear recombination and parasitic absorption loss in the back metal and B-BSF as “rear losses.”

Figure 9.11 plots the losses as related to EQE and Table 9.2 shows the corresponding short-circuit current gain calculated from the loss analysis. The losses were then calculated by removing all parasitic losses one by one to isolate the losses. Good agreement occurs between the simulated and measured reflection as well as the EQE. There are three main losses corresponding to Si subcell design that are reducing the EQE of the Si bottom cell: front recombination, rear parasitic absorption, and front photon escape. This front recombination loss can be mitigated to a great degree with the use of a shallow diffusion (~300 nm) with a similar peak doping. Reduction of the losses associated with the highly non-optimum front junction should allow the impact on the EQE of the rear to be determined in future devices. The large rear losses which consist of parasitic absorption and rear recombination are due to the rear diffusion and full area metal contact without any passivation layer on the rear of the Si surface. These and the front escape losses, due to incomplete absorption of reflected photons can be mitigated by implementing shallower rear diffusion and/or a rear dielectric passivation layer that also would also boost internal reflection for infrared light and rear texturing for light trapping.

The Si bottom cell V_{OC} can be estimated by subtracting the typical isotype top cell V_{OC} (at the same TDD and E_g) from the Gen-5 tandem cell. This suggests a bottom cell V_{OC} of only 570-590 mV, which is far from optimal and underperforming those demonstrated by others in the field of Si-based tandems. Employing a higher performance rear passivation scheme, such as the AlO_x/SiN_x dielectric approach demonstrated by Feifel et al. [190] or the a-Si of Fan et al. [25], [191], should enable subcell V_{OC} well in excess of 600 mV and J_{SC} far greater than that produced by the top cell at the current TDD. Thus, a clear and present path forward to improving bottom cell performance is identified.

9.3. THE NEAR-TERM PATHWAY TO ~27% EFFICIENT TANDEMS

As none of the above devices have made use of the improved $GaAs_{0.75}P_{0.25}$/Si virtual substrates developed through the efforts detailed in Chapter 8, there stands significant room for improvement in addition to the discussion of the Si subcell in the above subsection. Using the integrated IQE values from the 650 °C dopant grade $GaAs_{0.75}P_{0.25}$ top cell and assuming a top cell limited I-V characteristic. Rough estimates of efficiency for the next round (Gen-6) of tandem cells can be made. The values used in the efficiency projection are detailed in Table 9.3. If the Si bottom cell can provide enough photocurrent to promote top cell limited behavior and a V_{OC} of 625 mV, assumptions that are reasonable based on collaborator modeling, then the projected

Table 9.3 Tabulated projections of tandem efficiency using redesigned $GaAs_{0.75}P_{0.25}$ top cell and improved Si bottom cell. This is done assuming Top cell limited I-V characteristics and a 5% SWR ARC.

	V_{OC}	J_{SC} (5% SWR ARC)	FF	Efficiency
Experimentally demonstrated Top cell	1.19 V	18.0 mA/cm^2	83.0%	17.8%
Projected Si Bottom Cell	0.625 V	>19 mA/cm^2	~80%	9.5%
Tandem	1.815 V	18.0 mA/cm^2	83.0%	27.1%

tandem efficiency should exceed 27%. This would be a ~3.5% absolute improvement over the current state of the art, a monumental leap forward for a technology that appears primed to continue pressing towards higher efficiencies.

9.4. QUANTIFYING THE PATHWAY TO 30% EFFICIENT TANDEM CELLS

Looking beyond the near term to better understand how tandem efficiency should trend as TDDs are further reduced, modeling was done to understand the maximum achievable performance at every TDD. Based on the analytical modeling of the $GaAs_{0.75}P_{0.25}$ top cell performance as a function of TDD developed in Chapters 6 and 7, the performance of the near ideal $GaAs_{0.75}P_{0.25}$/Si tandem solar cell can be plotted as a function of TDD.

To do this we need to make a few assumptions. First, we will assume that all of these devices are slightly top cell limited and therefore the J_{SC} and FF of the tandem cell can be approximated as the J_{SC} and FF of the $GaAs_{0.75}P_{0.25}$ top cell. While this has not been always the case because of underperforming Si subcells, the Si subcell really should not be the problem that it has been in the past once a robust method for rear passivation is developed. Second, we can assume that the bulk lifetime/diffusion length is the same as extracted from the TC-3 top cell grown on the GaAs-based virtual substrate (2.7 μm), and that the use of a dopant grade is not employed in this cell. The precise impact of this dopant grade is more difficult to model across TDD as the necessity for it will likely be removed as TDD is reduced further. It is for this reason that it is left out of this analysis. Next, we assume that it is indeed the TDD that is limiting the V_{OC} and not some other point defects or alternate SRH recombination centers. This has not always been the case

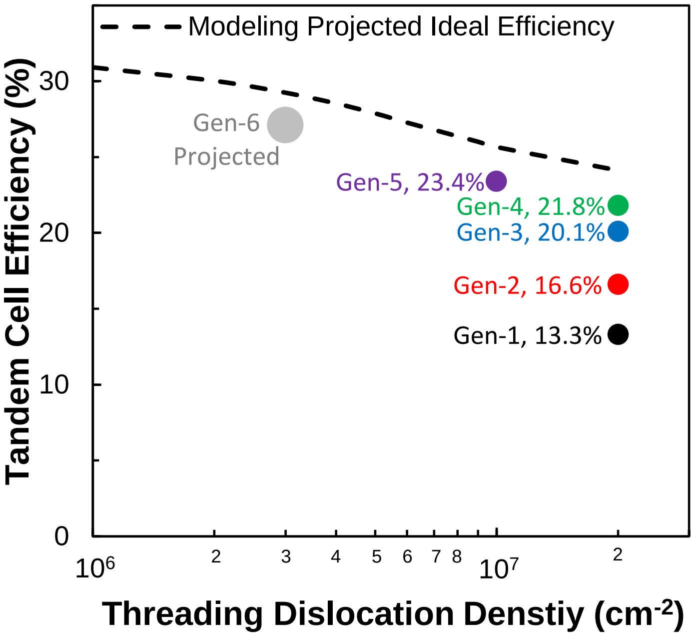

Figure 9.12 Modeled ideal performance of $GaAs_{0.75}P_{0.25}P$/Si tandem solar cells as a function of TDD with experimentally demonstrated $GaAs_{0.75}P_{0.25}$/Si cells.

when growing on the new low TDD Si-based virtual substrates; however, proper growth condition optimization experiments (growth temperature, doping, V:III ratio etc.) on the $GaAs_{0.75}P_{0.25}$ top cell should yield improvements to the V_{OC} as this parameter space has really not been effectively explored during my tenure other than a few necessary changes to improve performance. Indeed, we know it is possible through proper growth parameters to achieve a W_{OC} of 0.45 V at a TDD of 1-2×10^6 cm^{-2} based on the results of the TC-3 growth on the GaAs-based virtual substrate. Lastly, we can assume that the Si subcell produces 625 mV based on modeling from collaborators at UNSW and a current greater than 19 mA/cm^2 to ensure top cell limited conditions at every TDD modeled.

Using the models described in Chapter 5. The J_{SC}, FF, and V_{OC} have all been interpolated as a function of TDD. The projection of tandem efficiency vs. TDD is shown in Figure 9.12 with the Gen-1 through Gen-5 devices and projected Gen-6 device indicated. It is easy to see that the majority of the work in this dissertation has served to maximize efficiency for a given TDD and push closer to the theoretical limits placed by TDD on tandem efficiency.

As mentioned previously, the reductions in TDD via collaborative work with other lab group members (J. Boyer) detailed in Chapter 8 came within the final 1.5 years of my Ph.D. work and thus have yet to be incorporated into a tandem cell. The residual distance between the Gen-5 device and the dashed black line is a result of the underperforming Si bottom cell and thus a less than desirable ARC SWR. It is also expected that the upcoming Gen-6 device will also slightly under performed the ideal dashed black line due to a lower than ideal V_{OC} by ~50-70 mV. This modeling indicates that if TDD can be reduced to 1×10^{6} cm^{-2} then realistic efficiencies of greater than 30% are indeed possible.

9.5. CONCLUSIONS

Overall, the rapid improvements to tandem efficiency from 13.3% to 23.4% was enabled by a combination of top and bottom cell improvements that were largely made without improvements to the resident TDD in the $GaAs_{0.75}P_{0.25}$ top cell. This includes a redesign of the $GaAs_{0.75}P_{0.25}$ top cell, the addition of an ex-situ produced Si subcell, and the addition of an Al_2O_3/TiO_x ARC. The Gen-5 device was analyzed and root causes of FF losses and current losses in the Si subcell are presented. With the recent advances to material quality detailed in Chapter 8 and the use of a dopant grade as detailed in Chapter 6, the next generation of tandem devices are projected to exceed 27% AM1.5G efficiency. Lastly, the ceiling for performance as a function of TDD was explored indicating that if the TDD can be further reduced to 1×10^{6} cm^{-2} then efficiency should exceed 30% based on demonstrated $GaAs_{0.75}P_{0.25}$ subcells. Overall, this provides a clear path forward to achieve >30% tandem solar cells in the near future.

CHAPTER 10:

CONCLUSIONS AND FURTHER WORK

10.1. CONCLUSIONS

This dissertation has explored various aspects of $GaAs_{0.75}P_{0.25}$/Si tandem solar cells with the intent of gaining scientific understanding about the impact of crystalline defects on critical device characteristics and cell performance of $GaAs_{0.75}P_{0.25}$ top cells, extracting maximum performance for a given TDD through the development and implementation of defect resilient designs, and of course improving overall tandem efficiency.

To understand the impact of crystalline defects on $GaAs_{0.75}P_{0.25}$ cell performance, the $GaAs_{0.75}P_{0.25}$ top cell was first coarsely optimized through model informed design changes to the emitter and window layers resulting in high performance $GaAs_{0.75}P_{0.25}$ cells on low TDD GaAs-based virtual substrates [11]. Porting this identical design to a higher TDD Si-based virtual substrate allows for the extraction of performance as a function of TDD [12]. Analytical modeling was used to properly quantify the impact of TDD on transport properties for better informed model-based design.

To create defect resilient designs both transport- and optics-based strategies were employed to improve performance at a given TDD. Critical aspects of recombination associated with threading dislocations was exploited by using a rear-emitter design to improve V_{OC} by 30 mV over the front-emitter design [13], [14]. During this study, the critical role of the window layer properties on passivation was discovered [15] and has turned out to be impactful not only in this work but on other III-V materials such as wide bandgap GaInP cells [192]. Optically speaking, a model-based exploration, informed by experimental data, of a GaInP/AlInP DBR was performed in order to shorten the base thickness and provide resilience against TDD induced diffusion length shortening. Modeling indicates an increase in J_{SC} of ~0.5mA/cm^2 is possible at 10^7 cm^{-2} TDD.

Lastly the improvement of tandem solar cells was driven by a combination of the device design improvements in Chapter 6, ex-situ produced Si subcells provided by our collaborators, and the application of an ARC. These advancements raised the AM1.5G efficiency of the $GaAs_{0.75}P_{0.25}$/Si tandem solar cell to 23.4%, a current verified world record for this technology. Notably this work resulted in the first certified demonstration of efficiency >20% for a monolithic III-V/Si cell, outperforming the best 3-junction device at the time [43]. Based on the recent advancements in material quality in Chapter 8 and device design via implementation of the dopant grade cell in Chapter 6, the near-term expectation is for efficiency to exceed 27% in the next round of tandem devices. Lastly, the pathway to >30% efficient tandem cells was explored through data informed analytical modeling. These results indicate that if TDD can be reduced to 1×10^6 cm^{-2}, then efficiencies of greater than 30% should be achievable after proper optimization to the subcells.

10.2. FURTHER WORK

The next round of tandem solar cells has been grown and is currently in the fabrication process flow. These devices will include the new low-TDD Si-based virtual substrate, the dopant grade $GaAs_{0.75}P_{0.25}$ top cell, and an ex-situ produced Si subcell with a dielectric and/or a-Si based BSF. This device as stated before should provide >27% AM1.5G efficiency. Moving beyond this device, I think that there is still substantial room for optimization of the $GaAs_{0.75}P_{0.25}$ top cell and overall tandem design. If I had more time, there are 4 key areas where I believe research efforts are warranted.

One of the areas that was really lacking in the explorations presented in this dissertation is the impact of base doping on device performance. While the dopant grade explored this a little bit, the dopant grade really did not help to fully quantify the role of doping on device performance or its impact on transport properties. Because of point defects associated with dopant atoms the relationship between doping, diffusivity, and lifetime is hard to determine theoretically and therefore must be empirically determined. Additionally, the exact position and magnitude of the dopant grade has yet to be optimized and should provide for higher voltages, or even improved long wavelength collection.

Secondly, a full optimization of the $GaAs_{0.75}P_{0.25}$ growth conditions including further exploration of growth temperature as well as V:III ratio is warranted as is does appear that there are other recombination mechanisms beyond TDD at play in the

$GaAs_{0.75}P_{0.25}$ top cell. These are currently limiting the top cell voltage in the dopant grade cell. These recombination centers that are not associated with TDD limit both diffusion length in the base as well as create additional SRH centers in the depletion region increasing J_{02} dark current.

Next, a better understanding of the optimal base thickness is necessary especially as TDD becomes lower and diffusion lengths improve. To do this a better understanding of the near band edge optical data is critical. Test PIN diode structures can be used as unity collection photodetectors for the purpose of extracting absorption coefficients through IQE measurements. Further optimization of the base thickness in the $GaAs_{0.75}P_{0.25}$ cell must be performed, not as a single junction optimization to extract maximum performance, but as a holistic tandem device understanding as photons transmitted out of the back of the $GaAs_{0.75}P_{0.25}$ cell can still be collected by the Si subcell.

Lastly, the SGB and TJ at present are not currently perfectly transparent to all photons of interest. The TJ was designed as if all in band photons are absorbed by the $GaAs_{0.75}P_{0.25}$ top cell; however, when material quality is less than ideal, as in the case of dislocated materials, subcell thinning and transmission of some in-band photons to the Si subcell can improve top cell collection efficiency and overall tandem efficiency. As such, the TJ should really be transparent to all photons with energy below 1.9 eV rather than the 1.72 eV it is currently designed for. Along the same lines, the abrupt addition of Al as a temporary method for improving transparency in the SGB places interfaces that can increase internal reflectances in the buffer. Instead a smooth bandgap profile is preferred using slowly increasing Al content in the last few layers of the SGB.

Overall, these changes should help push the $GaAs_{0.75}P_{0.25}$/Si tandem solar cells much closer to the fundamental limits placed upon them by recombination associated with TDD. Beyond that worthwhile endeavor, combining both of the strategies presented in Chapter 7, DBRs and rear-emitter cells, could provide a pathway to push beyond the classical limitations placed by TDD and improve efficiencies even further.

As a further broad desire to implement optoelectronic devices onto the ubiquitous Si platform, I believe that the material quality has now gotten to the point whereby other optoelectronic devices without the tight production cost requirements of PV are potentially more viable. This includes GaInP P-HEMTs, AlGaInP LEDs, GaAs laser diodes for Si based photonic applications etc. These devices are usually small area and can therefore take advantage of high quantities of devices per wafer and therefore a greater tolerance to higher production costs. These devices could provide an area of funding and research while epitaxy costs and residual TDD are still reducing to amenable levels for technology deployment in the PV sector.

REFERENCES

[1] S. Essig *et al.*, “Raising the one-sun conversion efficiency of III–V/Si solar cells to 32.8% for two junctions and 35.9% for three junctions,” *Nat. Energy*, vol. 2, no. 9, p. 17144, Sep. 2017, doi: 10.1038/nenergy.2017.144.

[2] M. A. Green, E. D. Dunlop, D. H. Levi, J. Hohl-Ebinger, M. Yoshita, and A. W. Y. Ho-Baillie, “Solar cell efficiency tables (version 54),” *Prog. Photovolt. Res. Appl.*, vol. 27, no. 7, pp. 565–575, 2019, doi: 10.1002/pip.3171.

[3] T. J. Grassman *et al.*, “Nucleation-related defect-free GaP/Si(100) heteroepitaxy via metal-organic chemical vapor deposition,” *Appl. Phys. Lett.*, vol. 102, no. 14, p. 142102, Apr. 2013, doi: 10.1063/1.4801498.

[4] V. Narayanan, S. Mahajan, K. J. Bachmann, V. Woods, and N. Dietz, “Antiphase boundaries in GaP layers grown on (001) Si by chemical beam epitaxy,” *Acta Mater.*, vol. 50, no. 6, pp. 1275–1287, Apr. 2002, doi: 10.1016/S1359-6454(01)00408-6.

[5] I. Németh, B. Kunert, W. Stolz, and K. Volz, “Heteroepitaxy of GaP on Si: Correlation of morphology, anti-phase-domain structure and MOVPE growth conditions,” *J. Cryst. Growth*, vol. 310, no. 7, pp. 1595–1601, Apr. 2008, doi: 10.1016/j.jcrysgro.2007.11.127.

[6] V. Narayanan, S. Mahajan, K. J. Bachmann, V. Woods, and N. Dietz, “Stacking faults and twins in gallium phosphide layers grown on silicon,” *Philos. Mag. A*, vol. 82, no. 4, pp. 685–698, Mar. 2002, doi: 10.1080/01418610208243196.

[7] C. L. Andre, D. M. Wilt, A. J. Pitera, M. L. Lee, E. A. Fitzgerald, and S. A. Ringel, “Impact of dislocation densities on n+/p and p+/n junction GaAs diodes and solar cells on SiGe virtual substrates,” *J. Appl. Phys.*, vol. 98, no. 1, p. 014502, Jul. 2005, doi: 10.1063/1.1946194.

[8] C. L. Andre *et al.*, “Impact of dislocations on minority carrier electron and hole lifetimes in GaAs grown on metamorphic SiGe substrates,” *Appl. Phys. Lett.*, vol. 84, no. 18, pp. 3447–3449, Apr. 2004, doi: 10.1063/1.1736318.

[9] M. Yamaguchi, A. Yamamoto, and Y. Itoh, “Effect of dislocations on the efficiency of thin-film GaAs solar cells on Si substrates,” *J. Appl. Phys.*, vol. 59, no. 5, pp. 1751–1753, Mar. 1986, doi: 10.1063/1.336439.

[10] M. Yamaguchi, K.-H. Lee, K. Araki, N. Kojima, and Y. Ohshita, “Potential and Activities of III-V/Si Tandem Solar Cells,” *ECS J. Solid State Sci. Technol.*, vol. 5, no. 2, pp. Q68–Q73, Jan. 2016, doi: 10.1149/2.0311602jss.

[11] A. C. Silvaggio, D. L. Lepkowski, D. J. Chmielewski, J. T. Boyer, S. A. Ringel, and T. J. Grassman, “Optimization of a GaAsP Top Cell for Implementation in a III-V/Si Tandem Structure,” in *2017 IEEE 44th Photovoltaic Specialist Conference (PVSC)*, Jun. 2017, pp. 2554–2557, doi: 10.1109/PVSC.2017.8366475.

[12] T. J. Grassman *et al.*, “Toward >25% Efficient Monolithic Epitaxial GaAsP/Si Tandem Solar Cells,” in *2019 IEEE 46th Photovoltaic Specialists Conference (PVSC)*, Jun. 2019, pp. 0734–0737, doi: 10.1109/PVSC40753.2019.8980574.

[13] D. L. Lepkowski, J. T. Boyer, D. J. Chmielewski, A. C. Silvaggio, S. A. Ringel, and T. J. Grassman, “Investigation of Rear-Emitter GaAsP Top Cells for use in III-V/Si Tandem Photovoltaics,” in *2018 IEEE 7th World Conference on Photovoltaic Energy Conversion (WCPEC) (A Joint Conference of 45th IEEE PVSC, 28th PVSEC 34th EU PVSEC)*, Jun. 2018, pp. 2642–2647, doi: 10.1109/PVSC.2018.8547748.

[14] D. L. Lepkowski, J. T. Boyer, D. J. Chmielewski, A. C. Silvaggio, S. A. Ringel, and T. J. Grassman, “Investigation of Rear-Emitter GaAs0.75P0.25 Top Cells for Application to III–V/Si Tandem Photovoltaics,” *IEEE J. Photovolt.*, vol. 9, no. 6, pp. 1644–1651, Nov. 2019, doi: 10.1109/JPHOTOV.2019.2939069.

[15] D. L. Lepkowski, T. Kasher, J. T. Boyer, D. J. Chmielewski, T. J. Grassman, and S. A. Ringel, “The Critical Role of AlInP Window Design in III–V Rear-Emitter Solar Cells,” *IEEE J. Photovolt.*, vol. 10, no. 3, pp. 758–764, May 2020, doi: 10.1109/JPHOTOV.2020.2978863.

[16] “Transition in Energy, Transport – 10 Predictions for 2019,” *BloombergNEF*, Jan. 16, 2019. https://about.bnef.com/blog/transition-energy-transport-10-predictions-2019/ (accessed Oct. 06, 2019).

[17] M. Green, E. Dunlop, J. Hohl-Ebinger, M. Yoshita, N. Kopidakis, and X. Hao, “Solar cell efficiency tables (version 57),” *Prog. Photovolt. Res. Appl.*, vol. 29, no. 1, pp. 3–15, 2021, doi: https://doi.org/10.1002/pip.3371.

[18] A. Richter, M. Hermle, and S. W. Glunz, “Reassessment of the Limiting Efficiency for Crystalline Silicon Solar Cells,” *IEEE J. Photovolt.*, vol. 3, no. 4, pp. 1184–1191, Oct. 2013, doi: 10.1109/JPHOTOV.2013.2270351.

[19] K. Yoshikawa *et al.*, “Silicon heterojunction solar cell with interdigitated back contacts for a photoconversion efficiency over 26%,” *Nat. Energy*, vol. 2, no. 5, pp. 1–8, Mar. 2017, doi: 10.1038/nenergy.2017.32.

[20] G. L. Pearson, “Conversion of Solar to Electrical Energy,” p. 9.

[21] D. Lackner *et al.*, “Two-Terminal Direct Wafer-Bonded GaInP/AlGaAs//Si Triple-Junction Solar Cell with AM1.5g Efficiency of 34.1%,” *Sol. RRL*, vol. 4, no. 9, p. 2000210, 2020, doi: 10.1002/solr.202000210.

[22] “Stacking faults and twins in gallium phosphide layers grown on silicon,” p. 14.

[23] M. Feifel *et al.*, “Advances in Epitaxial GaInP/GaAs/Si Triple Junction Solar Cells,” in *2020 47th IEEE Photovoltaic Specialists Conference (PVSC)*, Jun. 2020, pp. 0194–0196, doi: 10.1109/PVSC45281.2020.9300594.

[24] T. J. Grassman *et al.*, “TOWARD >25% EFFICIENT MONOLITHIC EPITAXIAL GAASP/SI TANDEM SOLAR CELLS,” presented at the IEEE PVSC, Chicago, 2019.

[25] S. Fan *et al.*, “Current-Matched III–V/Si Epitaxial Tandem Solar Cells with 25.0% Efficiency,” *Cell Rep. Phys. Sci.*, vol. 1, no. 9, p. 100208, Sep. 2020, doi: 10.1016/j.xcrp.2020.100208.

[26] C. Andre, “III-V Semiconductors on SiGe Substrates for multijunction photovoltaics,” Ohio State University.

[27] M. R. Lueck, C. L. Andre, A. J. Pitera, M. L. Lee, E. A. Fitzgerald, and S. A. Ringel, “Dual junction GaInP/GaAs solar cells grown on metamorphic SiGe/Si substrates with high open circuit voltage,” *IEEE Electron Device Lett.*, vol. 27, no. 3, pp. 142–144, Mar. 2006, doi: 10.1109/LED.2006.870250.

[28] A. M. Carlin, E. A. Fitzgerald, and S. A. Ringel, “III–V/SiGe on Si radiation hard space cells with Voc>2.6V,” in *2015 IEEE 42nd Photovoltaic Specialist Conference (PVSC)*, Jun. 2015, pp. 1–4, doi: 10.1109/PVSC.2015.7355600.

[29] “Oxford PV pushes tandem SHJ/perovskite cell conversion efficiency to record 29.52%,” *PV Tech*. https://www.pv-tech.org/news/oxford-pv-pushes-tandem-shj-perovskite-cell-conversion-efficiency-to-record-29.52 (accessed Feb. 04, 2021).

[30] D. P. McMeekin *et al.*, “A mixed-cation lead mixed-halide perovskite absorber for tandem solar cells,” *Science*, vol. 351, no. 6269, pp. 151–155, Jan. 2016, doi: 10.1126/science.aad5845.

[31] N. Ahn *et al.*, “Trapped charge-driven degradation of perovskite solar cells,” *Nat. Commun.*, vol. 7, no. 1, pp. 1–9, Nov. 2016, doi: 10.1038/ncomms13422.

[32] G. Divitini, S. Cacovich, F. Matteocci, L. Cinà, A. D. Carlo, and C. Ducati, “In situ observation of heat-induced degradation of perovskite solar cells,” *Nat. Energy*, vol. 1, no. 2, pp. 1–6, Jan. 2016, doi: 10.1038/nenergy.2015.12.

[33] K. Domanski, E. A. Alharbi, A. Hagfeldt, M. Grätzel, and W. Tress, “Systematic investigation of the impact of operation conditions on the degradation behaviour of perovskite solar cells,” *Nat. Energy*, vol. 3, no. 1, pp. 61–67, Jan. 2018, doi: 10.1038/s41560-017-0060-5.

[34] S.-W. Lee *et al.*, “UV Degradation and Recovery of Perovskite Solar Cells,” *Sci. Rep.*, vol. 6, p. 38150, Dec. 2016, doi: 10.1038/srep38150.

[35] M. Grätzel, “The Rise of Highly Efficient and Stable Perovskite Solar Cells,” *Acc. Chem. Res.*, vol. 50, no. 3, pp. 487–491, Mar. 2017, doi: 10.1021/acs.accounts.6b00492.

[36] N. J. Jeon *et al.*, “A fluorene-terminated hole-transporting material for highly efficient and stable perovskite solar cells,” *Nat. Energy*, vol. 3, no. 8, pp. 682–689, Aug. 2018, doi: 10.1038/s41560-018-0200-6.

[37] N.-G. Park, M. Grätzel, T. Miyasaka, K. Zhu, and K. Emery, “Towards stable and commercially available perovskite solar cells,” *Nat. Energy*, vol. 1, no. 11, pp. 1–8, Oct. 2016, doi: 10.1038/nenergy.2016.152.

[38] Q. Tai *et al.*, “Efficient and stable perovskite solar cells prepared in ambient air irrespective of the humidity,” *Nat. Commun.*, vol. 7, no. 1, pp. 1–8, Apr. 2016, doi: 10.1038/ncomms11105.

[39] C. Algora, “Reliability of III–V concentrator solar cells,” *Microelectron. Reliab.*, vol. 50, no. 9, pp. 1193–1198, Sep. 2010, doi: 10.1016/j.microrel.2010.07.045.

[40] M. Vázquez, C. Algora, I. Rey-Stolle, and J. R. González, “III-V concentrator solar cell reliability prediction based on quantitative LED reliability data,” *Prog. Photovolt. Res. Appl.*, vol. 15, no. 6, pp. 477–491, 2007, doi: 10.1002/pip.753.

[41] J. F. Geisz and D. J. Friedman, “III N V semiconductors for solar photovoltaic applications,” *Semicond. Sci. Technol.*, vol. 17, no. 8, pp. 769–777, Jul. 2002, doi: 10.1088/0268-1242/17/8/305.

[42] W. Shockley and H. J. Queisser, “Detailed Balance Limit of Efficiency of p-n Junction Solar Cells,” *J. Appl. Phys.*, vol. 32, no. 3, pp. 510–519, Mar. 1961, doi: 10.1063/1.1736034.

[43] M. Feifel *et al.*, “Direct Growth of III–V/Silicon Triple-Junction Solar Cells With 19.7% Efficiency,” *IEEE J. Photovolt.*, vol. 8, no. 6, pp. 1590–1595, Nov. 2018, doi: 10.1109/JPHOTOV.2018.2868015.

[44] M. Vaisman *et al.*, “15.3%-Efficient GaAsP Solar Cells on GaP/Si Templates,” *ACS Energy Lett.*, vol. 2, no. 8, pp. 1911–1918, Aug. 2017, doi: 10.1021/acsenergylett.7b00538.

[45] K. N. Yaung, J. R. Lang, and M. L. Lee, “Towards high efficiency GaAsP solar cells on (001) GaP/Si,” in *2014 IEEE 40th Photovoltaic Specialist Conference (PVSC)*, Jun. 2014, pp. 0831–0835, doi: 10.1109/PVSC.2014.6925043.

[46] E21 Committee, “Standard Solar Constant and Zero Air Mass Solar Spectral Irradiance Tables,” ASTM International. doi: 10.1520/E0490-00AR19.

[47] “ASTM G173 - 03(2020) Standard Tables for Reference Solar Spectral Irradiances: Direct Normal and Hemispherical on 37° Tilted Surface.” https://www.astm.org/Standards/G173 (accessed Feb. 23, 2021).

[48] H. Hovel, “Semiconductors and Semimetals Volume 11 Solar Cells,” in *Semiconductors and Semimetals Volume 11 Solar Cells*, Academic Press, 1975, pp. 16–44.

[49] M. Green, *Solar Cells: Operating Principles, Technology, and System Applications*, 1st ed. Prentice Hall, Inc., 1982.

[50] A. Smets, *Solar Energy: the physics and engineering of photovoltaic conversion technologies and systems*, 1st ed. UIT cambridge, 2016.

[51] S. Fonash, *Solar Cell DEevice Physics*, 2nd ed. Burlington, MA: Academic Press, 2010.

[52] R. R. King *et al.*, “Band gap-voltage offset and energy production in next-generation multijunction solar cells,” *Prog. Photovolt. Res. Appl.*, vol. 19, no. 7, pp. 797–812, 2011, doi: https://doi.org/10.1002/pip.1044.

[53] E. D. Kosten, B. M. Kayes, and H. A. Atwater, “Experimental demonstration of enhanced photon recycling in angle-restricted GaAs solar cells,” *Energy Environ. Sci.*, vol. 7, no. 6, pp. 1907–1912, 2014, doi: 10.1039/C3EE43584A.

[54] X. Sheng *et al.*, “Device Architectures for Enhanced Photon Recycling in Thin-Film Multijunction Solar Cells,” *Adv. Energy Mater.*, vol. 5, no. 1, p. 1400919, 2015, doi: https://doi.org/10.1002/aenm.201400919.

[55] W. Shockley and W. T. Read, “Statistics of the Recombinations of Holes and Electrons,” *Phys. Rev.*, vol. 87, no. 5, pp. 835–842, Sep. 1952, doi: 10.1103/PhysRev.87.835.

[56] J. T. Boyer, D. L. Lepkowski, D. J. Chmielewski, and T. J. Grassman, “Modeling and experimental demonstration of short-wavelength carrier collection enhancement in Ga0.51In0.49P solar cells using graded (AlzGa1-z)xIn1-xP window-emitter structures,” *Sol. Energy Mater. Sol. Cells*, vol. 202, p. 110133, Nov. 2019, doi: 10.1016/j.solmat.2019.110133.

[57] J. T. Boyer, D. L. Lepkowski, D. J. Chmielewski, S. A. Ringel, and T. J. Grassman, “Graded (AlzGa1-z)xIn1-xP Window-Emitter Structures for Improved Short-Wavelength Response,” in *2017 IEEE 44th Photovoltaic Specialist Conference (PVSC)*, Jun. 2017, pp. 2079–2083, doi: 10.1109/PVSC.2017.8366356.

[58] R. R. King, P. C. Colter, J. H. Ermer, and M. Haddad, “Wide-bandgap Lattice-mismatched Window Layer for a Solar Energy Conversion Device,” US2003/0070707 A1, Apr. 17, 2003.

[59] J. F. Geisz *et al.*, “Six-junction III–V solar cells with 47.1% conversion efficiency under 143 Suns concentration,” *Nat. Energy*, vol. 5, no. 4, Art. no. 4, Apr. 2020, doi: 10.1038/s41560-020-0598-5.

[60] NREL, “Best Research-Cell Efficiency Chart,” 2020. https://www.nrel.gov/pv/cell-efficiency.html (accessed Mar. 24, 2020).

[61] R. Tsu and L. Esaki, “Tunneling in a finite superlattice,” *Appl. Phys. Lett.*, vol. 22, no. 11, pp. 562–564, Jun. 1973, doi: 10.1063/1.1654509.

[62] D. J. Chmielewski, “III-V Metamorphic Materials and Devices for Multijunction Solar cells grown by MBE and MOCVD,” PhD Disseration, The Ohio State University, Columbus, OH, 2018.

[63] “24% efficient perl silicon solar cell: Recent improvements in high efficiency silicon cell research,” *Sol. Energy Mater. Sol. Cells*, vol. 41–42, pp. 87–99, Jun. 1996, doi: 10.1016/0927-0248(95)00117-4.

[64] E. García-Tabarés, J. A. Carlin, T. J. Grassman, D. Martín, I. Rey-Stolle, and S. A. Ringel, “Evolution of silicon bulk lifetime during III–V-on-Si multijunction solar cell epitaxial growth,” *Prog. Photovolt. Res. Appl.*, vol. 24, no. 5, pp. 634–644, 2016, doi: https://doi.org/10.1002/pip.2703.

[65] C. Yi, N. J. Western, F.-J. Ma, A. Ho-Baillie, and S. P. Bremner, “The Role of Grown-In Defects in Silicon Minority Carrier Lifetime Degradation During Thermal Treatment in Epitaxial Growth Chambers,” *IEEE J. Photovolt.*, vol. 10, no. 5, pp. 1299–1306, Sep. 2020, doi: 10.1109/JPHOTOV.2020.3008791.

[66] J. Ohlmann *et al.*, “Influence of Metal–Organic Vapor Phase Epitaxy Reactor Environment on the Silicon Bulk Lifetime,” *IEEE J. Photovolt.*, vol. 6, no. 6, pp. 1668–1672, Nov. 2016, doi: 10.1109/JPHOTOV.2016.2598254.

[67] “Silicon Minority-carrier Lifetime Degradation During Molecular Beam Heteroepitaxial III-V Material Growth,” *Energy Procedia*, vol. 92, pp. 617–623, Aug. 2016, doi: 10.1016/j.egypro.2016.07.027.

[68] N. Ashcroft and N. D. Mermin, *Solid State Physics*. Harcourt College Publishers, 1976.

[69] U. W. Pohl, *Epitaxy of Semiconductors: Introduction to Physical Principles*. Berlin Heidelberg: Springer-Verlag, 2013.

[70] H. J. Queisser, “Defects in Semiconductors: Some Fatal, Some Vital,” *Science*, vol. 281, no. 5379, pp. 945–950, Aug. 1998, doi: 10.1126/science.281.5379.945.

[71] N. Wang, I. K. Sou, and K. K. Fung, “Transmission electron microscopy study of stacking faults and the associated partial dislocations in pseudomorphic epilayers of ZnSe/GaAs(001),” *J. Appl. Phys.*, vol. 80, no. 9, pp. 5506–5508, Nov. 1996, doi: 10.1063/1.363482.

[72] H. Kroemer, “Polar-on-nonpolar epitaxy,” *J. Cryst. Growth*, vol. 81, no. 1–4, pp. 193–204, Feb. 1987, doi: 10.1016/0022-0248(87)90391-5.

[73] R. L. Schwoebel and E. J. Shipsey, “Step Motion on Crystal Surfaces,” *J. Appl. Phys.*, vol. 37, no. 10, pp. 3682–3686, Sep. 1966, doi: 10.1063/1.1707904.

[74] K. Volz *et al.*, “GaP-nucleation on exact Si (0 0 1) substrates for III/V device integration,” *J. Cryst. Growth - J CRYST GROWTH*, vol. 315, pp. 37–47, Jan. 2011, doi: 10.1016/j.jcrysgro.2010.10.036.

[75] T. J. Grassman *et al.*, “Control and elimination of nucleation-related defects in GaP/Si(001) heteroepitaxy,” *Appl. Phys. Lett.*, vol. 94, no. 23, p. 232106, Jun. 2009, doi: 10.1063/1.3154548.

[76] K. L. Schulte *et al.*, “Heteroepitaxy of GaAs on (001) ==> 6° Ge substrates at high growth rates by hydride vapor phase epitaxy,” *J. Appl. Phys.*, vol. 113, pp. 174903-174903–9, May 2013, doi: 10.1063/1.4803037.

[77] M. Henzler and J. Clabes, “Structural and Electronic Properties of Stepped Semiconductor Surfaces,” *Jpn. J. Appl. Phys.*, vol. 13, no. S2, p. 389, Jan. 1974, doi: 10.7567/JJAPS.2S2.389.

[78] R. Kaplan, “LEED STUDY OF THE STEPPED SURFACE OF VICINAL Si (100),” p. 14.

[79] R. Alcotte *et al.*, “Epitaxial growth of antiphase boundary free GaAs layer on 300 mm Si(001) substrate by metalorganic chemical vapour deposition with high mobility,” *APL Mater.*, vol. 4, no. 4, p. 046101, Apr. 2016, doi: 10.1063/1.4945586.

[80] A. R. Laracuente and L. J. Whitman, “Step structure and surface morphology of hydrogen-terminated silicon: (001) to (114),” *Surf. Sci.*, vol. 545, no. 1–2, pp. 70–84, Nov. 2003, doi: 10.1016/j.susc.2003.08.038.

[81] M. Feifel *et al.*, “MOVPE Grown Gallium Phosphide-Silicon Heterojunction Solar Cells,” *IEEE J Photovolt*, vol. 7, no. 2, pp. 502–507, Mar. 2017, doi: 10.1109/JPHOTOV.2016.2642645.

[82] J. E. Ayers, *Heteroepitaxy of Semiconductors*. CRC Press, 2007.

[83] M. S. Abrahams, L. R. Weisberg, C. J. Buiocchi, and J. Blanc, “Dislocation morphology in graded heterojunctions: GaAs1−xPx,” *J. Mater. Sci.*, vol. 4, no. 3, pp. 223–235, Mar. 1969, doi: 10.1007/BF00549922.

[84] J. Matthews, “Defects in epitaxial multilayers I. Misfit dislocations,” *J. Cryst. Growth*, vol. 27, pp. 118–125, Dec. 1974, doi: 10.1016/0022-0248(74)90424-2.

[85] J. W. Matthews, S. Mader, and T. B. Light, “Accommodation of Misfit Across the Interface Between Crystals of Semiconducting Elements or Compounds,” *J. Appl. Phys.*, vol. 41, no. 9, pp. 3800–3804, Aug. 1970, doi: 10.1063/1.1659510.

[86] I. Yonenaga, K. Sumino, G. Izawa, H. Watanabe, and J. Matsui, “Mechanical property and dislocation dynamics of GaAsP alloy semiconductor,” *J. Mater. Res.*, vol. 4, no. 2, pp. 361–365, Apr. 1989, doi: 10.1557/JMR.1989.0361.

[87] I. Yonenaga, “Mechanical Properties and Dislocation Dynamics in III-V Compounds,” *J Phys III Fr.*, vol. 7, no. 7, pp. 1435–1450, Jul. 1997, doi: 10.1051/jp3:1997198.

[88] I. Yonenaga and K. Sumino, “Dynamic activity of dislocations in gallium phosphide,” *J. Appl. Phys.*, vol. 73, no. 4, pp. 1681–1685, Feb. 1993, doi: 10.1063/1.353203.

[89] I. Yonenaga and K. Sumino, “Behaviour of dislocations in GaAs revealed by etch pit technique and X-ray topography,” *J. Cryst. Growth*, vol. 126, no. 1, pp. 19–29, Jan. 1993, doi: 10.1016/0022-0248(93)90223-J.

[90] E. A. Fitzgerald, “Relaxed GexSi1−x structures for III–V integration with Si and high mobility two-dimensional electron gases in Si,” *J. Vac. Sci. Technol. B Microelectron. Nanometer Struct.*, vol. 10, no. 4, p. 1807, Jul. 1992, doi: 10.1116/1.586204.

[91] J. M. Baribeau, T. E. Jackman, D. C. Houghton, P. Maigné, and M. W. Denhoff, “Growth and characterization of Si1−xGex and Ge epilayers on (100) Si,” *J. Appl. Phys.*, vol. 63, no. 12, pp. 5738–5746, Jun. 1988, doi: 10.1063/1.340312.

[92] E. A. Fitzgerald *et al.*, “Totally relaxed Ge $_{x}$ Si $_{1-x}$ layers with low threading dislocation densities grown on Si substrates,” *Appl. Phys. Lett.*, vol. 59, no. 7, pp. 811–813, Aug. 1991, doi: 10.1063/1.105351.

[93] M. T. Currie, S. B. Samavedam, T. A. Langdo, C. W. Leitz, and E. A. Fitzgerald, “Controlling threading dislocation densities in Ge on Si using graded SiGe layers and chemical-mechanical polishing,” *Appl. Phys. Lett.*, vol. 72, no. 14, pp. 1718–1720, Apr. 1998, doi: 10.1063/1.121162.

[94] G. B. Stringfellow, *Organometallic Vapor-Phase Epitaxy: Theory and Practice*, 2nd edition. San Diego: Academic Press, 1998.

[95] J. Tsao, *Materials Fundamentals of Molecular Beam Epitaxy*. Elsevier, 1993.

[96] R. Jaeger, *Introduction to Microelectronic Fabrication: Volume 5 of Modular Series on Solid State Devices*, 2nd edition. Upper Saddle River, N.J: Pearson, 2001.

[97] S. A. Campbell, *Fabrication Engineering at the Micro- and Nanoscale*, 4th edition. New York: Oxford University Press, 2012.

[98] D.K Bowen and B. K. Tanner, *High Resolution X-Ray Diffractometry And Topography*. CRC Press, 1998.

[99] *Heteroepitaxy of Semiconductors : Theory, Growth, and Characterization, Second Edition*. CRC Press, 2016.

[100] P. F. Fewster, "Reciprocal space mapping," *Crit. Rev. Solid State Mater. Sci.*, vol. 22, no. 2, pp. 69–110, Jun. 1997, doi: 10.1080/10408439708241259.

[101] S. A. Speakman, "Introduction to High Resolution X-Ray Diffraction of Epitaxial Thin Films," p. 53.

[102] R. Pierret, *Semiconductor fundementals*, 2nd ed., vol. 1. Addison-Wesley Publishing Company, 1983.

[103] S. D. Carnevale *et al.*, "Rapid misfit dislocation characterization in heteroepitaxial III-V/Si thin films by electron channeling contrast imaging," *Appl. Phys. Lett.*, vol. 104, no. 23, p. 232111, Jun. 2014, doi: 10.1063/1.4883371.

[104] S. D. Carnevale *et al.*, "Applications of Electron Channeling Contrast Imaging for the Rapid Characterization of Extended Defects in III–V/Si Heterostructures," *IEEE J. Photovolt.*, vol. 5, no. 2, pp. 676–682, Mar. 2015, doi: 10.1109/JPHOTOV.2014.2379111.

[105] J. I. Deitz, S. D. Carnevale, S. A. Ringel, D. W. McComb, and T. J. Grassman, "Electron Channeling Contrast Imaging for Rapid III-V Heteroepitaxial Characterization," *JoVE J. Vis. Exp.*, no. 101, p. e52745, Jul. 2015, doi: 10.3791/52745.

[106] K. N. Yaung *et al.*, "Threading dislocation density characterization in III–V photovoltaic materials by electron channeling contrast imaging," *J. Cryst. Growth*, vol. 453, pp. 65–70, Nov. 2016, doi: 10.1016/j.jcrysgro.2016.08.015.

[107] X. Chen *et al.*, "Large Area and Depth-Profiling Dislocation Imaging and Strain Analysis in Si/SiGe/Si Heterostructures," *Microsc. Microanal.*, vol. 20, no. 5, pp. 1521–1527, Oct. 2014, doi: 10.1017/S1431927614012963.

[108] O. Marcelot, S. I. Maximenko, and P. Magnan, "Plan View and Cross-Sectional View EBIC Measurements: Effect of e-Beam Injection Conditions on Extracted Minority Carrier Transport Properties," *IEEE Trans. Electron Devices*, vol. 61, no. 7, pp. 2437–2442, Jul. 2014, doi: 10.1109/TED.2014.2323997.

[109] "Study of misfit dislocations by EBIC, CL and HRTEM in GaAs/InGaAs lattice-strained multi-quantum well p-i-n solar cells," *Mater. Sci. Eng. B*, vol. 42, no. 1–3, pp. 43–51, Dec. 1996, doi: 10.1016/S0921-5107(96)01681-9.

[110] E. Hieckmann *et al.*, "Comprehensive Characterization of Extended Defects in Semiconductor Materials by a Scanning Electron Microscope," *J. Vis. Exp. JoVE*, no. 111, May 2016, doi: 10.3791/53872.

[111] L. Pasemann, "Theory of electron-beam-induced current and cathodoluminescence imaging of crystal defects: some new results," *Mater. Sci. Eng. B*, vol. 24, no. 1–3, pp. 15–22, May 1994, doi: 10.1016/0921-5107(94)90290-9.

[112] K. A. Emery, "Solar simulators and I–V measurement methods," *Sol. Cells*, vol. 18, no. 3–4, pp. 251–260, Sep. 1986, doi: 10.1016/0379-6787(86)90124-9.

[113] NASA, "Terrestrial photovoltaic measurement procedures," NASA, (NASA-TM-737C2), Jun. 1977.

[114] E44 Committee, "Test Method for Electrical Performance of Photovoltaic Cells Using Reference Cells Under Simulated Sunlight," ASTM International. doi: 10.1520/E0948-16R20.

[115] M. Meusel, R. Adelhelm, F. Dimroth, A. W. Bett, and W. Warta, "Spectral mismatch correction and spectrometric characterization of monolithic III–V multi-junction solar cells," *Prog. Photovolt. Res. Appl.*, vol. 10, no. 4, pp. 243–255, 2002, doi: https://doi.org/10.1002/pip.407.

[116] S. H. Lim, J.-J. Li, E. H. Steenbergen, and Y.-H. Zhang, “Luminescence coupling effects on multijunction solar cell external quantum efficiency measurement,” *Prog. Photovolt. Res. Appl.*, vol. 21, no. 3, pp. 344–350, 2013, doi: https://doi.org/10.1002/pip.1215.

[117] J.-J. Li and Y.-H. Zhang, “Accurate measurement of the external quantum efficiency of multi-junction solar cells,” in *Conference on Lasers and Electro-Optics 2012*, San Jose, California, 2012, p. CF1J.4, doi: 10.1364/CLEO_SI.2012.CF1J.4.

[118] E. Barrigón, P. Espinet-González, Y. Contreras, and I. Rey-Stolle, “Implications of low breakdown voltage of component subcells on external quantum efficiency measurements of multijunction solar cells,” *Prog. Photovolt. Res. Appl.*, vol. 23, no. 11, pp. 1597–1607, 2015, doi: https://doi.org/10.1002/pip.2597.

[119] J. Li, S. H. Lim, C. R. Allen, D. Ding, and Y. Zhang, “Combined Effects of Shunt and Luminescence Coupling on External Quantum Efficiency Measurements of Multijunction Solar Cells,” *IEEE J. Photovolt.*, vol. 1, no. 2, pp. 225–230, Oct. 2011, doi: 10.1109/JPHOTOV.2011.2172188.

[120] *Fundamentals of Infrared and Visible Detector Operation and Testing*, 1st ed. John Wiley & Sons, Ltd, 2015.

[121] A. G. Aberle, S. R. Wenham, and M. A. Green, “A new method for accurate measurements of the lumped series resistance of solar cells,” in *Conference Record of the Twenty Third IEEE Photovoltaic Specialists Conference - 1993 (Cat. No.93CH3283-9)*, May 1993, pp. 133–139, doi: 10.1109/PVSC.1993.347065.

[122] S. J. Robinson, A. G. Aberle, and M. A. Green, “Departures from the principle of superposition in silicon solar cells,” *J. Appl. Phys.*, vol. 76, no. 12, pp. 7920–7930, Dec. 1994, doi: 10.1063/1.357902.

[123] H. Hovel, “Theoretical and experimental evaluations of GaAl As-GaAs solar cells,” 1974, pp. 25–30.

[124] A.-A. S. Al-Omar, “The collection probability and spectral response in isotype heterolayers of tandem solar cells,” *Solid-State Electron.*, vol. 50, no. 9–10, pp. 1656–1666, Sep. 2006, doi: 10.1016/j.sse.2006.07.009.

[125] M. A. Green, “Generalized relationship between dark carrier distribution and photocarrier collection in solar cells,” *J Appl Phys*, vol. 81, p. 268, 1997.

[126] A. Morales-Acevedo, “Analytical model for the photocurrent of solar cells based on graded band-gap CdZnTe thin films,” *Sol. Energy Mater. Sol. Cells*, vol. 95, no. 10, pp. 2837–2841, 2011, doi: 10.1016/j.solmat.2011.05.045.

[127] A. A. S. Al-Omar, “The collection probability and spectral response in isotype heterolayers of tandem solar cells,” *Solid-State Electron.*, vol. 50, no. 9–10, pp. 1656–1666, 2006, doi: 10.1016/j.sse.2006.07.009.

[128] M. P. Lumb *et al.*, “Simulation of novel InAlAsSb solar cells,” in *Proceedings SPIE 8256*, Feb. 2012, p. 82560S, doi: 10.1117/12.909324.

[129] K. J. Kim, M. H. Lee, J. H. Bahng, K. Shim, and B. D. Choe, “Optical constants and electronic interband transitions of disordered GaAs1−xPx alloys,” *J. Appl. Phys.*, vol. 84, no. 7, pp. 3696–3699, Oct. 1998, doi: 10.1063/1.368546.

[130] C. Alibert, G. Bordure, A. Laugier, and J. Chevallier, “Electroreflectance and Band Structure of Ga_xIn_1-xP,” *Phys. Rev. B*, vol. 6, no. 4, pp. 1301–1310, Aug. 1972, doi: 10.1103/PhysRevB.6.1301.

[131] T. J. Kim *et al.*, “Dielectric functions and interband transitions of InxAl1 − xP alloys,” *Curr. Appl. Phys.*, vol. 14, no. 9, pp. 1273–1276, Sep. 2014, doi: 10.1016/j.cap.2014.06.026.

[132] S. Adachi, *Optical Constants of Crystalline and Amorphous Semiconductors*. Boston, MA: Springer US, 1999.

[133] E. Ochoa-Martínez *et al.*, “Refractive indexes and extinction coefficients of n- and p-type doped GaInP, AlInP and AlGaInP for multijunction solar cells,” *Sol. Energy Mater. Sol. Cells*, vol. 174, no. April 2017, pp. 388–396, 2018, doi: 10.1016/j.solmat.2017.09.028.

[134] W. Yuan and D. C. Hall, “Variable-angle spectroscopic ellipsometry of InAlP native oxide dielectric layers for GaAs metal–oxide–semiconductor field effect transistor applications,” *J. Appl. Phys.*, vol. 113, no. 10, p. 103515, Mar. 2013, doi: 10.1063/1.4794817.

[135] S. Y. Hwang *et al.*, “Dielectric function and critical points of AlP determined by spectroscopic ellipsometry,” *J. Alloys Compd.*, vol. 587, pp. 361–364, Feb. 2014, doi: 10.1016/j.jallcom.2013.10.205.

[136] S. R. Kurtz, J. M. Olson, D. J. Friedman, J. F. Geisz, K. A. Bertness, and A. E. Kibbler, “Passivation of Interfaces in High-Efficiency Photovoltaic Devices,” *MRS Proc.*, vol. 573, no. May, p. 95, Jan. 1999, doi: 10.1557/PROC-573-95.

[137] C. C. Katsidis and D. I. Siapkas, “General transfer-matrix method for optical multilayer systems with coherent, partially coherent, and incoherent interference,” *Appl. Opt.*, vol. 41, no. 19, pp. 3978–3987, Jul. 2002, doi: 10.1364/AO.41.003978.

[138] O. S. Heavens, *Optical Properties of Thin Solid Films*. Dover Publications Inc., 1991.

[139] C. J. R. Sheppard, “Approximate calculation of the reflection coefficient from a stratified medium,” *Pure Appl. Opt. J. Eur. Opt. Soc. Part A*, vol. 4, no. 5, pp. 665–669, Sep. 1995, doi: 10.1088/0963-9659/4/5/018.

[140] Md. S. Islam, “Analytical modeling of organic solar cells including monomolecular recombination and carrier generation calculated by optical transfer matrix method,” *Org. Electron.*, vol. 41, pp. 143–156, Feb. 2017, doi: 10.1016/j.orgel.2016.10.040.

[141] M. P. Lumb *et al.*, “Extending the 1-D Hovel Model for Coherent and Incoherent Back Reflections in Homojunction Solar Cells,” *IEEE J. Quantum Electron.*, vol. 49, no. 5, pp. 462–470, May 2013, doi: 10.1109/JQE.2013.2252148.

[142] D. L. Lepkowski, T. Kasher, T. J. Grassman, and S. A. Ringel, “Designing an Epitaxially-Integrated DBR for Dislocation Mitigation in Monolithic GaAsP/Si Tandem Solar Cells,” *IEEE J. Photovolt.*, pp. 1–8, 2020, doi: 10.1109/JPHOTOV.2020.3043105.

[143] J. E. Northrup and S. B. Zhang, “Dopant and defect energetics: Si in GaAs,” *Phys. Rev. B*, vol. 47, no. 11, pp. 6791–6794, Mar. 1993, doi: 10.1103/PhysRevB.47.6791.

[144] V. Swaminathan, “Defects in GaAs,” *Bull Mater Sci*, vol. 4, no. 4, pp. 403–442, 1982.

[145] J. T. Boyer, A. N. Blumer, Z. H. Blumer, D. L. Lepkowski, and T. J. Grassman, “Reduced Dislocation Introduction in III–V/Si Heterostructures with Glide-Enhancing Compressively Strained Superlattices,” *Cryst. Growth Des.*, vol. 20, no. 10, pp. 6939–6946, Oct. 2020, doi: 10.1021/acs.cgd.0c00992.

[146] Y. Gu, Y. G. Zhang, H. Li, A. Z. Li, and C. Zhu, “Gas source MBE growth and doping characteristics of AlInP on GaAs,” *Mater. Sci. Eng. B*, vol. 131, no. 1, pp. 49–53, Jul. 2006, doi: 10.1016/j.mseb.2006.03.026.

[147] I. Vurgaftman, J. R. Meyer, and L. R. Ram-Mohan, “Band parameters for III–V compound semiconductors and their alloys,” *J. Appl. Phys.*, vol. 89, no. 11, pp. 5815–5875, Jun. 2001, doi: 10.1063/1.1368156.

[148] S. M. Sze, *Physics of Semiconductor Devices*, 2nd ed. John Wiley & Sons, Ltd, 1981.

[149] I. Sakata and H. Kawanami, “Band Discontinuities in Gallium Phosphide/Crystalline Silicon Heterojunctions Studied by Internal Photoemission,” *Appl. Phys. Express*, vol. 1, no. 9, p. 091201, Aug. 2008, doi: 10.1143/APEX.1.091201.

[150] X. M. Dai, M. A. Green, and S. R. Wenham, “High efficiency n-silicon solar cells using rear junction structures,” in *Conference Record of the Twenty Third IEEE Photovoltaic Specialists Conference - 1993 (Cat. No.93CH3283-9)*, May 1993, pp. 153–156, doi: 10.1109/PVSC.1993.347062.

[151] J. F. Geisz, M. A. Steiner, I. García, S. R. Kurtz, and D. J. Friedman, “Enhanced external radiative efficiency for 20.8% efficient single-junction GaInP solar cells,” *Appl. Phys. Lett.*, vol. 103, no. 4, p. 041118, Jul. 2013, doi: 10.1063/1.4816837.

[152] M. A. Steiner, J. F. Geisz, I. García, D. J. Friedman, A. Duda, and S. R. Kurtz, “Optical enhancement of the open-circuit voltage in high quality GaAs solar cells,” *J. Appl. Phys.*, vol. 113, no. 12, p. 123109, Mar. 2013, doi: 10.1063/1.4798267.

[153] E. Yablonovitch, B. J. Skromme, R. Bhat, J. P. Harbison, and T. J. Gmitter, “Band bending, Fermi level pinning, and surface fixed charge on chemically prepared GaAs surfaces,” *Appl. Phys. Lett.*, vol. 54, no. 6, pp. 555–557, Feb. 1989, doi: 10.1063/1.100929.

[154] H. Hasegawa, M. Akazawa, A. Domanowska, and B. Adamowicz, “Surface passivation of III–V semiconductors for future CMOS devices—Past research, present status and key issues for future,” *Appl. Surf. Sci.*, vol. 256, no. 19, pp. 5698–5707, Jul. 2010, doi: 10.1016/j.apsusc.2010.03.091.

[155] H. Hasegawa and M. Akazawa, “Surface passivation technology for III–V semiconductor nanoelectronics,” *Appl. Surf. Sci.*, vol. 255, no. 3, pp. 628–632, Nov. 2008, doi: 10.1016/j.apsusc.2008.07.002.

[156] A. Huijser, J. van Laar, and T. L. van Rooy, “Electronic surface properties of uhv-cleaved III–V compounds,” *Surf. Sci.*, vol. 62, no. 2, pp. 472–486, Feb. 1977, doi: 10.1016/0039-6028(77)90096-6.

[157] C. L. Hinkle *et al.*, “Detection of Ga suboxides and their impact on III-V passivation and Fermi-level pinning,” *Appl. Phys. Lett.*, vol. 94, no. 16, p. 162101, Apr. 2009, doi: 10.1063/1.3120546.

[158] L. Lin and J. Robertson, “Defect states at III-V semiconductor oxide interfaces,” *Appl. Phys. Lett.*, vol. 98, no. 8, p. 082903, Feb. 2011, doi: 10.1063/1.3556619.

[159] J. M. Gee and T. J. Drummond, “A theoretical investigation of effective surface recombination velocity in AlGaAs/GaAs heteroface solar cells,” Sandia National Labs., Albuquerque, NM (USA), SAND-90-2597C; CONF-9011118-2, Jan. 1990. Accessed: Sep. 02, 2019. [Online]. Available: 3.

[160] J. M. Olson, R. K. Ahrenkiel, D. J. Dunlavy, B. Keyes, and A. E. Kibbler, “Ultralow recombination velocity at Ga0.5In0.5P/GaAs heterointerfaces,” *Appl. Phys. Lett.*, vol. 55, no. 12, pp. 1208–1210, Sep. 1989, doi: 10.1063/1.101656.

[161] J. H. Zhao, J. Lee, Z. Q. Fang, T. E. Schlesinger, and A. G. Milnes, “The effects of the nonabrupt depletion edge on deep-trap profiles determined by deep-level transient spectroscopy,” *J. Appl. Phys.*, vol. 61, no. 12, pp. 5303–5307, Jun. 1987, doi: 10.1063/1.338265.

[162] Institution of Electrical Engineers, *Physics and Technology of Heterojunction Devices*. IET, 1991.

[163] S. Suckow, T. M. Pletzer, and H. Kurz, “Fast and reliable calculation of the two-diode model without simplifications,” *Prog. Photovolt. Res. Appl.*, vol. 22, no. 4, pp. 494–501, 2014, doi: https://doi.org/10.1002/pip.2301.

[164] “Recombination at semiconductor surfaces and interfaces,” *Surf. Sci.*, vol. 132, no. 1–3, pp. 406–421, Sep. 1983, doi: 10.1016/0039-6028(83)90550-2.

[165] S. M. Durbin, “A computational approach to the analysis of distributed Bragg reflectors in direct-gap solar cells,” in *Conference Record of the Twenty Fifth IEEE Photovoltaic Specialists Conference - 1996*, May 1996, pp. 69–72, doi: 10.1109/PVSC.1996.563948.

[166] R. M. France, P. Espinet-Gonzalez, N. J. Ekins-Daukes, H. Guthrey, M. A. Steiner, and J. F. Geisz, “Multijunction Solar Cells With Graded Buffer Bragg Reflectors,” *IEEE J. Photovolt.*, vol. 8, no. 6, pp. 1608–1615, Nov. 2018, doi: 10.1109/JPHOTOV.2018.2869550.

[167] M. Z. Shvarts, O. I. Chosta, I. V. Kochnev, V. M. Lantratov, and V. M. Andreev, “Radiation resistant AlGaAs/GaAs concentrator solar cells with internal Bragg reflector,” *Sol. Energy Mater. Sol. Cells*, vol. 68, no. 1, pp. 105–122, Apr. 2001, doi: 10.1016/S0927-0248(00)00349-4.

[168] S. P. Tobin, S. M. Vernon, M. M. Sanfacon, and A. Mastrovito, “Enhanced light absorption in GaAs solar cells with internal Bragg reflectors,” in *The Conference Record of the Twenty-Second IEEE Photovoltaic Specialists Conference - 1991*, Oct. 1991, pp. 147–152 vol.1, doi: 10.1109/PVSC.1991.169199.

[169] M. Yamaguchi, “Multi-junction solar cells and novel structures for solar cell applications,” *Phys. E Low-Dimens. Syst. Nanostructures*, vol. 14, no. 1, pp. 84–90, Apr. 2002, doi: 10.1016/S1386-9477(02)00362-4.

[170] K. Forghani, R. Reddy, D. Rowell, and R. Tatavarti, “MOVPE Growth of AlInP–InGaP Distributed Bragg Reflectors,” *IEEE J. Photovolt.*, vol. 10, no. 3, pp. 754–757, May 2020, doi: 10.1109/JPHOTOV.2020.2971145.

[171] D.-X. Wang *et al.*, "Enhanced Efficiency of Metamorphic Triple Junction Solar Cells for Space Applications," *Chin. Phys. Lett.*, vol. 34, no. 6, p. 068801, Jun. 2017, doi: 10.1088/0256-307X/34/6/068801.

[172] Y. Jiang, M. J. Keevers, P. Pearce, N. Ekins-Daukes, and M. A. Green, "Design of an intermediate Bragg reflector within triple-junction solar cells for spectrum splitting applications," *Sol. Energy Mater. Sol. Cells*, vol. 193, pp. 259–269, May 2019, doi: 10.1016/j.solmat.2019.01.011.

[173] Y. Horikoshi, M. Kawashima, and H. Yamaguchi, "Migration-Enhanced Epitaxy of GaAs and AlGaAs," *Jpn. J. Appl. Phys.*, vol. 27, no. 2R, p. 169, Feb. 1988, doi: 10.1143/JJAP.27.169.

[174] Y. Takagi, H. Yonezu, K. Samonji, T. Tsuji, and N. Ohshima, "Generation and suppression process of crystalline defects in GaP layers grown on misoriented Si(100) substrates," *J. Cryst. Growth*, vol. 187, no. 1, pp. 42–50, Apr. 1998, doi: 10.1016/S0022-0248(97)00862-2.

[175] A. Usui and H. Sunakawa, "GaAs Atomic Layer Epitaxy by Hydride VPE," *Jpn. J. Appl. Phys.*, vol. 25, no. 3A, p. L212, Mar. 1986, doi: 10.1143/JJAP.25.L212.

[176] R. D. Hool *et al.*, "Relaxed GaP on Si with low threading dislocation density," *Appl. Phys. Lett.*, vol. 116, no. 4, p. 042102, Jan. 2020, doi: 10.1063/1.5141122.

[177] K. N. Yaung, M. Vaisman, J. Lang, and M. L. Lee, "GaAsP solar cells on GaP/Si with low threading dislocation density," *Appl Phys Lett*, vol. 109, no. 3, p. 032107, Jul. 2016, doi: 10.1063/1.4959825.

[178] T. J. Grassman, D. J. Chmielewski, S. D. Carnevale, J. A. Carlin, and S. A. Ringel, "GaAs0.75P0.25/Si Dual-Junction Solar Cells Grown by MBE and MOCVD," *IEEE J. Photovolt.*, vol. 6, no. 1, pp. 326–331, Jan. 2016, doi: 10.1109/JPHOTOV.2015.2493365.

[179] C. L. Hinkle *et al.*, "GaAs interfacial self-cleaning by atomic layer deposition," *Appl. Phys. Lett.*, vol. 92, no. 7, p. 071901, Feb. 2008, doi: 10.1063/1.2883956.

[180] H. D. Trinh, E. Y. Chang, Y. Y. Wong, C. Y. Chang, and C. C. Yu, "Self-cleaning Effects on Atomic Layer Deposition (ALD) of Al_2O_3 on InGaAs with Several Surface Treatments," presented at the The Japan Society of Applied Physics, Sep. 2015, doi: https://doi.org/10.7567/SSDM.2009.P-6-3.

[181] V. Kumar and B. S. R. Sastry, "Thermal Expansion Coefficient of Binary Semiconductors," *Cryst. Res. Technol.*, vol. 36, no. 6, pp. 565–569, 2001, doi: https://doi.org/10.1002/1521-4079(200107)36:6<565::AID-CRAT565>3.0.CO;2-F.

[182] W. M. Yim and R. J. Paff, "Thermal expansion of AlN, sapphire, and silicon," *J. Appl. Phys.*, vol. 45, no. 3, pp. 1456–1457, Mar. 1974, doi: 10.1063/1.1663432.

[183] T. J. Grassman, J. A. Carlin, C. Ratcliff, D. J. Chmielewski, and S. A. Ringel, "Epitaxially-grown metamorphic GaAsP/Si dual-junction solar cells," in *2013 IEEE 39th Photovoltaic Specialists Conference (PVSC)*, Jun. 2013, pp. 0149–0153, doi: 10.1109/PVSC.2013.6744117.

[184] D. J. Chmielewski, D. L. Lepkowski, J. T. Boyer, J. A. Carlin, T. J. Grassman, and S. A. Ringel, "High Performance Metamorphic Tunnel Junctions for GaAsP/Si Tandem Solar Cells Grown via MOCVD," in *2018 IEEE 7th World Conference on Photovoltaic Energy Conversion (WCPEC) (A Joint Conference of 45th IEEE PVSC, 28th PVSEC 34th EU PVSEC)*, Jun. 2018, pp. 2631–2634, doi: 10.1109/PVSC.2018.8547444.

[185] D. J. Chmielewski, D. L. Lepkowski, J. T. Boyer, T. J. Grassman, and S. A. Ringel, "Metamorphic Tunnel Junctions Grown Via MOCVD Designed for GaAs0.75P0.25/Si Tandem Solar Cells," *IEEE J. Photovolt.*, vol. 11, no. 2, pp. 408–414, Mar. 2021, doi: 10.1109/JPHOTOV.2021.3052773.

[186] I. Almansouri *et al.*, "Designing Bottom Silicon Solar Cells for Multijunction Devices," *IEEE J. Photovolt.*, vol. 5, no. 2, pp. 683–690, Mar. 2015, doi: 10.1109/JPHOTOV.2014.2381875.

[187] K. R. McIntosh, T. G. Allen, S. C. Baker-Finch, and M. D. Abbott, "Light Trapping in Isotextured Silicon Wafers," *IEEE J. Photovolt.*, vol. 7, no. 1, pp. 110–117, Jan. 2017, doi: 10.1109/JPHOTOV.2016.2621347.

[188] D. A. Clugston and P. A. Basore, "PC1D version 5: 32-bit solar cell modeling on personal computers," in *Conference Record of the Twenty Sixth IEEE Photovoltaic Specialists Conference - 1997*, Sep. 1997, pp. 207–210, doi: 10.1109/PVSC.1997.654065.

[189] K. J. Kim, M. H. Lee, J. H. Bahng, K. Shim, and B. D. Choe, “Optical constants and electronic interband transitions of disordered GaAs1−xPx alloys,” *J. Appl. Phys.*, vol. 84, no. 7, pp. 3696–3699, Oct. 1998, doi: 10.1063/1.368546.

[190] M. Feifel *et al.*, “Gallium Phosphide Window Layer for Silicon Solar Cells,” *IEEE J. Photovolt.*, vol. 6, no. 1, pp. 384–390, Jan. 2016, doi: 10.1109/JPHOTOV.2015.2478062.

[191] S. Fan *et al.*, “20%-efficient epitaxial GaAsP/Si tandem solar cells,” *Sol. Energy Mater. Sol. Cells*, vol. 202, p. 110144, Nov. 2019, doi: 10.1016/j.solmat.2019.110144.

[192] Y. Sun, B. D. Li, R. D. Hool, S. Fan, M. Kim, and M. L. Lee, “Importance of Long-lifetime n-GaInP for High-efficiency GaInP Solar Cells Grown by MBE,” in *2020 47th IEEE Photovoltaic Specialists Conference (PVSC)*, Jun. 2020, pp. 0011–0013, doi: 10.1109/PVSC45281.2020.9300745.

APPENDIX: SELECTED CODE

SolarCellSimulator

Contributors:

Daniel Lepkowski

Tal Kasher

Revision date:

May, 20 2020

Limitations at present:

Outputs:

Quantum efficiency	EQE and IQE curves of the solar cell
Illuminated IV curves	LIV plot including the ideal IV curve, I-V curve after grid metal, and optionally the LIV including voltage dependent collection

Inputs:

Structure Input File

Structure File A single CSV file which includes all of the epitaxial/substrate layers and the back metal and their necessary transport properties.

A screenshot of an example file is shown below. See the Readme in the Structures folder for further details

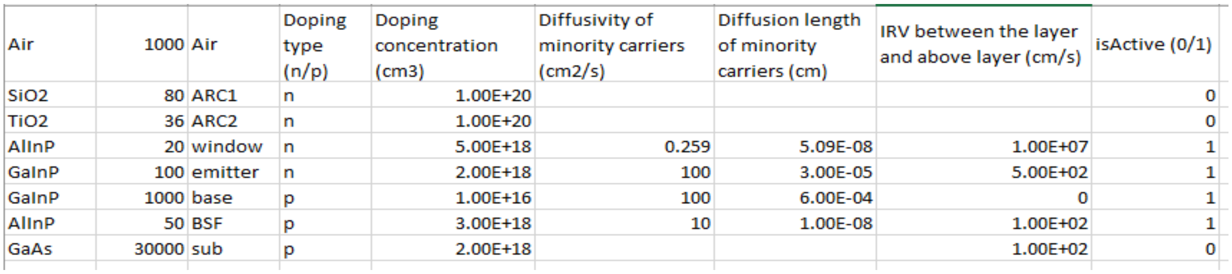

Air	1000	Air	Doping type (n/p)	Doping concentration (cm3)	Diffusivity of minority carriers (cm2/s)	Diffusion length of minority carriers (cm)	IRV between the layer and above layer (cm/s)	isActive (0/1)
SiO2	80	ARC1	n	1.00E+20				0
TiO2	36	ARC2	n	1.00E+20				0
AlInP	20	window	n	5.00E+18	0.259	5.09E-08	1.00E+07	1
GaInP	100	emitter	n	2.00E+18	100	3.00E-05	5.00E+02	1
GaInP	1000	base	p	1.00E+16	100	6.00E-04	0	1
AlInP	50	BSF	p	3.00E+18	10	1.00E-08	1.00E+02	1
GaAs	30000	sub	p	2.00E+18			1.00E+02	0

```
structureFileName='GaInPCell.csv';
```

Global Input Variables:

kT	Thermal constant (0.0259 eV)
q	Electron charge (1.602e-19 C)
binSize	Unit length step in the depth direction (cm) all values must be in 1e-# size (i.e. no 2e-7)
E0	Permittivity in Vaccuum (8.854E-14 F/cm)
rounding	Used to round depletion region widths to a multiple of the binsize

```
tic
global kT;
kT = 0.0259;
global q;
q = 1.6E-19;
global binSize;
binSize = 1e-7;  %1e-7 doesnt work
rounding = -log10(binSize);
E0 = 8.854E-14;
```

Parameters for I-V Simulation:

Spectrum	A string which holds the name of the desired solar spectrum ('AM0' or 'AM1p5G')
V_{min}	Minimum voltage for the ideal diode (not including series resistance)
V_{max}	Maximum voltage for the ideal diode (not including series resistance) This is set by the built-in voltage of the diode
V_{step}	Voltage step for the ideal diode (not including series resistance)
voltageDependentCollection	Boolean allowing user to toggle voltage dependent collection on an off
numOfVsteps	Number of voltage steps used in voltage dependent collection. Voltage step is not constant for improved simulation time

```
Vmin = 0;
Vstep = 0.0001;
voltageDependentCollection = 1;
numOfVsteps = 100;
spectrum='AM1p5G';
```

Parameters of QE simulation:

λ_{min}	Minimum wavelength for plotting
λ_{max}	Maximum wavelength for plotting

```
lambdaMin=350;
lambdaMax=1200;
```

Unit Cell Description:

A	*Dimension of the cell along the unit length of the busbar (cm)*
B	*Dimension of the cell along the grid finger length (cm)*

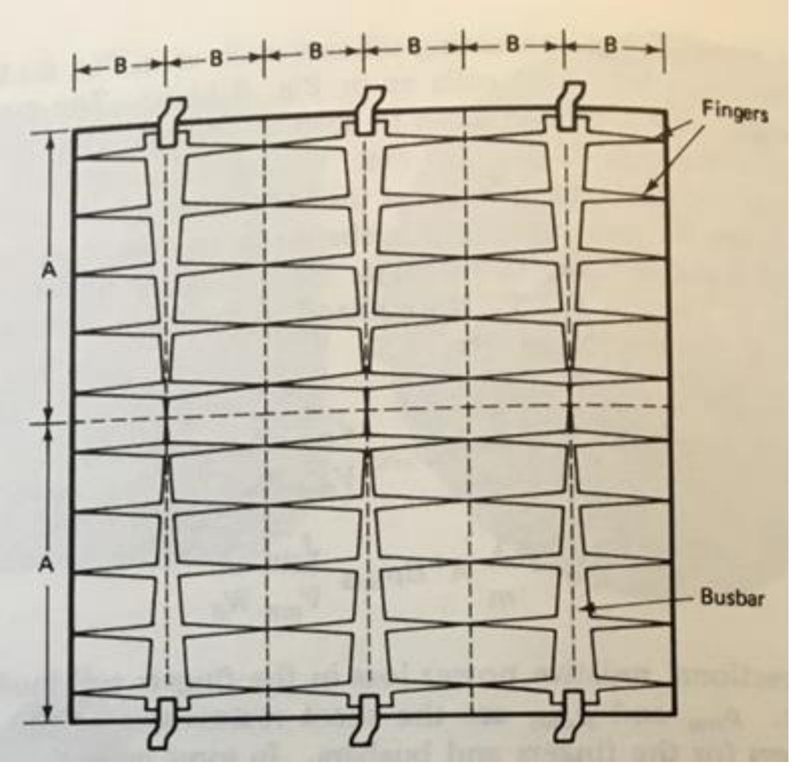

```
A = 7.8;
B = 2.6;
```

Parameters for grid metal:

ρ_S	Semiconductor sheet resistivity
t	Thickness of the grid metal
W_F	Width of the grid fingers
m_f	Variable which accounts for tappering of grid fingers ($m_f\ = 4$ linearly tapered) ($m_f\ = 3$ for constant width)
m_b	Variable which accounts for tappering of busbar ($m_f\ = 4$ linearly tapered) ($m_f\ = 3$ for constant width)
fixedGrid	Boolean variable that allows user to specify a fixed grid or the optimal grid (0/1)
W_B	Average Width of the Busbar (cm) (only used if fixedGrid=1)
S	Spacing between grid fingers (cm) (only used if fixedGrid=1) **Must be greater than W_F**

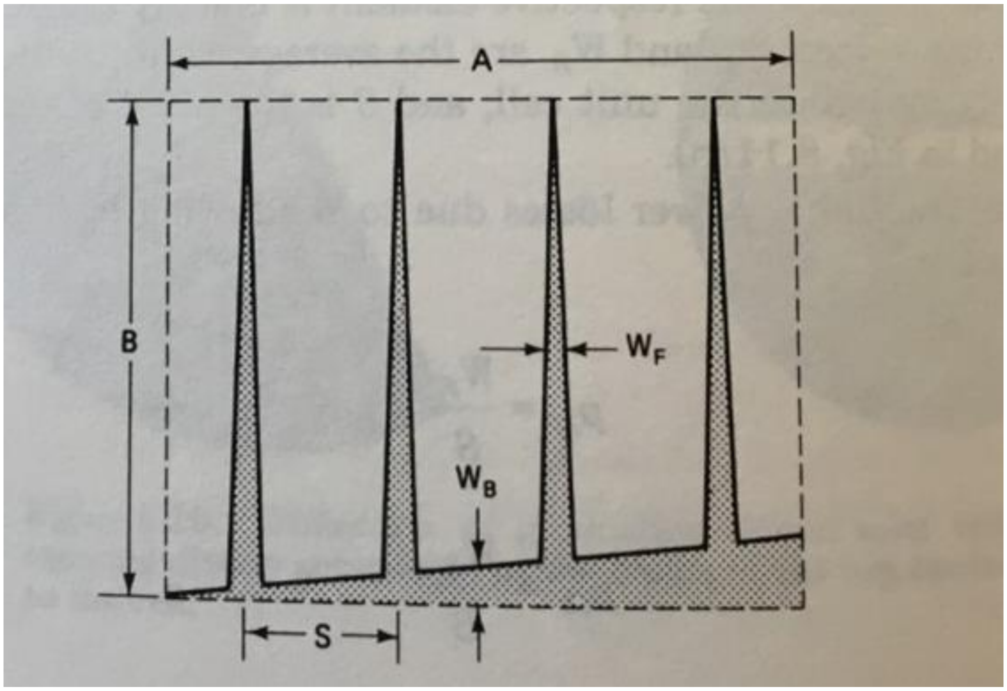

```
fixedGrid = 0;
rho_S = 1000;
mf = 3;
mb = 4;
t = 5E-4;
W_F = 1E-3;
```

Only used if fixedGrid=1

```
W_B = 1E-1;
S = 8E-2;
```

Error handling in case the user puts in non-physical values

```
if S <= W_F
    error('It is not physical for the gridfinger pitch to be less than
the width of a finger')
end
```

User Controled Parameters for Double Diode:

n_2	Ideality factor of the junction-recombination current diode
$R_{\text{series Vertical}}$	Vertical component of the series resistance to be used as a fitting parameter $(\Omega \cdot \text{cm}^2)$
R_{Shunt}	Area normalized shunt resistance $(\Omega \cdot \text{cm}^2)$
τ_d	Lifetime in the depletion region (s)

```
Rshunt = 1e4;
RseriesVertical = 1E-3;
n2=2;
tau_d = 1e-6;
```

Materials parameters:

There are some materials parameters that are not yet automatically updated

n_i	The intrisic carrier concentration (cm^{-3})

	(GaAs=2.1e6) (GaInP ~1000)
ϵ_s	relative permitivity
	(GaAs=12.88) (GaInP(11.8)

```
ni = 500;
Es = 11.8;
```

Read in CSV files:

Directory setup

```
tic
homeDirectory= pwd;
addpath(strcat(homeDirectory,'\Functions\'));
opticalDataBase = strcat(homeDirectory,'\Optical Data\');
structureFilePath =
strcat(strcat(homeDirectory,'\Structures\'),structureFileName);
spectrumFilePath=
strcat(homeDirectory,strcat('\Spectra\',strcat(spectrum,'.csv')));
```

```
[Thickness,layerType,numOfLayers,Materials,dopingType,dopingLevel,diffusi
vity,diffusionLength,IRV,isActive] = getStructure(structureFilePath);
```

Using the Structure as a guide, retrieve the necessary optical data

```
[nComplex] = getOpticalData(opticalDataBase,Materials,numOfLayers);
```

Retrieve the desired spectrum

```
solarSpectrum  = readvars(spectrumFilePath);
```

Variables extracted from CSV files:

Thickness	An array with the thickness of each layer

layerType	An array of strings with the layer names. This is used to determine the substrate
Materials	An array of strings with material names. Please follow the material naming guide in the strucutres readme
dopingType	An array of strings indicating 'n' or 'p' type material
dopingLevel	An array which contains the doping concentration in each layer (cm^{-3})
diffusivity	An array which contains the diffusivity of each layer (cm^2/s)
diffusionLength	An array which contains the diffusion length of each layer (cm)
IRV	An array which contains the IRV of all of the layers to its adjacent layer on the top. (cm/s)
nComplex	An array of complex indicies of refraction (n+ik)
solarSpectrum	An array which contains the wavelength depedent solar flux (A/cm^2)
isActive	An array of booleans that determine whether or not the layer is active in collection. (0/1)

Parse Structure:

Search for the substrate layer

```
 substrateLayer = 0; %Not going to do a infinite check on substrate if
there is no substrate in structure file
 for layerIndex = 1:length(layerType)
     if strcmp(layerType(layerIndex),'substrate') ||
strcmp(layerType(layerIndex),'Substrate') ||
strcmp(layerType(layerIndex),'sub') || strcmp(layerType(layerIndex),'Sub')
         substrateLayer = layerIndex;
      elseif strcmp(layerType(layerIndex),'emitter') ||
strcmp(layerType(layerIndex),'Emitter')
         emitterLayer = layerIndex;
     elseif strcmp(layerType(layerIndex),'base') ||
strcmp(layerType(layerIndex),'Base')
         baseLayer = layerIndex;
     end
 end
```

Search for the junction and assign properties to the layers adjacent to the junction for LIV

```
 NonP = 0;
 PonN =0;
 junctionTopIndex = 0;
 junctionBottomIndex = 0;
 for dopingIndex = 1:length(dopingType)-1
     if strcmp(dopingType(dopingIndex),'n') &&
strcmp(dopingType(dopingIndex+1),'p')
         junctionTopIndex = dopingIndex;
         junctionBottomIndex = dopingIndex+1;
         Nd = dopingLevel(junctionTopIndex);
         Na = dopingLevel(junctionBottomIndex);
         Dp = diffusivity(junctionTopIndex);
         Dn = diffusivity(junctionBottomIndex);
         Lp = diffusionLength(junctionTopIndex);
         Ln = diffusionLength(junctionBottomIndex);
         Sp = IRV(junctionTopIndex);
         Sn = IRV(junctionBottomIndex+1);
         NonP = 1;
     elseif strcmp(dopingType(dopingIndex),'p') &&
strcmp(dopingType(dopingIndex+1),'n')
         junctionTopIndex = dopingIndex;
         junctionBottomIndex = dopingIndex+1;
         Na = dopingLevel(junctionTopIndex);
         Nd = dopingLevel(junctionBottomIndex);
         Dn = diffusivity(junctionTopIndex);
         Dp = diffusivity(junctionBottomIndex);
         Ln = diffusionLength(junctionTopIndex);
         Lp = diffusionLength(junctionBottomIndex);
         Sn = IRV(junctionTopIndex);
         Sp = IRV(junctionBottomIndex+1);
         PonN = 1;
     end
 end
```

Error Handling: If the junction is not found or if it is found more than once

```
 if (junctionTopIndex == 0 || junctionBottomIndex == 0) || NonP == PonN
     error('Active junction not properly defined. Check doping type
definitions.')
 end
```

Quantum Efficiency:

For future functionallity: embedded drift fields can enhance diffusion length.

```
E = [0,0,0,0,0,0,0,0,0,0,0,0,0,0,0,0,0];
```

Calculation of depletion width and rounding tto the nearest binsize so that the discrete nature of the CP piecewise curve will work

```
 Vbi = kT*log(Nd*Na/(ni^2));
 W_dep_Emit = sqrt((2*E0*Es/q)*(Na/Nd)*(1/(Na+Nd))*Vbi);
 W_dep_Base = sqrt((2*E0*Es/q)*(Nd/Na)*(1/(Na+Nd))*Vbi);
 W_dep_Emit = round(W_dep_Emit,rounding);
 W_dep_Base = round(W_dep_Base,rounding);

 if W_dep_Emit > Thickness(emitterLayer) || W_dep_Base >
Thickness(baseLayer)
     error('Either the Emitter or Base is Fully Depleted')
 end
```

Calculating EQE, IQE, and Rfront

```
 %------------------------------------------------------------------------
--
 % EQE - Does not account for grid metal coverage (small spot measurement)
 %------------------------------------------------------------------------
--
 [Jphoto,EQE,IQE,Rfront] =
QuantumEfficiency(junctionTopIndex,junctionBottomIndex,substrateLayer,diff
usionLength,diffusivity,IRV,E,W_dep_Emit,W_dep_Base,nComplex,Thickness,isA
ctive,numOfLayers,solarSpectrum);
```

Plotting EQE

```
 figure(2)
 lambda = (350:1:1200);
 plot(lambda,EQE,lambda,Rfront,lambda,IQE)
 ylabel('EQE (%)')
 xlabel('Wavelength (nm)')
 xlim([lambdaMin lambdaMax])
```

```
ylim([0 1])
```

Illuminated I-V

Set Vmax based on Vbi. Sometimes this will fail and give negative eff. just need to decrease Vbi multiplier to fix.

```
Vmax = round(0.95*Vbi,1);
```

Get standard LIV

this function returns 3 key things.

1. The ideal I-V curve with no grid metal (and stats
2. The I-V curve including series resistance
3. The Grid metal parameters

```
[V,JlightmA,Vdiode,JlightIdealmA,Rseries,Rshunt,J01,J02,percentMetal,FFGrid,FFIdeal,EffGrid,EffIdeal,Jsc,Voc,Jmp,Vmp] = LIV(spectrum,Dn,Dp,Ln,Lp,tau_d,Sn,Sp,Rshunt,...
    RseriesVertical,n2,ni,...
    Nd,Na,Jphoto*(1E-3),rho_S,Thickness(emitterLayer),Thickness(baseLayer),W_dep_Emit,W_dep_Base,A,B,Vmin,Vmax,Vstep,mf,mb,t,S,W_F,fixedGrid,W_B);
```

Plotting the LIV data

Dont plot if you are going to plot it later.

```
if voltageDependentCollection == 0
    figure(3)
    plot(V,JlightmA,Vdiode,JlightIdealmA)
    title(structureFileName)
    xlim([Vmin round((Voc+0.1),1)])
    ylim([0 1.2*max(Jphoto)])
    xticks(Vmin:0.1:round((Voc+0.1),1))
    yticks(0:5:1.2*max(Jphoto))
    xlabel('Voltage (V)')
```

```
     ylabel('Current Density (mA/cm^2)')
     set(gca,'YMinorTick','on','XMinorTick','on')
     txt = {['\eta_{grid} = ' num2str(round(EffGrid,1))
'%'],['\eta_{ideal} = ' num2str(round(EffIdeal,1)) '%'],...
     ['FF_{grid} = ' num2str(round(FFGrid*100,1)) '%'],['FF_{ideal} = '
num2str(round(FFIdeal*100,1)) '%'],...
     ['J_{SC} = ' num2str(round(Jsc*1000,1)) 'mA'], ['V_{OC} = '
num2str(round(Voc,3)) 'V']};
     text(Voc/30,Jsc*1000/1.6,txt)
     legend('J_{grid}','J_{Ideal}','Location','southwest')

     T = table(FFIdeal,FFGrid,Ln)
 end
```

Voltage Dependent Carrier Collection

```
 if voltageDependentCollection == 1
```

create the voltage dependent voltage array. this is cdone creativly so that we have move datapoints around max power point

```
     VdiodeVDCC = [linspace(Vmin,0.9*Vmp,numOfVsteps/3)
linspace(0.91*Vmp,1.1*Vmp,numOfVsteps/3)
linspace(1.11*Vmp,Vmax,numOfVsteps/3)];
```

calculating voltage dependent photocurrent

```
    for i = 1:length(VdiodeVDCC)
         W_dep_Emit = sqrt((2*E0*Es/q)*(Na/Nd)*(1/(Na+Nd))*(Vbi-
VdiodeVDCC(i)));
         W_dep_Base = sqrt((2*E0*Es/q)*(Nd/Na)*(1/(Na+Nd))*(Vbi-
VdiodeVDCC(i)));
         W_dep_Emit = round(W_dep_Emit,rounding);
         W_dep_Base = round(W_dep_Base,rounding);
         Jphoto(i) =
QuantumEfficiency(junctionTopIndex,junctionBottomIndex,substrateLayer,diff
usionLength,diffusivity,IRV,E,W_dep_Emit,W_dep_Base,nComplex,Thickness,isA
ctive,numOfLayers,solarSpectrum);
    end
```

Calculating the I-V curve inlcuding VDCC

```
    [Vvdcc,JlightVDCC,FFVDCC,EffVDCC] =
LIV_VDCC(spectrum,Rshunt,Rseries,n2,Jphoto*(1E-
3),VdiodeVDCC,J01,J02,percentMetal);
```

Plotting the LIV data

```
    figure(3)
    plot(V,JlightmA,Vdiode,JlightIdealmA,Vvdcc,JlightVDCC,'--o')
    title(structureFileName)
    xlim([Vmin round((Voc+0.1),1)])
    ylim([0 1.2*max(Jphoto)])
    xticks(Vmin:0.1:round((Voc+0.1),1))
    yticks(0:5:1.2*max(Jphoto))
    xlabel('Voltage (V)')
    ylabel('Current Density (mA/cm^2)')
    set(gca,'YMinorTick','on','XMinorTick','on')
    legend('J_{grid}','J_{Ideal}','J_{VDCC}','location',"southwest")
    txt = {['\eta_{grid} = ' num2str(round(EffGrid,1)) '%'],['\eta_{ideal}
= ' num2str(round(EffIdeal,1)) '%'],['\eta_{VDCC} = '
num2str(round(EffVDCC,1)) '%'],...
        ['FF_{grid} = ' num2str(round(FFGrid*100,1)) '%'],['FF_{ideal} = '
num2str(round(FFIdeal*100,1)) '%'],['FF_{VDCC} = '
num2str(round(FFVDCC*100,1)) '%'],...
        ['J_{SC} = ' num2str(round(Jsc*1000,1)) 'mA'], ['V_{OC} = '
num2str(round(Voc,3)) 'V']};
    text(Voc/30,Jsc*1000/1.6,txt)
    T = table(FFIdeal,FFGrid,FFVDCC,Ln)
    else
  toc
 end
```

Get Structure

Function to Read Structure from User Excel Sheets

This will not work with Pre 2019 MATLAB

```
 function
[Thickness,layerType,NumOfLayers,Materials,dopingType,dopingLevel,diffusiv
ity,diffusionLength,IRV,isActive] = getStructure(structureFilename)

 [Materials,Thickness,layerType,dopingType,dopingLevel,diffusivity,diffusi
onLength,IRV,isActive]  = readvars(structureFilename);

 Thickness(:) = Thickness(:)*1e-7;
 NumOfLayers = length(Materials);

 end
```

getOpticalData

Function to Optical Data from User Excel Sheets

Returns relevant data to TMM script

This will not work with Pre 2019 MATLAB

```
 function [nComplex] =
getOpticalData(opticalDataBase,Materials,numOfLayers)

 nComplex = ones(851,numOfLayers);
 n = ones(851,1);
 k = ones(851,1);

 for j = 1:numOfLayers
     if strcmp(Materials(j),'Air')
        [n(:,j),k(:,j)] = readvars(strcat(opticalDataBase,'Air.csv'));
     elseif strcmp(Materials(j),'Al')
         [n(:,j),k(:,j)] = readvars(strcat(opticalDataBase,'Al.csv'));
     elseif strcmp(Materials(j),'Al2O3')
         [n(:,j),k(:,j)] = readvars(strcat(opticalDataBase,'Al2O3.csv'));
     elseif strcmp(Materials(j),'AlInP')
         [n(:,j),k(:,j)] = readvars(strcat(opticalDataBase,'AlInP.csv'));
     elseif strcmp(Materials(j),'Ga64In36P')
         [n(:,j),k(:,j)] =
readvars(strcat(opticalDataBase,'Ga64In36P.csv'));
     elseif strcmp(Materials(j),'GaAs75P25')
         [n(:,j),k(:,j)] =
readvars(strcat(opticalDataBase,'GaAs75P25.csv'));
     elseif strcmp(Materials(j),'GaAsP_3p5')
         [n(:,j),k(:,j)] =
readvars(strcat(opticalDataBase,'GaAsP_3p5.csv'));
```

```
      elseif strcmp(Materials(j),'GaAsP_7')
          [n(:,j),k(:,j)] = 
readvars(strcat(opticalDataBase,'GaAsP_7.csv'));
      elseif strcmp(Materials(j),'GaAsP_10p5')
      [n(:,j),k(:,j)] = readvars(strcat(opticalDataBase,'GaAsP_10p5.csv'));
      elseif strcmp(Materials(j),'GaAsP_14')
      [n(:,j),k(:,j)] = readvars(strcat(opticalDataBase,'GaAsP_14.csv'));
      elseif strcmp(Materials(j),'GaAsP_17p5')
      [n(:,j),k(:,j)] = readvars(strcat(opticalDataBase,'GaAsP_17p5.csv'));
      elseif strcmp(Materials(j),'GaAsP_21')
      [n(:,j),k(:,j)] = readvars(strcat(opticalDataBase,'GaAsP_21.csv'));
      elseif strcmp(Materials(j),'GaAsP_24p5')
      [n(:,j),k(:,j)] = readvars(strcat(opticalDataBase,'GaAsP_24p5.csv'));
      elseif strcmp(Materials(j),'GaAsP_28')
      [n(:,j),k(:,j)] = readvars(strcat(opticalDataBase,'GaAsP_28.csv'));
      elseif strcmp(Materials(j),'GaAsP_31p5')
      [n(:,j),k(:,j)] = readvars(strcat(opticalDataBase,'GaAsP_31p5.csv'));
      elseif strcmp(Materials(j),'GaAsP_35')
      [n(:,j),k(:,j)] = readvars(strcat(opticalDataBase,'GaAsP_35.csv'));
      elseif strcmp(Materials(j),'GaAsP_38p5')
      [n(:,j),k(:,j)] = readvars(strcat(opticalDataBase,'GaAsP_38p5.csv'));
      elseif strcmp(Materials(j),'GaAsP_42')
      [n(:,j),k(:,j)] = readvars(strcat(opticalDataBase,'GaAsP_42.csv'));
      elseif strcmp(Materials(j),'GaAsP_45p5')
      [n(:,j),k(:,j)] = readvars(strcat(opticalDataBase,'GaAsP_45p5.csv'));
      elseif strcmp(Materials(j),'GaAsP_49')
      [n(:,j),k(:,j)] = readvars(strcat(opticalDataBase,'GaAsP_49.csv'));
      elseif strcmp(Materials(j),'GaAsP_52p5')
      [n(:,j),k(:,j)] = readvars(strcat(opticalDataBase,'GaAsP_52p5.csv'));
      elseif strcmp(Materials(j),'GaAsP_56')
      [n(:,j),k(:,j)] = readvars(strcat(opticalDataBase,'GaAsP_56.csv'));
      elseif strcmp(Materials(j),'GaAsP_59p5')
      [n(:,j),k(:,j)] = readvars(strcat(opticalDataBase,'GaAsP_59p5.csv'));
      elseif strcmp(Materials(j),'GaAsP_63')
      [n(:,j),k(:,j)] = readvars(strcat(opticalDataBase,'GaAsP_63.csv'));
      elseif strcmp(Materials(j),'GaAsP_66p5')
      [n(:,j),k(:,j)] = readvars(strcat(opticalDataBase,'GaAsP_66p5.csv'));
      elseif strcmp(Materials(j),'GaAsP_70')
      [n(:,j),k(:,j)] = readvars(strcat(opticalDataBase,'GaAsP_70.csv'));
      elseif strcmp(Materials(j),'GaAsP_73p5')
      [n(:,j),k(:,j)] = readvars(strcat(opticalDataBase,'GaAsP_73p5.csv'));
      elseif strcmp(Materials(j),'GaP')
      [n(:,j),k(:,j)] = readvars(strcat(opticalDataBase,'GaP.csv'));
      elseif strcmp(Materials(j),'Si')
      [n(:,j),k(:,j)] = readvars(strcat(opticalDataBase,'Si.csv'));
```

```
    elseif strcmp(Materials(j),'TiO2')
    [n(:,j),k(:,j)] = readvars(strcat(opticalDataBase,'TiO2.csv'));
    elseif strcmp(Materials(j),'GaAs')
    [n(:,j),k(:,j)] = readvars(strcat(opticalDataBase,'GaAs.csv'));
    elseif strcmp(Materials(j),'Ga2O3')
    [n(:,j),k(:,j)] = readvars(strcat(opticalDataBase,'Ga2O3.csv'));
    elseif strcmp(Materials(j),'SiO2')
    [n(:,j),k(:,j)] = readvars(strcat(opticalDataBase,'SiO2.csv'));
    elseif strcmp(Materials(j),'GaInP')
    [n(:,j),k(:,j)] = readvars(strcat(opticalDataBase,'GaInP.csv'));
    elseif strcmp(Materials(j),'Al31GaAs')
    [n(:,j),k(:,j)] = readvars(strcat(opticalDataBase,'Al31GaAs.csv'));
    end
    nComplex(:,j) = n(:,j)+1i*k(:,j);
end
end
```

Quantum Efficiency

This function calculates the quantum efficiency of any single junction cell.

Contributors:

Daniel Lepkowski

Tal Kasher

Revision date:

May, 21 2020

```
 function [Jphoto,EQE,IQE,Rfront] =
QuantumEfficiency(junctionTopIndex,junctionBottomIndex,substrateLayer,diff
usionLength,diffusivity,IRV,E,W_dep_Top,...

W_dep_Bottom,nComplex,Thickness,isActive,numOfLayers,solarSpectrum)
 global binSize;

 firstcase=1;
 for i=1:numOfLayers
     if isActive(i)==1
         [PGtemp,x,Rfront] =
Photogenerate(i,substrateLayer,nComplex,Thickness,numOfLayers);
         if firstcase==1
             PG = PGtemp(:,1:length(x));
         else
             [PG] = [PG PGtemp(:,1:length(x)-1)];
         end
         firstcase=0;
     end
 end
 k=1;

 for j=1:junctionTopIndex-1
     if isActive(j)==1

         W(k)=Thickness(j);
         isDepleted(k)=0;
         LD(k)=diffusionLength(j);
         D(k)=diffusivity(j);
         S(k)=IRV(j);

         k=k+1;
```

```
    end
end

        W(k)=Thickness(junctionTopIndex)-W_dep_Top;
        isDepleted(k)=0;
        LD(k)=diffusionLength(junctionTopIndex);
        D(k)=diffusivity(junctionTopIndex);
        S(k)=IRV(junctionTopIndex);

        W(k+1) = W_dep_Top;
        isDepleted(k+1)=1;
        LD(k+1)=diffusionLength(junctionTopIndex);
        D(k+1)=diffusivity(junctionTopIndex);
        S(k+1)=IRV(junctionTopIndex);
        depTopIndex=k+1;

        W(k+2)=W_dep_Bottom;
        isDepleted(k+2)=1;
        LD(k+2)=diffusionLength(junctionBottomIndex);
        D(k+2)=diffusivity(junctionBottomIndex);
        S(k+2)=IRV(junctionBottomIndex);
        depBottomIndex=k+2;

        W(k+3)=Thickness(junctionBottomIndex) - W_dep_Bottom;
        isDepleted(k+3)=0;
        LD(k+3)=diffusionLength(junctionBottomIndex);
        D(k+3)=diffusivity(junctionBottomIndex);
        S(k+3)=IRV(junctionBottomIndex);

k=k+4;
for j=junctionBottomIndex+1:numOfLayers
    if isActive(j)==1
        W(k) = Thickness(j);
        isDepleted(k)=0;
        LD(k)=diffusionLength(j);
        D(k)=diffusivity(j);
        S(k)=IRV(j);
        k=k+1;
    end
end
% Eventually to be repalced with user definition per structure
xTotalFront=0;
%Away from Depletion Region to the Front
for l = depTopIndex:-1:1
```

```
     if l==depTopIndex
         x = W(l):-binSize:0;
         CP0 = 1;
     else
         x = W(l)-binSize:-binSize:0;
         CP0 = CP(1,1);
     end
     clear CP_temp;
     [CP_temp] =
ProbOfCollection(LD(l),E(l),D(l),W(l),S(l),CP0,isDepleted(l),x);

     if l==depTopIndex
         CP = CP_temp;
     else
         CP = [CP_temp CP];
     end
     xTotalFront = xTotalFront+length(x);
 end

 %Including both sides of the Depletion Region to the Back
 xTotalBack = xTotalFront;
 for l = depBottomIndex:length(W)

     x = 0:binSize:W(l)-binSize;

     clear CP_temp;

     [CP_temp] =
ProbOfCollection(LD(l),E(l),D(l),W(l),IRV(l+1),CP0,isDepleted(l),x);

     if l==depTopIndex
         CP0 = 1;
     else
         CP0=CP(1,xTotalBack);
     end

     CP = [CP CP_temp];

     xTotalBack = length(x) + xTotalBack;
 end
 EQE = CP.*PG;

 EQE = EQE.';
 EQE = sum(EQE).*binSize;
 IQE = EQE./(1-Rfront');
```

```
 Jphoto = sum(EQE.*solarSpectrum')*1000; %[mA/cm^2]
 end
```

Photogenerate

TMM Model - returns PG, and some info about the structure

Contributors:

Daniel Lepkowski

Tal Kasher

Revision date:

May, 21 2020

```
 function [PG,x,Rfront] =
Photogenerate(activeLayer,substrateLayer,nComplex,thickness,numOfLayers)

 global binSize;

 k = imag(nComplex);
 n = real(nComplex);

 lambda = [350e-7:1e-7:1200e-7];
 x= [0:binSize:thickness(activeLayer)];
```

Calculating the Interface Matrix for each layer (o) and each wavelength (n)

```
 I = ones(2,2,length(n),numOfLayers-1);
 for o = 1:numOfLayers-1
     for m = 1:length(n)
         I(:,:,m,o) =
[(nComplex(m,o)+nComplex(m,o+1))./(2*(nComplex(m,o))), (nComplex(m,o)-
(nComplex(m,o+1)))./(2*(nComplex(m,o))); (nComplex(m,o)-
(nComplex(m,o+1)))./(2*(nComplex(m,o))),
(nComplex(m,o)+(nComplex(m,o+1)))/(2*(nComplex(m,o)))];
     end
 end
```

Calculating the Layer Matrix for each layer (o) and each wavelength (n)

```
 L = ones(2,2,length(n),numOfLayers-2);
```

```
alpha = ones(length(n),numOfLayers-1);
for o = 1:numOfLayers-2
    for m = 1:length(n)
        alpha(m,o+1) = 4*pi.*k(m,o+1)./lambda(m);
        L(:,:,m,o) = [exp(-
1*1i*2*pi.*nComplex(m,o+1).*thickness(o+1)./lambda(m)),0;0,
exp(1i*2*pi.*nComplex(m,o+1).*thickness(o+1)./lambda(m))];
    end
end
```

Calculating the Scattering Matricies Pre active layer

```
Spre  = zeros(2,2,length(n));
Spre(1,1,:) = ones(1,1,length(n));
Spre(2,1,:) = zeros(1,1,length(n));
Spre(1,2,:) = zeros(1,1,length(n));
Spre(2,2,:) = ones(1,1,length(n));
for o1 = 1:activeLayer-2
    for m = 1:length(n)
        Spre(:,:,m) = Spre(:,:,m)*I(:,:,m,o1)*L(:,:,m,o1);
    end
end
for m = 1:length(n)
    Spre(:,:,m) = Spre(:,:,m)*I(:,:,m,activeLayer-1);
end
```

Calculating the Scattering Matrices Post active layer

```
Spost  = zeros(2,2,length(n));
Spost(1,1,:) = ones(1,1,length(n));
Spost(2,1,:) = zeros(1,1,length(n));
Spost(1,2,:) = zeros(1,1,length(n));
Spost(2,2,:) = ones(1,1,length(n));
for o3 = activeLayer:numOfLayers-2
    for m = 1:length(n)
        Spost(:,:,m) = Spost(:,:,m)*I(:,:,m,o3)*L(:,:,m,o3);
    end
end
for m = 1:length(n)
    Spost(:,:,m) = Spost(:,:,m)*I(:,:,m,numOfLayers-1);
end

%Calculating the Scattering Matrices of total structure
```

```
Sfront  = zeros(2,2,length(n));
Sfront(1,1,:) = ones(1,1,length(n));
Sfront(2,1,:) = zeros(1,1,length(n));
Sfront(1,2,:) = zeros(1,1,length(n));
Sfront(2,2,:) = ones(1,1,length(n));
for o = 1:numOfLayers-2
    for m = 1:length(n)
        Sfront(:,:,m) = Sfront(:,:,m)*I(:,:,m,o)*L(:,:,m,o);
    end

end
for m = 1:length(n)
    Sfront(:,:,m) = Sfront(:,:,m)*I(:,:,m,numOfLayers-1);
end
```

Front Reflection and Transmission

```
rfront= Sfront(2,1,:)./Sfront(1,1,:);
rfront = permute(rfront,[3 2 1]);
Rfront=abs(rfront).^2;
tfront = 1./Sfront(1,1,:);
tfront = permute(tfront,[3 2 1]);
Tfront=real(n(:,numOfLayers))./real(n(:,1)).*abs(tfront).^2;


rpre = Spre(2,1,:)./Spre(1,1,:);
rpre = permute(rpre,[3 2 1]);
tpre = 1./Spre(1,1,:);
tpre = permute(tpre,[3 2 1]);
Tpre=real(n(:,activeLayer))./real(n(:,1)).*abs(tpre).^2;
Rpre=(abs(rpre)).^2;

rpost= Spost(2,1,:)./Spost(1,1,:);
rpost = permute(rpost,[3 2 1]);

%whitewash
test2=isfinite(rpost(:));
for m=2:length(n)
    if test2(m)==0
        rpost(m) = rpost(m-1);
    end

end
```

```
 Rpost=(abs(rpost)).^2;

 tpost = 1./Spost(1,1,:);
 tpost = permute(tpost,[3 2 1]);
 Tpost=real(n(:,numOfLayers))./real(n(:,activeLayer)).*abs(tpost).^2;
```

%Calculation of Light Intensity and Photogeneration as function of wavelength and depth

```
 I0 = ones(length(n),1);
%for QE this is 1
 Iactive = zeros(length(n),length(x));
 PG = zeros(length(n),length(x));
 for m = 1:length(n)
         Iactive(m,:) = Tpre(m)*I0(m)*(exp(-alpha(m,activeLayer).*x(:)) +
...
             abs(rpost(m))*2*exp(-
alpha(m,activeLayer).*(2*thickness(activeLayer)-x(:))) + ...
              2*abs(rpost(m))*exp(-
alpha(m,activeLayer)*thickness(activeLayer))*...

(cos((4*pi*n(m,activeLayer)/lambda(m)).*(thickness(activeLayer)-
x(:))+angle(rpost(m)))));
         PG(m,:) = alpha(m,activeLayer).*Iactive(m,:);
 end

 end
```

ProbOfCollection

Calculates the collection probability for any layer given it's transport properties and whether or not its depleted

Contributors:

Daniel Lepkowski

Tal Kasher

Revision date:

May, 19 2020

Inputs:

L_D Minority carrier diffusion length in the region of interest (cm)

E Constant electric field in the region of interest (V/cm)

D Diffusivity of minority carriers ($\frac{\mathrm{cm}^2}{s}$).

W Width of the layer of interest (cm).

x An array of x values with x=0 starting at the interface closest to the depletion region. (cm)

CP_0 the collection probability at the end of the layer touching x=0.

IRV The minority carrier interface recombination velocity at x=W. (cm/s)

isDepleted A boolean value which states whether or not a layer is part of the depletion region. (0/1)

```
function [CP] = ProbOfCollection(LD,E,D,W,IRV,CP0,isDepleted,x)
```

We start by defining the necessary constants

```
kT = 0.0259;
```

If the layer is part of the depletion region the collection probability is assumed to be unity throughout the entire layer

```
    if isDepleted == 1

        CP = ones(1,length(x));
```

```
    else
```

Next, We calculate the effective diffusion length (or Drift diffusion length) in the presence of a constant electric field.
L_D is the native diffusionlength without electric field in cm^{-1}

E is the electric field in V/cm

$$L_{D-D} = \frac{L_D}{\left(\sqrt{\left(1 + \frac{(L_D * \mathrm{E})^2}{2 * \mathrm{kT}}\right)} - \frac{L_D * \mathrm{E}}{(2 * \mathrm{kT})}\right)}$$

```
Ld =  LD/(sqrt(1+((LD*E)/(2*kT))^2)-((LD*E)/(2*kT)));
```

Next, we calculate the collection probability for a given undepleted region using the equation given by Al Omar et al. and assuming continuous collection probability across interfaces givens:

CP_0 Collection probability at the boundary closest to the depletion region

D The diffusivity of minority carrriers in the layer of interest

W The width of the undepleted region of interest

L_d The effective diffusion length of minority carriers

x The position in the layer with x=0 being defined at the edge closest to the depletion region

IRV The interface recombination velocity of minority carriers at x=W

$$\mathrm{CP} = \mathrm{CP}_0 * \frac{\left(D * \cosh\left(\frac{(W - x)}{L_D}\right) + \mathrm{IRV} * L_D * \sinh\left(\frac{(W - x)}{L_D}\right)\right)}{\left(D * \cosh\left(\frac{W}{L_D}\right) - \mathrm{IRV} * L_D * \sinh\left(\frac{W}{L_D}\right)\right)}$$

```
    num = D*cosh((W-x)./Ld)+IRV*Ld*sinh((W-x)./Ld);
    denom = D*cosh(W/Ld)+IRV*Ld*sinh(W/Ld);

    CP = CP0*num./denom;

    end
```

The function returns the collection probability array with stepsize given by the input array x

```
end
```

getRfront-

Calculates the front surface reflectance for any given structure

Contributors:

Daniel Lepkowski

Tal Kasher

Revision date:

May, 20 2020

```
function [Rfront] =
getRfront(SubstrateLayer,nComplex,Thickness,NumOfLayers)
```

Inputs:

SubstrateLayer An integer which specifies what layer is the substrate so that this layer can be treated as a massive layer rather than an epi layer

nComplex An array which contains the wavelength dependent n/k data for every layer

Thickness An array which containes the thicknesses of all of the layers (cm)

NumOfLayers An integer which specifies the total number of layers including the manditory ambient layer (aka air)

Program:

parse nComplex into n and k separately

```
k = imag(nComplex);

n = real(nComplex);
```

Setting up the wavelength axis

```
lambda = [350e-7:1e-7:1200e-7];
```

Transfer Matrix Method

The transfer matric method is a way to account for mutiple reflections and constructive and destructive interference within a structure. It works by lumping layers into Layer Matricies (*L*) and interfaces into interface matricies (*I*).

Then the total transfer matrix for the entire system (*S*) is defined as:

$$S = \prod_{n=1}^{m} \left(I_{(n-1)n} \times L_n\right) \times I_{n(n+1)}$$

for example in a 3 layer system:

$$S = I_{01} \times L_1 \times I_{12} \times L_2 \times I_{23} \times L_3 \times I_{34}$$

where I_{01} is the interface matrix between the ambient (layer 0) and the first layer (layer 1)

and L_1 is the layer matrix for the layer L_1

Calculating the Interface matricies:

The layer matrix L has the form:

$$I_{\mathrm{jk}} = \begin{bmatrix} \frac{n_{j\,\mathrm{complex}} + n_{k\,\mathrm{complex}}}{2\,n_{j\,\mathrm{complex}}} & \frac{n_{j\,\mathrm{complex}} - n_{k\,\mathrm{complex}}}{2\,n_{j\,\mathrm{complex}}} \\ \frac{n_{j\,\mathrm{complex}} - n_{k\,\mathrm{complex}}}{2\,n_{j\,\mathrm{complex}}} & \frac{n_{j\,\mathrm{complex}} + n_{k\,\mathrm{complex}}}{2\,n_{j\,\mathrm{complex}}} \end{bmatrix}$$

Calculating the layer matrix for each layer counted by the variable 'o' and each wavelength counted by the variable 'n'

The 'NumOfLayers-1' nomencalture was needed for including ambient on the front of the cell.

The resulting 4D matrix includes a 2x2 I matrix for every interface and every wavelength

```
% Calculating the Interface Matrix for each layer (o) and each wavelength
(n)

I = ones(2,2,length(n),NumOfLayers-1);

for o = 1:NumOfLayers-1

    for m = 1:length(n)

        I(:,:,m,o) =
[(nComplex(m,o)+nComplex(m,o+1))./(2*(nComplex(m,o))), (nComplex(m,o)-
(nComplex(m,o+1)))./(2*(nComplex(m,o))); (nComplex(m,o)-
(nComplex(m,o+1)))./(2*(nComplex(m,o))),
(nComplex(m,o)+(nComplex(m,o+1)))/(2*(nComplex(m,o)))];

    end

end
```

Calculating the layer matricies:

The layer matrix L has the form:

$$L = \begin{bmatrix} \exp\left(-i\left(\frac{2\pi\, n_{\text{complex}}}{\lambda}\right)d\right) & 0 \\ 0 & \exp\left(i\left(\frac{2\pi\, n_{\text{complex}}}{\lambda}\right)d\right) \end{bmatrix}$$

Calculating the layer matrix for each layer counted by the variable 'o' and each wavelength counted by the variable 'n'

The 'NumOfLayers-2' nomencalture was needed for including ambient on the front and rear of the cell. Rear of the cell is usually metal and front of the cell is usually air

The 'o+1' nomencalure was needed due to including the ambient on the top of the device

The resultant 4D matrix contains a 2x2 L matrix for every layer in the structure and wavlength

```
L = ones(2,2,length(n),NumOfLayers-2);

alpha = ones(length(n),NumOfLayers-1);

for o = 1:NumOfLayers-2

    for m = 1:length(n)

        alpha(m,o+1) = 4*pi.*k(m,o+1)./lambda(m);

        L(:,:,m,o) = [exp(-
1*1i*2*pi.*nComplex(m,o+1).*Thickness(o+1)./lambda(m)),0;0,
exp(1i*2*pi.*nComplex(m,o+1).*Thickness(o+1)./lambda(m))];

    end

end
```

Correcting the substrate layer:

Daniel found out that for wavelengths strongly absorbed in very thick layers, the intermediate values get infinitely large and breaks matlab. This block of code forces L11 and L22 to an equal value which forces total absorption.

This probably is not the best way to be doing this but it works in a pinch.

```
%whitewach substrate

if SubstrateLayer ~= 0
```

```
    for  m = 1:length(n)
        L(:,:,m,SubstrateLayer-1) =
[exp(2*pi.*k(m,SubstrateLayer).*Thickness(SubstrateLayer)./lambda(m)),0;0,
exp(-2*pi.*k(m,SubstrateLayer).*Thickness(SubstrateLayer)./lambda(m))];
    end
    test1=isfinite(L(1,1,:,SubstrateLayer-1));


    for m=1:length(n)
        if test1(1,1,m)==0
            L(1,1,m,SubstrateLayer-1)=1;
            L(2,2,m,SubstrateLayer-1)=1;
        end
    end
end
```

Calculating the total scattering matrix

Using the quation above the total scatterin matrix is calculated

First the array is allocated to avoid dynamic allocation.

```
Sfront  = zeros(2,2,length(n));
Sfront(1,1,:) = ones(1,1,length(n));
Sfront(2,1,:) = zeros(1,1,length(n));
Sfront(1,2,:) = zeros(1,1,length(n));
Sfront(2,2,:) = ones(1,1,length(n));
```

This loop calculates the scattering matrix for equal number of layer and interface matricies 'o' is the variable which controls the layer number and 'm' controls the wavelength

```
for o = 1:NumOfLayers-2
    for m = 1:length(n)
        Sfront(:,:,m) = Sfront(:,:,m)*I(:,:,m,o)*L(:,:,m,o);
    end
```

```
end
```

This final loop adds the last interface at the back

```
for m = 1:length(n)

    Sfront(:,:,m) = Sfront(:,:,m)*I(:,:,m,NumOfLayers-1);

end
```

Calculation of Reflectance

Fresnel coefficiecnts can be calculated from the total transfer matrix as follows:

$$r_{\text{front}} = \frac{S_{21}}{S_{11}}$$

```
rfront= Sfront(2,1,:)./Sfront(1,1,:);
```

This permute command makes the primary dimension wavelength

```
rfront = permute(rfront,[3 2 1]);
```

Again, due to very very strong absorption in thick layers, the rfront values can be infinitely small causing issues in matlab. This code approximates the reflectances at these troubled wavelengths by setting it equal to the wavelength immedately to the left.

This again is not the best way to do this, but thus far we have not run into instances where it is an issue.

```
test2=isfinite(rfront(:));

for m=2:length(n)

    if test2(m)==0

        rfront(m) = rfront(m-1);

    end


end
```

the Reflectance R is equal to the magnitude of the fresnel coefficients r squared

$$R = |r|^2$$

```
Rfront=abs(rfront).^2;
```

The program returns the reflectance Rfront

```
end
```

LIV

The LIV function takes in basic transport parameters and the photocurrent and calulates the illuminated I-V curve including parasitic losses from grid metal and shunt resistance. This program separately calculates the ideal I-V curve based on just transport parameters (i.e. just J01 and J02 and shunt) and then adds the effect of series. It is done this way inorder to find an approximate Jmp and Vmp for optimal grid calculation.

Contributors:

Daniel Lepkowski

Tal Kasher

Revision date:

May, 19 2020

```
function
[V,JlightmA,Vdiode,JlightIdealmA,Rseries,Rshunt,J01,J02,percentMetal,FF,FF
Ideal,Eff,EffIdeal,Jsc,Voc,Jmp,Vmp]...

    =
LIV(spectrum,Dn,Dp,Ln,Lp,tau_d,Sn,Sp,Rshunt,RseriesVertical,n2,ni,Nd,Na,Jp
hoto,rho_S,Wemit,Wbase,W_dep_Emit,W_dep_Base, ...

          A,B,Vmin,Vmax,Vstep,mf,mb,t,S,W_F,fixedGrid,W_B)
```

Inputs:

Device description:

A ***Dimension of the cell along the busbar length(cm).***

B ***Dimension of the cell along the grid finger length(cm).***

W_{emit} Metalurgical width of the N-type doped layer (cm)

W_{base} Metalurgical width of the P-type doped layer (cm)

$W_{\mathrm{dep\ emit}}$ Depletion width on the N-type side of the junction (cm)

$W_{\mathrm{dep\ base}}$ Depletion width on the P-type side of the junction (cm)

N_a Doping density on the P-type side of the junction (cm^{-3})

N_d Doping density on the N-type side of the junction (cm^{-3})

J_{photo} Photo generated current calculated from integrated EQE (A/cm^{-2})

Desired parameters for I-V curve:

Spectrum A string which holds the name of the desired solar spectrum ('AM0' or 'AM1p5G')

$V_{\min}$ Minimum voltage for the ideal didode (not including series resistance)

$V_{\max}$ Maximum voltage for the ideal diode (not including series resistance)

V_{step} Voltage step for the ideal diode (not including series resistance)

Transport Properties for diode dark currents

D_n Diffusivity of minority carrier electrons in the P-type layer (cm^2/s)

D_p Diffusivity of minoirty carrier holes in the N-type layer (cm^2/s)

L_p Diffusion length of minority carrier holes in the N-tpe layer (cm)

L_n Diffusion length of minority carrier electrons in the p-type layer (cm)

S_n Surface recombination velocity of electrons in the p-type layer at the surface away from the junction (cm/s)

S_p Surface recombination velocity of holes in the n-type layer at the surface away from the junction (cm/s)

τ_d Average minority carrier lifetime in the depletion region (s)

n_2 ideality factor of the junction recombination current diode

$R_{\text{series Vertical}}$ Vertical component of the series resistance to be used as a fitting parameter ($\Omega \cdot \text{cm}^2$)

n_i Intrinisic carrier concentration of base and emitter material (homojunction assumed) (cm^{-3})

R_{Shunt} Area normalized shunt resistance ($\Omega \cdot \text{cm}^2$)

Parameters for grid metal

ρ_S Semiconductor sheet resistivity

t Thickness of the grid metal

W_F Width of the grid fingers

m_f Variable which accounts for tappering of grid fingers ($m_f = 4$ linearly tapered) ($m_f = 3$ for constant width)

m_b Variable which accounts for tappering of busbar ($m_f = 4$ linearly tapered) ($m_f = 3$ for constant width)

fixedGrid Boolean variable that allows user to specify a fixed grid or the optimal grid (0/1)

W_B Average Width of the Busbar (cm) (only used if fixedGrid=1)

S Spacing between grid fingers (cm) (only used if fixedGrid=1)

Global Input Variables

kT thermal constant (0.0259 eV)

q electron charge (1.602e-19 C)

Outputs:

V Array of voltages from terminal to terminal for the total illuminated J-V curve (i.e. including series resistance) (V)

$J_{\text{light mA}}$ The array of currents which corresponds to V to create the J-V curve (mA/cm^2)

J_{SC} Short circuit current density (A/cm^2)

V_{OC} Open Circuit Voltage (V)

FF Fill factor of the illuminated I-V curve inlcuding series resistance expressed as a decimal

J_{mp} Current density at the max power point (A/cm^2)

V_{mp} Voltage at the Max power point (V)

Eff Solar Conversion Effeiciency including series resistance expressed as a percent (%)

V_{diode} Array of voltages which correspond to the voltage across the junction (i.e. ideal diode no series resistance) (V)

$J_{\text{light ideal mA}}$ The array of current for the ideal J-V curve (i.e. no series resistance) (mA/cm^2)

FF_{ideal} Fill factor of the ideal diode (no series resistance) expresses as a decimal

$\text{Eff}_{\text{ideal}}$ Efficiency of the cel without series resistance expressed as a percent (%)

R_{Series} Total area normalized series resistance ($R_{\text{grid}} + R_{\text{series Vertical}}$)($\Omega \cdot \text{cm}^2$)

R_{Shunt} Area normalized shunt resistance ($\Omega \cdot \text{cm}^2$)

J_{01} Diffusion current density (A/cm^2)

J_{02} Junction recombiniation current density (A/cm^2)

percentMetal Percent metal coverage of the cell expressed as a decimal

Program:

Recall global Variables

```
global kT;

global q;
```

Calculate the undepleted width of the N- an P-type regions and the total width of the depletion region

```
Wn = Wemit-W_dep_Emit;

Wp = Wbase-W_dep_Base;

Wd = W_dep_Emit + W_dep_Base;
```

Calculate the Dark Diode Diffusion Current (J_{01})

Contribution to J01 from each side of the diode is calculated and summed together:

$$J_{01p} = q * n_i^2 * \frac{D_p}{N_d} \frac{\left(\frac{D_p}{L_p} * \sinh\left(\frac{W_n}{L_p}\right) + S_p * \cosh\left(\frac{W_n}{L_p}\right)\right)}{\frac{D_p}{L_p} * \cosh\left(\frac{W_n}{L_p}\right) + S_p * \sinh\left(\frac{W_n}{L_p}\right)}$$

$$J_{01n} = q * n_i^2 * \frac{D_n}{N_a} \frac{\left(\frac{D_n}{L_n} * \sinh\left(\frac{W_p}{L_n}\right) + S_n * \cosh\left(\frac{W_p}{L_n}\right)\right)}{\frac{D_n}{L_n} * \cosh\left(\frac{W_p}{L_n}\right) + S_n * \sinh\left(\frac{W_p}{L_n}\right)}$$

```
num_p = (Dp/Lp)*sinh(Wn/Lp)+Sp*cosh(Wn/Lp);
denom_p = (Dp/Lp)*cosh(Wn/Lp)+Sp*sinh(Wn/Lp);

J01p = q*(ni^2)*Dp/(Nd*Lp)*(num_p/denom_p);



num_n = (Dn/Ln)*sinh(Wp/Ln)+Sn*cosh(Wp/Ln);
denom_n = (Dn/Ln)*cosh(Wp/Ln)+Sn*sinh(Wp/Ln);

J01n = q*(ni^2)*Dn/(Na*Ln)*(num_n/denom_n);
```

```
J01 = J01n+J01p;
```

Calculate the Dark Junction Recombination Current (J_{02})

$J_{02} = \frac{q * n_i * W_{\text{dep}}}{\tau_{\text{dep}}}$ Some people argue that the denominator is $2\tau_{\text{dep}}$ but since this is a fitting parameter in the first place it doesnt really matter

```
J02 = q*ni*Wd/tau_d;
```

The Ideal Diode Simulation

Setting up the simulation of the dark current calculated via the double-diode model without series resistance, using user specified voltage range

```
Vdiode = Vmin:Vstep:Vmax;

Jdark = J01*(exp((Vdiode)/(kT))-1)+J02*(exp((Vdiode)/(n2*kT))-
1)+Vdiode/Rshunt;
```

Calulating the illuminated I-V curve using the solar industry standard (1st quadrant = power generation.)

```
JlightIdeal = Jphoto-Jdark;
```

Calculating the ideal max power point for simulation of ideal grid metal and lateral series resistance

```
PlightIdeal = JlightIdeal.*Vdiode;



[~,indexJmpIdeal] = max(PlightIdeal);
JmpIdeal =JlightIdeal(indexJmpIdeal);

VmpIdeal = Vdiode(indexJmpIdeal);
```

Calculating $V_{\text{OC Ideal}}$ by looking for the minimum value of current

```
[~,indexJVocIdeal] = min(abs(JlightIdeal));

VocIdeal = Vdiode(indexJVocIdeal);
```

Calculating J_{SC}(this is an approximation and could be refined)

```
[~,indexVJscIdeal] = min(abs(Vdiode));

JscIdeal = JlightIdeal(indexVJscIdeal);
```

Calculating the series resistance and percent metal using either a user specified fixed grid or the optimal grid and adding in the vertical series resistance fitting parameter.

```
[Rseries,percentMetal] =
getSeriesResistance(rho_S,JmpIdeal,VmpIdeal,A,B,mf,mb,t,S,W_F,fixedGrid,W_
B);

Rseries = Rseries + RseriesVertical;
```

Recalculating the I-V curve including shadowing losses

```
Jlight= Jphoto*(1-percentMetal)-Jdark;
```

Calulating the new voltage array based on the series resisance losses (this is technically an approximation as the general solution to the double diode model with series resistance is not solvable analytically)

```
V = Vdiode-Jlight*Rseries;
```

Extracting the important I-V metrics

Calculating $J_{mp}$and V_{mp}

```
Plight = Jlight.*V;

[~,indexJmp] = max(Plight);

Jmp = Jlight(indexJmp);

Vmp = V(indexJmp);
```

Calculating V_{OC} by looking for the minimum value of current

```
[~,indexJVoc] = min(abs(Jlight));

Voc = V(indexJVoc);
```

Calculating J_{SC}(this is an approximation and could be refined)

```
[~,indexVJsc] = min(abs(V));
```

```
Jsc = Jlight(indexVJsc);
```

Calculating FF and AM1.5G efficiency

```
FF = (Jmp*Vmp)/(Voc*Jsc);

FFIdeal = (JmpIdeal*VmpIdeal)/(VocIdeal*JscIdeal);

Eff = Jmp*Vmp*1000;

EffIdeal = JmpIdeal*VmpIdeal*1000;
```

Accounting for AM0 spectrum

```
if strcmp(spectrum,'AM0')

    Eff=Eff/1.367;

    EffIdeal=EffIdeal/1.367;

end
```

Changing units to $\mathrm{mA/cm^2}$ for easier plotting.

```
JlightmA = Jlight*1000;

JlightIdealmA = JlightIdeal*1000;



end
```

getSeriesResistance

This function determines the Series resistance and metal shadowing. The user can either specify a grid or have it optimized for a given Jmp and Vmp

Adapted from: *Martin Green's Solar Cells Operating Principals, Technology, and System Applications pg. 155-158*

Contributors:

Daniel Lepkowski

Tal Kasher

Revision date:

May, 19 2020

```
function [Rseries,percentMetal] =
getSeriesResistance(rho_S,Jmp,Vmp,A,B,mf,mb,t,S,W_F,fixedGrid,W_B)
```

Inputs:

t Thickness of the grid metal (cm)

W_F Width of the grid fingers (cm)

ρ_s Sheet resistivity of the semiconductor (Ω/square)

A ***Dimension of the cell along the grid finger length(cm). FORGOT WHICH DIRECTION WAS WHICH***

B ***Dimension of the cell along the grid finger length(cm).***

J_{mp} estimation of the current density at max power output (mA/cm^2)

V_{mp} estimation of the voltage at max power output (V)

m_f Variable which accounts for tappering of grid fingers ($m_f = 4$ linearly tapered) ($m_f = 3$ for constant width)

m_b Variable which accounts for tappering of busbar ($m_f = 4$ linearly tapered) ($m_f = 3$ for constant width)

fixedGrid Boolean variable that allows user to specify a fixed grid or the optimal grid (0/1)

W_B Average Width of the Busbar (cm) (only used if fixedGrid=1)

S Spacing between grid fingers (cm) (only used if fixedGrid=1)

Outputs:

R_{Series} Area normalized series resistance of the grid ($\Omega \cdot \text{cm}^2$)

percentMetal Percent metal coverage as a decimal

Program:

Set up metal parameters

ρ_{mf} resistivity of the metal fingers stack (Ω/cm)

ρ_{mb} resistivity of the metal busbar stack (Ω/cm)

ρ_c Specific contact resistivity between semiconductor and metal (Ω/cm^2)

```
rho_mf = 2.4E-10; %resistivity of the metal fingers stack [Ohm/cm]

rho_mb = 2.4E-10; %resistivity of the metal busbars stack [Ohm/cm]

rho_C = 1E-5; %Specific Contact Resistiviity  [Ohm/cm^2]
```

Calculate sheet resistance of grid metal

ρ_{smf} Sheet resistance of the busbar metal.

ρ_{smb} Sheet resistance of the gridfinger metal.

$$\rho_{\text{Sheet}} = \frac{\rho}{t}$$

```
rho_smf = rho_mf/t;

rho_smb = rho_mb/t;
```

Calculate the ideal grid if desired

```
if fixedGrid == 0
```

Calculate ideal busbar width from M. Green book.

```
     W_B = A*B*sqrt((rho_smb/mb)*(Jmp/Vmp)); %without contact resistnace
for busbars
```

Set up to find optimal grid spacing (Sopt)

```
    S = 0.001:0.001:1;

    Pleft = ones(1,length(S));
```

```
    Pright = ones(1,length(S));
```

In order to caclulate the ideal grid metal the resistive losses and shadowing losses are calculated as a function of contact spacing (S). The optimal S is determined where the derivative of the shadowing losses is equal to the derivative of the contact losses.

$$\frac{d}{\mathrm{d}S}P_{\mathrm{res}}(S_{\mathrm{opt}}) = \frac{d}{\mathrm{d}S}P_{\mathrm{shadow}}(S_{\mathrm{opt}})$$

These power losses (Pleft and Pright) will be used to determine ideal S

```
    for i = 1:length(S)

        [Prf,~,Psf,~,Pcf,Ptl] =
ContactSpacing(mf,mb,t,W_F,A,B,Jmp,Vmp,rho_mf,rho_mb,rho_C,rho_S,S(i),W_B)
;

        Pleft(i) = Prf+Pcf+Ptl;

        Pright(i) = Psf;

    end
```

Take the derivative of the resistive and shadowing power loss as a function of grid spacing.

```
    dPleft = diff(Pleft)./diff(S);

    dPright = diff(Pright)./diff(S);
```

Find the minimum of the differences in derivative and calculate Sopt
i.e. Where does the derrivative of resistive power loss equal the derrivative of shadowing power loss

```
    dP = abs(dPleft + dPright);

    [~,index] = min(dP);

    Sopt = S(index);
```

Rerun the power loss caclulator with the opitmal grid spacing.

```
    [Prf,Prb,Psf,Psb,Pcf,Ptl] =
ContactSpacing(mf,mb,t,W_F,A,B,Jmp,Vmp,rho_mf,rho_mb,rho_C,rho_S,Sopt,W_B)
;
```

Calculate the relative resistive and shadowing losses

```
    Pres = Prf+Prb+Pcf+Ptl;
```

```
    Pshadow = Psf+Psb;
```

Percent metal coverage is equal to the relative shadowing power loss.

```
    percentMetal = Pshadow; %power loss [%]
```

Calculate the area normalized series resistance ($\Omega \cdot \mathrm{cm}^2$) from the relative resistive power loss (Pres):

$$P_{\mathrm{resistive}} = \frac{R_{\mathrm{series}} * J_{\mathrm{mp}}^2}{P_{\mathrm{ideal}}}$$

$$R_{\mathrm{series}} = \frac{(P_{\mathrm{resistive}} * J_{\mathrm{mp}} * V_{\mathrm{mp}})}{(J_{\mathrm{mp}}^2)}$$

```
    Rseries = Pres*(Jmp*Vmp)/(Jmp^2); %[Ohm*cm^2]
```

Fixed grid

If the user wants a fixed grid, calculate the resistive losses and shadowing losses

```
else

    [Prf,Prb,Psf,Psb,Pcf,Ptl] = 
ContactSpacing(mf,mb,t,W_F,A,B,Jmp,Vmp,rho_mf,rho_mb,rho_C,rho_S,S,W_B);



    Pres = Prf+Prb+Pcf+Ptl;

    Pshadow = Psf+Psb;
```

Percent metal coverage is equal to the relative shadowing power loss.

```
    percentMetal = Pshadow;
```

Calculate the area normalized series resistance ($\Omega \cdot \mathrm{cm}^2$) from the relative resistive power loss (Pres):

$$P_{\mathrm{resistive}} = \frac{R_{\mathrm{series}} * J_{\mathrm{mp}}^2}{P_{\mathrm{ideal}}}$$

$$R_{\mathrm{series}} = \frac{(P_{\mathrm{resistive}} * J_{\mathrm{mp}} * V_{\mathrm{mp}})}{(J_{\mathrm{mp}}^2)}$$

```
    Rseries = Pres*(Jmp*Vmp)/(Jmp^2);

end
```

Return the percent metal and the area normalized series resistance

```
end
```

LIV_VDCC

This function calculates an illuminated I-V curve from double diode parameters and an array of voltage dependent light current. Effectively this is a simpler version of the LIV program as it does not need to calculate transport parameters. This code assumes a fixed grid outputted from a prior iteration of the getSeriesResistance function.

Contributors:

Daniel Lepkowski

Tal Kasher

Revision date:

May, 19 2020

```
function [V,JlightmA,FF,Eff] =
LIV_VDCC(spectrum,Rshunt,Rseries,n2,Jphoto,Vdiode,J01,J02,percentMetal)
```

Inputs:

spectrum string which contains the name of the spectrum used ('AM0' or 'AM1p5G')

V_{diode} Array of voltages which correspond to the voltage across the junction (i.e. ideal diode no series resistance) (V)

R_{Series} Total area normalized series resistance $(R_{\text{grid}} + R_{\text{series Vertical}})$ $(\Omega \cdot \text{cm}^2)$

R_{Shunt} Area normalized shunt resistance $(\Omega \cdot \text{cm}^2)$

J_{01} Diffusion current density (A/cm^2)

J_{02} Junction recombiniation current density (A/cm^2)

n_2 Ideality factor of the junction recombination current diode

percentMetal Boolean variable that allows user to specify a fixed grid or the optimal grid (0/1)

J_{photo} An array of voltage dependent photocurrents calculated by evaluating the EQE at various bias

Global Variables

kT Thermal constant (0.0259 eV)

Outputs:

V Array of voltages from terminal to terminal for the total illuminated J-V curve (i.e. including series resistance) (V)

$J_{\text{light mA}}$ The array of currents which corresponds to V to create the J-V curve ($\mathrm{mA/cm^2}$)

`FF` Fill factor of the illuminated I-V curve inlcuding series resistance expressed as a decimal

`Eff` **AM 1.5G Solar Conversion Effeiciency including series resistance expressed as a percent (%) NEED TO INCORPORATE AM0**

Program:

Import global variables

```
global kT;
```

Calculating the dark J-V curve without series resistance

```
Jdark = J01*(exp((Vdiode)/(kT))-1)+J02*(exp((Vdiode)/(n2*kT))-
1)+Vdiode/Rshunt;
```

Calculating the illuminated J-V curve without series resistance.
Remember in this case J_{photo} is a voltage dependent array

```
Jlight = Jphoto*(1-percentMetal)-Jdark;
```

Creating a new voltage axis to incorporate series resistance.
This is technically an approximation as the general solution to the double diode model with series resistance is not solvable analytically

```
V = Vdiode-Jlight*Rseries;
```

Calculating the max power point

```
Plight = Jlight.*V;

[~,indexJmp] = max(Plight);

Jmp= Jlight(indexJmp);

Vmp = V(indexJmp);
```

Calculating V_{OC} by looking for the current value closest to zero

```
[~,indexJVoc] = min(abs(Jlight));
```

```
Voc = V(indexJVoc);
```

Calculating J_{SC} by looking for the voltage value closest to zero

```
[~,indexVJsc] = min(abs(V));

Jsc = Jlight(indexVJsc);
```

Calculating `FF` and efficiency

```
FF = (Jmp*Vmp)/(Voc*Jsc);

Eff = Jmp*Vmp*1000;
```

Accounting for AM0 spectrum

```
if strcmp(spectrum,'AM0')

    Eff=Eff/1.367

end
```

Unit conversion to make plotting easier

```
JlightmA = Jlight*1000;



end
```